Microphones as Airspeed Sensors for Micro Air Vehicles

MSc Thesis Report

Momchil Makaveev

TU Delft

Microphones as Airspeed Sensors for Micro Air Vehicles

MSc Thesis Report

Thesis report

by

Momchil Makaveev

to obtain the degree of Master of Science
at the Delft University of Technology
to be defended publicly on January 31, 2023 at 13:00

Thesis committee:

Chair:	Dr. Guido de Croon
Supervisor:	Dr. Ewoud Smeur
External examiner:	Dr. Alessandro Bombelli
Place:	Faculty of Aerospace Engineering, Delft
Project Duration:	February, 2021 - January, 2023
Student number:	4373154

An electronic version of this thesis is available at `http://repository.tudelft.nl/`.

Faculty of Aerospace Engineering · Delft University of Technology

Preface

This report outlines the work I performed in relation to my Master thesis and it is the final piece of my Master's degree in Control & Simulation at the faculty of Aerospace Engineering at Delft University of Technology. My thesis was filled with a lot of firsts for me, allowing me to develop new skills, while its interdisciplinary nature required of me to learn a lot about different fields of science and engineering. There were many challenging and difficult moments, and looking back on them, I am actually grateful as due to them I was able to grow immensely, not only in professional, but also in personal sense.

No man journeys alone and this project was no exception. There were many people that helped me along the way and I would not have reached to this point without their support. As such, I would like to use this opportunity to express my gratitude to them. Of course, I want to start with my thesis supervisor, Ewoud Smeur, who has guided me throughout all steps of the thesis, helped me with all of its different aspects and was always there for me when I ran into problems or was not sure how to go forward. Next, I would like to thank Colin Van Dercreek and Daniele Ragni who were instrumental for the successful conduction of the wind tunnel experiments. Another person who helped me was Mirjam Snellen, whose expertise were invaluable in understanding and analyzing the experimental data. Next to that, I would like to thank my good friend Emiliyan Mihaylov who taught me everything I know about 3D printing, as well as Kaloyan Kirilov, Stanimir Stoev and Ricardo Van Der Plijm who provided me with valuable and detailed feedback for my scientific paper. Finally, I would like to thank my friends and family for their never ending support and for always believing in me. You kept me up during the tough days and shared my joy during the good ones. Cheers!

Dear reader, I hope you will enjoy reading these pages. I have worked hard and put many hours towards getting here for a really long time.

Momchil Makaveev
Delft, January 2023

Contents

Nomenclature

List of Abbreviations

AC	Alternating Current
ADC	Analog to Digital Converter
ANC	Adaptive Noise Cancellation
ANN	Artificial Neural Network
AoA	Angle of Attack
DC	Direct Current
DNS	Direct Numerical Simulation
FFT	Fast Fourier Transform
GPS	Global Positioning System
LBL	Laminar Boundary Layer
MAV	Micro Air Vehicle
PSD	Power Spectral Density
RMSE	Root-Mean-Square Error
RPM	Rounds per Minute
SPL	Sound Pressure Level
TBL	Turbulent Boundary Layer
TF	Transfer Factor
UAV	Unmanned Aerial Vehicle
VTOL	Vertical Take-off and Landing

List of Symbols

δ	Boundary Layer Thickness
ΔV	Voltage Change
δ^*	Displacement Thickness
μ	Adaptive Learning Parameter
μ	Dynamic Viscosity
ω_0	Angular Frequency
$\overline{P^2}$	Mean-square Pressure
Φ	Wall-pressure spectrum
ρ	Density
e	Model Error
H	Hidden Neurons
J	Jacobian Matrix
M	Mach Number
p'	Fluctuating Component of Pressure
p'_a	Fluctuating Acoustic Component of Pressure
p'_{TBL}	Fluctuating Pseudo-sound Component of Pressure
p'_v	Fluctuating Vibrational Component of Pressure
p_{ref}	Reference Pressure ($= 20 \times 10^{-6}$)
q_∞	Dynamic Pressure
Re_x	Reynolds number based on distance
S_i	First-order Sobol Index
Sh	Strouhal Number
U_∞	Free-stream Velocity
$V(Y)$	Total Output Variance
V_i	Input Variance
V_{left}	Left-mounted microphone signal
V_{right}	Right-mounted microphone signal
V_{sub}	Subtracted signal
$w(n)$	Window Function (of length n)
w_t	Artificial Neural Network's Weights

List of Figures

List of Tables

1

Introduction

For aerial vehicles, especially those with fixed wings, airspeed measurement is crucial for safe and effective flight. It is an important flight parameter as the dynamic pressure scale with with the airspeed squared, which in turn governs the aerodynamic forces and moments acting on the vehicle and impacts the effectiveness of the vehicle's aerodynamic surfaces [1]. In the context of unmanned aerial vehicles (UAVs), the airspeed measurement is used by their flight control system to calculate the required control inputs for longitudinal control [2].

Typically, Pitot tubes are implemented on aircraft and small UAVs to measure the vehicle's airspeed. Their working principle can be described as sensing the dynamic pressure, caused by the movement of the vehicle within the mass of air, and subsequently translating that to a measure of the aircraft's airspeed [3]. While being mechanically simple, they could be too large or heavy to use on some MAVs. Furthermore, the accuracy of a Pitot tube decreases as the airspeed gets lower [4] due to the measured dynamic pressure being proportional to the airspeed squared. Additionally, the Pitot tube needs to be aligned to the direction of the airflow, in order to give accurate readings. Under large angles of attack the Pitot tube will be misaligned with respect to the airflow, leading to a reduced dynamic pressure reading, and potentially an increased static pressure reading, resulting in an overall lower measured airspeed. This becomes a serious issue for slow flying UAVs of the hybrid tailsitter type, which combine both hovering and forward flight capabilities by tilting themselves forward to transition from vertical to horizontal flight [5].

Alternative methods for airspeed measurement include hot-wire anemometers and GPS sensors. The hot-wire anemometer works by measuring the electrical power needed to keep the hot element at its target temperature as the colder flow passes. The power provides a measure of the airspeed as it gets higher more flow would pass, thus needing more power to maintain the hot element's temperature. The hot-wire anemometer does not suffer from reduced accuracy at low airspeeds [6] and does not necessarily need to be aligned to the direction of the airflow. However, it is fragile and requires precise calibration to yield accurate results. The GPS sensor gives measure of the vehicle's ground speed, not the airspeed [7]. To measure the airspeed with a GPS sensor, it needs to be used in combination with the vehicle's inertial sensors and a model of the vehicle dynamics. Furthermore, environmental factors could potentially deteriorate the accuracy of the GPS or render its use completely unfeasible. Examples include high buildings and terrain, tunnels, or areas of restricted GPS coverage. These drawbacks of the GPS sensor are especially impactful for small UAVs, which often operate at lower altitudes, in urban areas, or in remote areas. As such, there is an existing need for an alternative airspeed sensor for small UAVs - one that can operate in the different flight modes of the vehicle, at any time and geographical location, without requiring frequent maintenance and calibration.

For a body in motion in a fluid, a thin viscous region of flow forms immediately adjacent to its surface, known as the boundary layer. The flow in the boundary layer is slowed down compared to the free stream flow due to the effects of friction. Just past the leading edge, the flow regime of the boundary layer is laminar. Traveling downstream along the surface, instabilities start to develop in the laminar flow, in a region known as the transition layer. These instabilities lead to varying components of dynamic pressure, exerted in different directions within the boundary layer, which in turn amplify said instabilities, turning them into fully turbulent flow structures forming the turbulent boundary layer (TBL) [8]. The type of flow structures present in the TBL are of rotational nature, such as vortices and eddies that mix together across

the various layers of the TBL, and introduce fluctuations in the dynamic pressure that are transmitted throughout the TBL. Literature shows that the spectral features of these fluctuations at the surface beneath the TBL are affected by the free-stream velocity [9, 10]. This suggests that there might be an alternative method to measure airspeed by capturing the TBL-induced wall-pressure fluctuations, also known as pseudo-sound [11], using microphones and relating them to the vehicle's airspeed.

The current report describes a novel concept for an airspeed instrument that tackles the drawbacks of the currently existing instruments available for airspeed measurements. The report includes a detailed review of the relevant theory, as well as a proposal for the design of such an instrument, together with an evaluation of said design. The underlying working principle of the instrument is to relate the Power Spectral Density (PSD) of the wall-pressure fluctuations in the TBL to the vehicle's airspeed. Microphones are used to capture the TBL-induced fluctuations at the surface and their PSD is related to the vehicle's airspeed using dedicated models, constructed as part of the project. The models are created with data obtained from both wind tunnel and flight experiments, also performed as part of the project.

The work carried out as part of the current research is interdisciplinary and tackles a broad problem relevant on both academic and industry level. The academic interests include the investigation of the nature and behavior of the TBL, the effects of the flow velocity upon the TBL-induced pressure fluctuations, and the development of accurate and precise models relating the two. The findings could be relevant not only for the purposes of the current research but also other research areas, such as for more detailed understanding of the noise characteristics of turbulent airflow for sound intensity measurements in noise control engineering [12]. On an industry level, the interest is mainly in filling a gap in airspeed instrument offerings that could be installed on a variety of MAVs with different sizes and configurations, be able to provide reliable airspeed measurements under wide range of flight and environmental conditions, and be easy to maintain.

1.1. Research Formulation

The research project is aimed at designing and evaluating an airspeed instrument concept, able to provide accurate measurements even at low airspeeds and for a wide range of angles of attack, that makes use of the relation between the spectral characteristics of the TBL-induced pressure fluctuations and the vehicle's airspeed as a working principle. After analyzing on-board footage from a hybrid MAV in flight, it was confirmed that the loudness and pitch of the sound noise recorded by the microphone changes with the velocity of the vehicle. As such, it is decided to further investigate the impact airspeed has upon the resulting sound noise's pressure level and frequency spectrum distribution captured by the microphone, and study the feasibility of using these characteristics as the working basis for an airspeed instrument.

A microphone placed onto the vehicle's surfaces, taking sound measurements during flight, will capture noise of many different sources, e.g. engine noise, environmental noise (e.g. rain), and noise due to the air particles' movement within the airflow. The latter will be the focus of the research and will serve as the working principle of the proposed instrument since it is dependent on the vehicle's airspeed. The source of this noise stems from phenomena inside the boundary layer that forms over the vehicle's surfaces (wings, fuselage, etc.), which is the topic of Subsection 3.2.2. Therefore, the relation between the airspeed and the resulting sound noise from the boundary layer will be investigated.

The chosen working basis for the instrument, especially the application of microphones for capturing sounds, will have two major implications. The first one will be that the airspeed instrument will require a processing unit that will register the microphone measurements and also compute the vehicle's airspeed, as well as a memory unit that will hold the models used to perform the airspeed estimation based on the microphone measurements. The second implication is that microphones have specific performance characteristics and are not perfect sound measuring devices [13]. As such, the direct application of any analytical models from theory might not yield a satisfactory accuracy. Therefore, it might be better to construct the models based on data gathered from experiments where the same microphones are utilized.

Before the microphone measurements can be used as data for modeling the relation between the characteristics of the pressure fluctuations stemming from the boundary layer and the vehicle's airspeed, they need to be processed. This includes signal processing, as well as filtering acoustic sounds originating from other sources. All of this is investigated in Subsection 3.2.3. Afterwards, the model development can take place. Many different model structures, optimization algorithms and data sampling algorithms

are available for mapping the relation between input and output parameters from collected data. In the development of models from datasets, machine learning techniques can be employed, which are at the forefront of the field of mathematical modeling [14]. Furthermore, their use is currently growing in many different areas including in the field of sound processing, meaning that there is continuous improvement and wide support available. This makes them an attractive option to consider, as discussed in Subsection 3.2.4.

Finally, the overarching goal of the research project can be formulated as the creation of an airspeed instrument, that is accurate even at low airspeeds and for a wide range of angles of attack, and whose working principle is to relate the characteristics of the TBL-induced pressure fluctuations, which are filtered in order to isolate them from sounds originating from other sources, and pertain them to the vehicle's airspeed using developed models relating the two. This presents the major contribution of the research project to the body of knowledge.

The research project will involve theories and techniques from many different research areas and fields of engineering. Their integration within the framework of the project might pose challenges and will be touched upon in the literature review in Section 3.2. Furthermore, the research work will need to tackle existing gaps in both the scientific body of knowledge as well as the technological state-of-the-art. All of the identified research areas, engineering practices, and technologies, that will be relevant for the research project can be seen on the mind map in Figure 1.1.

Figure 1.1: Mind map of the different research areas and fields relevant for the research project.

1.1.1. Research Objectives

Based on the research project description and the definition of its overarching goal, the following main research objective can be formulated:

Research Objective

The research objective is to develop an accurate mean for the flight control system of a hybrid micro air vehicle to determine the drone's airspeed by designing a novel instrument that estimates the vehicle's airspeed by relating it to the power spectral density of the pressure fluctuations originating from the boundary layer.

The fulfillment of the above stated objective will involve activities of different nature, which can be grouped in different phases. One of the most important parts of the project is the model of the relation between the vehicle's airspeed and the PSD of the pressure fluctuations that arises from the phenomena in the boundary layer, since it will form the working basis of the instrument. As such, the following sub-goal for the research project is defined:

"Establish a model for the relation between the vehicle's airspeed and the corresponding power spectral density of the pressure fluctuations arising from the boundary layer phenomena."

An important consideration is the fact that microphones will be utilized in order to capture the TBL-induced pressure fluctuations. Since microphones are not perfect pressure transducers, the computed spectra might differ from those computed theoretically for the same airspeed. As such, it is recommended that microphone-specific data is collected by carrying out practical experiments in a wind tunnel and in-flight over the range of airspeeds of interest. Furthermore, dissimilar types and models of microphones might differ in their performance parameters, meaning that the microphones utilized as part of the proposed airspeed instrument will have to be the same - or have the similar performance characteristics - as those used in the data collecting experiments. Therefore, another sub-goal can be defined be:

"Obtain microphone-specific data about the properties of the pressure fluctuations caused by the phenomena inside the boundary layer over a range of airspeeds of interest by performing practical experiments, processing the collected measurements, and adjusting the mathematical models correspondingly."

1.1.2. Research Questions

Since the working principle of the instrument will be to estimate the vehicle's airspeed based on the measured characteristics of the sounds originating from the boundary layer, the following main research question can be formulated:

Research Question 1

"How is the power spectral density of the pressure fluctuations stemming from the boundary layer related to the vehicle's airspeed?"

Following the project description, the research question can be broken down into multiple sub-questions that will tackle the main aspects of the research work. The relation between the parameters of interest will be modeled using experimental data, where specific microphones will be used to record the resulting sound at different airspeeds. A microphone that is mounted on the vehicle will capture acoustic sound contributions from many different sources, e.g. the engines, the environment, etc. To make sure that only the sound of interest for the research is taken, a method will be needed to filter the contribution of any unwanted sources to the microphone measurements. As such, the following sub-question will be defined:

Research Question 1.1

"What part of the captured sound's power spectral density can be attributed to the pressure fluctuations induced by the phenomena inside the boundary layer and how it can be isolated from the overall microphone signals?"

Having the answer to the question above will allow for the relation between the vehicle's airspeed and the characteristics of the boundary layer pressure fluctuations to be developed. However, the separation of flow from the vehicle's surfaces will affect the nature of the pressure fluctuations generated by phenomena inside the flow [15], as it will be elaborated in Subsection 3.2.2. Due to the fact that the main parameter governing flow separation is the vehicle's angle of attack [16], its state will have an impact upon the recorded sound by the microphone. Therefore, another research question will be formulated as:

Research Question 1.2

"How does the angle of attack affect the characteristics of the pressure fluctuations captured by a microphone mounted on the vehicle's surface?"

Another important consideration is the mounting location of the microphone or the microphone array [17]. It might have an impact upon the levels of the captured engine noise, or the sounds from the environment. Furthermore, mounting a microphone on different types of surfaces needs to be considered, where the behavior of the formed boundary layer might differ and affect the traits of the TBL-induced pressure fluctuations (e.g. wings, fuselage, etc.). Thus, the following research question will be stated:

Research Question 1.3

"How does the microphone mounting location affect the measured characteristics of the pressure fluctuations stemming from the boundary layer?"

The final aspect of the research project is the physical construction and integration of the airspeed instrument. This will involve identifying the required components for such an instrument and how they will work together. This will outline the final research question to be answered:

Research Question 1.4

"What are the required hardware components that will constitute an airspeed instrument, whose working principle is to estimate the vehicle's airspeed by relating it to the characteristics of the pressure fluctuations originating from the phenomena inside the boundary layer?"

And once this has been answered, one last sub-question will be defined, covering the final part of the research project:

Research Question 1.5

"How can the different airspeed instrument components be integrated to form a functioning system?"

By answering all of the research questions and sub-questions stated, the project can be concluded and its findings evaluated.

1.2. Structure of the Report

The purpose of this report is to describe the work carried out as part of the thesis project, whose goal is to design and evaluate a novel airspeed instrument aimed at micro air vehicles. It includes a detailed elaboration on the working principle of the instrument, together with an extended review of the relevant theory and airspeed modeling methods, a proposed instrument design suitable for micro air vehicles, and an evaluation of the feasibility to utilize the proposed working principle for the purposes of estimating the airspeed of vehicles in flight. Also included is a discussion on the potential of the proposed airspeed instrument concept, together with proposals for improving or extending its functionality.

The report is divided into 4 major parts. Part I focuses on the scientific article, which is shown in Chapter 2. The paper details the design of the proposed airspeed instrument, describes the different

experiments conducted as part of the research, together with the gathered data and its processing, elaborates on the structure and training of the models used to estimate the airspeed from the PSD of the microphones' signals and gives the achieved accuracy of the constructed models. The impact of the angle of attack is also studied by training models that include this parameter as a separate input next to the PSD of the microphones signals. Lastly, the PSD of the microphones' recordings from the wind tunnel experiments is compared to the predictions of selected semi-empirical single-point frequency spectrum models as well as to the PSD of recording from microphones mounted on a flat plate placed in the same wind tunnel. Part II contains the Preliminary Analysis made out of Chapter 3 and Chapter 4. It outlines the first steps of the research project. Chapter 3 contains the Literature Review that has been assessed for the course AE4020 Literature Study. It provides a detailed review of the theory of sound and flow structures in boundary layers with the aim of relating the two. It also summarize the work of other researchers in the field. Chapter 4 elaborates on the research methodology. Part III, containing only Chapter 5, provides further results from the wind tunnel experiments, namely the PSD of the collected microphones' recordings, corresponding to all airspeed values for a given angle of attack and vice versa, thus allowing to study the effects of the airspeed and the angle of attack upon the PSD shape independently. Lastly, Part IV provides closure to the report by summarizing the conclusions from the research work in Chapter 6, and suggesting recommendations for improvement and further investigation in Chapter 7.

Part I

Scientific Article

Microphones as Airspeed Sensors for Unmanned Aerial Vehicles

Momchil K. Makaveev* and Ewoud J. J. Smeur†
Delft University of Technology Delft, The Netherlands

This paper puts forward a novel design for an airspeed instrument aimed at small hybrid unmanned aerial vehicles. The working principle is to relate the power spectra of the wall-pressure fluctuations beneath the turbulent boundary layer formed over the vehicle's body to its airspeed. The instrument consists of two microphones, flush mounted on the UAV's nose cone, that capture the pseudo-sound caused by the coherent turbulent structures, and a micro-controller that processes the signals from the microphones and computes the airspeed. Dedicated models were constructed, using data obtained from wind tunnel and flight experiments, that take the power spectra of the microphones' signals as an input and provide the airspeed as an output. The model structure is a feed-forward neural network with a single hidden layer, trained using a second-order gradient descent algorithm, following a supervised learning approach. The models were validated using only flight data, with the best one achieving a mean approximation error of 0.043 m/s and having a standard deviation of 1.039 m/s. It was also shown that the airspeed could be successfully predicted for a wide range of angles of attack, given that they are known, thus necessitating the vehicle to be equipped with a dedicated angle of attack sensor.

I. Introduction

The airspeed is a crucial flight parameter for aerial vehicles such as drones and aircraft that is needed for the calculation of all aerodynamic forces and moments acting on the vehicle [1]. This makes it vital for both pilots and autonomous flight systems of unmanned aerial vehicles (UAV) to know the vehicle's airspeed at any point during flight, as airspeed control is necessary for achieving precise altitude and attitude, as well as safely performing critical maneuvers [2].

In aircraft, Pitot tubes are typically utilized in order to determine the vehicle's airspeed. However, the accuracy of a Pitot tube decreases as the airspeed gets lower [3]. Their working principle can be described as sensing the dynamic pressure, caused by the movement of the vehicle within the mass of air, and subsequently translating that to a measure of the aircraft's airspeed [4]. A traditional Pitot tube has static ports that measure the static pressure of the air stream. In order to provide accurate measurements, they need to be oriented normal to the direction of the airflow. This is especially problematic for UAVs of the hybrid tailsitter type, as they combine both hovering and forward flight capabilities, landing and taking-off vertically sitting on their tail, and tilting themselves forward for horizontal flight [5]. When not in horizontal flight, the static ports of the Pitot tube would begin to capture parts of the dynamic pressure of the airflow, thus causing inaccuracies in the estimated airspeed of the vehicle.

Another often used sensor for speed determination in aerial vehicles is the GPS. However, it can only determine the ground speed of the vehicle and not the airspeed [6]. Furthermore, environmental factors could potentially deteriorate the accuracy of the GPS or render its use completely unfeasible. Examples include high buildings and terrain, tunnels, or areas of restricted GPS coverage. These drawbacks of the GPS sensor are especially impactful for small UAVs, which often operate at lower altitudes, in urban areas, or in remote areas. Other instruments that can measure the velocity of an airflow include vane-type anemometer, hot-wire anemometer, jet-deflection velocity meter and ion-deflection velocity meter. However, those are fragile instruments, which also require frequent maintenance and recalibration to maintain high accuracy, making them impractical for prolonged use on aerial vehicles [7]. As such, there is an existing need for an alternative airspeed sensor for small UAVs - one that can operate in the different flight modes of the vehicle, at any time and geographical location, without requiring frequent maintenance.

A well-researched topic in aeroacoustics is the wall-pressure fluctuations beneath a turbulent boundary layer (TBL), whose spectral features are known to be affected by the free-stream velocity [8, 9]. Smol'yakov [10] and Rackl's [11] work in modeling these spectra is aimed at noise control, especially in aircraft cabins, while Laganelli [12] and Lowson [13] also consider the prospect for fatigue failure analysis and prediction of the aircraft's structure. Edelman [14] utilizes

*M.Sc. student, Control & Simulation Section, Faculty of Aerospace Engineering, P.O. Box 5058, 2600GB Delft, The Netherlands; m.k.makaveev@protonmail.com

†Assistant Professor, Control & Simulation Section, Faculty of Aerospace Engineering, P.O. Box 5058, 2600GB Delft, The Netherlands; e.j.j.smeur@tudelft.nl. Member AIAA

the spectral features to detect boundary layer separation. In all of these models aimed at predicting the TBL-induced surface pressure fluctuations, the free-stream velocity is an independent variable. While Moshkov [15] elaborates on the influence of the Mach number on the surface pressure fluctuation levels measured on the fuselage of a jet in subsonic flight and Panton [16] examines the pressure-velocity correlations for data from microphones mounted on the fuselage of a sailplane, no dedicated models with the airspeed as the dependent variable are put forward. As such, to the best of the researcher's knowledge, the utilization of the power spectral features of the TBL-induced pressure fluctuations at the surface of an aerial vehicle in flight for the purposes of predicting its airspeed has not been attempted.

The goal of this paper is to propose and evaluate a novel design for an airspeed sensor aimed at small UAVs, which tackles the drawbacks of the currently existing instruments available for airspeed measurements. The underlying working principle of the sensor is to relate the power spectral densities (PSD) of the wall-pressure fluctuations beneath a TBL to the vehicle's airspeed. To capture the wall-pressure fluctuations, the proposed airspeed instrument makes use of microphones. In order to relate the microphones signals' PSD to the airspeed, machine learning techniques and models are utilized. Therefore, data about the shape and magnitude of the PSD at the different airspeeds of interest is needed. This data is collected by performing both wind tunnel and flight experiments. After the experiments are completed, the experimental data from the microphones is analyzed and processed, prior to computing the PSD, which are subsequently organized into datasets, ready to be fed to a machine learning model, where they are used for training and determining the accuracy of the trained models. The Cyclone UAV of the TU Delft's MAVLab - shown in Figure 1 - is used as a development and testing platform for the proposed airspeed instrument.

Carrying out both wind tunnel and flight experiments allows for studying, and possibly filtering, the effects of any environmental factors upon the recorded microphone signals. Furthermore, the wind tunnel experiments allow to compare the gathered data from the microphones mounted on the UAV to that of microphones mounted on flat plates immersed in an airflow [17–20]. As a result, it can be judged whether the part of the UAV's body, where the microphones are mounted, could be assumed to be a flat plate. This would be of importance since this assumption could improve the generalization capabilities of the proposed instrument, thus allowing for easier implementation of the same sensor on different vehicles with similar body shape and configuration.

This paper is structured as follows, in Section II the working principle and the design of the airspeed instrument are described. Then, in Section III, both the wind tunnel and flight experiments are discussed, followed by an explanation of the processing of the experimental data in Section IV. Next, Section V discusses the modeling of the relation between the PSD of the microphones' signals, collected from the performed experiments, and the airspeed under different conditions. Lastly, Section VI elaborates on the results from the modeling efforts, and the subsequent performance of the airspeed instrument. In the same section, the effects of changing angle of attack (AoA) upon the calculated PSD are analyzed, the experimental data from the wind tunnel is compared to semi-empirical models from literature [10–13, 21, 22], and the flat plate assumption for the vehicle's body at the microphones' mounting location is evaluated. The conclusions from the research are given in Section VII, with recommendations for further research and improvements for the instrument.

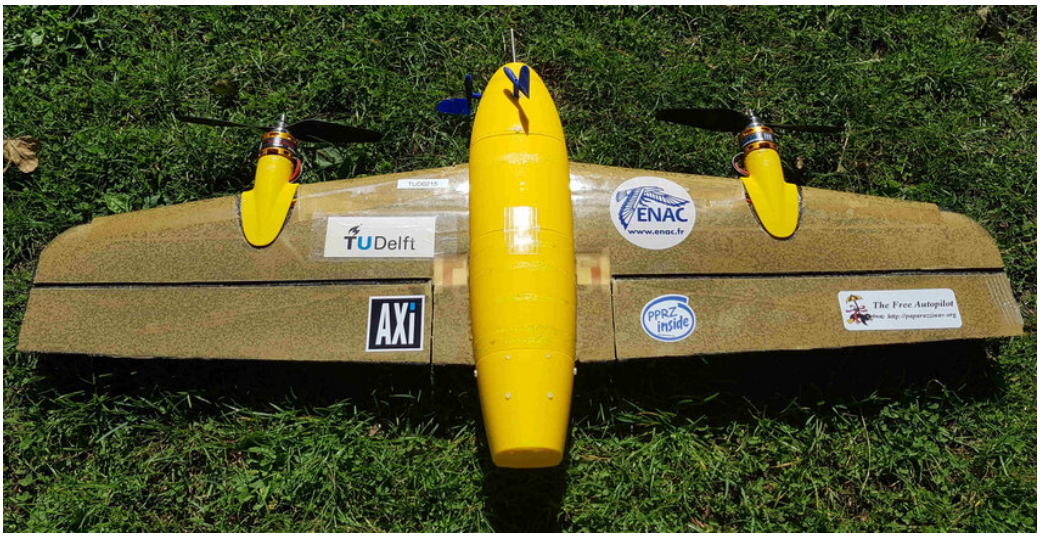

Fig. 1 The Cyclone hybrid tailsitter UAV developed at the TU Delft's MAVLab [23].

II. Design of the Airspeed Instrument

A. Working Principle

The type of flow structures present in the TBL are of rotational nature, such as vortices and eddies that mix together across the various layers of the TBL, and introduce fluctuations in the dynamic pressure that are transmitted throughout the TBL. Those pressure fluctuations can be seen as the result of mechanical waves propagating through the medium. This is an important conclusion since sound is defined as a vibration propagating through a medium (gas, liquid, or solid) in the form of an acoustic wave, and acoustic waves are a type of mechanical waves that introduce fluctuating dynamic pressure component in the medium [24]. However, the dynamic pressure fluctuations in the TBL are of hydrodynamic nature and are governed by the convective velocity of the turbulent flow structures [25]. By comparison, the fluctuations in the dynamic pressure introduced by acoustic waves of sound propagating in the medium are governed by the speed of sound for that particular medium. As such, the dynamic pressure fluctuations arising due to the flow structures in the TBL are referred to as pseudo-sound [19], but can still be captured by microphones. The difference between sound and pseudo-sound can be best explained by the fact that the first arises as a solution to the wave equation, while the latter arises as a solution to the convection equation inside the boundary layer.

The convection velocity of the turbulent flow structures in the TBL impacts the properties of the hydrodynamic pressure fluctuations inside the boundary layer, and as a consequence - the pseudo-sound's PSD [17]. As the convection velocity of the turbulent flow structures is proportional to the local mean flow velocity of the boundary layer's velocity profile, whose magnitude is in turn proportional to the free-stream velocity [1], it is expected that the convection velocity of the turbulent flow structures should increase as the free-stream velocity grows higher. This is an important consequence, as the root-mean-square magnitude of the hydrodynamic pressure fluctuations in the TBL is proportional to the square of the fluctuating velocity components of the fluid elements inside the TBL [26]. Therefore, as the airspeed increases, the magnitude of the overall hydrodynamic pressure fluctuations should become greater, and due to their wavenumber being governed by the convection velocity, also fluctuations of higher frequency should arise. This should result in the pseudo-sound having a PSD with overall greater magnitude and with more power being present in ever higher frequencies of the spectrum. These expectations are confirmed by numerous experiments [17, 20]. This is the underlying principle of which the proposed airspeed instrument makes use.

The discussion on the TBL so far is valid for an attached boundary layer. Once the flow separates, a wake of recirculating flow is created beneath it. The properties of the flow structures in the wake differ significantly from those found in the attached TBL, although they are of the same type. For instance, the vortical structures in the separated flow are of larger magnitude and tend to be stronger [21]. Therefore, the hydrodynamic pressure fluctuations in the wake are dissimilar to those in the attached TBL, for otherwise the same flow properties and environmental conditions, meaning that the shape and magnitude of their PSDs will differ as well.

B. Microphone Selection and Configuration

An instrument that could estimate the vehicle's airspeed by making use of the physical phenomena described above requires microphones to capture the pseudo-sound due to the turbulent flow structures in the TBL and a micro-controller to process the microphones' signals, compute the resulting PSD, and use it to estimate the airspeed. For the microphones, the most important characteristics are the size and shape, which are limiting factors for mounting them on the vehicle. Another important parameter is the weight, as they need to be as light as possible in order to reduce the impact on the vehicle's center of gravity. Following the same rationale, their power consumption is desired to be as low as possible since this will result in smaller and lighter battery needed to power the instrument. A flatter frequency response curve over the frequencies of interest is beneficial as it means that the signals from the microphones will better represent the true pseudo-sound caused by the turbulent flow structures in the TBL. For the same reason, a lower self-noise level is desired. Finally, the directionality of the microphones needs to be considered. In experiments measuring the hydrodynamic pressure fluctuations in the TBL, omnidirectional microphones are typically used [19]. The reason is that the turbulent flow structures are of three-dimensional nature, meaning that hydrodynamic pressure fluctuations are propagating from all direction around the microphone [27].

Based on the desired characteristics and performance of the microphones, the Sonion 8002 * is selected. It is an omnidirectional analog electret microphone with a cylindrical shape and a flat frequency response within ±3 dB from 1 kHz to 10 kHz. A notable benefit of the electret microphones is that the diaphragm is not attached to a coil, meaning that it can vibrate more freely, thus providing more precise representation of the dynamic pressure waves hitting the

*https://www.sonion.com/product/8002-2/

microphones [28]. An important parameter for electret microphones is the maximum input level, which is 112 dB_{SPL} at 1 kHz for the selected transducers. It is a measure of the pressure above which the output signal starts to distort due to overloading the circuitry of the microphone. When distortions are present, the output of the microphone is no longer representative of the captured input, resulting in severe degradation of the quality of the signal. A disadvantage of the electret microphones is the presence of active components, which makes moisture problematic, thus limiting the usability of the airspeed sensor in rainy weather.

The mounting configuration of the microphones is of importance for the capabilities and performance of the airspeed instrument, with possible options - shown in Figure 2 - being positioning them remote, positioning them in a cavity, mounting them flush with the surface, mounting them directly on top of the surface or positioning them in-flow. The most suitable configuration for the purpose of capturing the pseudo-sound due to the turbulent flow structures in the TBL is to flush mount the microphones on the vehicle's body. Having the microphones protruding from any surface of the vehicle could distort the boundary layer flow over that particular part of the surface, thus impacting the PSD of the pressure fluctuations [29], while mounting the microphones remote or in a cavity is found to attenuate the captured pseudo-sound of the hydrodynamic pressure fluctuations in the TBL [17].

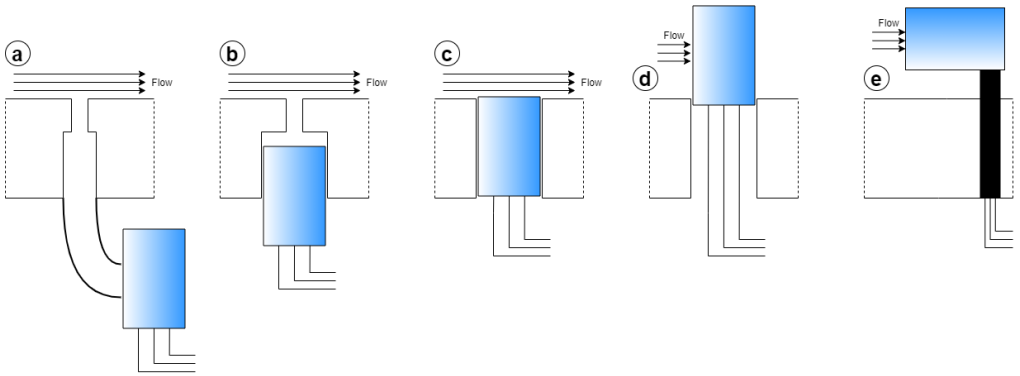

Fig. 2 Visualization of the different possible mounting configurations of the microphone on the UAV body: a) Remote mounted microphone, b) Cavity mounted microphone, c) Flush mounted microphone, d) Microphone mounted on top of the surface, e) In-flow mounted microphone.

The mounting location of the microphones on the vehicle's body is also of importance for the overall performance of the airspeed instrument, as it affects both the properties of the hydrodynamic pressure fluctuations, as well as the components of acoustic and vibrational pressure fluctuations. Another important factor in determining the microphone mounting location is the vehicle and its configuration and physical limitations. For the Cyclone UAV, mounting the microphones anywhere on the wings or on the fuselage's middle section is not feasible. The wing is made out of foam and is not hollow, while in the fuselage's middle section both the autopilot board and the drone's battery are situated. This leaves only two feasible mounting locations for the microphones, one being the nose cone and the other - the tail end of the vehicle. Out of those two options, the nose cone is chosen, as mounting the microphones on the vehicle's tail end introduces two major disadvantages. The first one is that the microphones will be located behind the motors, which could disturb the airflow, and could potentially impact the properties of the boundary layer flow over that part of the vehicle's body. The second disadvantage stems from the fact that boundary layer separation typically starts at the trailing edge and progresses upstream as the AoA increases [30]. Therefore, the boundary layer would remain attached to the surface of the body at the nose cone for higher angles of attack compared to the vehicle's tail end, where separation would already have occurred.

The microphones will also capture sounds from the surrounding environment, most notably from the motors and the propellers. The presence of such sounds in the signals of the microphones is not desired as only the pseudo-sound from the flow structures in the TBL is of interest. A technique to isolate the component of the hydrodynamic pressure fluctuations is to subtract the signals of microphones mounted at distinct locations [19, 29]. This method is based on the fact that the hydrodynamic pressure fluctuations at different points on the surface should be uncorrelated [31]. Generally, the pressure fluctuations captured by flush mounted microphones beneath a TBL can be contributed to 3 distinct sources, namely acoustic sound, hydrodynamic pressure fluctuations caused by turbulent flow structures and vibrations of the surface itself [29]:

$$p' = p'_a + p'_{TBL} + p'_v \tag{1}$$

The symbol p' denotes the fluctuating component of the pressure, p'_a refers to the contribution of the acoustic waves, p'_{TBL} - to the contribution of the pseudo-sound due to the turbulent flow structures in the TBL, and p'_v - to the pressure fluctuations caused by surface vibrations. Given that definition, if the subtraction method is applied to two distinct points in the TBL flow, the following holds for the mean of squares of the pressure fluctuations:

$$\overline{\left(p'_1 - p'_2\right)^2} = \overline{\left(\left(p'_a + p'_{TBL} + p'_v\right)_1 - \left(p'_a + p'_{TBL} + p'_v\right)_2\right)^2} \tag{2}$$

Assuming that the microphones are mechanically coupled (mounted on the same rigid surface), the mean vibrational component $\overline{p'_v}$ is canceled. Furthermore, assuming that the acoustic components of the pressure fluctuations are perfectly in-phase, they will be suppressed when taking their difference. Then, expanding Equation (2) and setting any terms containing uncorrelated coherent components to zero [29], the equation for the isolated pseudo-sound induced pressure fluctuations component is obtained:

$$\overline{(p'_1 - p'_2)^2} = 2\overline{(p'_{TBL})^2} \tag{3}$$

For microphones mounted flush on a surface beneath a TBL, studies in wind tunnels found that for the same streamwise position, a distance x past the leading edge, separation of at least one boundary layer thickness δ is needed between the microphones in order for any correlation between their signals to be attributed to the acoustic sound sources present in the environment. This is due to correlations between turbulent flow structures in the TBL occurring over distances that are shorter than the boundary layer thickness at the particular location [32]. Based on the discussed requirements, it is decided to have two microphones as part of the airspeed instrument, both flush-mounted on the UAV's nose cone at the same distance x past its leading edge as shown in Figure 3. In this configuration, the assumption that the acoustic components of the pressure fluctuations are perfectly in-phase is valid only for acoustic sounds whose wave fronts are perpendicular to the vehicle's longitudinal axis.

A major disadvantage of mounting the microphones on the nose cone is that the boundary layer flow might not have evolved into a completely turbulent one, due to it not having traveled enough distance downstream past the leading edge. In order to be confident that the boundary layer flow over the microphones' mounting location is fully turbulent, a zig-zag turbulator tape is placed upstream, tripping the boundary layer. The tape used on the Cyclone UAV is 60^o with a thickness of 0.5 mm, which can be seen in Figure 3. The zig-zag tape is positioned 20 mm behind the nose cone's leading edge, while the two microphones are mounted 30 mm behind the zig-zag tape. The microphones are spaced out at 40 mm apart, which is more than the expected boundary layer thickness of 2.2 mm at their mounting location, estimated from theory for incompressible TBL over a flat plate [33] (Reynolds number is taken for an airflow at standard sea level conditions and free-stream velocity of 20 m/s):

$$\delta = \frac{0.37x}{\mathrm{Re}_x^{1/5}}\left[1 + \left(\frac{\mathrm{Re}_x}{6.9 \times 10^7}\right)^2\right]^{1/10} \tag{4}$$

C. Micro-controller Selection

Typically, UAVs have an autopilot board, often based on commercial micro-controllers. As such, those can be used to acquire and process the signals from the microphones. This has the advantage that the airspeed instrument then consists only of the microphones, thus being lighter and taking less space. However, there is the disadvantage of having to program the autopilot of every UAV that would utilize the instrument. Furthermore, the autopilot's computing power might not be sufficient to read and process the data from the microphones in real-time. Therefore, it is decided to implement a dedicated micro-controller as part of the airspeed instrument. This also makes it easier to install the instrument on different UAVs. The primary requirement for the micro-controller is the performance as the aim is to read and process the microphones' signals in real-time and give the estimated airspeed. Other important characteristics include the weight, size and the power consumption. It also needs an SD card slot in order to have sufficient storage to save microphone data collected during the flight experiments, described in Section III.B. Based on those criteria, the Teensy®4.1[†] development board is selected, that incorporates an ARM Cortex-M7 processor, which should be powered by a source at 5 V.

[†]https://www.pjrc.com/store/teensy41.html

D. Supporting Components and Configuration of the Instrument Board

The airspeed instrument is completed by an analog-to-digital converter (ADC), a dedicated battery, a linear voltage regulator and an on/off switch. The ADC is needed as the Teensy®4.1's internal ADC has a maximum resolution of 12 bits. It also takes more time for the micro-controller to sample and quantize analog signals using its internal ADC than to read digital data [‡], which is a limiting factor for the achievable sampling rate of analog signals. Considering that the analog signals from the microphones need to be sampled at a rate in the order of forty thousand per second, the Teensy®4.1 might not be able to process them fast enough for real-time operation. The primary requirement for the ADC is to have at least two channels, one for each microphone. The other characteristics to consider are size, weight and power consumption. Based on the discussed requirements, the TI PCM1808 [§] is chosen as it also supports the I2S digital interface. The need for a dedicated battery powering all the components of the airspeed instrument stems from the fact that during the flight tests it was found that the voltage from the UAV's battery is not clean, leading to the microphones' signals being too noisy to be of use. Furthermore, having its own battery makes it easier to readily install the instrument on different vehicles. The battery needs to be light and compact, but it should has sufficient capacity to power the airspeed instrument for the whole duration of the UAV's flight. Based on that, the Hubsan H502s 7.4 V two-cell (2S) battery pack with capacity of 610 mAh is chosen. Lastly, the linear voltage regulator is required in order to drop the battery voltage from 7.4 V to 5 V before using it to power the Teensy®4.1. Figure 4 shows the instrument board, mounted on its housing box, which is positioned in the nose cone, while Figure 5 depicts its block diagram. The airspeed instrument has a total weight of 71 grams, with length of 87 mm, width of 57 mm and height of 33 mm, taking into account the housing box, and a total power consumption of up to 120 mA at 5V.

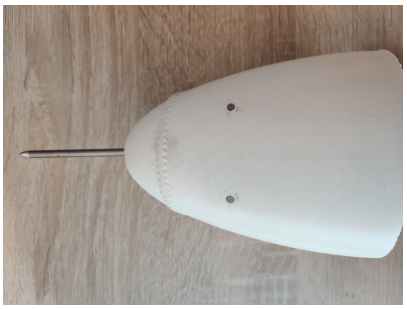

Fig. 3 The nose cone of the Cyclone UAV with the microphones and zig-zag tape mounted on it.

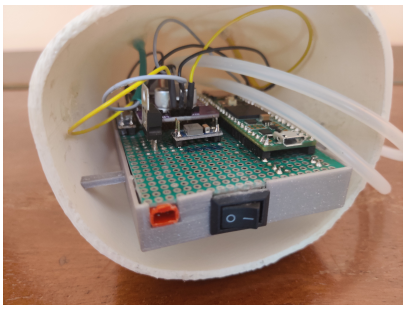

Fig. 4 The airspeed instrument board inside the Cyclone UAV's nose cone.

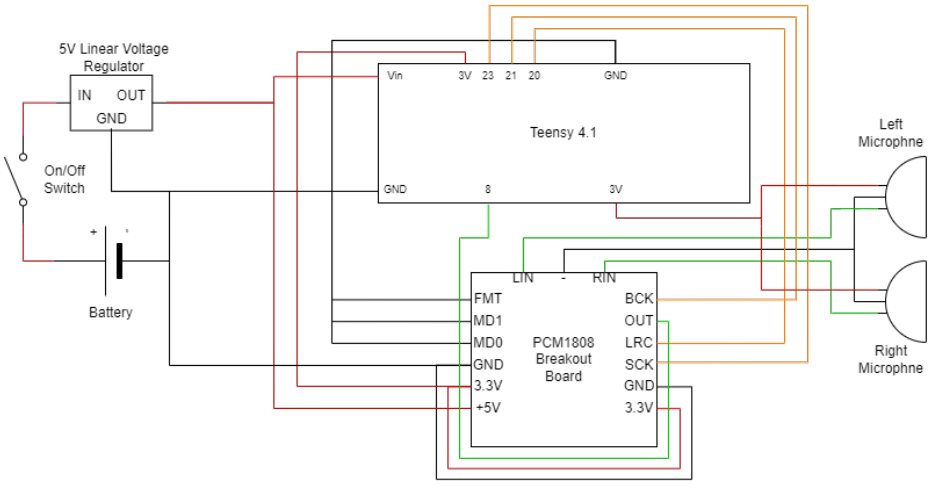

Fig. 5 Block diagram of the airspeed instrument.

[‡]https://www.arduino.cc/reference/en/language/functions/analog-io/analogread/
[§]https://www.ti.com/lit/ds/symlink/pcm1808.pdf

III. Experiments

Single-point frequency spectrum models have been described that aim to predict the flow-induced wall-pressure fluctuations in a TBL [34]. However, those models are semi-empirical, meaning that they have been - at least to some extend - developed using data from experiments. Furthermore, different models are better suited for distinct flow conditions and regimes [33]. As such, using any of the semi-empirical models will introduce sources of errors related either to the scaling of the model to the airspeed and regimes of interest, or to the experimental setup used to obtain the data with which the particular model has been developed. Therefore, it is beneficial to perform dedicated experiments to gather data about the specific wall-pressure fluctuations, induced by the flow structures in the TBL, at the microphones' mounting location on the vehicle's body, and study their dependence on the airspeed and AoA using the same microphones and processing techniques as those that are part of the airspeed instrument. The experiments include both wind tunnel and flight tests. The wind tunnel experiments can be well-controlled and are thus useful to understand the underlying relations between the spectrum of the wall-pressure fluctuations and the airspeed for a wide range of AoA, while the flight experiments gather data that is representative of real flight, affected by environmental factors.

A. Wind Tunnel Experiments

The wind tunnel experiments are carried out at the A-Tunnel of the TU Delft's Low Speed Laboratory. It is a vertical low turbulence tunnel with an open test section, where the inflow comes through a circular exit with diameter of 0.6 m. The turbulence level of the airflow is below 0.1%, achievable due to the high contraction ratio of the settling chamber. It is semi-anechoic aeroacoustic wind tunnel with low operating noise, making it ideal for the planned experiments. The cut-off frequency of the wind tunnel's chamber is approximately 200 Hz, meaning that above this frequency the chamber can be assumed free of echoes. The maximum achievable flow velocity is 45 m/s [35].

Fig. 6 The Cyclone drone mounted on the rig in the A-Tunnel of the TU Delft's Low Speed Laboratory.

The wind tunnel experiments are characterized by three independent variables: the airflow velocity (measured in meters per second), the angle of attack (measured in degrees) and the UAV's motor configuration. The last independent variable has the following states defined: propellers dismounted (D), propellers mounted, but motors are turned-off (M) and propellers are mounted, and motors are running at 30% throttle (R). There is only one dependent variable defined for the wind tunnel experiments, namely the microphones' voltage signals. Each experimental run consists of 15 seconds of recorded signals and corresponds to a given combination of the independent variables. It should be noted that high angles of attack are not tested at high airspeeds as this is not a flight condition of interest, since the higher angles of attack are encountered during the hybrid UAV's transition to vertical hover, which usually takes places at lower airspeeds. Figure 7 below depicts the experiment matrix for the wind tunnel experiments. The matrix is valid for all three motor configurations of the UAV.

Wind tunnel flow velocity (m/s)	Anle of Attack (deg)									
	0	5	10	15	20	30	45	60	75	90
5	×	×	×	×	×	×	×	×	×	✓
7	✓	✓	✓	✓	✓	✓	✓	✓	✓	✓
10	✓	✓	✓	✓	✓	✓	✓	✓	✓	✓
12	✓	✓	✓	✓	✓	✓	✓	✓	×	×
15	✓	✓	✓	✓	✓	×	×	×	×	×
18	✓	✓	✓	×	×	×	×	×	×	×

Fig. 7 Experiment matrix for the wind tunnel experiments. Valid for all three motor configurations (D, M, R) defined as part of the experiments. Each cell corresponds to a single experimental run.

During the wind tunnel experiments, a National Instruments CompactRIO is utilized instead of the instrument's hardware, described in Section II, to acquire the microphones' voltage signals. This makes the process of data acquisition easier and faster. The acquisition system has a built-in ADC that outputs a digital signal with a resolution of 24-bit and sampling frequency of 51.2 kHz[¶].

B. Flight Experiments

The flight experiments are carried out at the Valkenburg airfield near Leiden, characterized by piloted flights with isolated phases of steady forward flight at the different airspeed values of interest. The data gathered during those phases of steady forward flight is the one of importance. In total, two flights are carried out, the first one with a duration of approximately 13 minutes, and the second one having a length of approximately 15 minutes.

The independent variables of the flight experiments are the vehicle's airspeed, the angle of attack and the motors' RPM. The airspeed is measured using a Pitot tube connected to the autopilot board, while the motor RPM are calculated based on the current drawn and both are saved to the autopilot's log. Next to that, a GPS sensor is present that provides data about the vehicle's ground speed components in all 3 axes. However, the UAV lacked an AoA sensor during the flights experiments, meaning that the AoA could not been recorded. As a consequence, this parameter is not included in the collected flight data. The dependent variable is the microphones' voltage signals. A single measurement of the dependent variable corresponds to a microphone recording of a steady forward flight phase with length of 1 second at a particular airspeed. It should be noted that due to environmental factors such as wind and thermal gusts, the airspeed is not typically constant over the whole steady forward flight phase. Therefore, an allowed range of 0.5 m/s is defined. As such, if the airspeed as registered by the Pitot tube within one second of data has a range of less than 0.5 m/s, it is accepted as corresponding to a steady forward flight phase with the airspeed value taken to be the average one over the 1 second measurement.

Since the airspeed instrument's micro-controller and the autopilot have their own clocks, the data logged by them needs to be synchronized. This is achieved using reference points, which are clearly visible in both the microphone and autopilot log. The first reference point is the vehicle's take-off. At that instance, the motors spin up to higher RPM, leading to distinct sound that is audible in the microphones' recordings. At the same time, the increase in the motor RPM is clearly visible in the corresponding autopilot's log. Since the Pitot tube is connected to the autopilot as well, the same time instance of take-off from the motor RPM data corresponds to the take-off point in the airspeed data. The second reference point is the vehicle's landing, indicated by the engines switching-off, which is also visible in both the autopilot and microphones data.

No experiment matrix is defined for the flight experiments as only the airspeed is varied over its defined range, while the corresponding motor RPM for a given airspeed might differ due to wind gusts. The airspeed values recorded in the steady forward flight phases start from as low as 6 m/s and reach up to 20 m/s. During the flight experiments, the airspeed instrument is utilized, as described in Section II. The ADC outputs a digital signal with a 16-bit resolution and sampling frequency of approximately 43 kHz, which is saved to the SD card inserted in binary format and is later reconstructed when downloaded.

[¶]https://www.ni.com/en-rs/support/documentation/supplemental/17/specifications-explained–c-series-modules.html#ADCresolution

IV. Data Processing

The data obtained from the experiments is in the form of a signal of the voltage change (ΔV) between a microphone's diaphragm and backplate over time. The data from the wind tunnel experiments is in the form of a 15-second recording for a given combination of the independent variables mentioned in Section III, while the flight data is in the form of a recording of the complete flight. From the gathered datasets, smaller segments of interest are extracted. For the wind tunnel data, a window of fixed length of 1 second is defined that extracts the microphone signal within its boundaries. The window moves over the recording by 0.1 seconds each step. A window of the same length is used when extracting flight data, but it moves over the airspeed data logged to the autopilot by the Pitot tube. At each step, both the average and the range of the airspeed data in the window are calculated, and given that the minimum airspeed and data range requirements are met, the corresponding microphones' signals for that time segment are extracted and saved.

The microphones' signals collected from the wind tunnel experiments are dominated by a 50 Hz component. After analyzing the experimental setting and setup, the conclusion is that the reason behind the 50 Hz component in the wind tunnel data is that the current used to power the microphones was not successfully converted to DC. A power station connected to a wall plug in the wind tunnel chamber was used in order to provide current to power the microphones. The power station is supposed to convert the AC input from the electrical socket to a DC output at the selected voltage and current values. However, it is likely that the station was either faulty, or not correctly setup, thus not being able to convert the AC from the wall plug to a DC output. This is further substantiated by the fact that the alternating current available at the electrical sockets in Europe has a frequency of 50 Hz[‖]. In addition, the 50 Hz component is not present in the flight data, where a battery is used to power the microphones. This issue is resolved by passing the microphone signals through a second-order high-pass filter, with the cut-off frequency set at 250 Hz, chosen to be also higher than the cut-off frequency of the wind tunnel's semi-anechoic chamber. Figure 8 depicts an example of the resulting time-domain signals, taken for the left-mounted microphone, upon applying the high-pass filter.

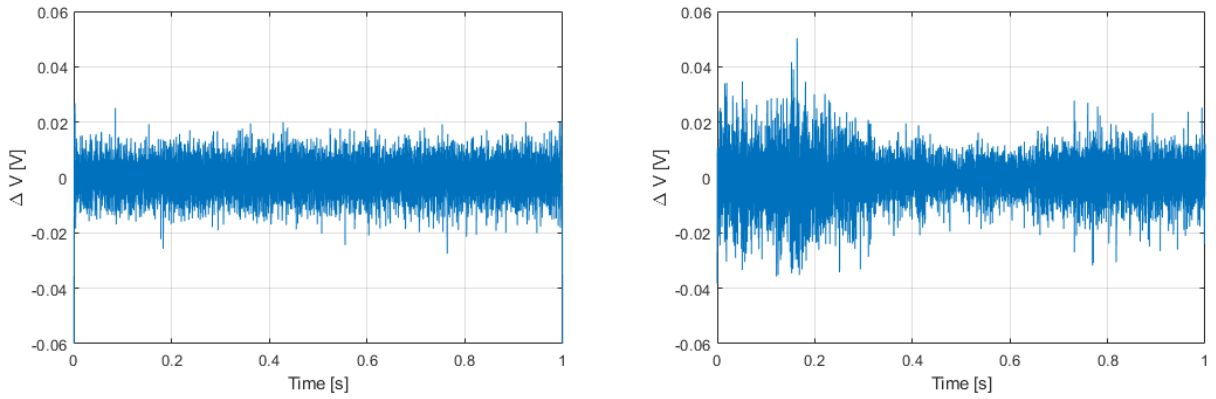

Fig. 8 Left microphone data segments from wind tunnel experimental run at flow velocity of 12 m/s, AoA of 0° and UAV motor configuration - R (left plot) and flight data from a phase of steady forward flight at an average airspeed of 12 m/s (right plot).

The next step in the data processing is to compute the PSD for all extracted segments of microphones' signals, both from the wind tunnel and flight experiments. To do so, Welch's method is utilized, where the PSD estimation is performed by dividing the time signal into successive segments, forming periodogram for each segment, and then averaging. The reason behind choosing this approach is that the variance of the periodogram is reduced by breaking the time series signal into segments that typically overlap [36]. The m^{th} windowed segment from a time-series signal x is given as:

$$x_m(n) = w(n)x(n + mR), \;\; n = 0, 1, \ldots, M - 1, \;\; m = 0, 1, \ldots, K - 1 \tag{5}$$

where $w(n)$ is the window function, whose purpose is to reduce the side-lobe levels in the PSD estimate (at the expense of the frequency resolution), R is the window hop size, M is the length of a single segment, and K - the number of segments. Then, the periodogram of the m^{th} segment is defined as:

[‖] https://www.mainsfrequency.com

$$P_{x_m,M}(\omega_k) = \frac{1}{M}\left|FFT_{N,k}(x_m)\right|^2 = \frac{1}{M}\left|\sum_{n=0}^{N-1} x_m(n)e^{-j2\pi nk/N}\right|^2 \tag{6}$$

resulting in the Welch's estimate for the PSD to be given as [37]:

$$\hat{S}_x^W(\omega_k) = \frac{1}{K}\sum_{m=0}^{K-1} P_{x_m,M}(\omega_k) \tag{7}$$

The window function used as part of the Welch's estimation is a Hamming window of length $M = 1024$ samples. As the amount of samples in the window is an even number, the overlap between adjacent windows is set to 50% as recommended for Hamming windows, resulting in window hop size of $R = 512$ samples [38].

The frequency range of interest for the PSDs is bounded by their characteristics and behavior. The lower limit is defined by the high-pass filter's cut-off frequency, while the upper limit is set at 14 kHz as for higher frequencies the PSDs corresponding to the different airspeeds exhibit high degree of similarity. Within that range, it was found that working with the frequencies between 1 kHz and 10 kHz yielded models with comparable accuracy in predicting the airspeed, while needing less sample points from the PSD function. The resulting estimates obtained using the Welch's method for the wind tunnel and flight microphone signal segments can be seen in Figure 9. The plots shown in orange correspond to the PSD of the wind tunnel microphone data segment shown on the left-hand side in Figure 8, while the plots in blue - to the flight microphone data segment shown on the right-hand side in Figure 8. The magnitude of the PSD is expressed in dB_{SPL}:

$$\mathrm{PSD}_{dB}(f) = 10\log_{10}\left(\frac{\mathrm{PSD}(f)}{P_{ref}^2}\right) \tag{8}$$

where P_{ref} is the reference pressure, taken to be $20{\times}10^{-6}$ Pa, which is the threshold of human hearing. PSD(f) is computed using Welch's method for a signal expressed in units of Pa. As such, the ΔV signals from the microphones need to be converted to a pressure measure in Pa prior to estimating their PSD. To do so, the sensitivity of the microphones is used and the transfer factor (TF) is computed, which corresponds to the ΔV that will be registered by the microphone when exposed to a sound wave having a pressure of 1 Pa:

$$\mathrm{TF} = 10^{dBV/20} \tag{9}$$

where the dBV value corresponds to the sensitivity of the microphone. The conversion of the microphones' signals from ΔV to a pressure measure is carried out by multiplying the ΔV signals by the inverse of the TF, which is in units of Pa/V and depicts the sound pressure corresponding to a microphone ΔV signal of 1 V. Expressing the PSDs in dB_{SPL} also allows to easily check whether the maximum input level of the microphones has been exceeded in any of the recorded signals during the experiments. The highest sound pressure level (SPL) of a recording is found to be 98.4 dB_{SPL}, corresponding to the right microphone during the wind tunnel experiments for motor configuration R and airspeed of 10 m/s at an AoA of 45°. This is below the microphone's maximum input level, meaning that there should not be any distortions present in the recorded signals.

The signal subtraction method is applied to the microphone signals in the time domain as the recorded microphone voltage is related to the corresponding magnitude of the pressure fluctuations captured by the microphone only by a scaling factor determined by the microphone's sensitivity. Therefore, the signal subtraction can be performed directly on the microphone ΔV signals:

$$V_{sub} = V_{left} - V_{right} \tag{10}$$

The V_{sub} signal is treated in the same manner as the ΔV signals from the microphones with the PSD computed using Welch's method and its magnitude subsequently expressed in dB_{SPL}. Figure 10 depicts the PSDs of the $\overline{(V_{TBL})}$ signals for both the wind tunnel and flight microphone data segments shown in Figure 8. The plot in orange corresponds to the PSD of the signal obtained from the wind tunnel data, while the plot in blue - to the signal from the flight data. From the plots it can be seen that the PSD of the resulting signal from the wind tunnel microphone data has less energy in the frequencies below 2 kHz, compared to its flight data equivalent. Next to that, there is a spike at 8.7 kHz present only in the wind tunnel data. This behavior for the wind tunnel PSDs is observed in all experimental trials. Its lower PSD magnitude in the low frequency region could point towards stronger turbulent structures of lower convection velocity

forming in the TBL during flight, while the peak present close to 9 kHz could be attributed to a harmonic of the 50 Hz component from the AC as it is present in all PSDs of the subtracted microphones' signals collected during the wind tunnel experiments, even for the scenario when the vehicle's motors are turned off and the propellers are dismounted.

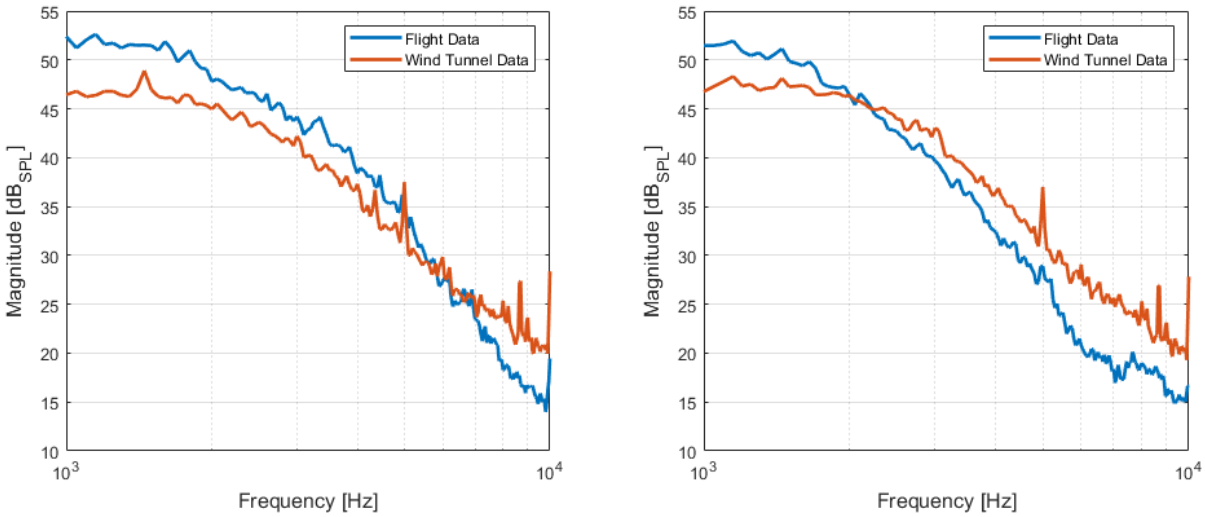

Fig. 9 PSD expressed in dB$_{SPL}$ of both left-mounted (left plots) and right-mounted (right plots) microphone's data segments at airspeed of 12 m/s computed using Welch's method. The wind tunnel data segment corresponds to an AoA of 0^o and UAV motor configuration - R.

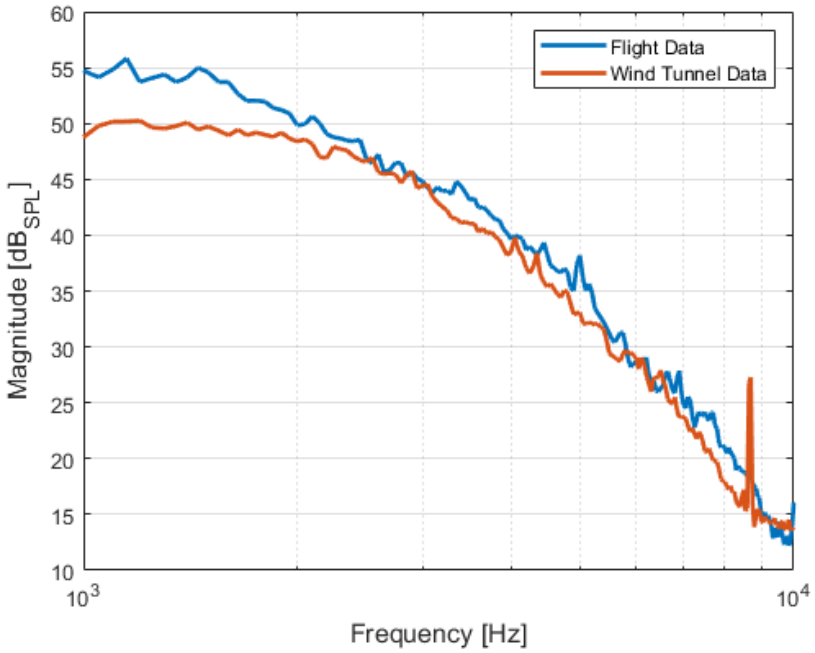

Fig. 10 PSD expressed in dB$_{SPL}$ of the subtracted microphone signals data segments computed using Welch's method at 12 m/s. The wind tunnel data segment corresponds to an AoA of 0^o and UAV motor configuration - R.

V. Modeling

To model the relationship between the PSD of the microphones' signals and the airspeed, a supervised learning approach is applied that tackles a parametric nonlinear regression problem, where the independent variable is the PSD of the microphones' signals and the dependent one the airspeed of the vehicle. To construct the models, the PSD of the microphones' voltage signals are used, expressed in dB and having a reference of unity. This is done to reduce the computational load of processing the signals and computing the PSD with the aim of achieving real-time operation of the airspeed instrument. The downside of not expressing the signals in terms of the pressure is that they become dependent on the microphone's sensitivity, meaning that the constructed models could only be utilized if the airspeed instrument is fitted with microphones of similar sensitivity.

The chosen model structure is a feed-forward artificial neural network (ANN), as it can be used for any kind of input-output mapping, making it a suitable choice for the problem at hand. Furthermore, it can fit any finite input-output mapping problem with just one hidden layer, given that there are enough hidden neurons [39]. The labeled input-output dataset used for training the feed-forward ANN is constructed from the processed experimental data obtained from both the wind tunnel and flight experiments. More specifically, the inputs correspond to the 215 sample points constituting the PSD's magnitude at the frequencies of interest, while the output is the corresponding airspeed at which the particular microphones' signals are recorded. All of this data needs to be divided in training and validation datasets. The training dataset is made out of all of the wind tunnel data, and 75% of the data from each of the two flight tests. The remaining 25% of the data from both flights constitute the validation dataset. The indices of the flight data are randomized prior to dividing them with the aim of obtaining more diverse data for the validation dataset. Models are constructed for each of the different types of data collected from the performed experiments - signals from the left and right microphones, as well as the subtracted signals. Figure 11 depicts the architecture of the feed-forward ANN.

The feed-forward ANN is trained with a second-order gradient descent method, in the form of Levenberg–Marquardt algorithm. This family of methods take into account the local geometry of the function, thus providing a more global view and increases the probability of finding a global minimum. The Levenberg-Marquardt algorithm adaptively varies the ANN weight updates between the first-order steepest-descent and the Gauss-Newton method, thus converging faster compared to first-order algorithms [40]. The algorithm updates the weights according to:

$$w_{t+1} = w_t - (J^T J + \mu I)^{-1} J^T e \tag{11}$$

where w_t is the vector containing the current values of the network's weights, J is the Jacobian of the model error that can also be expressed as $\frac{\partial \mathbf{e}}{\partial \mathbf{w}_t}$, μ is the adaptive learning parameter, and e - the vector that contains the model errors for all data points in the current epoch.

The activation function of the hidden neurons is chosen to be the hyperbolic tangent. It was found to yield higher accuracy in predicting the airspeed over unfamiliar flight data, compared to other suitable activation functions such as the Sigmoid, Gaussian, or Rectified Linear Unit. The comparison is based on the achieved RMSE over the validation dataset.

The initialization of the weights and biases of the feed-forward ANN has a significant impact upon the training process and the resulting model accuracy. In order to initialize these parameters, the Nguyen-Widrow algorithm is used, aiming to reduce the training time by choosing initialization values such that the active region of each neuron in a given layer is about evenly distributed across the layer's input space [41].

Lastly, the number of neurons in the hidden layer needs to be chosen. A lower number of hidden neurons will prevent overfitting to the training data, thus improving the ability of the network to generalize and it will decrease the time it takes to complete the training. However, having too few hidden neurons will lead to underfitting, which again worsens the accuracy of the trained models [42]. In order to determine the optimal number of neurons in the hidden layer, a recursive algorithm based on successive addition of nodes is used. For the algorithm to find a meaningful solution, every ANN model should be trained under the same hyperparameters, except for the number of hidden neurons. The algorithm is initialized with $H^0 = 65$ neurons, which is 30% of the size of the network's input layer and during each iteration $\Delta H = 3$ hidden neurons are added. The algorithm is stopped once the maximum allowed number of hidden neurons is reached, set to be equal to the number of input neurons of the network [43], or once overfitting behavior is exhibited. For the algorithm to be terminated due to overfitting, the validation error must have increased while the training error steadily decreased over the last 4 consecutive ANN structures. If the algorithm is terminated due to reaching the maximum allowed number of hidden neurons, the ANN structure with the lowest validation error is taken as the optimal one. But if termination is due to overfitting, then the ANN structure with the lowest validation error, outside of the last 4, is taken as the optimal one. Using the algorithm, it was found that a network having 140 hidden neurons yields the most optimal performance.

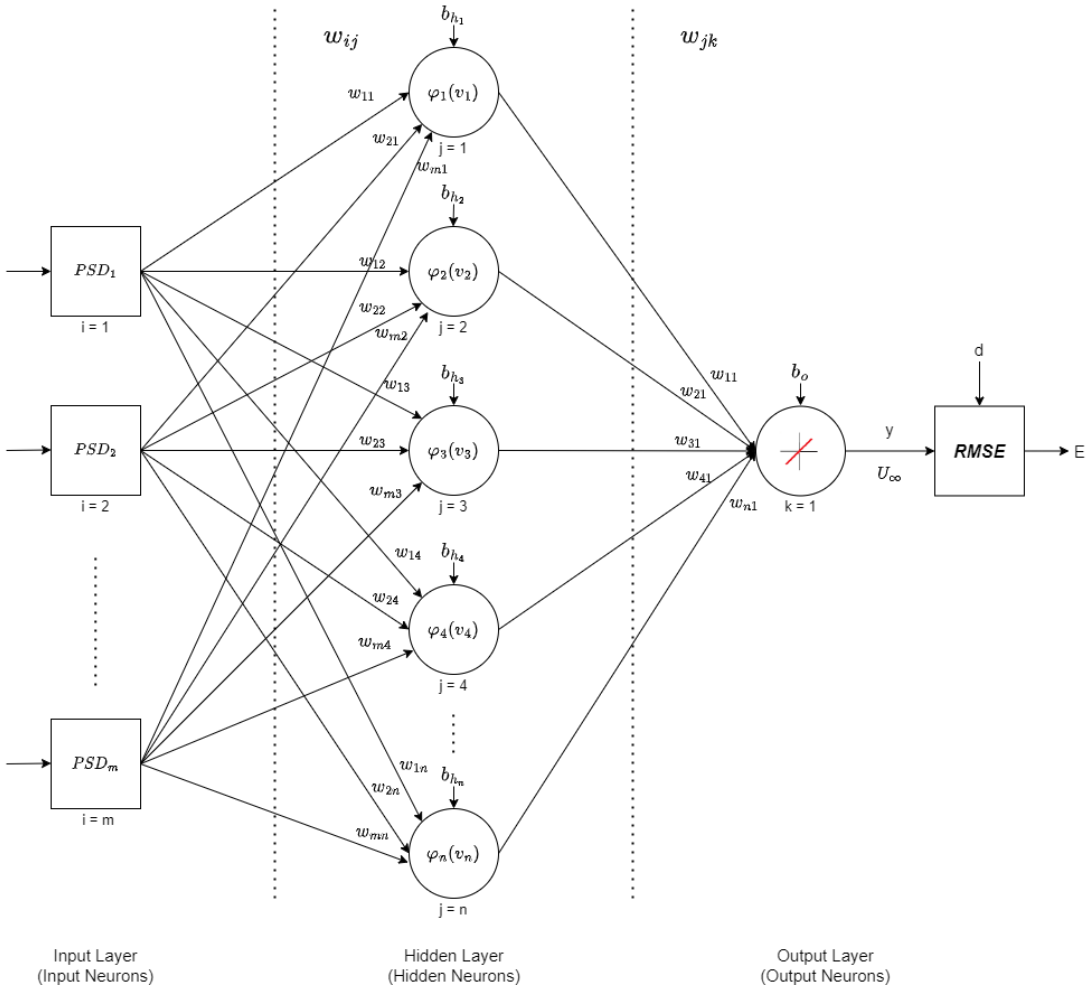

Fig. 11 Structure of the feed-forward neural network used to model the relationship between the PSD of the microphone signals and the vehicle's airspeed.

In order to study the sensitivity of the resulting models, a global sensitivity analysis in the form of Sobol indices is carried out. The Sobol method decomposes the variance of the model's output into fractions that can be attributed to each input or sets of inputs [44]. This method is chosen as it is global, meaning it could also analyze the effects of interactions between the different inputs, and it can be used with nonlinear models. However, the downside is that the required amount of runs grows exponentially for increasing the number of inputs and the range of their uncertainty [45]. Since the Sobol method's attributions are expressed in fractions, the Sobol Indices, denoted as S_i, should take on values between zero and one - $0 < S_i < 1$ [46]:

$$S_i = \frac{V(E(Y|X_i))}{V(Y)} = \frac{V_i}{V(Y)} \tag{12}$$

where $V(E(Y|X_i))$ is the contribution of each individual input to the total output variance $V(Y)$. Furthermore, the summation of all Sobol Indices should be equal to 1 [46]:

$$1 = \sum_{i=1}^{n} S_i + \sum_{1 \le i \le j \le n} S_{ij} + \ldots + S_{1,\ldots,n} \tag{13}$$

where S_i corresponds to the first-order Sobol indices that quantify the impact of each input alone, and the $S_{1,\ldots,n}$ term represents higher order indices that characterize the effects of interactions between multiple inputs.

VI. Results

The wind tunnel data, part of the input-output dataset utilized when training the feedforward ANN model structures, contains only data corresponding to an AoA of up to 5^o for each motor configuration. The reason behind limiting the wind tunnel datasets is that it was found that the models trained on this wind tunnel data alone, next to the data from the flight experiments, achieved the best prediction accuracy over the validation dataset.

In total, 5 models are trained with the aim of selecting a set of initial hyperparamters giving a model with better accuracy. All training processes are initialized using the Nguyen-Widrow algorithm. It was found that models constructed with the PSD data of the left-mounted microphone have lower average RMSE compared to those constructed with the PSD data of the right-mounted microphone or the PSD data of the subtracted microphones' signals. The models trained with the PSD data of the left-mounted microphone had an average RMSE of 1.091 m/s. Among those, the best model has a RMSE of 1.037 m/s. Its mean approximation error is 0.043 m/s with a standard deviation of 1.039 m/s.

For this particular model, Figure 12 depicts the approximation errors between the model's predictions and the observations given by the validation dataset, as well as the model's prediction accuracy expressed in percentages using box plots. The central line inside the box represents the median, while the top and bottom sides of the box indicate the 25^{th} and 75^{th} percentiles, respectively. The whiskers extend to the most extreme data points that are not considered as outliers, while the outliers are depicted by the red '+' symbol. The plot on the left-hand side relates to the achieved approximation error, where the median is found to be -0.0396 m/s and in total 15 prediction are marked as outliers, which is 9.3% of the validation dataset. The plot on the right-hand side shows the model's prediction accuracy, where the median is found to be 96.0% and in total 12 predictions being marked as outliers, equating to 7.5% of the validation dataset.

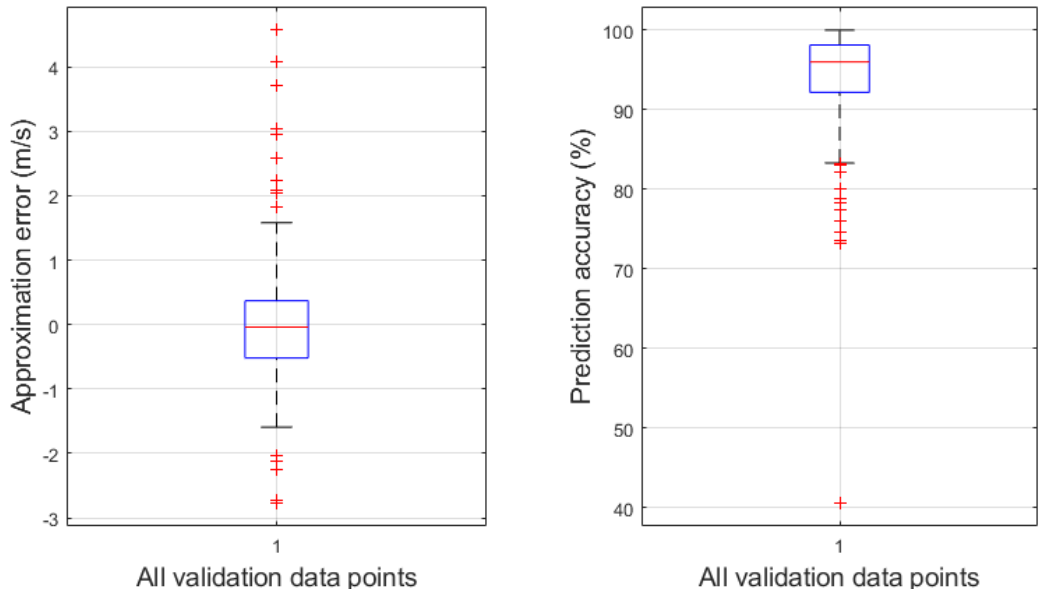

Fig. 12 Approximation errors (left plot) and prediction accuracy (right plot) of the model with lowest RMSE over the validation dataset.

A. Effects of Changing Angle of Attack

One of the main advantages of the proposed instrument over the Pitot tube is its ability to provide accurate measures of the airspeed for a wide range of AoA. Therefore, the impact of changing AoA on the resulting PSD estimates for the microphone signals is analyzed. Figure 13 depicts the PSDs, with magnitude expressed in dB_{SPL}, of microphone signals recorded during the wind tunnel experiments for motor configuration - R, chosen since running motors represent more closely the reality during flight, at an airspeed of 10 m/s which is the highest airspeed spanning all defined values of the AoA that are part of the wind tunnel experiments (see Figure 7).

From the PSD graphs it can be seen that as the AoA goes from 0^o up to 30^o, there is an apparent increase in the power in the lower frequencies up until about 2 kHz, with the slope of the PSD plot also becoming steeper as the AoA

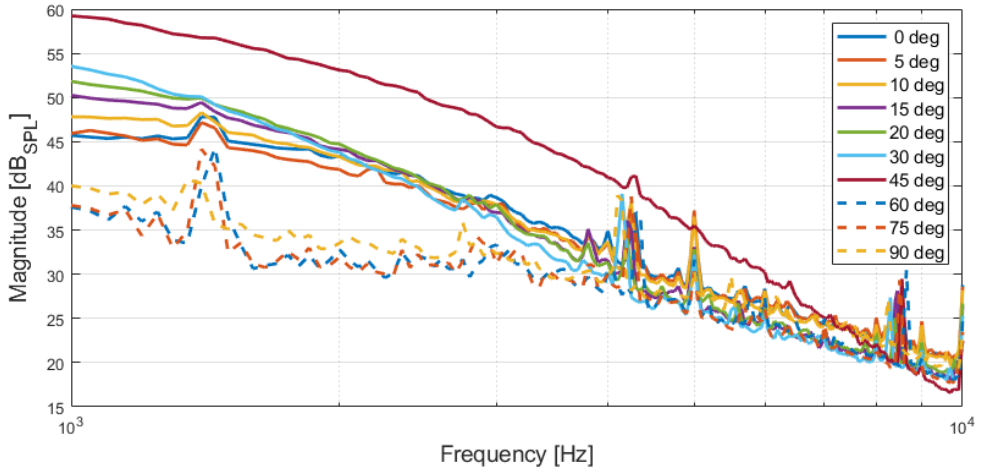

Fig. 13 PSD expressed in dB$_{SPL}$ of microphone signals recorded as part of the wind tunnel experiments for UAV motor configuration R at airspeed of 10 m/s for all angles of attack.

grows larger. A more notable increase in the power is present at an AoA of 45° for frequencies up to 7 kHz. Finally, there is an abrupt decrease in the power of frequencies up to 4 kHz for angles of attack of 60° and higher. This demeanor could be explained by a combination of factors. Firstly, as the AoA increases, the nose cone's geometry could lead to higher local flow velocity and dynamic pressure over its top side, for otherwise the same free flow velocity [47]. This typically holds while the boundary layer is still attached to the nose cone's surface. Secondly, the formation of a wake could contribute to the overall power of the microphones' signals [21]. Most likely, at an AoA of 45°, the boundary layer flow over the microphones is completely separated with a wake having formed beneath it, that would contain larger and stronger vortical structures as explained in Section II.A. This would consequently lead to the noticeably higher PSD magnitude. For angles of attack of 60° and higher, it is likely that an area of lower pressure forms over the top side of the nose cone where the microphones are mounted [47, 48], which would result in the recorded signals having lower PSD magnitude. In order to confirm the hypothesis outlined above, and possibly determine the exact point when the boundary layer flow detaches, particle image velocimetry could be used.

In order to judge the capability of the proposed instrument to predict the airspeed at various angles of attack, a model is created, with the same structure and hyper-parameters as those described in Section V, but having as inputs not only the PSD, but also the AoA. In an operational scenario, this would correspond to having an AoA sensor mounted on the vehicle's body that would provide this data to the airspeed instrument. Due to the AoA being measured only during the wind tunnel testing, currently only data gathered from those experiments can be used to construct the models. The wind tunnel data for all motor configurations is collected and compiled into a single dataset, which is then divided into training and validation datasets according to the 75%/25% division, respectively. Data indices are again randomized prior to dividing them among the two datasets.

The training procedure is again repeated in total 5 times in order to find a set of initial hyperparamters that results in a trained model with better accuracy. Every training process is initialized using the Nguyen-Widrow algorithm. The models are again constructed with data from the left-mounted microphone.The average RMSE of the resulting models over the validation dataset is 0.159 m/s. Among the trained models, the best one has an RMSE of 0.152 m/s. In order to illustrate the work of a real world AoA sensor, an uncertainty of up to 15% is applied to the validation input data corresponding to the AoA [49]. Taking the best model, its RMSE becomes 0.364 m/s. The mean approximation error is 0.027 m/s with a standard deviation of 0.486 m/s.

Figure 14 shows the approximation errors between the model's predictions and the observations given by the validation dataset, with the uncertainty applied to the AoA validation inputs. The box plot on the left-hand side corresponds to the model's approximation error, where its median is found to be 4.433×10^{-4} m/s, while 513 model predictions are marked as outliers, which is 13.2% of the validation dataset. The box plot on the right-hand side corresponds to the model's prediction accuracy. Its median is at 98.9% and in total 603 predictions are marked as outliers, equating to 15.5% of the validation dataset. The reason for having significantly more outliers compared to what is shown in Figure 12 is the shorter interquartile range.

The sensitivity analysis is performed by assuming an uncertainty of up to ±10% for the microphone PSD inputs and up to ±15% for the AoA input. The goal is to determine whether the model is more sensitive towards the microphones' PSD input data, or the AoA input data. For this purpose, all model inputs representing the PSD are grouped together, with the same uncertainty being applied to each of them in every model evaluation. Computing the corresponding Sobol indices over 3 000 model evaluations with various levels of uncertainty (within the defined ranges) applied to the PSD and AoA inputs gives $S_{PSD} = 3.573 \times 10^{-3}$ and $S_{AoA} = 3.547 \times 10^{-7}$, respectively. This means that the trained model is more sensitive to variations in the PSD inputs than to variations in the AoA input.

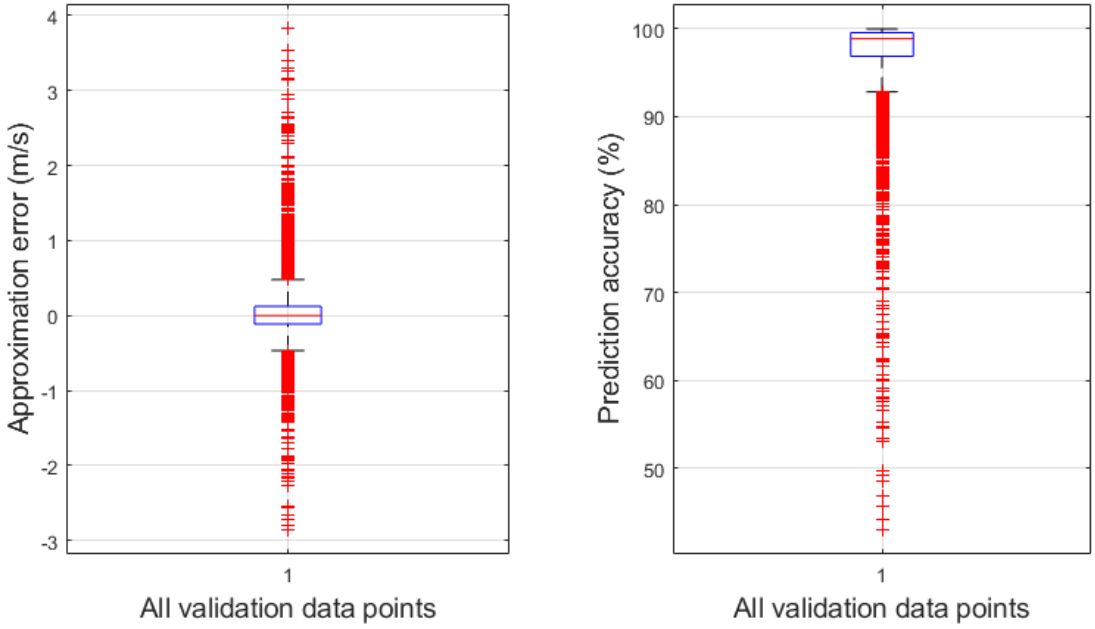

Fig. 14 The best model's approximation errors (left plot) and prediction accuracy (right plot) over the validation dataset for uncertainty of up to 15% applied to the AoA model inputs.

B. Comparison of Experimental Data with Semi-empirical Single-point Frequency Spectrum Models

The semi-empirical single-point frequency spectrum models considered in this research describe the TBL-induced wall-pressure fluctuations in terms of their power spectrum with the goal of characterizing the cabin noise of an aircraft in-flight [50]. They have been developed partially using data from either wind tunnel experiments with flat plates, or flight tests. They assume a fully developed and attached TBL flow with zero-mean pressure gradient. As a result, the flow can be considered as stationary and homogeneous in the plane of the wall. A further assumption is that the aerodynamic excitation can be treated in isolation from the structure [33].

The semi-empirical single-point frequency spectrum models of Efimtsov [51], Laganelli [12], Lowson [13], Goody [21], Robertson [22] and Smol'yakov [10] are evaluated and compared to the PSD of the microphones' signals recorded during the wind tunnel experiments in the range of 1 kHz to 10 kHz. The reason behind opting for experimental data from the wind tunnel is that there is accurate information available about the environmental conditions (air density, dynamic and absolute pressure and temperature) coming from sensors mounted in the wind tunnel's chamber. Their values are required in order to evaluate the single-point frequency spectrum models. Furthermore, these models do not account for the contributions of a vehicle's engines or motors to the predicted frequency spectrum, making the wind tunnel data corresponding to motor configuration D the most suitable experimental dataset to compare against. Another limitation of these models stems from the fact that they do not consider the AoA as an independent parameter. It should also be noted that the microphone signal needs to be converted from a voltage measure (V) to a pressure measure (Pa), as explained in Section IV, to be able to compare the resulting PSD with those predicted by the single-point frequency spectrum models.

In order to determine how well the semi-empirical models are able to predict the PSDs of the microphones' signals from the wind tunnel dataset, the RMSE between them is calculated. Based on that metric, it is found that Robertson's

model is able to most closely predict the wind tunnel PSDs, with lowest average RMSE of 6.558 dB_{SPL} over all airspeed values, achieved for the left-mounted microphone, realized at 0^o AoA. However, the model of Goody best predicted the PSD decay rate. Robertson's model is defined as [22]:

$$\Phi(f) = \frac{q_\infty^2 \left(\frac{\overline{P^2}}{q_\infty^2}\right)}{\omega_0 \left(1 + \left(\frac{2\pi f}{\omega_0}\right)^{0.9}\right)^2} \tag{14}$$

with:

$$\frac{\overline{P^2}}{q_\infty^2} = \frac{(0.006)^2}{(1+0.14M^2)^2}, \quad \omega_0 = \frac{U_\infty}{2\delta^*}, \quad \delta^* = \frac{\delta[1.3+0.43M^2]}{10.4+0.5M^2[1+2\times10^{-8}Re_x]^{1/3}} \quad \text{and} \quad \delta = \frac{0.37x}{\mathrm{Re}_x^{1/5}}\left[1+\left(\frac{\mathrm{Re}_x}{6.9\times10^7}\right)^2\right]^{1/10}$$

where q_∞ is the dynamic pressure, $\overline{P^2}$ - mean-square pressure, M - Mach number of the airflow, ω_0 - angular frequency, U_∞ - free-stream velocity, δ - boundary layer thickness, δ^* - displacement thickness and Re_x - Reynolds number based on distance. Figure 15 shows the wind tunnel PSDs with magnitude expressed in dB_{SPL} for motor configuration D and 0^o AoA, together with the prediction of the Robertson's model for the same environmental conditions as those measured in the wind tunnel chamber, namely temperature of 22 ^{o}C and air density of 1.194 kg/m^3. The dynamic viscosity of air is taken to be $\mu = 1.837\text{x}10^{-5}$ kg/(m· s). It is observed that the similarity between the PSDs predicted by the semi-empirical model and the experimental PSDs decreases as the airspeed increases, which is also confirmed by the corresponding RMSE for each airspeed value. For the airspeeds reported in Figure 15 of 7 m/s, 10 m/s, 12 m/s, 15 m/s and 18 m/s, the RMSE between the predicted PSD by Robertson's model and the experimental PSD is 2.158 dB_{SPL}, 6.294 dB_{SPL}, 8.388 dB_{SPL}, 9.091 dB_{SPL} and 6.857 dB_{SPL}, respectively.

The significant dissimilarity between the spectra predicted by the semi-empirical single-point frequency spectrum models and those of the experimental data provided by the microphones could be attributed to the scaling of the models to the flow conditions of interest [34]. Other researchers report similar discrepancies for data collected from flush mounted microphones on a flat plate placed in a wind tunnel [33]. They identified the absence of a sizable overlap region, caused by an under-developed logarithmic region of the boundary layer, as the potential root-cause for the discrepancies between their microphones' measurements and the models' predictions for frequencies above 0.8 kHz. In conclusion, the resulting large error between the single-point frequency spectrum models' predictions and the microphones' measurements means that PSDs predicted by these models cannot be used to develop a relation that can be used to estimate the airspeed of an actual vehicle in-flight with satisfactory accuracy.

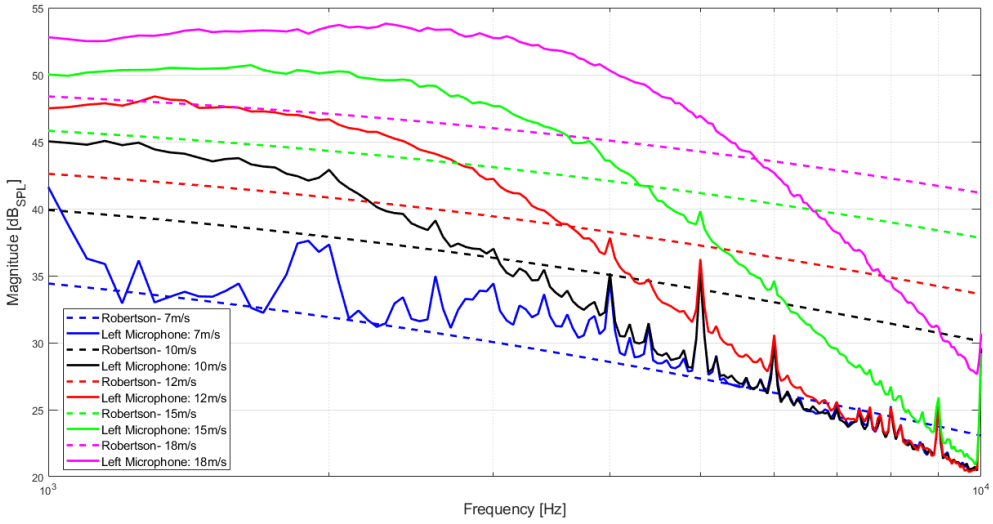

Fig. 15 PSD expressed in dB_{SPL} of left microphone wind tunnel data for motor configuration D and AoA of 0^o (solid lines) and those predicted by the Robertson model under the same conditions (dashed lines).

C. Flat Plate Assumption for the Vehicle's Nose Cone

Lastly, it is investigated whether the part of the Cyclone UAV's nose cone, where the microphones are mounted, can be assumed to be a flat plate. This is done by comparing the PSDs from the wind tunnel experiment, described in Section III.A, to the PSD of signals collected during experiment in the same wind tunnel for flush mounted microphone on a flat plate [17]. The dataset of motor configuration R is not used here, since no motors or propellers were present for the flat plate experiments. Furthermore, from the remaining datasets, only the parts corresponding to AoA of 0^o are relevant, as the flat plate was mounted at that angle with respect to the oncoming airflow.

It is important to state that there are differences in the experimental setup and equipment used between the wind tunnel tests for the flat plate and the Cyclone UAV. Firstly, the microphones are different, with the Sonion 8044 ** being utilized for the flat plate experiments. Therefore, the ΔV signals of the microphones need to be converted to pressure measurements in Pa using their sensitivity in order to be able to compare the captured TBL-induced noise. Secondly, the microphones are mounted at different distances from the leading edge. Both microphones on the Cyclone's nose cone are mounted 55 mm behind its leading edge and 30 mm behind the zig-zag tape, while the microphone on the flat plate is mounted at a distance of 400 mm downstream from the leading edge. Thirdly, in the experiment with the flat plate, the boundary layer was not artificially tripped using a turbulator, which is also why the microphone is mounted further downstream. However, it is assumed that the TBL is fully formed over the microphones in both experiments. The lowest flow velocity tested as part of the flat plate experiment is 20 m/s. The only experimental run from the Cyclone's wind tunnel testing that has a similar flow velocity - 19.5 m/s - is for motor configuration D at an AoA of 0^o.

Figure 16 depicts the PSDs of the signals from the flat plate microphone and the two microphones mounted on the Cyclone at the experimental conditions mentioned above. The magnitude of the PSD is expressed in dB_{SPL}. The metric used to compare the PSDs from the different experiments is again the RMSE, which turns out to be 12.218 dB_{SPL} between the flat plate PSD and the Cyclone's left-mounted microphone PSD, and 13.066 dB_{SPL} for the right-mounted one. While the RMSE is substantial, it should be noted that to an extend it could be attributed to differences in equipment, experimental setup and environmental conditions. A promising prospect is the fact that the slope of the flat plate's PSD exhibits high similarity with the slopes of the Cyclone's PSDs for frequencies higher than 3 kHz. In fact, in the range 3 kHz to 10 kHz, the flat plate PSD has a slope of -4.393×10^{-3} dB_{SPL}/Hz, while the PSDs corresponding to the Cyclone's left- and right-mounted microphones have a slope of -3.540×10^{-3} dB_{SPL}/Hz and -3.959×10^{-3} dB_{SPL}/Hz, respectively. However, in the frequency range between 1 kHz and 3 kHz, the PSDs from the two experiments differ in shape, with the flat plate one continuing to follow the same linear pattern, while those corresponding to the Cyclone have concave shape. The flat plate PSD carry over the same behavior also for frequencies below 1 kHz. It is unlikely that the disparity in the shape of the PSDs in the lower frequencies is caused by differences in the control variables of the two experiments. While the similar behavior of the PSDs above 3 kHz could substantiate the validity of assuming the part of the Cyclone's nose cone where the microphones are mounted to be a flat plate, more data is needed, ideally from experiments that more closely resemble the equipment and setup of those conducted with the Cyclone UAV.

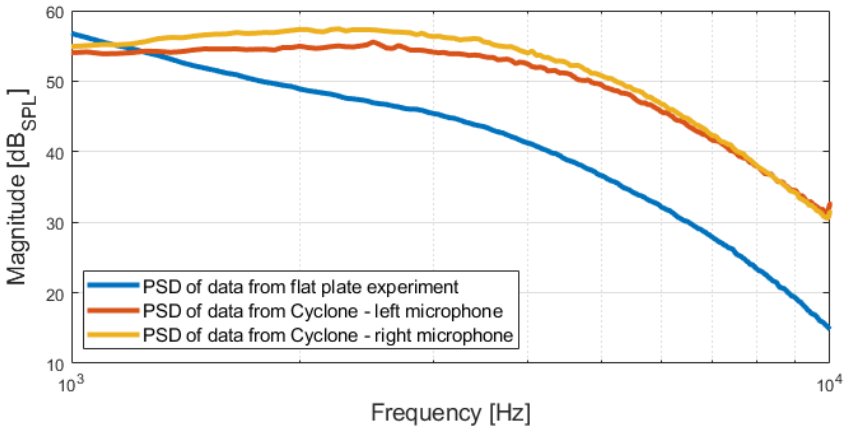

Fig. 16 PSDs of microphone signals converted to pressure measurements (Pa) of wind tunnel data from flat plate experiments (airflow speed = 20 m/s, AoA = 0^o) and from Cyclone experiments (motor configuration D, airflow velocity = 19.5 m/s, AoA = 0^o). The PSD magnitude is expressed in dB_{SPL}.

**https://www.sonion.com/product/8044-2/

VII. Conclusions & Recommendations

This paper outlined and gauged a novel design for an airspeed instrument aimed at small hybrid UAVs that utilizes flush mounted microphones on the vehicle's nose cone, used to capture the pseudo-sound caused by the TBL flow-induced wall-pressure fluctuations. In total, two microphones were installed on the Cyclone's nose cone, both at a distance of 55 mm downstream from its leading edge, or 30 mm downstream from the zig-zag tape, and separated 40 mm apart. This configuration was chosen with the aim of being able to subtract the microphone signals, which would suppress acoustic sounds captured by the microphones. However, the pseudo-sound due to the flow structures in the TBL was dominant in the microphones' recordings, resulting in the microphones' signals subtraction having minimal benefits. To estimate the airspeed, the power spectral density estimates of the microphones' signals are used, which necessitates the creation of dedicated models relating the two. Feed-forward artificial neural networks were selected as model structure, trained by applying a supervised learning approach, with the PSD of microphones' signals and corresponding airspeed measures obtained from both wind tunnel and flight experiments constituting the input-output dataset. It was found that models trained on the PSDs of the left-mounted microphone's signals alone achieved the lowest approximation error over the validation dataset, lower than those trained on the PSDs of the subtracted signals, which is a further argument for the lack of need for the signal subtraction method. The best model achieved a RMSE of 1.037 m/s with a mean approximation error of 0.043 m/s and a standard deviation of 1.039 m/s. Next to that, models including the AoA as an additional input were trained. Here, only PSD data from the wind tunnel experiments was used as there the AoA was recorded. An uncertainty of up to 15% was added to the AoA inputs that were part of the validation dataset to simulate the performance of a non-perfect sensor. The resulting best model had a RMSE of 0.364 m/s and a mean approximation error of 0.027 m/s with a standard deviation of 0.486 m/s. Lastly, the sensitivity analysis showed that the model is more sensitive towards the PSD of the microphones' signals than towards the AoA. From these results it could be concluded that the utilization of the proposed instrument concept for estimating the airspeed of a vehicle in-flight at a wide range of angles of attack is feasible, thus substantiating its further development.

Additional work is required in order to improve the instrument's functionality and bring it to a technology demonstration level. The first recommendation stems from the fact that microphones' signals subtraction is not really needed. As such, the microphone mounting configuration could be changed to have the microphones behind one another at different distances downstream. This can be used to detect boundary layer flow separation, or separation bubbles. Alternatively, the number of microphones can be reduced to just one. This has the benefit of also decreasing the amount of data fed to the micro-controller, thus lowering the computational load of the data processing. Secondly, new flight experiments should be carried out with a dedicated AoA sensor installed on the vehicle, allowing to collect data about this parameter during flight. Next to that, an additional airspeed instrument such as hot-wire anemometer could be installed to validate the collected Pitot tube's measurements. Thirdly, it is recommended to carry out new wind tunnel experiments where the airspeed instrument would be in the same form and configuration as in the flight experiments. This would eliminate all differences between the wind tunnel and flight data stemming from the distinct equipment and experimental setup used. Furthermore, it could serve to confirm that the 50 Hz component present in the collected wind tunnel data is indeed caused by a piece of equipment utilized during the wind tunnel experiments. Fourthly, experiments to study the effects of air density, temperature and humidity on the resulting PSD of the microphones' signals, and consequently on the performance of the airspeed instrument, are recommended. Lastly, building a custom PCB with an integrated microprocessor for the instrument could substantially decrease its size and weight and it could improve the acquired signal quality by reducing the electrical noise. Limiting the electrical and power supply noise should remove the large discrepancies in the peaks present in the wind tunnel and flight PSDs. This could lead to the PSDs of the subtracted microphones' signals being better suited for constructing the models.

As changing the AoA has a distinct effect upon the PSD of the microphones' signals, it could be investigated whether the proposed instrument would be able to also predict the vehicle's AoA in conjunction with the airspeed. This could be achieved by modifying the structure of the model to have two outputs, one being the airspeed, and the other - the AoA, while the inputs would still be the PSD of the microphones' signals.

References

[1] Anderson, J., *Fundamentals of Aerodynamics*, McGraw-Hill Education, New York, NY, United States, 2016.

[2] Stengel, R. F., *Flight Dynamics*, 1st ed., Princeton University Press, Princeton, NJ, USA, 2004.

[3] de Oliveira Buscarini, I., Barsaglini, A. C., Jabardo, P. J. S., Taira, N. M., and Nader, G., "Impact of Pitot tube calibration on

the uncertainty of water flow rate measurement," *Journal of Physics: Conference Series*, Vol. 648, 2015, pp. 12005–12015. https://doi.org/10.1088/1742-6596/648/1/012005.

[4] Pallet, E. H. J., and Coombs, L. F. E., *Aircraft Instruments & Integrated Systems*, 1st ed., Pearson, London, 1992.

[5] Verling, S. L., Stastny, T., and Siegwart, R., "Full Envelope System Identification of a VTOL Tailsitter UAV," *Proceedings of American Institute of Aeronautics and Astronautics: Scitech Forum 2021*, 2021. https://doi.org/10.2514/6.2021-1054.

[6] Reddy, G. P. O., and Singh, S. K., *Geospatial Technologies in Land Resources Mapping, Monitoring and Management*, 1st ed., Springer Berlin Heidelberg, Berlin Heidelberg, 2018.

[7] Hayward, A. T. J., *Flowmeters: A Basic Guide and Source-Book for Users*, 1st ed., Palgrave Macmillan, London, United Kingdom, 1979.

[8] Willmarth, W. W., "Pressure Fluctuations Beneath Turbulent Boundary Layers," *Annual Review of Fluid Mechanics*, Vol. 7, No. 1, 1975, pp. 13–36. https://doi.org/10.1146/annurev.fl.07.010175.000305.

[9] Brungart, T. A., Lauchle, G. C., Deutsch, S., and Riggs, E. T., "Outer-flow effects on turbulent boundary layer wall pressure fluctuations," *The Journal of the Acoustical Society of America*, Vol. 105, No. 4, 1999, pp. 2097–2106. https://doi.org/10.1121/1.426815.

[10] Smolyakov, A., "Calculation of the spectra of pseudosound wall-pressure fluctuations in turbulent boundary layers," *Acoustical Physics*, Vol. 46, 2000, pp. 342–347.

[11] Rackl, R. G., and Weston, A. R., "Modeling of Turbulent Boundary Layer Surface Pressure Fluctuation Auto and Cross Spectra - Verification and Adjustments Based on TU-144LL Data," 2005.

[12] Laganelli, A. L., and Wolfe, H. F., "Prediction of fluctuating pressure in attached and separated turbulent boundary-layer flow," *Journal of Aircraft*, Vol. 30, No. 6, 1993, pp. 962–970. https://doi.org/10.2514/3.46440.

[13] Lowson, M. V., "Prediction of boundary layer pressure fluctuations," 1968.

[14] Edelman, L., Pensado, A., Robinson, S., and Dam, C., "Low-Cost Detection of Boundary Layer Separation with Dynamic Pressure Measurements," 2016. https://doi.org/10.2514/6.2016-3623.

[15] Moshkov, P., "Experimental determination of wall pressure fluctuations on a Superjet 100 fuselage at level flight conditions," *Aerospace Systems*, 2022. https://doi.org/10.1007/s42401-022-00174-6.

[16] Panton, R. L., Goldman, A., Lowery, R., and Reischman, M., "Low-frequency pressure fluctuations in axisymmetric turbulent boundary layers," *Journal of Fluid Mechanics*, Vol. 97, No. 2, 1980, pp. 299–319.

[17] VanDercreek, C. P., Merino-Martínez, R., Sijtsma, P., and Snellen, M., "Evaluation of the effect of microphone cavity geometries on acoustic imaging in wind tunnels," *Applied Acoustics*, Vol. 181, 2021, p. 108154.

[18] Yokoi, Y., "Experimental Study of Internal Flow Noise Measurement by Use of a Suction Type Low Noise Wind Tunnel," *Wind Tunnel Designs and Their Diverse Engineering Applications*, edited by N. Ahmed, IntechOpen, Sydney, Australia, 2013, Chap. 7, pp. 147–164.

[19] Roger, M., "Microphone Measurements in Aeroacoustic Installations," Tech. rep., University of Lyon, 36 Avenue Guy de Collongue, 69134 Ecully cedex, France, December 2017. https://doi.org/10.14339/STO-EN-AVT-287-03-PDF.

[20] Barnard, A. R., "Flow Induced Noise Reduction Techniques for Microphones in Low Speed Wind Tunnels," Primary research report, Michigan Technological University, 1400 Townsend Dr, Houghton, MI 49931, United States, October 2014.

[21] Goody, M., Simpson, R., and Chesnakas, C., *Surface pressure fluctuations and pressure-velocity correlations produced by a separated flow around a prolate spheroid at incidence*, AIAA, 1997. https://doi.org/10.2514/6.1997-485.

[22] Robertson, J. E., "Prediction Of In Flight Fluctuating Pressure Environments Including Protuberance Induced Flow," Tech. rep., Wyle Labs Inc., March 1971.

[23] Smeur, E., Bronz, M., and Croon, G., "Incremental Control and Guidance of Hybrid Aircraft Applied to a Tailsitter Unmanned Air Vehicle," *Journal of Guidance, Control, and Dynamics*, 2018. https://doi.org/10.2514/1.G004520.

[24] Giancoli, D. C., *Physics for Scientists & Engineers with Modern Physics*, 4th ed., Pearson, London, United Kingdom, 2008.

[25] White, F. M., *Viscous Fluid Flow*, McGraw-Hill international edition, McGraw-Hill, New York, NY, United States, 2006.

[26] Long, M., "2 - Fundamentals of Acoustics," *Architectural Acoustics (Second Edition)*, edited by M. Long, Academic Press, Boston, 2014, second edition ed., pp. 39–79. https://doi.org/10.1016/B978-0-12-398258-2.00002-7.

[27] Lee, C., and Jiang, X., "Flow structures in transitional and turbulent boundary layers," *Physics of Fluids*, Vol. 31, 2019. https://doi.org/10.1063/1.5121810.

[28] Eargle, J., *The Microphone Book: From Mono to Stereo to Surround - a Guide to Microphone Design and Application*, Taylor & Francis, Boca Raton, FL, United States, 2012.

[29] Lane, C., "Measurement of Turbulent Boundary Layer Induced Surface Pressure Fluctuations," Master's thesis, University of Toronto, North York, ON M3H 5T6, Canada, 7 2018.

[30] Zhu, J., and Shih, T., *Calculations of Turbulent Separated Flows*, NASA technical memorandum, National Aeronautics and Space Administration, 1993.

[31] Wambsganss, M. W., and Zaleski, P., "Measurement, interpretation, and characterization of near-field flow noise," Tech. rep., Argonne National Laboratory, Lemont, IL, USA, 1970.

[32] Simpson, R. L., Ghodbane, M., and Mcgrath, B. E., "Surface pressure fluctuations in a separating turbulent boundary layer," *Journal of Fluid Mechanics*, Vol. 177, 1987, p. 167–186. https://doi.org/10.1017/S0022112087000909.

[33] Blitterswyk, J. V., and Rocha, J., "Prediction and measurement of flow-induced wall-pressure fluctuations at lowmach numbers," *Canadian Acoustics - Acoustique Canadienne*, 2014.

[34] Thomson, N., and Rocha, J., "Comparison of Semi-Empirical Single Point Wall Pressure Spectrum Models with Experimental Data," *Fluids*, Vol. 6, 2021, p. 270. https://doi.org/10.3390/fluids6080270.

[35] Casalino, D., Grande, E., Romani, G., Ragni, D., and Avallone, F., "Towards the definition of a benchmark for low Reynolds number propeller aeroacoustics," *Journal of Physics: Conference Series*, Vol. 1909, 2021, p. 012013. https://doi.org/10.1088/1742-6596/1909/1/012013.

[36] Stoica, P., and Moses, R., *Spectral Analysis of Signals*, Pearson Prentice Hall, 2005.

[37] Welch, P. D., "The use of fast Fourier transform for the estimation of power spectra: A method based on time averaging over short, modified periodograms," *IEEE Transactions on Audio and Electroacoustics*, Vol. 15, 1967, pp. 70–73.

[38] Harris, F., "On the Use of Windows for Harmonic Analysis With the Discrete Fourier Transform," *Proceedings of the IEEE*, Vol. 66, 1978, pp. 51 – 83. https://doi.org/10.1109/PROC.1978.10837.

[39] Parekh, R., *Fundamentals of image, audio, and video processing using MATLAB®*, 2021. https://doi.org/10.1201/9781003019718.

[40] Ye, C., Yang, Y., Fermüller, C., and Aloimonos, Y., "On the Importance of Consistency in Training Deep Neural Networks," *CIDSE, Arizona State University*, 2017.

[41] Mishra, K. K., Mittal, N., and Mirja, M. H., "Image Compression Using Multilayer Feed Forward Artificial Neural Network with Nguyen Widrow Weight Initialization Method," 2014.

[42] Fletcher, L., Katkovnik, V., Steffens, F., and Engelbrecht, A., "Optimizing the number of hidden nodes of a feedforward artificial neural network," *1998 IEEE International Joint Conference on Neural Networks Proceedings. IEEE World Congress on Computational Intelligence (Cat. No.98CH36227)*, Vol. 2, 1998, pp. 1608–1612 vol.2. https://doi.org/10.1109/IJCNN.1998.686018.

[43] Heaton, J., *Introduction to Neural Networks with Java*, Heaton Research, 2008.

[44] Sobol, I. M., "Global sensitivity indices for nonlinear mathematical models and their Monte Carlo estimates," *Mathematics and Computers in Simulation*, 2001.

[45] Saltelli, A., and Tarantola, S., "On the Relative Importance of Input Factors in Mathematical Models," *Safety Assessment for Nuclear Waste Disposal*, 2011. https://doi.org/10.1198/016214502388618447.

[46] Sobol, I. M., "Sensitivity estimates for nonlinear mathematical models," *Mathematical Modelling and Computational Experiments*, 1993.

[47] Mishra, A., and Singh, A., "Analysis of flow variation over elliptical nose cone at different angle of attack," Vol. 20, 2020, pp. 01–06.

[48] Afgan, I., Benhamadouche, S., Han, X., Sagaut, P., and Laurence, D., "Flow Over a Flat Plate with Uniform and Coherent Gust Inlets," *Journal of Fluid Mechanics*, Vol. 720, 2013, pp. 457–485. https://doi.org/10.1017/jfm.2013.25.

[49] Sankaralingam, L., and Ramprasadh, C., "A comprehensive survey on the methods of angle of attack measurement and estimation in UAVs," *Chinese Journal of Aeronautics*, Vol. 33, No. 3, 2020, pp. 749–770. https://doi.org/https://doi.org/10.1016/j.cja.2019.11.003, URL https://www.sciencedirect.com/science/article/pii/S1000936119304078.

[50] Maestrello, L., "Measurement of noise radiated by boundary layer excited panels," *Journal of Sound and Vibration*, Vol. 2, No. 2, 1965, pp. 100–115. https://doi.org/https://doi.org/10.1016/0022-460X(65)90088-X, URL https://www.sciencedirect.com/science/article/pii/0022460X6590088X.

[51] Efimtsov, B., "The Prediction of the Pressure Fluctuation Field Characteristics of the TBL," Tech. rep., TsAGI, 1995.

Part II

Preliminary Analysis

*This part has been assessed for the course AE4020 Literature Study.

3

Literature Review

3.1. Introduction

This chapter will present the literature review conducted as part of the research project regarding a novel airspeed instrument for vertical take-off and landing (VTOL) tailsitter micro aerial vehicles (MAV). Also known as hybrid MAVs, this type of drone combines hovering capabilities and a fixed wing for fast forward flight. Tailsitter vehicles land on their tail, and sit vertically on it in takeoff and landing, while tilting the vehicle forward during horizontal flight [5]. Just as with traditional airplanes in horizontal flight, the effectiveness of the aerodynamic surfaces in-flight - and as a result the required control input - is dependent on the dynamic pressure of the airflow, which in turn is governed by the air mass density and velocity. It is important to note that the dynamic pressure is proportional to the square of the airspeed, making it more sensitive towards changes in the airspeed than to the air density. Therefore, as the control derivatives for both the symmetric and asymmetric motions are related to the dynamic pressure, knowing the precise airspeed of the vehicle at any time is vital for control purposes [18]. Furthermore, the airspeed is a critical flight parameter needed for the calculation of all aerodynamic forces and moments equations. Precise airspeed control is necessary for achieving precise altitude and heading, climbs and descents at given rates, as well as safely performing critical maneuvers.

The instrument that has been used for decades in aviation to determine the airspeed of an airplane is the Pitot tube. Its working principle is to sense the dynamic pressure, caused by the movement of the vehicle within the mass of air, and translate that to a measure of the airspeed. However, the Pitot tube provides increasingly inaccurate measurements as the speed of the airflow reduces [4]. This presents an issue, since hybrid MAVs typically move at a lot lower speeds, when compared to conventional airplanes. After the introduction of the Global Positioning System (GPS), GPS sensors have been heavily used in aviation. They can provide a measure of the vehicle's ground speed, but not the airspeed, based on the Doppler shift of the signals received by the sensors from each GPS satellite [7]. As such, information from the GPS sensors cannot be used to compute aerodynamic forces and moments because they depend on the airspeed and not the ground speed. Furthermore, the maximum specified speed of an aerial vehicle is typically expressed in terms of its airspeed. Next to that, GPS also has few significant drawbacks. Firstly, its signal could be completely blocked, or at least partially reflected from buildings or terrain, thus giving rise to multi-path effects, which could deteriorate the accuracy of the position and velocity estimates. Secondly, there are areas in the world that do not have GPS coverage, thus limiting the usage of GPS sensors. As such, there is a clear need for an alternative way to reliably and accurately measure the airspeed in MAVs. This is the main motivation behind the proposed research project.

While the Pitot tube is the most widely used flow velocity measuring instrument to determine the airspeed of an aircraft, there are other instruments that could be utilized to measure the velocity of an airflow at a given point. These include vane-type anemometers, hot-wire anemometers, jet-deflection velocity meter, and ion-deflection velocity meter [19]. The vane-type anemometers consist of a free-spinning rotor placed axially in the flow, and a system - either electrical or mechanical - that counts the motor revolutions. Electrical vane-type anemometers can be used to provide an instantaneous measure of the flow velocity, however more often they are used to obtain the mean velocity over a given time period. While an instrument of this type can be used to sense the airspeed of an aerial vehicle, they are not utilized due to their fragility. The bearings can be easily damaged and affected by dirt in the flow, and the motor blades can be bent

by high velocity flows. As such, this instrument requires frequent recalibration in order to maintain high accuracy of measurements. The hot-wire anemometers utilize an electrically heated element placed in the flow. This type of instrument makes use of the fact that higher velocity tends to cool the element more, thus relating the change in temperature to the velocity of the flow. This is possible since changes in the temperature of the element result in changes in its electrical resistance. By keeping the current in the element constant, any changes in the resistance can be measured and since they are proportionate to the temperature of the element, the change in temperature can be known. From that, the velocity of the flow can be determined. Another method is to keep the temperature of the element constant. In that case, as the flow cools down the element and changes its resistance, the required current to bring the element to its initial temperature will be different. The change in the needed current is proportional to the flow velocity and is thus used to determine it. However, the disadvantages of frequent recalibration to maintain high accuracy, the tendency of radiation error when the anemometer is placed close to a solid surface, and the required trade-off between high accuracy and robustness limit the applicability of hot-wire anemometers for practical use on aerial vehicles for prolonged period of time. The jet-deflection velocity meter relies on measurement of differential pressure, much like the Pitot tube. It operates by shooting a gas stream out of a nozzle, in a direction normal to the traveling flow, towards two receiver nozzles, one located to the left and one to the right. If there is no flow going between the issuing and receiving nozzles, then there will be no difference in the pressure sensed at the receiving nozzles due to the issued stream of gas. However, if there is flow moving in-between, the stream will deviate towards one side, meaning that the receiving nozzles will sense different pressures. This pressure difference is directly proportionate to the flow velocity, and is used to calculate it. While this type of instrument can provide readouts at very low velocities, has no moving parts, and can response fast to fluctuating flow, its accuracy is worse than that of most other types of instruments, and requires a supply of compressed gas, which adds weight and limit the period of usage of the instrument. Furthermore, slight damage to the nozzles will greatly impact their accuracy, thus requiring frequent inspection and recalibration. The ion-deflection velocity meter is similar to the jet-deflection velocity meter but makes use of a stream of ions instead of a gas. It has the same drawbacks as the jet-deflection velocity meter but the benefit of being able to tolerate a dusty environment. However, its practical use of aerial vehicles is still limited. The proposed airspeed instrument aims to overcome most of the drawbacks of the other available types of flow velocity measuring instruments.

3.2. Literature Review

As the airspeed instrument will read audio data, sound is the first topic of interest tackled in Subsection 3.2.1. In Subsection 3.2.2, the focus is on the nature of the boundary layer and its contribution to giving rise to sound waves. Subsection 3.2.3 provides a discussion on the current state-of-the-art in signal processing and filtering techniques, which will be relevant for the isolation of the sound signal of interest from all others. Finally, Subsection 3.2.4 tackles the modeling techniques relevant for establishing the relation between the measured sound levels and the airspeed.

3.2.1. Sound

As explained in Section 1.1, the changing airspeed of the drone led to changes in the recorded sound by the on-board equipment. This is the principle upon which the airspeed will be estimated by the proposed instrument design. Therefore, having a solid understanding of the characteristics of sound, and the technologies used to measure them, is vital for successfully carrying out the research project.

The Nature of Sound

The term sound has different use in the field of physics than those in physiology and psychology. The American National Standards Institute (ANSI) gives the following physical definition of sound: *"Oscillation in pressure, stress, particle displacement, particle velocity, etc., propagated in a medium with internal forces (e.g., elastic or viscous), or the superposition of such propagated oscillation"* [20]. In a physical sense, sound is a vibration propagating through a medium (gas, liquid, or solid) in the form of an acoustic wave. The acoustic waves are a type of mechanical waves, with the latter being defined as an oscillation of matter, thus transferring energy through a medium [21]. As such, mechanical waves can only exist in media that possess both elasticity and inertia, meaning that they cannot propagate through vacuum. The frequency spectrum of acoustic waves can be divided in 3 parts: infrasonic, audio, and ultrasonic. The audio frequency range refers to sounds that can be registered by the human ear and it includes the frequencies from 20 Hz to 20 000 Hz. The frequency is related to the concept of sound pitch, with higher

frequency sounds being perceived as of higher pitch and vice versa. The infrasonic range refers to the frequencies below 20 Hz, while the ultrasonic range includes the frequencies above 20 000 Hz [22].

Acoustic waves are generated by an acoustic source, which typically works by exciting vibrations in the surrounding medium. The acoustic source can be an object, but also a natural process that results in pressure fluctuations, or particle displacement, in the medium. With time, the vibrations caused by the acoustic source will propagate in space, at the speed of sound for the given medium, forming the acoustic- or sound wave. At a distance x away from the source, the pressure, velocity and particle displacement of the medium are a function of time. Meanwhile, at a time instant t, the pressure, velocity and particle displacement of the medium are a function of the distance x [23]. It should be noted that the particles in the medium do not travel with the acoustic wave, they are just displaced from their equilibrium position, thus forming the wave-fronts which propagate at the speed of sound for that particular medium. Therefore, the average position of the particles in the medium does not change in time. As a sound wave travels through the medium, it can be reflected, refracted, or attenuated based on the characteristics of the medium [24].

A sound wave can be described in terms of its fundamental characteristics, including the sound (or acoustic) pressure, the particle displacement, the particle velocity, and the sound (or acoustic) intensity [22]. The sound pressure is the magnitude of the local pressure deviation from the ambient (or equilibrium) pressure of the given medium, caused by the presence of a sound wave. In air, it will be defined as the local pressure deviation from the atmospheric pressure. The sound wave introduces a dynamic pressure component to the ambient static pressure, thus resulting in total pressure, which is defined as [25]:

$$p_{total} = p_{stat} + p \tag{3.1}$$

with p_{total} being the total pressure, p_{stat} - the static local ambient pressure, and p - the (dynamic) sound pressure. The sound pressure caused by a sound source attenuates as the acoustic wave travels away from the source. The decrease is sound pressure is according to the inverse-proportional law:

$$p(x) \propto \frac{1}{x} \tag{3.2}$$

The sound pressure's SI unit is the Pascal (Pa), however measurements are often presented in terms of the sound pressure level (SPL) [26]. It is a logarithmic measure of the effective pressure of an acoustic wave relative to a defined reference. The SPL is denoted by L_p and is typically measured is decibels (dB):

$$L_p = \ln\left(\frac{p}{p_0}\right) \overset{\text{dB}}{=} 20\log_{10}\left(\frac{p}{p_0}\right) \tag{3.3}$$

where p is the root mean square of the sound pressure, and p_0 is the reference sound pressure, usually taken to be $p_0 = 20 \times 10^{-6}$ Pa in air [20], which is the threshold of human hearing [27]. The SPL is related to the concept of loudness of a sound, with higher pressure sound waves being perceived as louder and vice versa. The particle displacement is a measure of the distance over which a particle is displaced when transmitting a mechanical wave through the medium [28]. Its SI unit is the meter (m) and can be used to measure the displacement due to both longitudinal and transverse waves. The particle displacement, denoted δ, is related to the particle velocity, associated with the wave traveling through the medium:

$$\delta = \int_t v dt \tag{3.4}$$

The next characteristic of a sound wave, the particle velocity, is a measure of the velocity at which particles are displaced from their equilibrium position when transmitting a wave through the medium. In the context of a sound wave traveling through a fluid medium (e.g. air), the particle velocity can be thought as the physical speed of a volume of the fluid as it oscillates back and forth in the direction of propagation of the wave. It should be noted that the particle velocity is not the same as the velocity at which the wave itself is traveling, which for acoustic waves is the speed of sound for the given medium. Typically, the particles oscillate about their equilibrium positions slower than the speed at which the wave propagates. Lastly, the particle velocity is also different than the velocity of the individual molecules of the medium, which may vary drastically between different molecules [29]. The particle velocity, denoted v, is related to the particle displacement:

$$v = \frac{\partial \delta}{\partial t} \tag{3.5}$$

The final characteristic of interest is the sound intensity. It is a measure of the power carried by a wave over a unit area in a direction that is perpendicular to the plane of the unit area. The sound intensity is measured in Watt per square meter (W/m^2) in SI units. Occasionally, also the sound intensity level is used, measured in decibels (dB), similar to the SPL. Figure 3.1 depicts a visualization of the idea of sound intensity for an acoustic wave at a distance r away from the acoustic source.

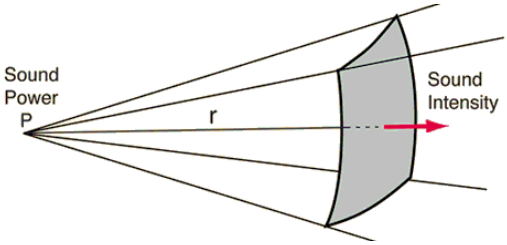

Figure 3.1: Visualization of the concept of sound intensity[1].

The sound intensity is denoted by the symbol I and is defined as [22]:

$$I = \frac{P}{A} = pv \tag{3.6}$$

with p being the (dynamic) sound pressure, and v the particle velocity. The direction of the sound intensity is given by the average direction of the energy flow of the wave. Most often, the quantity of interest is the average sound intensity over a period of time, or over the period of a single wave T:

$$\langle \mathbf{I} \rangle = \frac{1}{T} \int_0^T p(t)\mathbf{v}(t)dt \tag{3.7}$$

Just as the sound pressure, the sound intensity also decreases as the sound wave travels away from the acoustic source. Due to the fact that the sound intensity is related to a unit area, rather than unit distance, it decreases according to the inverse-square law:

$$I(x) \propto \frac{1}{x^2} \tag{3.8}$$

Other characteristics of a sound wave include the sound energy W, the sound power P, the sound exposure E, and the acoustic impedance Z [22]. However, those characteristics are not considered in the context of the current research project.

In gases, plasma and liquids, sound propagates in the form of longitudinal waves. This type of waves cause the particles in the medium to displace, or vibrate, along an axis parallel to the propagation of the wave. Looking at a longitudinal wave traveling through a medium, regions of compression and rarefaction are observed. In the area of compression of a longitudinal wave the particles of the medium are the closest together and the pressure is the highest in the wave, while in the area of rarefaction the particles are the farthest apart and the pressure is the lowest [30]. Figure 3.2 depicts a longitudinal sound wave in air. The regions of compression and rarefaction are clearly visible. The longitudinal sound waves can also be seen as compression waves, or just pressure fluctuations in the medium. In solids, sound propagates as both longitudinal and transverse waves. The longitudinal component is still a wave of alternating pressure deviations from the static equilibrium pressure, while the transverse component is a wave of alternating shear stresses, perpendicular to the wave's direction of travel. In a transverse mechanical wave, the particles in the medium oscillate about their equilibrium position along an axis that is perpendicular to the direction of the wave propagation.

From the discussion carried out so far, it becomes apparent that the fundamental elements that form the basis of any sound are the pressure and the time (for a given point in space). As such, the longitudinal sound waves can be simplified and represented in terms of a sinusoidal plane waves in the time domain,

[1] http://hyperphysics.phy-astr.gsu.edu/hbase/Acoustic/invsqs.html

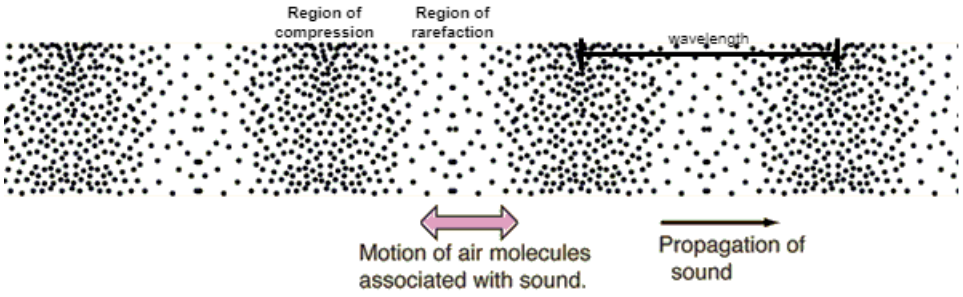

Figure 3.2: Visualization of a sound wave propagating in air. The wavelength is the distance between two sequential identical parts of the wave - in this example between sequential compressions[2].

which in turn can be used to describe every sound. Figure 3.3 depicts a longitudinal sound wave in air, described as a sinusoidal plane wave of oscillating pressure, for a given distance x away from the sound source. The different characteristics of the wave are also outlined. Every complex sound can be represented as a combination of various sound waves of different properties (frequencies and amplitudes) and noise [31].

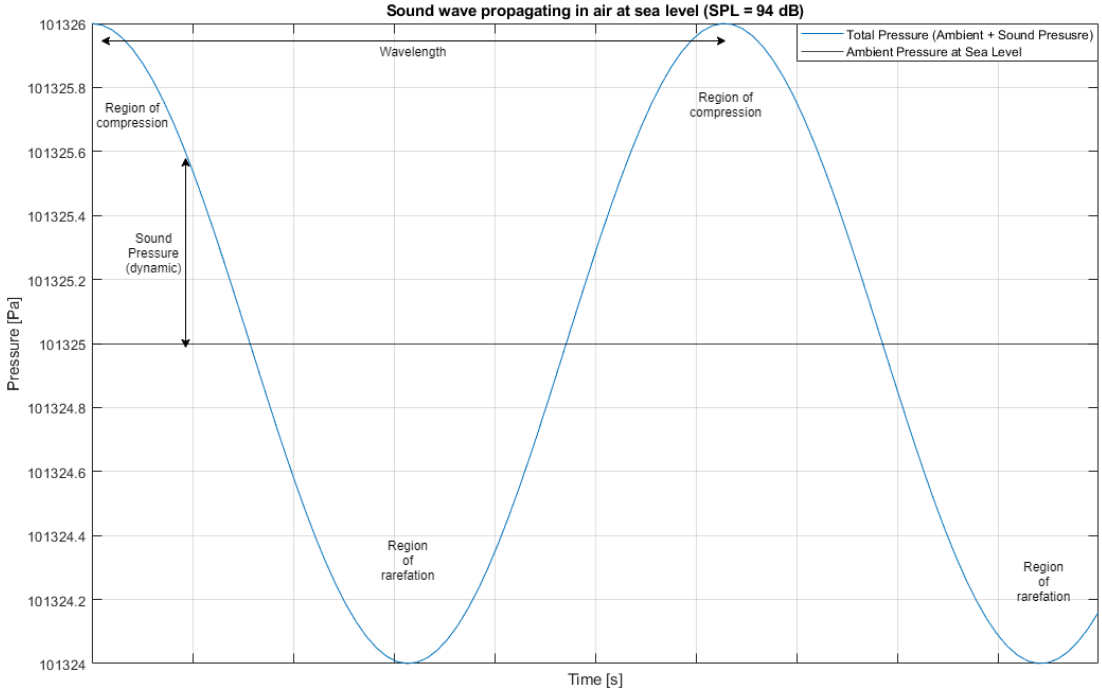

Figure 3.3: A sound wave of SPL = 94 dB (pressure amplitude of 1 Pa) propagating in air at sea level, described in terms on a sinusoidal plane wave for a given point in space.

When sound waves are depicted as sinusoidal plane waves of varying pressure, they are characterized by the following properties: frequency (or wavelength), amplitude (sound pressure), speed of sound, and the direction of propagation. The speed and direction properties can be combined into a velocity vector, while combining the wave number and the direction yields the wave vector. The sound pressure along the direction of propagation of the wave will then be given by the wave function:

$$p(x,t) = p_m \cos(kx - \omega t + \varphi_p) \tag{3.9}$$

with p_m being the amplitude of the sound pressure, k - the angular wavenumber, ω - the angular frequency, and φ_p - the initial phase shift of the sound pressure. Due to the fact that the pressure decreases as

[2] http://hyperphysics.phy-astr.gsu.edu/hbase/Sound/tralon.html

distance away from the sound source increases, according to the inverse-proportional law in Equation (3.2), the pressure amplitude p_m will vary in space. This can be taken into account by treating the p_m term in Equation (3.9) as a function of the distance x from the acoustic source - $p_m(x)$.

Figure 3.4 depicts the behavior and properties of a particle of the medium as a right going mechanical wave of Gaussian pulse form travels through it (the wave still travels at the speed of sound for that medium). The green dot represents the equilibrium location of the selected particle in the medium. The black arrow depicts the displacement of the selected particle from its equilibrium position, while the red arrow signifies its velocity. The pressure experienced by the particle is visualized using the blue graph, and the formed regions of compression and rarefaction are labeled in the medium.

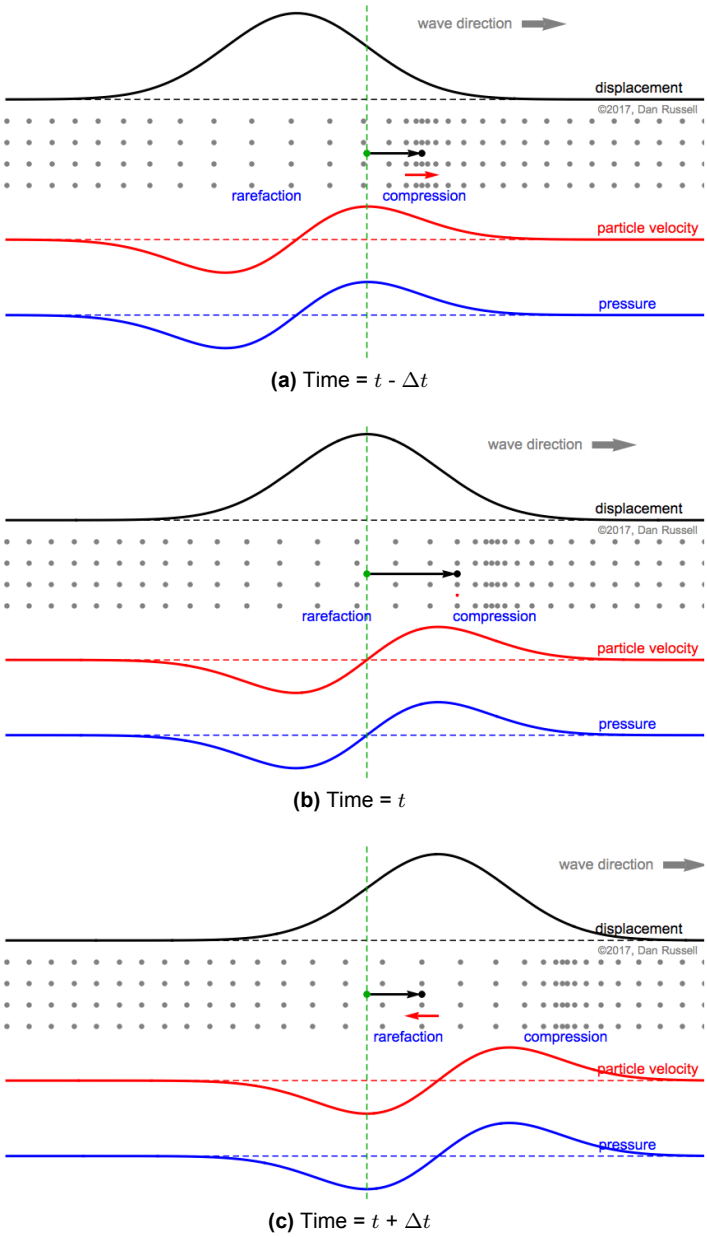

(a) Time = t - Δt

(b) Time = t

(c) Time = t + Δt

Figure 3.4: Behavior of a particle in a right going Gaussian pulse mechanical wave traveling through the medium. The particle displacement, the particle velocity, and the pressure are all depicted [3]

[3] https://www.acs.psu.edu/drussell/Demos/phase-p-u/phase-p-u.html

From the figures above it can be clearly seen that the particle velocity is given by the slope of the particle displacement as indicated by Equation (3.5). Furthermore, it is observed that the pressure varies in the same manner as the particle velocity. This is also predicted by the general formulation of the sound pressure along an acoustic wave, which is given by [22]:

$$p(x,t) = -\rho c^2 \frac{\partial \delta}{\partial x}(x,t) \tag{3.10}$$

with ρ being the density of the medium, and c - the speed of sound for that particular medium. From Equation (3.10) it can be noted that in case the wave depicted in Figure 3.4 was left going, the particle velocity and the sound pressure would have been of opposite phase (180 degrees out-of-phase) [32].

The speed of sound is a property of the medium and it depends on how fast vibrational energy can be transferred through it. For any mechanical wave propagating through a medium, its speed will depend on both the elastic properties and inertial properties of said medium. For ideal gases, the speed of sound is given by [33]:

$$v = \sqrt{\frac{\gamma R T_K}{M}} \tag{3.11}$$

with γ being the adiabatic index, R - the gas constant having a value of 8.31 J/mol $\cdot$ K, T_K - the absolute temperature measured in Kelvins, and M - the molecular mass of the gas. In general, mechanical waves travel faster in more rigid media (speed of sound is greater in steel, than it is in air [33]), but the speed of sound decreases as the medium becomes denser. This is evident from the relation between the density and temperature of an ideal gas, given by [34]:

$$\rho = \frac{p}{RT} \tag{3.12}$$

The speed of sound in air at standard sea level conditions is about 335 m/s. The standard sea level conditions are characterized by air density of $\rho = 1.225$ kg/m^3, ambient atmospheric pressure of $p_{stat} = 101\ 325$ Pa, and air temperature of $T = 15^{\circ}$ C [35].

Lastly, the governing equation of the propagation of acoustic waves through a medium is the acoustic wave equation. It describes the evolution of either the acoustic pressure p, or the particle velocity v, as a function of both space and time [36]:

$$\frac{\partial^2 p}{\partial x^2} + \frac{\partial^2 p}{\partial y^2} + \frac{\partial^2 p}{\partial z^2} - \frac{1}{c^2}\frac{\partial^2 p}{\partial t^2} = 0 \tag{3.13}$$

$$\nabla^2 p - \frac{1}{c^2}\frac{\partial^2 p}{\partial t^2} = 0 \tag{3.14}$$

In its simplest form, the acoustic wave equation governs the propagation of acoustic waves in a single spatial dimension, which is the case for the examples depicted in Figure 3.2 and Figure 3.4 and is given by [22]:

$$\frac{\partial^2 p}{\partial x^2} - \frac{1}{c^2}\frac{\partial^2 p}{\partial t^2} = 0 \tag{3.15}$$

when depicting the evolution of the acoustic pressure, with p being the sound pressure, and c - the speed of sound in the medium, and by:

$$\frac{\partial^2 v}{\partial x^2} - \frac{1}{c^2}\frac{\partial^2 v}{\partial t^2} = 0 \tag{3.16}$$

when depicting the evolution of the particle velocity, where v is the particle velocity in meters per second. Equation (3.15) and Equation (3.16) are both second-order partial differential equations and they will have solutions of the same form. The solution of a second-order partial differential equation can be obtained by applying the method of separation of variables and doing this for the acoustic wave equation yields the following results [36]:

$$p(x,t) = (C_1 e^{ikx} + C_2 e^{-ikx}) e^{i\omega t} \tag{3.17}$$

The solution of interest, which describes the physical behavior of the acoustic wave, is obtained by taking the real part of the complex formulation. The constants C_1 and C_2 can be determined by applying both

initial and boundary conditions. Since the acoustic wave equation describes periodic waves, any function of the following form will be a valid solution:

$$p(x,t) = f(kx - \omega t) + g(kx + \omega t) \tag{3.18}$$

The f and g functions represent two waves traveling in opposite directions from an acoustic source, with f depicting the right traveling wave and g - the left traveling wave. The solution for the particle velocity will be of exactly the same form. This result also agrees with Equation (3.9), which describes the sound pressure of a continuous right going sound wave, where f will be a sinusoidal function with amplitude p_m.

Taking Sound Measurements

The pressure in a medium, as well as any variations in it, can be measured with pressure transducers. Those devices convert an applied pressure to an electrical signal that is linear and proportional to the pressure applied. As mechanical waves that are propagating through a medium will result in fluctuations in the applied pressure throughout said medium, they can be detected and measured by pressure transducer devices. When dealing with acoustic waves in air, the devices that capture the air pressure variations caused by the propagation of sound are known as microphones.

There are two methods in which a microphone can capture the fluctuating air pressure due to sound waves. Based on that, it can be of dynamic or condenser type [13]. Dynamic microphones are based on electromagnetism principles, where the diaphragm is attached to a coil of wire, most often made out of copper, and wrapped around a strong magnet. As the sound waves hit the diaphragm, they make it vibrate, thus also resulting in movements of the coil with respect to the magnet. This creates an electrical current in the coil because it is being moved within a magnetic field created by the magnet. The current is then being channeled from the microphone along connected wires, which is essentially the output signal of the microphone. The few moving parts and simple design of the dynamic microphones make them robust and inexpensive. They are also resistant to moisture, which is important for outdoor usage. Furthermore, they are better suited to handle high sound pressures. This type of microphone generally do not require an internal amplifier as well as batteries or external power to be provided to it [37]. Condenser microphones, on the other hand, operate similar to a capacitor. The diaphragm is placed close to a fixed metal plate, typically in front of it, thus the plate is referred to as backplate. The sound waves striking the diaphragm make it vibrate, thus moving in closer and further away to the static backplate. Due to the fact that the two are electrically charged, as the distance between them is varied, so is the current. The change of current between the diaphragm and the backplate is the output signal of the microphone, which is proportional to the change of the diaphragm's position. However, this signal is usually weak and requires amplification before it is sent by the microphone. Furthermore, condenser microphones require DC power to be supplied to them in order for constant electrical charge to exist between the diaphragm and the backplate. In some cases this is done by placing a small battery inside the microphone casing, however in most modern condenser microphones, DC electric power is supplied via the microphone cable. This is known as phantom power. Compared to dynamic microphones, condenser ones are lighter and since the diaphragm is not attached to a coil, it can vibrate more freely. This results in more precise representation of the sound waves hitting the microphone, having greater detail and nuance [13]. However, due to the presence of electrical components, moisture could be problematic for a condenser microphone. Figure 3.5 depicts the components and inner workings of both a dynamic (left) and condenser (right) microphone.

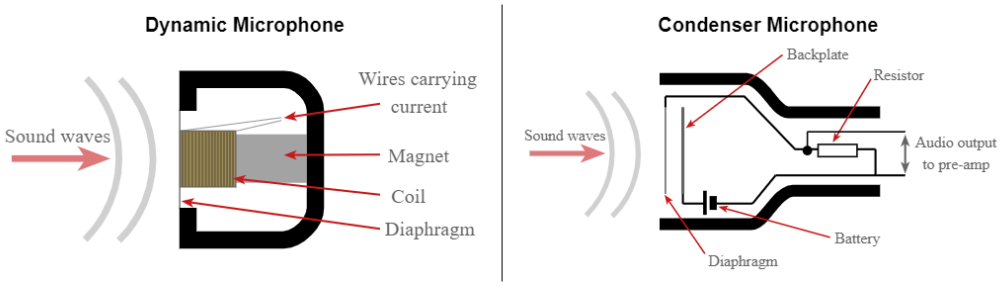

Figure 3.5: Diagrams of a dynamic microphone (left) and a condenser microphone (right) showing their components and inner working[4].

The performance of a microphone can be judged by a number of characteristics. Most of them are relevant for both dynamic and condenser microphones, and those include: frequency response, amplitude response, directionality, sensitivity, and self-noise (also known as equivalent noise) [38]. The power required as well as the temperature range will also need to be checked but only as far as to make sure that they will be satisfied under the expected conditions of operations. For condenser microphones, the sensitivity with respect to variations of humidity will be another performance parameter of interest.

The frequency response of a microphone gives the range of frequencies that can be captured with it, as well as to which frequencies it is more sensitive, relative to others [39]. Microphones are primarily designed to capture sounds, which are defined in the frequency range of 20 to 20 000 Hz, however their frequency response ranges vary from one model to another. Many microphones have a peak frequency - the upper limit of the frequency response range - of about 15 000 Hz, while others will also respond to either infrasonic or ultrasonic frequencies, or have frequency response range covering both spectra. The frequency response of a microphone can be depicted in the form of frequency response graph, as the one shown in Figure 3.6. Such a graph provides both the frequency response range, as well as the sensitivity to the different frequencies for the given microphone. Figure 3.6 is an example of a shaped frequency response, where the microphone is more sensitive to certain frequency ranges than others. The change in the response for a particular frequency range is expressed in decibels and is typically measured with respect to a reference point at 1 000 Hz. If a microphone is equally sensitive to all frequencies in its frequency response range, then the graph in Figure 3.6 will be a flat line. Such a microphone is said to have a flat frequency response.

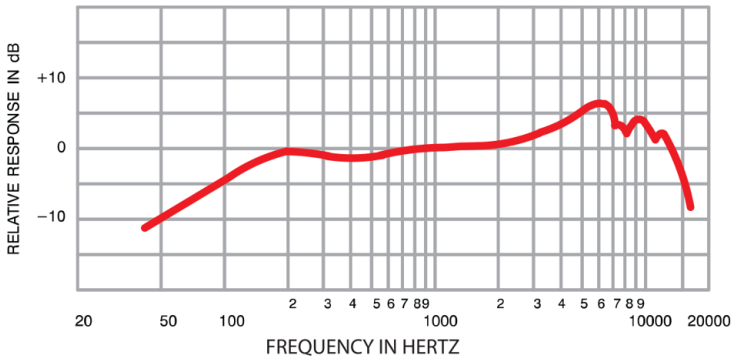

Figure 3.6: An example of a frequency response graph for a microphone[5].

The amplitude response of a microphone gives the range of sound pressure levels that can be captured, with the maximum SPL being of particular interest. It is a measure of the SPL above which the microphone output signal starts to distort, and is often expressed for a given single-frequency sound (known as a tone) [39]. The distortions are mainly caused by overloading of the microphone's circuitry, and since all condenser microphones have internal amplifiers, which can be overloaded more easily, the maximum SPL is typically more important for microphones of the condenser type. When distortions are present, the microphone's output will no longer be representative of the input sounds, thus severely degrading the quality of the recordings [13]. Figure 3.7 provides a reference for the different levels of sound pressure together with real world examples.

The directionality, also known as polar response or pattern, gives the directional sensitivity of a microphone. The fundamental polar patterns are omnidirectional, bidirectional, and unidirectional. More complex polar responses can be created by combinations of the fundamental patterns. An omnidirectional microphone will pick up sounds from all directions with equal sensitivity. In this type of microphone, the diaphragm is open to the exterior air pressure only on one side. A bidirectional polar response means that

[4] https://blog.accusonus.com/science-of-sound/how-microphones-work/

[5] https://www.shure.com/en-US/performance-production/louder/mic-basics-frequency-response

Sound sources (noise) Examples with distance	Sound pressure Level L_p dB SPL
Jet aircraft, 50 m away	140
Threshold of pain	130
Threshold of discomfort	120
Chainsaw, 1 m distance	110
Disco, 1 m from speaker	100
Diesel truck, 10 m away	90
Kerbside of busy road, 5 m	80
Vacuum cleaner, distance 1 m	70
Conversational speech, 1 m	60
Average home	50
Quiet library	40
Quiet bedroom at night	30
Background in TV studio	20
Rustling leaves in the distance	10
Hearing threshold	0

Figure 3.7: Chart of sound SPL with real world examples[6].

the microphone will be equally sensitive to sounds coming from directions that are 180 degrees apart, thus forming a figure-of-eight pattern. For example, a bidirectional microphone sensitive to sounds coming from the front and the rear, will have rings of silence which will reject any sounds coming from the side. In this case, the diaphragm is open and equally exposed to the external air pressure variations on both sides to which it is sensitive. Finally, the unidirectional microphones are mostly sensitive in one directional, typically the front. Their polar patterns can be described as cardioid-type. For those microphones, the diaphragm is still open on both sides, however it is not equally exposed to the exterior air pressure fluctuations caused by the sound waves along those directions [39]. It should be noted that the polar pattern are two-dimensional graphs, while microphones operate in three-dimensions. As such, the polar responses will be spherical, with rings and cones of silence, when depicted in three-dimensional space. Figure 3.8 to Figure 3.10 depict the fundamental polar pattern plots, as well as their visualization in three-dimensional space. Each circular division on the polar response graph is a measure of sensitivity in decibels, with the zero decibel circle referring to the highest level of sound expected from the microphone, and decreasing towards the center of the polar graph.

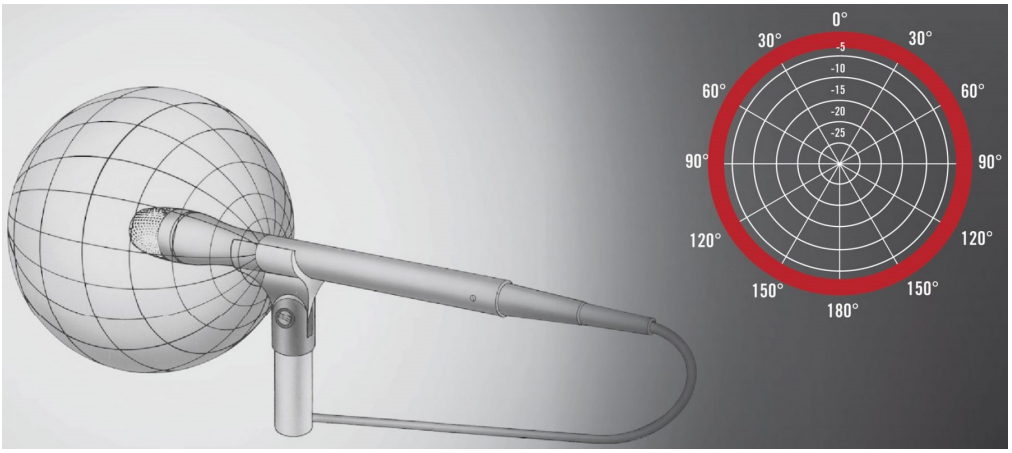

Figure 3.8: Omnidirectional polar pattern plot and its 3D visualization for a microphone[7].

[6] https://www.kentmargraves.com/blog2/2019/11/6/how-loud-is-your-worship

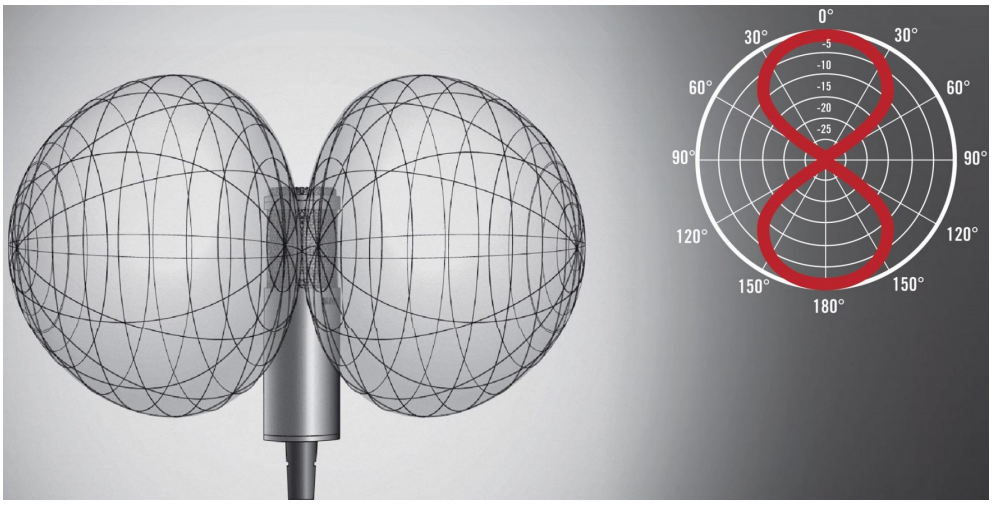

Figure 3.9: Figure-of-eight polar pattern plot and its 3D visualization for a bidirectional microphone[8].

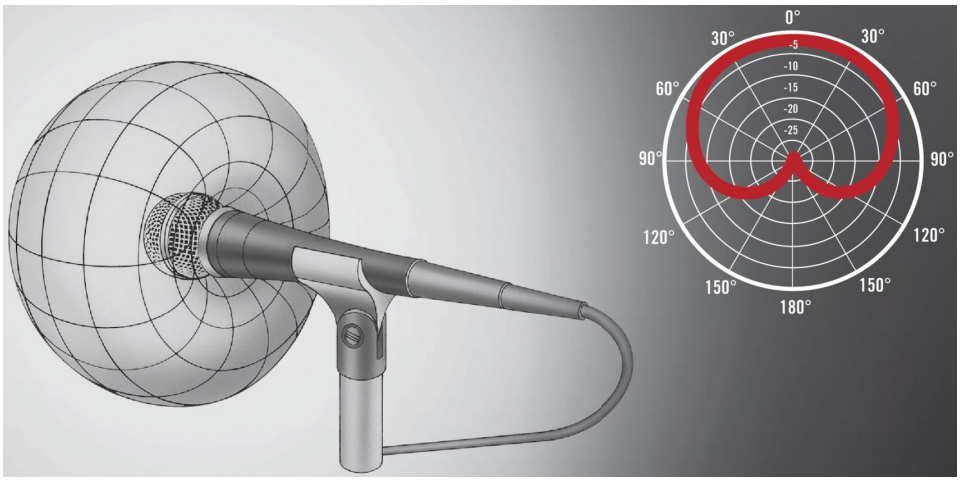

Figure 3.10: Cardioid polar pattern plot and its 3D visualization for a unidirectional microphone[9].

The sensitivity of a microphone is a measure of its output signal for a given specific acoustic input. In other words, it tells how effective the microphone acts as a transducer of sound energy to electrical energy [13]. Depending on its sensitivity rating, the gain required by the microphone can be determined, with less sensitive ones needing more gain and vice versa. To obtain the sensitivity of a microphone, a reference sound is used, typically a 1 kHz tone of 94 dB SPL, which is equivalent to an amplitude of 1 Pascal of the pressure fluctuations caused by the sound wave. Then, the microphone signal output is measured and compared to a theoretical case where it outputs 1 volt for the 94 dB SPL sound. The difference between the actual output and the theoretical case is the microphone sensitivity. It is typically expressed in decibels relative to 1 volt (dBV). The theoretical output of 1 volt is taken as the reference signal and serves as the zero dBV value. Real microphones have negative values of sensitivity in dBV, becasue their output is less than 1 volt for the reference 1 kHz 94 dB SPL tone [39]. Another way to report the sensitivity is to just state the microphone output, in milivolts (mV), for the reference sound.

[7] http://blogs.eciad.ca/sound/workshops/microphones/

[8] http://blogs.eciad.ca/sound/workshops/microphones/

[9] http://blogs.eciad.ca/sound/workshops/microphones/

The self-noise of a microphone is the level of noise produced by its active circuitry. As such, this characteristic is more relevant for condenser microphones. Due to the self-noise, a microphone will still output a signal, even if there are no external sounds affecting it. A lower equivalent noise will result in better signal-to-noise ratio, improving the quality of the recordings and being able to capture quieter sounds. The self-noise can be determined by placing the microphone in a soundproof space and recording its output signal, which is typically converted to decibels, thus it can be represented in terms of SPL. Therefore, a sound wave that has lower SPL than the self-noise for that particular wave frequency, will not be registered by the microphone. Furthermore, the stronger the sound wave, meaning the greater the amplitude of the pressure fluctuations caused by it, the better the signal-to-noise ratio will be [39].

The microphones that will be utilized for the current research will need to be as small as possible. This is to minimize any impact they could have upon the air flow and to make sure that the aerodynamic profile of the vehicle will remain unchanged. They also need to be light such that the center of mass is unaffected. Furthermore, they need to have low power requirements so they can be used throughout the whole flight without affecting the performance of the aerial vehicle. It should be noted that, as the size of the microphone decreases, so does the diaphragm, which has important consequences [13]. To start off, the smaller diaphragms are lighter, meaning that their low-frequency response will be improved, while their high-frequency one will worsen. However, a larger diaphragm will have a larger surface area, allowing it to capture more of the acoustic energy, which in turn will result in stronger output signal with lower signal-to-noise ratio. Finally, larger diaphragms are slightly quieter, having lower self-noise levels.

Most of the miniature microphones are of the condenser type, with the electret and the Micro-Electro-Mechanical System (MEMS) kind being the most popular ones. Both of them function by forming a condenser capsule, but it is charged in a different manner. While regular condenser microphones require an external charge to polarize the diaphragm and the backplate, electret and MEMS microphones utilize electret materials to maintain a permanent charge across the plates [40]. However, they are still active microphones and need power for their impedance converters or printed circuit boards (e.g. filters, amplifiers, ADC, etc.), even though their power requirements are lower compared to regular condenser microphones. MEMS microphones differ from the other electret microphones by their manufacturing process. They are etched into a semi-conductive silicon wafer via MEMS processing, which allows them to be smaller in size [41]. Furthermore, MEMS microphones are more resistant to mechanical vibrations and have lower impedance. However, electret condenser microphones offer better protection from dust and moisture, which is crucial in outdoor operations.

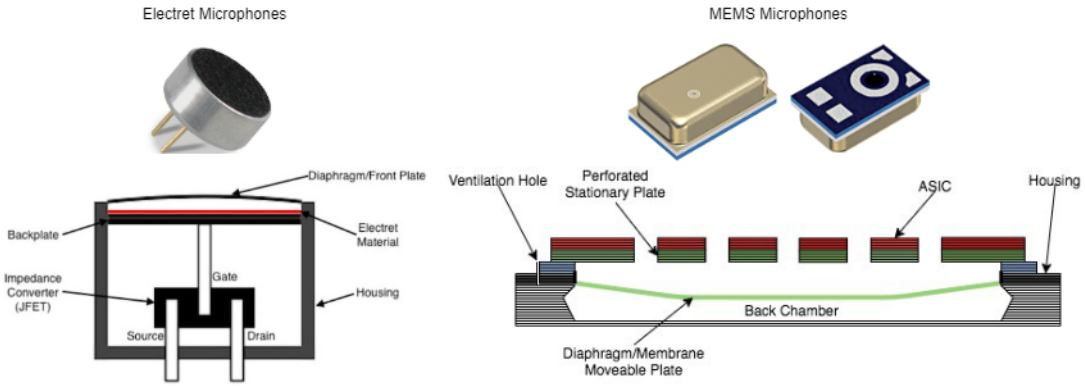

Figure 3.11: An electret condenser microphone (left) and MEMS microphone (right) with their cross-sectional diagrams. The application-specific integrated circuit (ASIC) in the MEMS microphone uses a charge pump to place a fixed charge between the stationary plate and the diaphragm.

Lastly, any sound measuring equipment has some type of frequency weighting implemented. Those are electronic filters that alter the sound levels over a range of frequencies in order to better adjust the sound measurements for their intended purpose [42]. The most widely used frequency weightings are the A, C, and Z ones. The A-weighting aims to account for the relative loudness of sounds of different frequencies as perceived by the human ear, which is most sensitive to the frequencies between 500 Hz and 6 000 Hz. As such, this frequency weighting scale attenuates sounds outside the above-mentioned range. The measurements taken using A-weighting are typically depicted in relative units of dBA. The

C-weighting is used for determining the peak sound pressure level. As such, it has flat response between the two half-power points of 31.5 Hz and 8 000 Hz. Furthermore, compared to the A-weighting, it focuses more on the effects of low frequency sounds. Measurements made with C-weighting are generally shown in dBC. Finally, the Z-weighting gives flat frequency response over the complete sound frequency range. It starts from 8 Hz and reaches all the way to 20 000 Hz. Thus, the sound measurements are not weighted at all and their true recorded levels are supplied. Measurements taken with Z-weighting are mostly depicted in relative units of dBZ, however sometimes dB is used. The three different types of frequency weighting curves are shown in Figure 3.12.

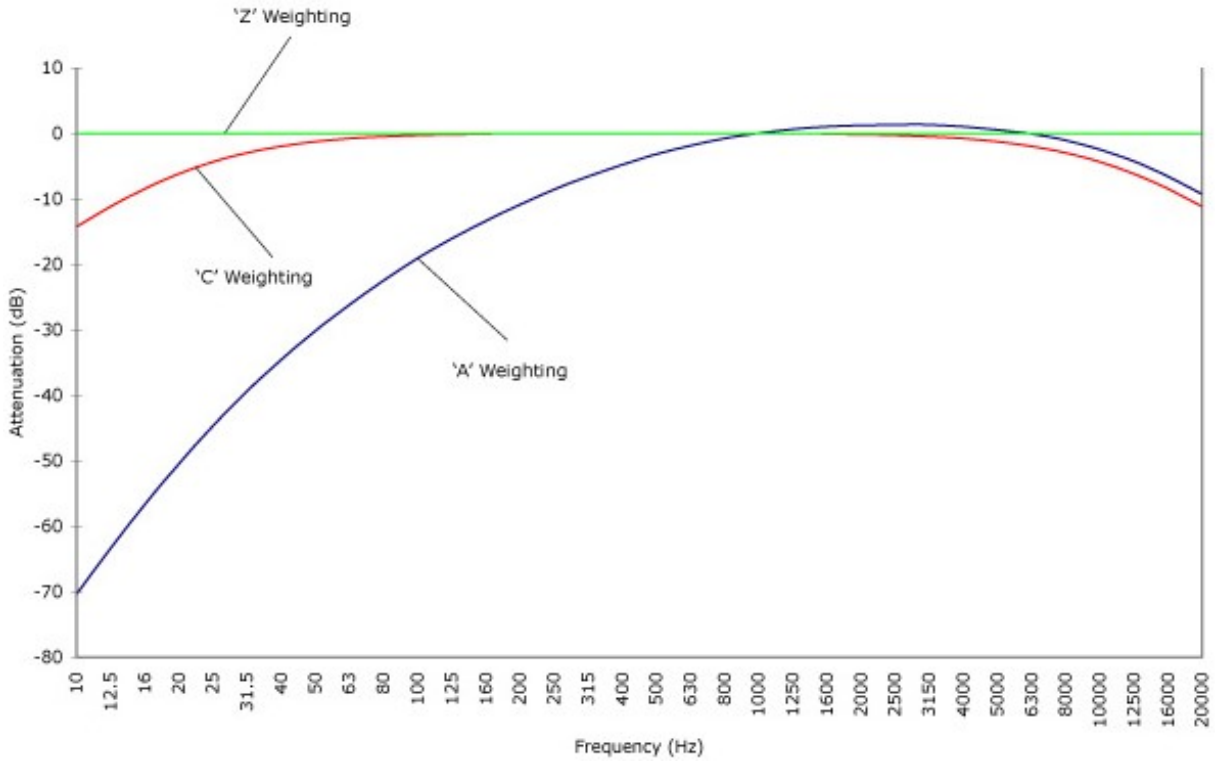

Figure 3.12: The sound attenuation for the A, C, and Z frequency weighting, expressed in dB[10].

3.2.2. Boundary Layers

This section of the literature review focuses on the phenomenon of boundary layers. They form over any body immersed in a flow of fluid, meaning that there was a boundary layer formed over the on-board equipment mentioned in Section 1.1, that has been used to make the sound recordings. As such, it will be beneficial to carry out a discussion on the nature of the boundary layers and any effects they might have upon sound generation.

The Nature of Boundary Layers

The boundary layer is a thin viscous region of flow that is immediately adjacent to the surface of a body immersed in a fluid flow. As the boundary layer forms over a surface, its height increases with the distance away from the leading edge. The phenomena inside the boundary boundary layer give rise to the skin friction and aerodynamic heating of the surface and are the reason for flow separation from the surface to occur. The flow inside the boundary layer has properties that are different than those of the free stream. Firstly, it is slowed down under the influence of friction between the fluid and the body's surface. Secondly, the temperature in the boundary layer varies across its height and is different than that of the free stream flow. When dealing with boundary layers, the assumption is made that the flow is viscous, where the effects of viscosity, thermal conduction, and mass diffusion need to be taken into account. In boundary layer

[10] https://www.nti-audio.com/en/support/know-how/frequency-weightings-for-sound-level-measurements

analysis it is typically assumed that the flow properties at the outer edge of the boundary layer (marked by the dashed line in Figure 3.13) are the same as the properties of surface flow from an inviscid flow analysis.

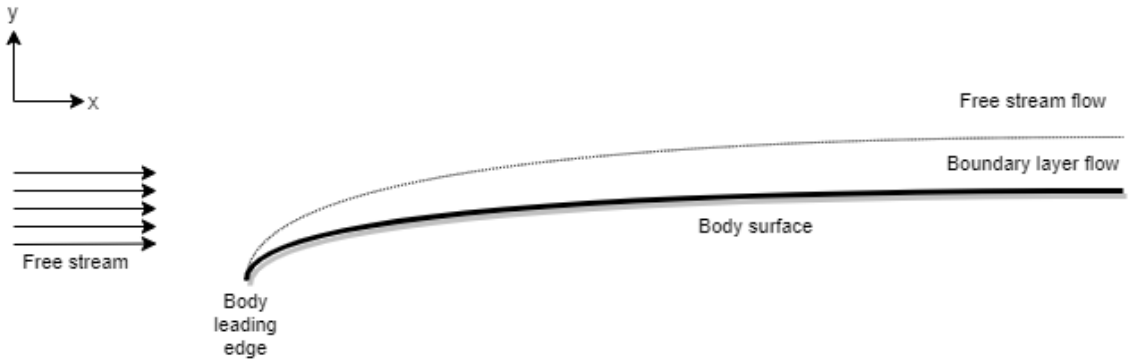

Figure 3.13: Depiction of the boundary layer formed over the surface of a body immersed in a flow. Size of the boundary layer is exaggerated for clarity.

The viscosity of a fluid is a measure of its resistance to deformation, and can be compared to the concept of thickness. It relates to the internal friction forces between adjacent layers of the fluid that arise when said layers are in motion relative to one another. As a side note, if a fluid is treated as having no friction forces in it as it flows, then it is known as an ideal fluid, or inviscid fluid. Due to the presence of friction forces in viscous fluid flows, the different layers of the fluid move at different velocities [43].

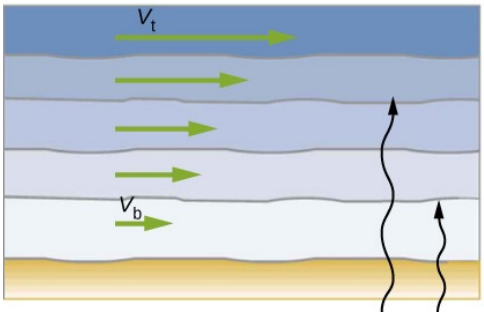

Figure 3.14: Depiction of different layers of a fluid in flow. Each layer has its own velocity, with the top layer having the highest velocity V_t, and the bottom layer - having the lowest V_b. Friction forces exists between the different layers[11].

Same phenomena occur in the boundary layers, and as result the velocity of the flow within the boundary layer varies with height above the the surface. Next to that, in viscous flows there are friction forces acting between the fluid that is immediately adjacent to the surface and the surface itself. As a result, the surface experiences a force in the direction of the flow, tangent to the surface, which gives rise to shear stresses. According to Newton's third law, the flow will experience an equal force in the opposite direction, and as a result it will be slowed down. In fact, immediately on the surface, the flow velocity is zero due to the presence of the friction forces. This is known as the no-slip condition and it dominates viscous flows [1]. As the height over the surface increases, the velocity becomes finite, but still slower than the free stream velocity. The flow velocity along the height of the boundary layer is given by the velocity profile, an example of which is shown in Figure 3.15. On a velocity profile graph - such as $u(y)$ on Figure 3.15 - the vertical axis depicts the perpendicular distance above the surface y, while the horizontal axis represents the magnitude of the flow velocity u. Due to the no-slip condition of viscous flow, the velocity profile at $y = 0$ has value of zero: $u(0) = 0$.

[11] https://cnx.org/contents/2IQXarkd@5/Viscosity-and-Turbulence

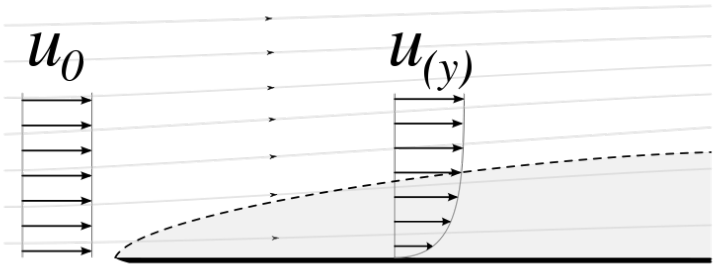

Figure 3.15: Velocity profile inside a boundary layer and in free stream over a flat plate. The boundary layer is indicated by the darker region over the plate. Free stream velocity is subsonic[12].

Another characteristic of viscous flows is their thermal conduction. A fluid flow has a given amount of kinetic energy, which is related to the flow velocity. Therefore, as the flow velocity decreases under the influence of friction forces, so does the kinetic energy, which in turn is transformed into heat (internal energy) of the fluid, causing the temperature of the flow to increase. This phenomenon is known as viscous dissipation within the fluid [1]. Due to the fact that the velocity differs along the height of the boundary layer, the amount of kinetic energy turned into heat will also differ, meaning that the temperature of the flow in the boundary layer will not be constant along a distance perpendicular to the surface. The temperature at any height above the surface in the boundary layer is given by the temperature profile, an example of which is shown in Figure 3.16. Just as with the velocity profile, the vertical axis of the temperature profile depicts vertical distance above the surface y, while the horizontal axis represents the magnitude of the temperature T. The shape of the temperature profile is opposite to that of the velocity profile, because greater decrease of velocity relates to greater amount of kinetic energy being turned into internal heat energy. However, the temperature at the wall - T_w on Figure 3.16 - could be lower than the maximum temperature in the boundary layer due to heat transfer from the fluid to the surface of the body. In the example above, the fluid is warmer than the surface, resulting in heat being transferred from the fluid flow to the surface. This in turn decreases the temperature of the fluid near the surface, compared to the temperature above in the boundary layer. The result is the surface heating up, a phenomenon referred to as aerodynamic heating [1]. In general, the higher the flow velocity, the greater the amount of kinetic energy being dissipated, resulting in greater heating of the surface.

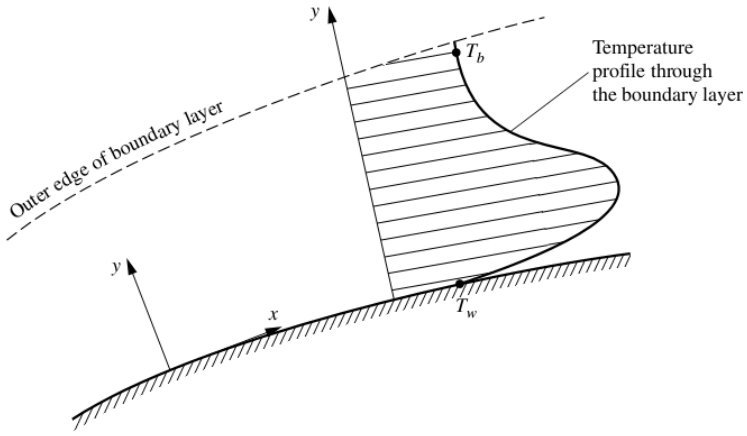

Figure 3.16: Temperature profile of a boundary layer over surface of a body. Flow velocity is subsonic[13].

[12] https://commons.wikimedia.org/wiki/File:Laminar_boundary_layer_scheme.svg

[13] https://i.stack.imgur.com/rNCHU.png

The final boundary layer characteristic of interest is the flow pressure. This is the other major contributor to the force acting on the surface, next to friction. When studying the pressure throughout a flow of fluid, it is beneficial to represent the flow in terms of streamlines. Those are lines that are tangent to the velocity vector of a fluid element as it travels through the flow. Streamlines are depicted in Figure 3.17.

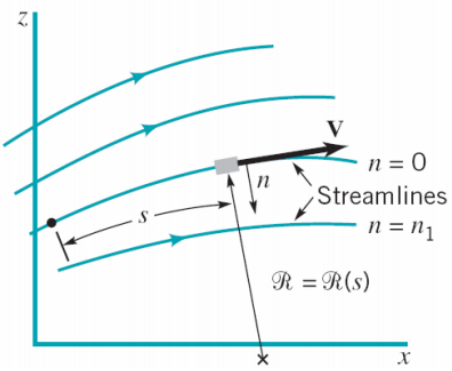

Figure 3.17: Depiction of flow using streamlines. The fluid element is represented by the gray rectangle[14].

As a fluid flows, pressure is exerted in both the direction along the streamlines s, as well as normal to them n. For an inviscid, incompressible flow, the Bernoulli equations hold [44]:

$$p + \frac{1}{2}\rho V^2 + \rho g z = const \tag{3.19}$$

along a streamline, where p is the hydrodynamic pressure, ρ the density of the fluid, V the speed of the flow, g the gravitational acceleration, and z the height above a predefined datum, and:

$$p + \rho \int \frac{V^2}{R} dn + \rho g z = const \tag{3.20}$$

across streamlines, or in a direction, perpendicular to the streamline, with R being the radius of curvature at the current location on the streamline. The $\rho g z$ term in the Bernoulli equations refers to the hydrostatic pressure exerted due to the weight of the fluid in the flow above the surface, while the $\frac{1}{2}\rho V^2$ and $\rho \int \frac{V^2}{R} dn$ terms represent the dynamic pressure exerted due to the velocity of the flow ($\frac{1}{2}\rho V^2$ referring to the component of velocity in the direction of the streamline and $\rho \int \frac{V^2}{R} dn$ - to the component of velocity normal to the streamline). The dynamic pressure can also be seen as the kinetic energy (per unit volume) of the fluid flow. In case the streamlines are exactly parallel, the radius of curvature would approach infinity, meaning that the pressure exerted across streamlines will only be due to the hydrostatic component. The Bernoulli equations stem from the conservation of energy inside the fluid flow, and are useful to obtain a basic physical understanding of the different components of flow pressure, however they cannot be applied inside the boundary layer, due to their assumption of inviscid flow.

The boundary-layer flow is not only viscous, but at given distance away from the leading edge, it typically becomes turbulent as well. Figure 3.18 depicts the boundary layer formed over a flat plate immersed in a fluid flow. The characteristics and behavior of the boundary layer are greatly impacted by the nature of the flow, namely whether it is laminar or turbulent. Focusing on a single fluid element, in a laminar boundary layer (LBL) it will flow smoothly, while in a turbulent boundary layer (TBL) - it will be agitated. This is due to the fact that the turbulent boundary layer contains vortices and eddies, or turbulent structures, that mix across the different layers in the TBL flow. On the other hand, in a laminar boundary layer the flow is structured and smooth, much like the one shown in Figure 3.14. Each layer is in contact with only adjacent to it layers and no mixing is occurring. As such, the exchange of mass and momentum inside the LBL flow takes place only between neighboring layers [45]. Just before the flow meets the leading edge of the body, its velocity and temperature profiles are uniform, at their free stream values, and the flow can

[14] http://homes.nano.aau.dk/lg/Lab-on-Chip2008_files/Lab-on-chip2008_2.pdf

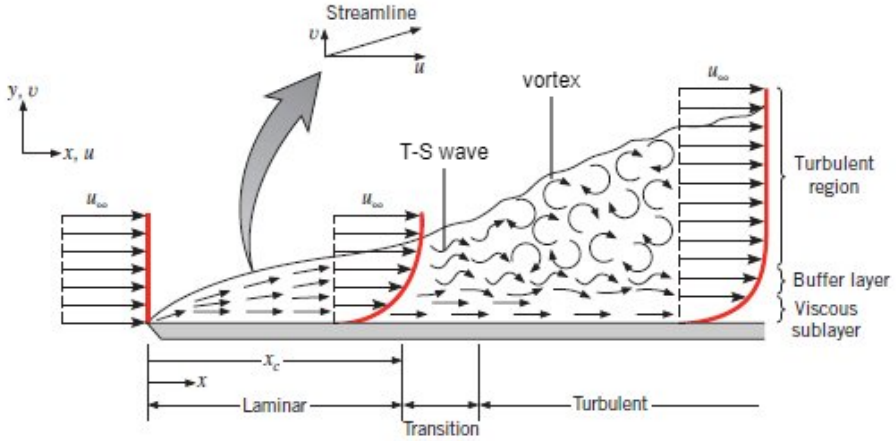

Figure 3.18: Boundary layer over a flat plate. The velocity profiles of the mean flow free stream, laminar boundary layer, and turbulent boundary layer are also shown [49]. The dimensions of the boundary layer are exaggerated for clarity.

be considered inviscid. Past the leading edge, the influence of friction will start to slow down the flow, forming a viscous laminar boundary layer. Traveling downstream along the surface, instabilities will start to develop in the laminar flow. They grow rapidly and cause the flow to become turbulent. The region in which the instabilities start to form and grow is known as the transition layer. In the laminar boundary layer, the instabilities are infinitesimal and take the form of Tollmien–Schlichting (T-S) waves [46]. T-S waves are two-dimensional wave-like disturbances, propagating in the direction of mean flow when incompressibility is assumed. Therefore, a fluid element traveling along the T-S wave will not follow a straight path but instead one that is curved and changing in direction. This will lead to varying components of dynamic pressure exerted in different directions inside the boundary layer. As T-S waves travel downstream in the transition layer, they are amplified to a point where they grow into turbulent flow structures, thus forming the turbulent boundary layer. The TBL is dominated by vortices and eddies. Due to their vorticity, a fluid element will follow a rotational path. As a result of the rotational flow, fluctuations in the dynamic pressure will be transmitted throughout the turbulent boundary layer [8]. The pressure fluctuations created by the different turbulent structures will vary in both space and time. Therefore, for a fixed location inside the turbulent boundary layer, these fluctuations can be represented as waves of alternating pressure in time, similar to the depiction in Figure 3.3. This means that the pressure fluctuations emerging from the turbulent structures can be thought of as mechanical waves. This is a key factor because sound is just mechanical waves in a given frequency range. Hence, when the frequency of the pressure fluctuations caused by the vortices and eddies in the TBL falls within the range of 20 - 20 000 Hz, they can be perceived as sound, and captured by microphones. These pressure fluctuations are referred to as hydrodynamic - typically related to the turbulence carried by the flow - and give rise to pseudo-sound [11]. Although this pseudo-sound can be picked up by microphones, it has different behavior and characteristics than the sound from acoustic sources. This is because the latter arises as a solution of the wave equation, but the former - of the convection equation. While the magnitude of the pressure fluctuations are very small compared to the overall boundary layer flow pressure, they are still significant enough to be picked up by contemporary microphones as demonstrated in many experiments [11, 47, 48]. The typical range of SPL measured for the pseudo-sound at the surface beneath a TBL is 80-90 dB [11], however it can vary outside this range depending on the surface geometry, the flow conditions, and the surrounding environment.

The transition from laminar to turbulent boundary layer can be influenced by various characteristics of the environment and the body. The most obvious one is the turbulence of the free stream. The more turbulent the free stream, the earlier instabilities will develop in the laminar flow past the leading edge of the body, thus encouraging transition to turbulent boundary layer. The surface roughness also plays an important role, as having a rough surface encourages transition to turbulent flow. In case a turbulent boundary layer is desired, a rough grit can be installed on the surface near the leading edge in order to trip the laminar flow into a turbulent one. This technique is often used in wind tunnel testing. Another way to affect the transition from laminar to turbulent boundary layer is by adjusting the pressure gradients

of the flow. Having an adverse pressure gradient will strongly favor an early transition to turbulent flow, while favorable pressure gradients will preserve the laminar flow. It should be noted that adverse pressure gradients may also result in flow separation, meaning that the boundary layer will no longer follow the shape of the surface. The instabilities in the laminar flow are also affected by the heat transfer between the surface and the boundary layer. If the temperature of the surface is higher than that of the adjacent fluid, heat will be transferred from the surface to the fluid and the flow instabilities will be amplified, thus encouraging transition to turbulent flow. On the other hand, colder surfaces tend to preserve the flow laminar for longer [1].

In order to be able to predict the flow patterns in the boundary layer, the fluid's ratio of inertial forces to viscous forces is often used. This ratio is known as the Reynolds number and is valid for fluids subjected to relative internal movements caused by varying fluid velocities, like the one shown in Figure 3.14 and also experienced by boundary layer flows. The Reynolds number is defined as [1]:

$$\mathrm{Re}_x = \frac{\rho_\infty V_\infty x}{\mu_\infty} \tag{3.21}$$

with ρ_∞ being the density of the free stream of the fluid, V_∞ - the fluid's free stream velocity, x - the location along the surface, and μ_∞ - the dynamic viscosity of the fluid in free stream. In general, flows at lower Reynolds number tend to be laminar with the viscous forces being dominant, while higher Reynolds number flows are more likely to be turbulent and to be dominated by inertial forces [50]. This is due to the fact that the relative internal movement of the fluid generates friction, which plays a role in the development of the turbulent flow, while the viscosity of the fluid restricts turbulence. As such, the Reynolds number can be used to predict the transition from laminar to turbulent boundary layer, typically expressed by the critical Reynolds number. Its value for a given object under specific circumstances is difficult to predict, however for a body in airflow at sea level, the critical Reynolds number is often taken as 500 000 [1]. Therefore, if the flow at given location on the body, x distance from the leading edge, has a Reynolds number considerably below 500 000, the flow can be assumed laminar at that location. On the other hand, if the Reynolds number is far higher than 500 000, the flow is most likely turbulent.

Depending on how the flow pressure in the direction of travel changes along the x-direction, there could either be an adverse pressure gradient, or a favorable pressure gradient. An adverse pressure gradient means that the pressure increases as the flow travels downstream. In this case, a fluid element of the flow will be further slowed down as it travels along the surface, having to overcome both the friction as well as the increase in pressure. As such, it is possible that, at a certain point along the surface, the fluid element will come to a stop and then starts moving in a reverse direction.

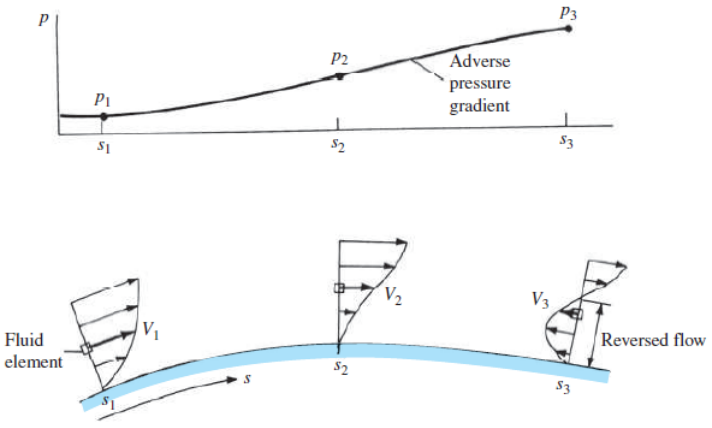

Figure 3.19: The effect of adverse pressure gradient on the velocity profile of the boundary layer. At point s_2 the velocity gradient at the surface is zero. This is the point of flow separation. At point s_3, the flow is reversed and a vortex is formed. This becomes part of the wake [1].

This is known as a reverse flow and is the cause of flow separating from the surface. As a result, a large wake of recirculating flow is typically created downstream, as depicted in Figure 3.20. Over the regions where the flow is separated, the pressure distribution over the surface is significantly changed [1]. It is

also possible for separation bubbles to form, where - due to a reverse flow vortex - the boundary layer separates from the body, not following its shape anymore, but reattaches to the surface after the region of reversed flow.

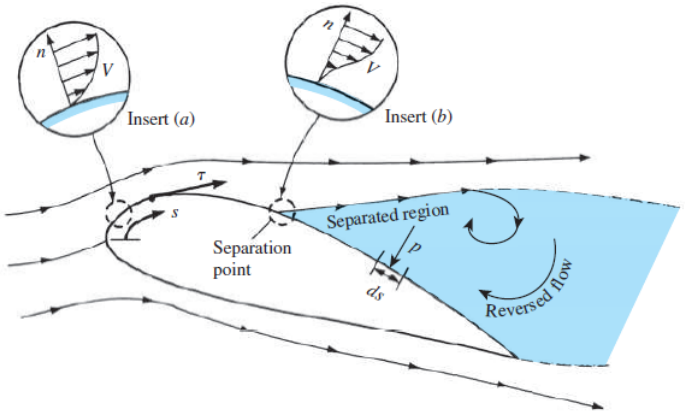

Figure 3.20: Separated flow over an airfoil. The reversed flow constitutes the wake. The flow no longer follows the shape of the body, rather the shape defined by the separated region. The two inserts depict the velocity profiles at the selected points, while τ is the shear stress on the surface [1].

On the other hand, favorable pressure gradient means that the pressure decreases as the flow travels downstream. Due to the lowering of the pressure, a fluid element will experience less resistance as it moves, allowing it to keep flowing downstream a greater distance, thus staying attached to the surface for longer. As a result, the point of flow separation is pushed further downstream, which also reduces the size of the wake.

A turbulent boundary layer typically remains attached to the surface for far greater distance downstream of the flow, compared to laminar boundary layer in the same conditions. This is due the fact that the higher energy fluid elements from the outer regions of the flow are pushed towards the body as they are agitated in the TBL. As a result, the kinetic energy of the elements near the surface is greater, meaning that more energy will be required to separate the flow. This is also the reason behind the larger velocity gradient at the surface under TBL. Since the laminar boundary layer is less stable and can separate easier, separation bubbles are more likely to form in it.

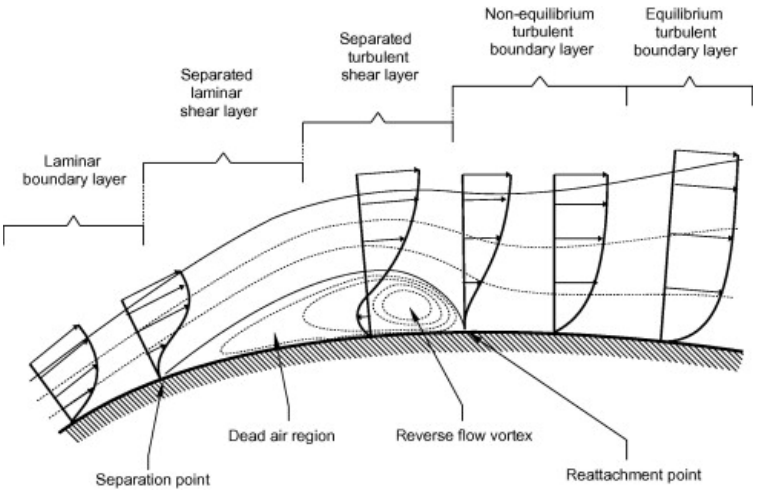

Figure 3.21: Separation bubble over a surface [51].

As the boundary layer separates from the surface, it is being referred to as a shear layer, but the nature of the flow in it experiences little change. As such, it could be either laminar or turbulent. What the separated region, or the wake, essentially does is to change the effective shape of the body that the boundary layer

follows, as it can be seen in Figure 3.21 and Figure 3.22. The wake itself is a region of disturbed flow, which is most often turbulent, due to the formed vortices of reversed flow. However, the properties of the vortices and eddies formed in the wake are quite different than of those in the attached TBL. As a result, the pressure fluctuations caused by the turbulent structures in the separated region will be of dissimilar character to those in the TBL, having distinct frequencies and amplitudes. This means that the power spectrum in the range of sound frequencies will likely differ between the separated flow and the attached TBL.

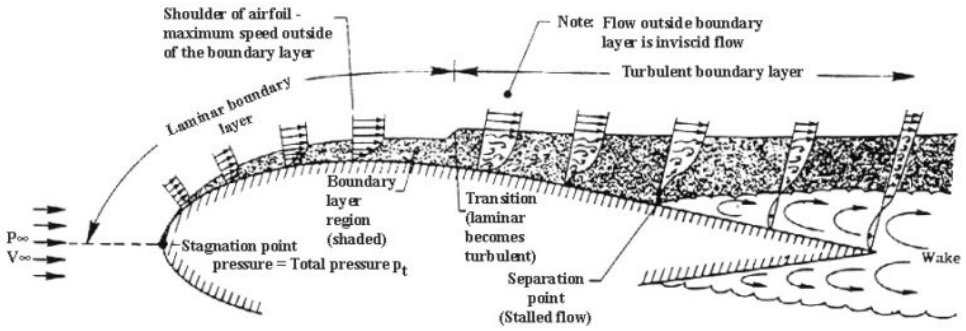

Figure 3.22: Typical boundary layer over an airfoil with layer separation over the top surface. The velocity profiles are depicted for increasing distance from the leading edge[15].

A major factor in flow separation is the angle of attack of the object. For many standard airfoils, flow separation begins near the trailing edge and starts moving forward - increasing the wake - as the angle of attack increases. This is depicted on Figure 3.23.

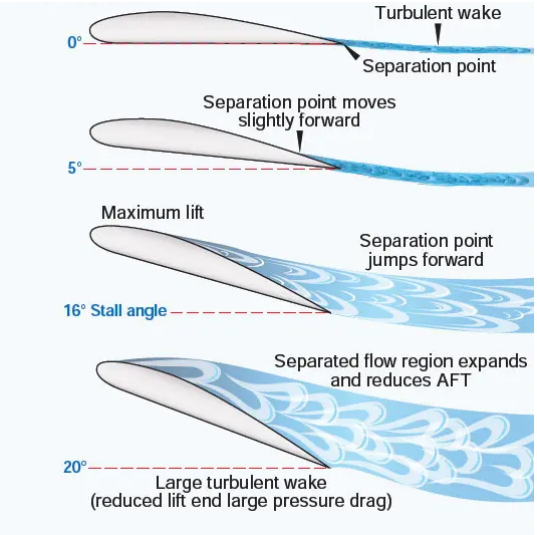

Figure 3.23: Effect of increasing angle of attack on boundary layer flow separation. The exact angles of attack shown are valid for that particular airfoil and will vary for different body shapes[16].

From the discussion carried out in this section, it can be concluded that the hydrodynamic pressure fluctuations causing pseudo-sound inside the turbulent boundary layers are greater than any occurring in laminar boundary layers, due to the presence of vortices and eddies. Furthermore, the laminar flow requires less energy to separate and it is more likely for separation bubbles to form in it, while the turbulent

[15] https://aerospaceengineeringblog.com/boundary-layer-separation-and-pressure-drag/

[16] https://www.flightliteracy.com/sources-of-flight-training-part-two/

flow stays attached for longer. As such, it is more beneficial to focus on the pressure fluctuations in the TBL, and their variation with the airspeed, to be used as the working basis for the airspeed instrument. The greater magnitude of the pressure fluctuations in the TBL, compared to the LBL, should result in a better signal-to-noise ratio. In turn, this will make it easier to identify the signal of the pseudo-sound brought about the hydrodynamic pressure fluctuations inside the turbulent flow and isolate it from all other sources of sound waves, which will be treated as noise in the context of the current research. Therefore, a more detailed discussion on turbulent boundary layers will be carried out hereafter, focusing on the turbulent structures and the resulting hydrodynamic pressure fluctuations and pseudo-sound due to their presence, as well as how they change with the velocity of the free stream. Furthermore, separated flow - or the wake - will also be briefly discussed and compared to the TBL.

The Turbulent Boundary Layer

In general, turbulence arise due to excessive kinetic energy of the flow that overcome the damping effects of the fluid's viscosity. As a result, the turbulent flow is characterized by unsteady vortices of various shapes and sizes which interact with each other. Studies performed on incompressible turbulent flows bounded to a surface revealed the presence of several types of flow structures [52]. In general, the flow structures recognized as part of the turbulent boundary layer can be divided into two categories: basic and composite structures. The composite structures can be made out of different types of basic structures or by merger of multiple basic structures of the same type. Table 3.1 provides a summary of the flow structures that are currently being suggested as part of the turbulent flow and governing its characteristics [53]. The presence of the flow structures introduces fluctuating velocity components for the fluid elements in the flow, which in turn results in the pressure fluctuations observed inside the turbulent boundary layer.

	Flow Structure	**Type of Structure**
1.	Hairpin (Horseshoe) Vortex	Basic Structure
2.	Typical Eddy	Basic Structure
3.	Pocket Structure	Basic Structure
4.	Streamwise Vortex	Basic Structure
5.	Hairpin Packet	Composite Structure
6.	Low-speed Streak	Composite Structure
7.	Very Large-Scale Coherent Motion (VLSM)	Composite Structure

Table 3.1: Summary of suggested flow structures inside the turbulent boundary layer [53].

The hairpin vortices are among the most important elementary sustained flow pattern in the turbulent boundary layer. A typical hairpin vortex consists of three parts: leg, neck, and head. The leg is usually attached to the surface, while the neck and the head are protruded away from the surface under the effect of disturbances. Due to the fact that the flow velocity increases with the height above the surface, the protruded part of the hairpin vortex is stretched. As the Reynolds number increases the hairpin vortices become more elongated, while at lower Reynolds numbers they tend to behave as vortex loops. Figure 3.24 depicts the geometry of the hairpin vortices for different Reynolds numbers. Hairpin vortices give rise to conditions which are favorable to the production of other such vortices [54]. Therefore, they can reproduce and form hairpin packets. A model based on hairpin vortex packets is proposed that aims to unify the disparate facts about the structure of the turbulent boundary layer [55]. In it, vortex packets of various sizes coexist within the TBL, usually layered on top of each other. The hairpin vortices retain their relative position and shape within the vortex packet as it moves downstream at its convection velocity. A depiction of the hairpin vortex packet model is given in Figure 3.25.

Typical eddies are micro-scale coherent motions typically observed across the TBL's outer region. When near the surface region, they impact the formation of pockets and hairpin vortices. Typical eddies have a ringlike configuration and are not attached to the surface like the majority of the hairpin vortices. They appear as laminar vortex rings at lower Reynolds numbers, and as wavy cored vortex rings at higher Reynolds numbers [57]. The shape of the eddies is governed by the characteristics of the perturbed vortical environment. Currently, it is thought that at least two mechanism are involved in the formation of the typical eddies. First one is by pinch-off and reconnection of hairpins that are lifted up from the surface,

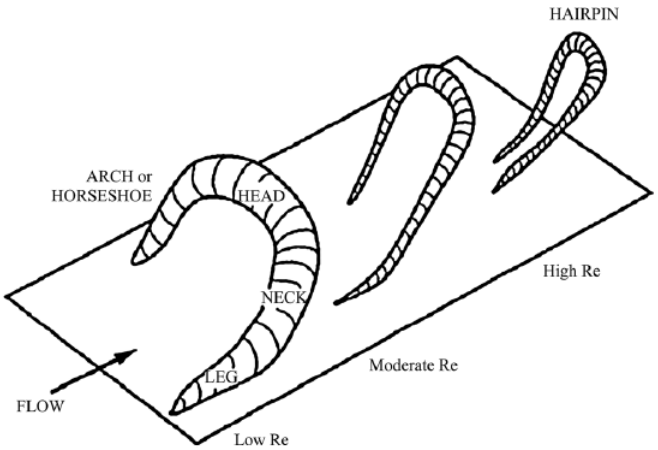

Figure 3.24: Depiction of the geometry of the hairpin (horseshoe) vortices for increasing Reynolds numbers [56].

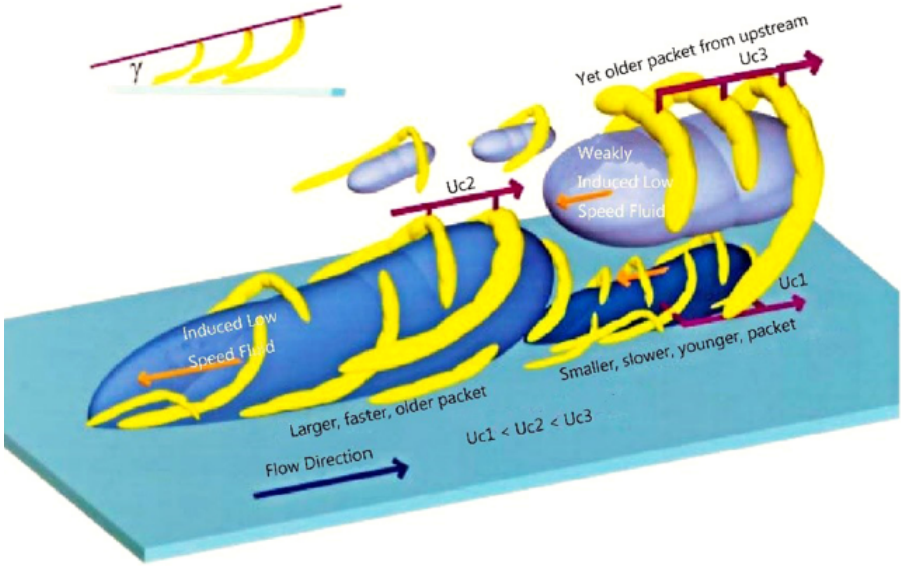

Figure 3.25: Depiction of the coherent hairpin vortex packet model for a turbulent boundary layer [55].

and the second is due to instability of local highly vortical fluid region nuder the effects of an impulsive force [53]. The typical eddies have a great impact upon the velocity fluctuations of the fluid inside the TBL, and thus also upon the pressure fluctuations. Furthermore, in the cases where they emerge from VLSM in the logarithmic region of the turbulent boundary layer, they tend to be convected towards the surface, contributing greatly to the surface pressure fluctuations.

Pocket structures are observed experimentally near the surface and it is thought that they are produced from typical eddies and that they could give rise to hairpin vortices [58]. A depiction of this process is provided in Figure 3.26. In this sense, pocket structures share similarities with the proposed low-speed streaks [59]. The low-speed streaks exhibit wavelike behavior, and they are ubiquitous in the TBL's near-surface region [53]. The latest research indicates that they are formed by merging solitonlike coherent structures found in the transitional boundary layer [60], although a historically held believe is that they are caused by long counter-rotating streamwise vortices [61, 62]. The convection velocity of the streaks is lower than the free stream velocity, resulting in the flow wrapping around the structure, which will cause a high-shear layer under a certain angle. This, in turn, will form a vortex of the hairpin type. In the hairpin vortex packet model shown on Figure 3.25, the low speed fluid structures, around which the hairpin vortices are wrapped, can be perceived as low-speed streaks. On the basis that a low-speed streak is composed

of waves [60], and that both the pocket structures and the low-speed streaks give rise to hairpin vortices, the proposal is made that the pocket is a local three dimensional wave of the low-speed streak [53].

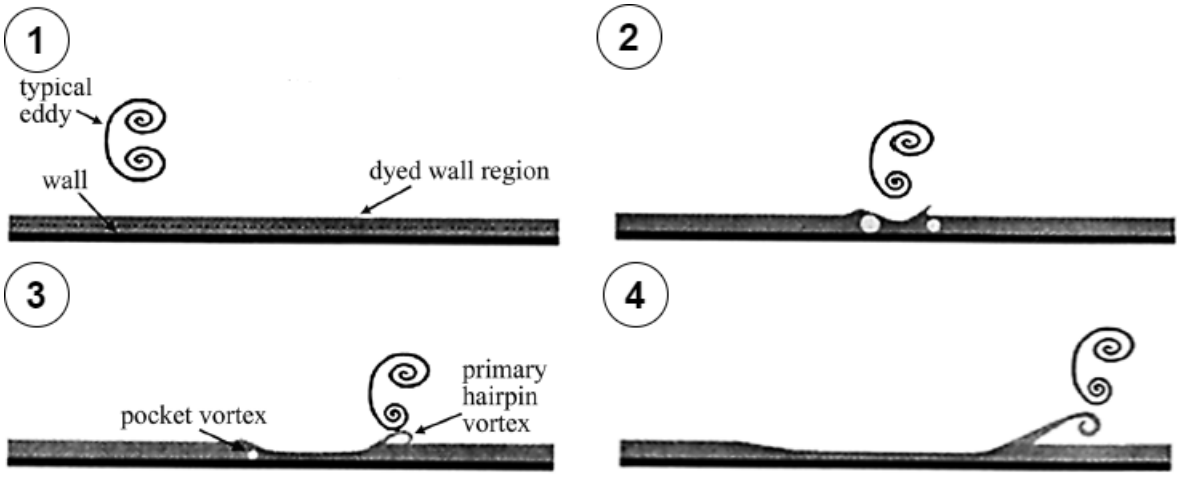

Figure 3.26: Depiction of the process of hairpin vortex generation by the means of a pocket structure created from a typical eddy [57].

The region near the surface is dominated by quasistreamwise vortices, whose upward inclination increases with height above the surface [56]. The main driver behind their formation is the Reynolds shear stress in the near-surface area. Furthermore, an already formed vortex on the surface could induce new ones at its upstream and downstream endpoints with the direction of rotation of the new vortices being opposite to that of the parent vortex [63]. This is possible when regeneration occurs at the main vortex's endpoints. As a result, a zig-zag line of quasistreamwise vortices is formed as shown in Figure 3.27.

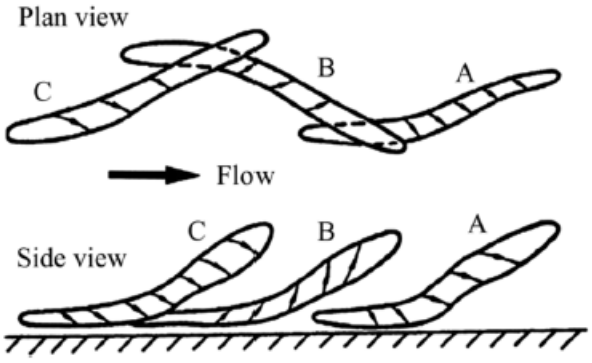

Figure 3.27: Depiction of streamwise vortices at the surface. The parent vortex B has given rise to the secondary vortices A and C [63].

Finally, the VLSM structures are predominantly concentrated in the logarithmic region of the turbulent boundary layer. This is the region of the turbulent flow where its velocity profile is proportionate to the logarithm of the distance above the surface. A detailed breakdown of the regions and sub-layers found in a turbulent boundary layer is provided in Figure 3.28. The VLSM structures typically have lengths of about 10 times the thickness of the TBL and they are characterized by velocity fluctuations of the flow in the extremely long-wavelength region [64]. They can encompass various other flow structures like low-speed streaks and hairpin vortices as demonstrated by particle image velocimetry [65]. Furthermore, VLSM are found to have a correction effect on small scale turbulent structures near the surface, with larger Reynolds numbers yielding stronger correction effects [66].

All of the flow structures discussed above contribute to changes in the velocity and direction of fluid elements inside the turbulent boundary layer. This in turn drives the hydrodynamic pressure fluctuations,

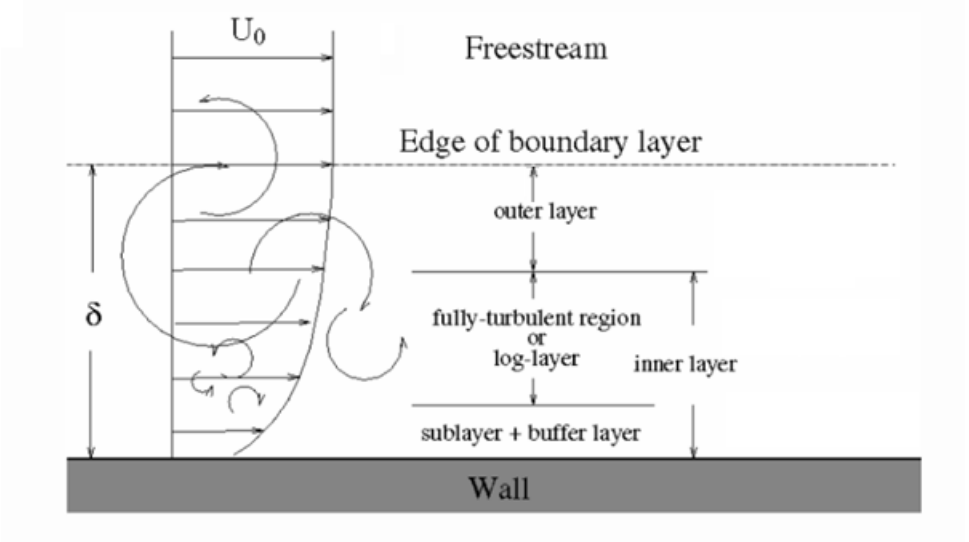

Figure 3.28: The regions and sub-layers of a turbulent boundary layer. The log-layer is the logarithmic region, where the average velocity of the turbulent flow is proportional to the logarithm of the distance of the point in the log-layer from the wall [17].

which are the main characteristic of interest in the context of the current research project. More specifically, the focus will be on the pseudo-sound near the wall because the microphones can only be mounted on the vehicle's surfaces. The pseudo-sound caused by the hydrodynamic pressure fluctuations due to the turbulent structures behaves differently than the sound created by an acoustic source. The major distinction is that the wavenumber of the pseudo-sound is governed by the convection velocity of the flow structures inside the turbulent boundary layer, rather than the speed of sound as it is the case for an acoustic wave [11]. Thus, the convection velocity will have an impact upon the pseudo-sound's frequency spectrum. Due to the fact that the speed of sound is far greater than the convection velocity in the TBL, the pseudo-sound is typically characterized by higher wave numbers, meaning that the wavelength of the hydrodynamic pressure fluctuations is smaller than the corresponding acoustic wavelength [67].

The convection velocity of the turbulent structures is dependent on the local mean flow velocity, given by the turbulent velocity profile at any height above the surface [68]. Typically, larger scale motions like VLSM are convected at higher velocities than smaller scale motions, since as the structure develops and grows in size, it gathers momentum from the large-scale motion. Nonetheless, their convection velocities are proportional to the local mean flow velocity of the velocity profile. In turn, the velocity profile's shape and magnitude is related to the free stream velocity [1]. An often used empirical relation for the turbulent boundary layer velocity profile is the 1/7th power law:

$$\frac{u}{u_e} = \left(\frac{y}{\sigma}\right)^{1/7} \rightarrow u(y) = u_e \left(\frac{y}{\sigma}\right)^{1/7} \tag{3.22}$$

with u being the value of the local mean flow velocity, which is a function of the distance above the surface y, and u_e being the boundary layer edge velocity, which is typically taken to be 99% of the free stream velocity $u_e = 0.99u_\infty$. The symbol u denotes that the streamwise component of the free stream flow V_∞ is considered. The above equation provides good approximation of the magnitude of $u(y)$ and clearly demonstrates that it increases as the free stream velocity increases, however it does not consider the fact that the velocity profile is also dependent on the Reynolds number. To take this into account, the law of the wake can be used, which is still based on empirical data [69]. Figure 3.29 depicts the TBL velocity profiles over a flat plate for increasing Reynolds numbers. It is obvious that the slope of the velocity profile increases as the Reynolds number grows larger, thus further contributing to the increase of the TBL convective velocity. As a result, it can be concluded that the convection velocity should increase as the free stream velocity grows higher.

[17] https://www.computationalfluiddynamics.com.au/y-plus_part1_understanding-the-physics-of-boundary-layers/

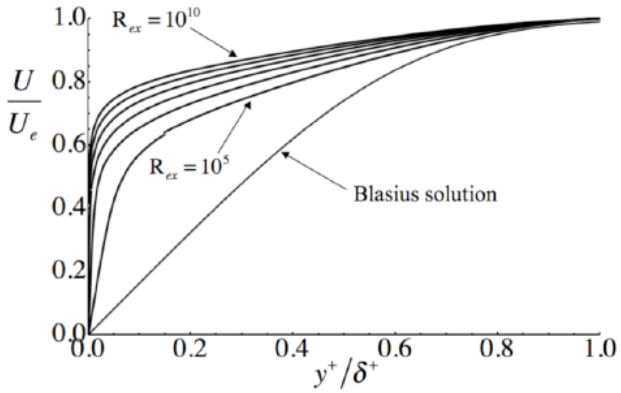

Figure 3.29: Velocity profiles for incompressible turbulent boundary layers of different Reynolds numbers. The Blasius solution refers to a laminar boundary layer [69].

The root-mean-square magnitude of the hydrodynamic pressure fluctuations in the TBL is proportional to the square of the fluctuating velocity components introduces by the turbulent structures described above [70]. The velocity fluctuations are of order v_*, which is the wall friction velocity defined as $v_* = \sqrt{\tau_w/\rho}$. Thus, the pressure fluctuations for an idealized model of homogeneous and isotropic turbulence are of order [71]:

$$p \approx \rho v_*^2 \tag{3.23}$$

The wall friction velocity is proportional to the shear stress at the wall τ_w, which is related to the slope of the velocity profile at the surface, according to the following relation [1]:

$$\tau_w = \mu \left(\frac{\partial u}{\partial y} \right)_{y=0} \tag{3.24}$$

For a given fixed location x along the surface, the Reynolds number will be related to the free stream velocity, as given by Equation (3.21). As the latter increases, the Reynolds number will also increase, meaning that the slope of the velocity profile at the wall will become steeper as shown in Figure 3.29. As a result, the shear stress at the wall will grow larger, subsequently increasing the wall friction velocity and thus the magnitude of the pressure fluctuations according to Equation (3.23). Therefore, it can be concluded that increasing the velocity of the free stream will lead to greater pressure fluctuations in the turbulent boundary layer. This means that the SPL of the pseudo-sound will increase as the free stream velocity gets higher.

Translating the discussion carried out so far to the context of the research project, it is expected that as the airspeed increases, both the convection velocity and the wall friction velocity will increase in the turbulent boundary layers formed over the UAV body. As a result, the pseudo-sound generated in the TBL will have higher SPL, and more energy in the higher frequencies. This has also been demonstrated in numerous experiments. Figure 3.30 depicts the results from an experiment where microphones were mounted on a wind tunnel's wall and floor and measured the the sound due to air flow traveling through the tunnel's chamber at different velocities [72]. Since the microphones were surface mounted, they were located beneath the turbulent boundary layer that forms over the wind tunnel walls, thus the recorded sound will be the pseudo-sound due to the hydrodynamic pressure fluctuations in the TBL. The two different graphs depict different microphone models, and each graph has two plots per flow condition, one corresponding to the wall mounted microphone and the other - to the floor mounted one. The narrow peaks which are most obvious in the data for flow velocities of 55 mph and 10 mph should be ignored because they arise from the resonance characteristics of the wind tunnel facility. The measurements from both microphones clearly agree with the expectations laid down from the discussion carried out so far. It is obvious that increasing the air flow velocity raises the overall SPL of the measured sound and also increases the amount of energy in the higher frequencies. Figure 3.31 depicts result from a similar experiment, but with the microphones mounted on a flat plate protruded from one of the rectangular nozzle edges of an open-jet geometry wind tunnel configuration [67]. The wind tunnel facility in this experiment

is anechoic, providing providing free-field sound propagation characteristics above frequencies of 200 Hz, reducing unwanted sound reflections that could contaminate the microphone measurements. The two plots compare measurements from the same microphones but at different velocities, with the left plot referring to free stream flow velocity of 20 m/s, while the right one - to 34 m/s. The measurements depicted in black on the graphs refer to microphones that are mounted flush on the flat plate, while the remaining measurements refer to microphones recessed in a cavity. In all cases, the results from Figure 3.31 also confirm the expectations described above. It should be noted that both experiments discussed here are of flat surfaces and thus with zero pressure gradients. The boundary layer flow over the UAV wings will most likely experience adverse pressure gradients, which are characteristic for many airfoils. As a result, the velocity profiles of the TBL will be distorted and the measured spectra of the surface pressure fluctuations will be of increased low frequency content compared to zero pressure gradient case [73]. However, it is reasonable to expect that the correlation between increasing free stream velocity and the pressure spectrum properties will remain the same, meaning that it is anticipated that the overall signal SPL will increase for higher airspeed as well as the spectrum will have increased content in its higher frequency regions. This will be valid as long as the flow over the microphone is that of an attached turbulent boundary layer.

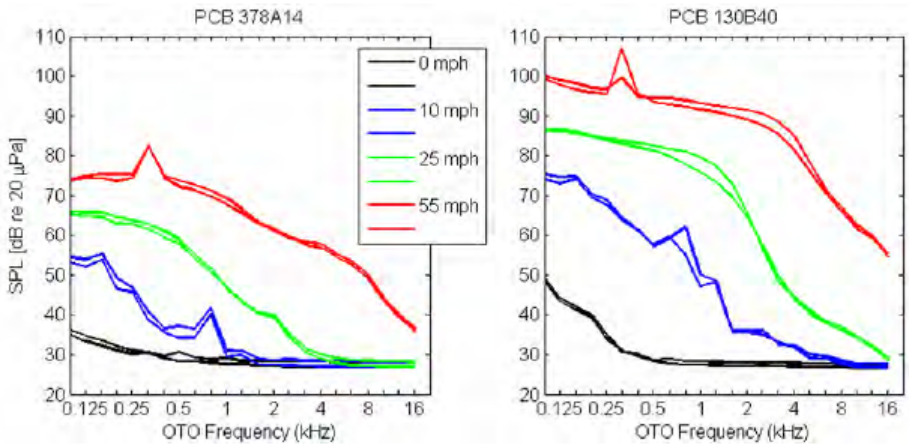

Figure 3.30: Spectra of pseudo-sound generated by a turbulent boundary layer at different free stream velocities. The narrow peaks in the spectra are caused by the resonant behavior of the wind tunnel at the given frequencies. Each measurement for a given flow velocity is presented with two lines, one corresponding to the surface mounted microphone, while the other to the floor mounted microphone [72].

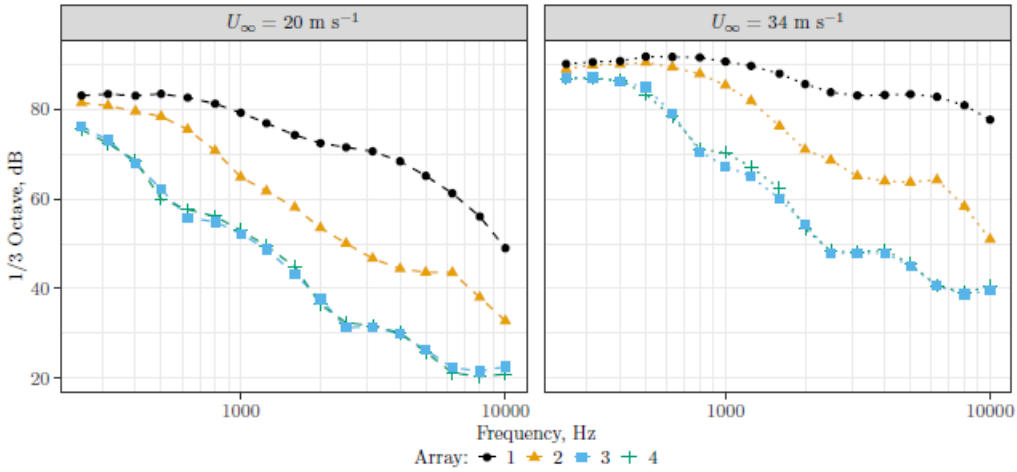

Figure 3.31: Pseudo-sound spectra of flush mounted microphones (black lines) and microphones recessed in cavities (remaining lines) at free stream velocity of 20 m/s and 34 m/s over a flat plate [67].

In reality, the presence of an adverse pressure gradient tends to lead to flow separation. Although the separated flow is of rotational nature, its properties differ than those of the attached turbulent boundary layer. For instance, the vortical structures in the separated flow are of larger magnitude and they tend to be stronger than their TBL counterparts. While the behavior and characteristics of separated flows are not as well described as those of attached boundary layers, and are harder to foresee, some models have been put forward aiming at predicting and explaining the behavior of the flow in the separated region, with one of the more popular ones being the model proposed by Goody [74]. An interesting case will arise at the separation point, where the magnitude of the pressure fluctuations will be at a minimum, due to the fact that the shear stress will be at a local minimum. This is expected since the slope of the velocity profile is close to zero at the separation point as depicted in Figure 3.20. If a microphone is located on the separation point, then the measured pseudo-sound SPL will be at its lowest. In this case, the obtained microphone measurements could no longer be used to estimate the free stream velocity since the drop in the pseudo-sound SPL would not necessarily be related to changes in said velocity. As such, starting with the separation point, there will be a mismatch between the observed wall pressure fluctuations and those corresponding to the attached TBL for the same free stream velocity. In case the separation points moves upstream - e.g. by increasing the vehicle's angle of attack - the microphone will be located beneath separated flow, which for most parts is characterized by pressure fluctuations of higher magnitude, compared to attached TBL for the same velocity of the free stream [74].

The literature reviewed so far has had the goal of explaining the physical phenomena in the boundary layers and proving that they can give rise to sounds that can be captured by microphones mounted in the vehicle's body. The discussions carried out so far prove that the sound captured by the microphone on the UAV in flight can indeed be attributed to phenomena inside the boundary layers, and more notably in the turbulent boundary layer, which give rise to fluctuating hydrodynamic pressure components. Subsequently, the features and behavior of these phenomena - identified to be different types of flow structures existing in the boundary layers - was studied in greater details and it was found that their properties, as well as the resulting hydrodynamic pressure fluctuations that they cause, are dependent on the free stream flow velocity. Therefore, it was proved that the changes in the loudness and pitch of the recorded sound from the UAV on-board footage discussed in Section 1.1 are indeed due to the impact that the airspeed has upon the flow structures inside the boundary layer as it was hypothesized. The existence of a relationship between the free stream flow velocity and the sound caused by the hydrodynamic pressure fluctuations in the boundary layer means that models can be created that relate the two parameters, therefore making it feasible for the relation between the two to be used as the working basis of this novel type of airspeed instrument. The remainder of the literature study is devoted to researching methods and techniques that will lead to microphone measurements of higher quality, which will in turn improve the accuracy of the airspeed estimation by the instrument, as well as researching the most optimal approaches to model the relation between the vehicle's airspeed and the properties of the sound caused by the hydrodynamic pressure fluctuations in the boundary layer.

Measuring Pressure Fluctuations in the Turbulent Boundary Layer

While the performance characteristics of the microphone play an important role in collecting sound measurement of high quality and relevance for the purposes of the research project, they are not the only deciding factor. The type of microphone mounting and the location of mounting on the surface of the UAV will have a substantial impact as well [11, 67].

The options for mounting a microphone on the body of the vehicle include positioning it in-flow, mounting in directly on the surface, mounting it flush, positioning it in a cavity, or having it remote. Figure 3.32 depicts the different microphone mounting options. Both the in-flow mounted microphone and the one positioned on top of the surface will be able to catch the direct contribution to the hydrodynamic pressure fluctuations of greater number of flow structures, while the remaining mounting configurations will register the pressure fluctuations as they are at the surface. Although the microphones protruded from the surface might capture the actual pressure fluctuations more accurately, they will interfere with the flow's path and behavior since they will act as obstacles to the flow. In fact, any deviations from the surface larger than $10 \times 10^{-6}\ m$ can cause distortion of the flow [73]. This might generate additional sound sources or introduce unwanted flow distortions, thus influencing the energy spectral density of the pressure fluctuations [11]. Furthermore, it might also impact the aerodynamic properties of the aerial vehicle in a negative way. Placing a microphone in-flow also poses a danger for its membrane, since it can be put outside of its typical operating range due to stresses caused by the stagnation-pressure effects, thus damaging it permanently. On the other hand,

both the remote and cavity mounted microphones are found to attenuate the pseudo-sound arising from the hydrodynamic pressure fluctuations in the turbulent boundary layer. As the TBL pseudo-sound is governed by the convection velocity of the turbulent boundary layer, the resulting sound waves will have dispersion relations that only permit imaginary wave numbers to propagate normal to the wall, which in turn means that they will decay exponentially [67]. This can be clearly seen on Figure 3.31, where a comparison is shown between flush and cavity mounted microphones taking measurements with only a turbulent boundary layer present over a flat plate for a free stream with the specified velocities. The black lines in both plots refer to the measurements taken with the flush mounted microphones and they evidently have the highest SPL distribution along the frequency spectrum, meaning that the signal-to-noise ratio will be better in case the pseudo-sound from the hydrodynamic pressure fluctuations is treated as the signal of interest. The remaining lines from the graphs depict microphones mounted in cavities of different geometries. Finally, flush mounted microphones posses another benefit over the cavity configurations, namely that they provide full dynamic response [73]. However, flush mounting a microphone has the drawback that the spatial resolution of the turbulent structures will be limited by the microphone diameter. As such, the following conditions must be met in order to ensure that both the spatial and temporal properties can be measured accordingly [75]:

$$d << \frac{\lambda}{2} \quad \text{and} \quad f_n >> \frac{U_\infty}{\lambda} \tag{3.25}$$

with d being the flush mounted microphone diameter, λ - the wavelength of the flow features measured, f_n - the microphone's frequency response, and U_∞ - the free stream flow velocity in the streamwise direction. In case the microphone a has diameter that is not small enough to measure finer flow structures of interest, the Corcos correction can be used [76].

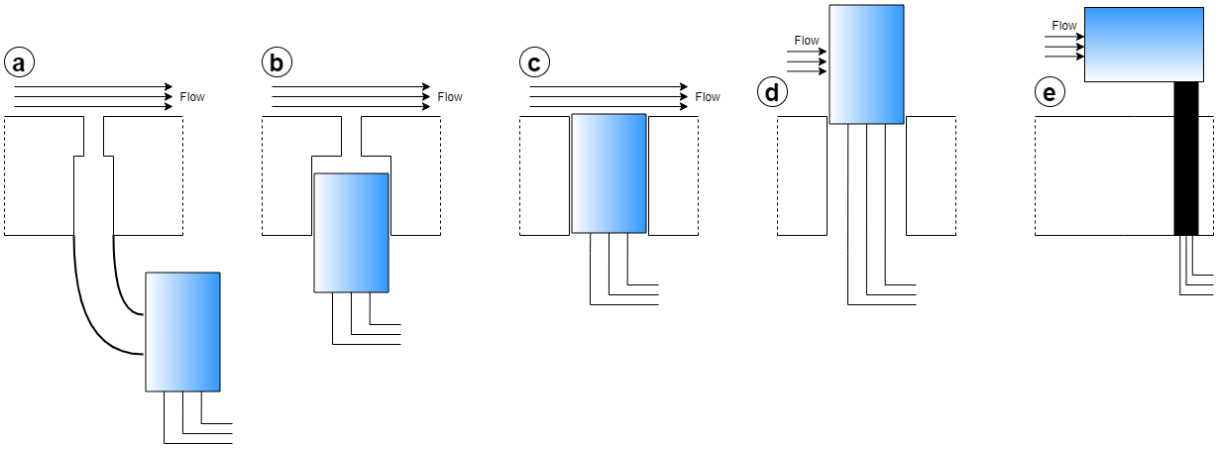

Figure 3.32: Visualization of the different possible mounting configurations of the microphone on the UAV body: a) Remote mounted microphone, b) Cavity mounted microphone, c) Flush mounted microphone, d) Microphone mounted on top of the surface, e) In-flow mounted microphone.

The microphones utilized in experiments relating to measurements of the hydrodynamic pressure fluctuations in turbulent boundary layers are typically omnidirectional [11]. The motivation behind this is the fact that the turbulent structures span the boundary layer in both directions normal to the surface and across it [53]. As such, pressure fluctuations will propagate from all directions. It should also be noted that the pressure fluctuations at the surface vary between different locations and the resulting pseudo-sound spectra might differ as well, with the coherence between them being low [67]. To take this into account, an array of microphones could be utilized, that can be arranged in different geometrical patterns, and take the averaged measurements over all microphones in the array. Finally, since the microphone measurements are used to study and characterize the SPL and spectrum of the pseudo-sound, they need to realistically represent the hydrodynamic pressure fluctuations. Therefore, the microphones used typically have a flat response, thus the measurements are Z-weighted. Furthermore, both the A- and C-weightings attenuate the SPL in the low frequencies, which is undesirable since most of the energy of the pseudo-sound will be concentrated in the lower frequency range.

3.2.3. Signal Processing and Filtering

A microphone mounted on a UAV will inevitable also capture sounds from other sources besides the pseudo-sound from the hydrodynamic pressure fluctuations in the boundary layer. In a wind tunnel, possible sources of additional sound could be the fans, the vibration of upstream or downstream components, any vibrations of the facility, as well as sound reflections from walls or sounds stemming from outside the facility, especially relevant in acoustically untreated facilities. During flight, the microphone would also capture sound from the motors and propellers, as well as any environmental sounds. The duality of the pressure fluctuations needs to be tackled as the current research focuses only on the hydrodynamic pressure fluctuations, thus making any other type of pressure fluctuation an undesired component of the overall microphone measurements.

Available techniques for the separation of acoustic and hydrodynamic pressure fluctuations make use of their differences in physical properties. For example, the acoustic pressure fluctuation - resulting as linear solution of the wave equation - is typically of small amplitude and coherent. On the other hand, the vortical motion caused by the flow structures in the turbulent boundary layer usually results in pressure fluctuations of greater amplitude but with poor coherence. Furthermore, the vortical motions are convected through the turbulent boundary layer, meaning that their phase speed is about the same as the local flow speed, or at least proportional to it. Conversely, the acoustic pressure fluctuations propagate at the speed of sound. These distinct characteristics of the different types of pressure fluctuations can be used as a basis to identify and separate them in a microphone signal [11].

An often applied technique to isolate the hydrodynamic pressure fluctuations information from microphone measurements is by subtraction of measurements from two different microphones beneath a turbulent boundary layer [73, 11]. The method is based on the fact that the hydrodynamic pressure fluctuation signals at different locations on the surface - sufficiently spaced from each other - beneath the turbulent boundary layer tend to be uncorrelated [77]. In a study of turbulent boundary layers in a wind tunnel, it was determined that for two microphones mounted flush with the surface and located beneath the TBL, at the same streamwise position, but separated by a distance of at least one boundary layer thickness in the spanwise direction, any correlation between their signals can be attributed to sound from acoustic sources because correlations between turbulent structures occur only over distances that are shorter than the boundary layer thickness at the current location [78]. In general, the pressure fluctuations

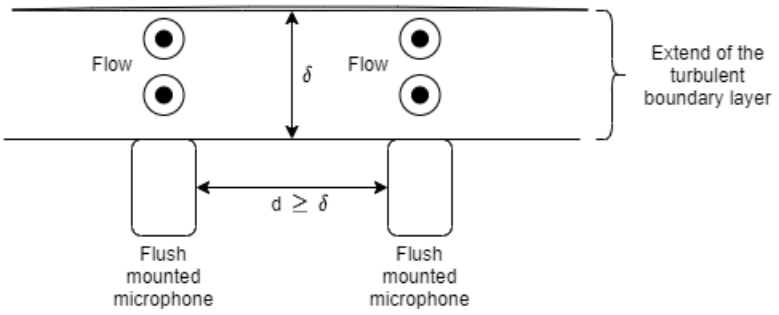

Figure 3.33: Depiction of the microphone mounting configuration that will allow for the subtraction filtering method to be utilized. The flow is traveling in a direction out of the page.

registered by a microphone at the wall can be assumed to arise from 3 distinct types of sources, namely due to acoustic sound, hydrodynamic pressure fluctuations caused by the turbulent structures in the TBL, and vibrations [73]. As such, the overall microphone signal of fluctuating pressure will be given by:

$$p' = p'_a + p'_{TBL} + p'_v \tag{3.26}$$

where the symbol p' denotes the fluctuating component of the pressure, with p'_a referring to the pressure fluctuations caused by acoustics, p'_{TBL} denoting the hydrodynamic pressure fluctuations, and p'_v indicating the pressure fluctuations caused by vibrations of the surface. Then, subtracting the measured pressure fluctuations of a second microphone and taking the mean square values will result in:

$$\overline{(p'_1 - p'_2)^2} = \overline{\left((p'_a + p'_{TBL} + p'_v)_1 - (p'_a + p'_{TBL} + p'_v)_2\right)^2} \tag{3.27}$$

By assuming that the two microphones are mechanically coupled, meaning that they are mounted on the same rigid surface, the mean vibrational components $\overline{p'_v}$ can be canceled. Furthermore, treating the acoustic components as being perfectly in-phase will suppress them when taking their difference. Then, Equation (3.27) can be expanded and by setting the terms that contain any uncorrelated coherent components to zero the proof for the subtraction filter is obtained [73]:

$$\overline{(p'_1 - p'_2)^2} = 2\overline{(p'_{TBL})^2} \tag{3.28}$$

In case the microphones cannot be positioned further than a distance δ apart, the above discussed filtering method will also remove part of the contribution of the hydrodynamic pressure fluctuations to the microphone signal [79]. In order to obtain the complete spectrum of p'_{TBL} for this scenario, a time delay can be applied to the reference microphone. It should be noted that the separation between the primary and reference microphones in this case should be less than $\delta/3$ [73]. Then, the signals from the two microphones will be:

$$p'(t) = p'_a(t) + p'_{TBL}(t) + p'_v(t) \tag{3.29}$$
$$p'(t+\tau) = p'_a(t+\tau) + p'_{TBL}(t+\tau) + p'_v(t+\tau) \tag{3.30}$$

Performing the subtraction in the same way as for Equation (3.27) yields this subtraction filter's proof [73]:

$$\overline{\left(p'_1(t) - p'_2(t+\tau)\right)^2} = 2\overline{(p'_{TBL})^2} \tag{3.31}$$

As a result, all acoustic and vibrational pressure fluctuation components are canceled for frequencies of $f = 1/\tau$ as well as for the higher harmonics. The introduced time delay τ is bounded by the criterion that $\tau > \delta/U_c$, where U_c refers to the convective velocity of pressure fluctuation wave with frequency f. This filtering technique utilizes the signal components' correlation in time rather than in space, making it better suited for closely spaced microphones. Furthermore, the time delay method can also be applied to the case when only a single microphone is available [80]. Comparing the two subtraction techniques, the one relying on the signals' spatial correlation has been proven to perform better in the low frequency range [81].

The filtering techniques proposed above have been widely adopted in filtering axial acoustic components from wind tunnel experiments aimed at collecting data about the hydrodynamic pressure fluctuations brought about the turbulent boundary layers [11, 73]. Axial acoustic disturbances propagate in the streamwise direction as shown in Figure 3.34, and in wind tunnels they are associated with the blade passing frequency of the tunnel fan, flow instabilities, standing waves within the tunnel, etc. On the other hand, non-axial acoustic disturbances typically do not propagate in the streamwise direction. In real flight conditions, the sources of acoustic noise might not be aligned with the streamwise orientation of the turbulent boundary layer over the UAV, thus making them non-axial disturbances. As such, the assumption of homogeneity of the acoustic plane-wave in the spanwise direction will need to be revised.

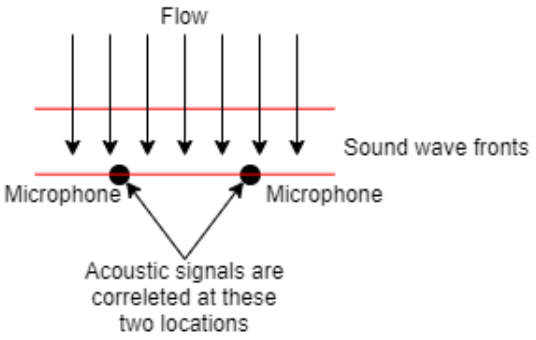

Figure 3.34: Axial acoustic disturbance propagating streamwise and being captured by microphones. The black dots represent the flush mounted microphones.

Another approach would be to implement Kalman filtering with unknown noise covariances [82]. In this case, the hydrodynamic pressure fluctuations signal will be the target signal, while all other components will be treated as noise. Due to the fact that the captured acoustic components can significantly vary in

their properties, it will be difficult to define the noise statistics for the filter. Furthermore, to make the filter able to estimate the hydrodynamic pressure fluctuations, it will need a precise model of the characteristics and behavior of the hydrodynamic component, which will also have to be microphone-specific since the microphone performance will impact the resulting measurements. Therefore, a more practical approach - albeit one that is less precise - is to determine only the major sources of acoustic disturbances during flight and characterize their spectra, subsequently subtracting them from the overall spectrum of pressure fluctuations, while neglecting any non-axial disturbances that might arise in the environment. Furthermore, mounting all microphones on the same vehicle body structure will negate any impact of the vibrational components. This approach is feasible since the major contributor to the acoustic disturbances during flight will be the engine noise, which can be readily characterized over its RPM range, while any other typically encountered environmental sounds will have much weaker intensity. In the end, this will leave the hydrodynamic pressure fluctuations as the dominant signal component. The typical SPL of the pseudo-sound caused by the hydrodynamic pressure fluctuations in a turbulent boundary layer is in the order of 80-90 dB. Experiments from Cal Poly further substantiated this claim, where it was found that the root-mean-square of the TBL hydrodynamic pressure fluctuations tend to be about 10% of the local free stream dynamic pressure q at low flow velocities (< 15 m/s) and decreasing to about 3.5% as q was increased, hence at higher flow velocities (< 47 m/s) [46]. The local free stream dynamic pressure is calculated as follows:

$$q = \frac{1}{2}\rho V^2 \tag{3.32}$$

with ρ being the local air density and V - the free stream flow velocity. The order of the expected pseudo-sound SPL is a lot higher than what is anticipated of the sounds that will reach the UAV during flight since most sources of environmental acoustic disturbances will be located on the ground and by the time their acoustic waves reach the UAV - which typically flies tens of meters above the ground - they will have lost a significant amount of their sound intensity. This means that any contribution of environmental acoustic disturbances will indeed be negligible, except for the engine noise, which will be characterized and subtracted from the microphone measurements.

3.2.4. Modeling the Turbulent Boundary Layer Pressure Fluctuations

The highly complex multi-scale and chaotic nature of turbulence makes it challenging to model it by an analytical approach. As such, most models of turbulence in use today are based to some extent on empirical data obtained from experiments. Due to the fact that the experiments differ in equipment and flow conditions, the resulting models will be distinct and will be better suited to model turbulence in a particular set of conditions, or to model a certain region of the turbulent flow. For example, some models have been developed based on newly acquired measurements from flight tests and wind tunnel tests, while others build upon existing sources of measurements. Some have been developed by modifying existing models such that they fit wider range of datasets. Lastly, models have also been obtained using fluid mechanics and thermodynamic principles and CFD simulations. As a result, turbulent boundary layer prediction models can be used to estimate many of the layer's parameters, however the ones of interest for the purposes of the current research are the wall pressure spectra and the fluctuating pressure component, as well as their relation with the free stream flow velocity. Therefore, the models discussed hereafter function to predict these parameters at single points along the surface using the available information about the properties of the TBL and the local free stream.

The power spectral density (PSD) of the wall pressure fluctuations signal describes the sound power distribution along the frequencies captured within the signal. As a side note, for signals existing over all time, or over a sufficiently large time period compared to the duration of a single measurement, the PSD will refer to the spectral energy distribution expected per unit time, and if converted to decibel it will represent the SPL spectral distribution per unit time in the case of a sound signal [83]. An often used model of the wall pressure spectrum, $\Phi(\omega)$, beneath a turbulent boundary layer is the Efimtsov's model. It was developed with data obtained from both low and high speed wind tunnels, as well as flight data from Tu-144 and Tu-22. The resulting equation for the wall pressure spectrum is [84]:

$$\Phi(\omega) = 2\pi\alpha U_\tau^3 \rho_\infty^2 \delta \frac{\beta}{(1+8\alpha^3 Sh^2)^{1/3} + \alpha\beta Re_\tau \left(\frac{Sh}{Re_\tau}\right)^{10/3}} \tag{3.33}$$

$$\alpha = 0.01; \quad \beta = \left[1 + \left(\frac{Re_{\tau 0}}{Re_\tau}\right)^3\right]^{1/3}; \quad Sh = \frac{\omega\delta}{U_\tau} \text{ (Strouhal Number)}; \quad Re_{\tau 0} = 3000$$

with U_τ being the friction velocity, Re_τ the friction Reynolds number. For the Efimtsov's model, the principle independent variables are two, namely the Strouhal number and the Reynolds number, both of which are affected by the free stream flow velocity. As a result, the model can be used to predict the wall pressure spectrum under varying airspeed. The sound spectra are typically expressed in Hertz, while the model depicts the wall pressure spectra in terms of the angular frequency ω. To express the PSD in Hertz the following transformation can be carried out:

$$\Phi(\omega) = 2\pi W(f)$$

Another well established model is the Chase-Howe model, which was builds up on the earlier Chase's model. Its equation is given as [73]:

$$\Phi(\omega) = \frac{2\left(\frac{\delta^*}{U_\infty}\right)^3 (\tau_w \omega)^2}{\left[\left(\frac{\omega\delta^*}{U_\infty}\right)^2 + 0.0144\right]^{3/2}} \tag{3.34}$$

with δ^* being the boundary layer displacement thickness and τ_w the shear stress at the wall. This model is constructed using data from wind tunnel experiments studying two-dimensional zero-pressure gradient boundary layer flows. Furthermore, by comparing the Chase-Howe model to other sets of experimental data for a wide range of Reynolds numbers, it was found that the model underestimates the lower frequency components of the wall pressure spectra and did not decay fast enough at the high frequency end.

Therefore, the Chase-Howe model was adjusted by Goody to fit it better to measured experimental data - still referring to zero pressure gradient boundary layer - with the modified equation being [85]:

$$\Phi(\omega) = \frac{3\left(\frac{\delta}{U_\infty}\right)^3 (\tau_w \omega)^2}{\left[\left(\frac{\omega\delta}{U_\infty}\right)^{0.75} + 0.5\right]^{3.7} + \left[\frac{1.1}{R_T^{0.57}}\left(\frac{\omega\delta}{U_\infty}\right)\right]^7} \tag{3.35}$$

The model created by Smol'yakov takes into account the fact that the TBL wall pressure spectra scale differently in the different frequency ranges. As such, the model incorporates three distinct equations for the low frequency, universal, and high frequency ranges respectively. They are semi-empirical with the experimental data coming from wind tunnel testing with flat plate [86].

$$\Phi(\omega) = \frac{1.49 \times 10^{-5} \tau_w^2 v Re_\theta^{2.74} \overline{\omega}^2}{U_\tau^2}\left[1 - 0.117 Re_\theta^{0.44} \overline{\omega}^{1/2}\right] \quad \text{for} \quad \overline{\omega} < \overline{\omega}_0 \tag{3.36}$$

$$\Phi(\omega) = \frac{2.75 \tau_w^2 v}{U_\tau^2 \overline{\omega}^{1.11}}\left[1 - 0.82 e^{-0.51\left(\frac{\overline{\omega}}{\overline{\omega}_0} - 1\right)}\right] \quad \text{for} \quad \overline{\omega}_0 < \overline{\omega} < 0.2 \tag{3.37}$$

$$\Phi(\omega) = \frac{(38.9 e^{-8.35\overline{\omega}} + 18.6 e^{-3.58\overline{\omega}} + 0.31 e^{-2.14\overline{\omega}}) \tau_w^2 v}{U_\tau^2}\left[1 - 0.82 e^{-0.51\left(\frac{\overline{\omega}}{\overline{\omega}_0} - 1\right)}\right] \quad \text{for} \quad \overline{\omega} > 0.2 \tag{3.38}$$

where

$$\overline{\omega} = \frac{\omega v}{U_\tau^2}; \quad \overline{\omega}_0 = 49.35 Re_\theta^{-0.88}$$

with Re_θ being the momentum thickness Reynolds number. The first terms in the equations above are the modeling terms, while the ones in the bracket serve the purpose to provide a smooth continuation between the frequency regions corresponding to the different equations.

There are also other models available to estimate the wall pressure spectra beneath a turbulent boundary layer, with each model being better suited for different data sets or measurement methods.

This is obvious by the fact that not all models exhibit high level of agreement between each other across the whole frequency range. Furthermore, data collected during wind tunnel testing might differ than data obtained from flight tests, even if the flow conditions were the same. As such, relying on the available (semi-)empirical models for the purposes of relating the TBL wall pressure spectra to the airspeed of the UAV will have significant drawbacks. First of all, most models are developed with aircraft applications in mind, meaning that the free stream velocities - represented in the Reynolds number - investigated are a lot higher than those of interest for the purposes of the current research project. While it is possible to scale the models such that they can be used for Reynolds numbers outside of the range tested by the experimental data, there is no single universally accepted scaling method that can produce satisfactory results. This is because the pressure fluctuations beneath a turbulent boundary layer are caused by flow structures that differ in the distinct regions of the TBL. As a result, the contributions of the flow structures from the inner region of the turbulent boundary layer will be scaled differently than those of the structures from the outer region [73]. Table 3.2 provides an overview of the typically used scaling variables when comparing measurements over a range of flow conditions. Furthermore, the performance characteristics of the equipment used to measure the wall pressure fluctuations will have an impact upon the data, and consequently upon the resulting models. Thus, utilizing any of the already existing models of the TBL wall pressure spectra as the working basis of the airspeed instrument will lead to errors, which will be further amplified in case the models have to be scaled, which will degrade the instrument's accuracy and hence its usability.

Scaling Variable	Spectrum Scaling	Frequency Scaling
Inner Scaling	$\Phi(\omega)U_\tau^2/\tau_w^2 v$	$\omega v/U_\tau^2$
Mixed Scaling	$\Phi(\omega)U_\tau/\tau_w^2\delta$	$\omega\delta/U_\tau$
Outer Scaling	$\Phi(\omega)U_\infty/q^2\delta^*$	$\omega\delta^*/U_\infty$

Table 3.2: Typically implemented scaling variables for wall pressure spectra [87].

The issues discussed above are also encountered when utilizing (semi-)empirical models to obtain the fluctuating pressure component. Most of these models predict the mean square pressure parameter, $\overline{p'^2}$, as it provides an estimate of the overall energy of the pressure fluctuations at the surface. One of the first model developed with the aim of predicting the pressure fluctuation component beneath a turbulent boundary layer is that of Kraichnan [88]:

$$\overline{p'^2} = (6\tau_w)^2 \tag{3.39}$$

The model was derived from the Navier-Stokes equation with the necessary terms being evaluated using data of zero pressure gradient TBL over a flat plate with the assumption of homogeneous TBL flow in adiabatic conditions. Furthermore, the rate of growth of the boundary layer was assumed to be slow. However, this particular model also assumes small compressibility of the flow, which makes it less suitable for the purposes of the current research, where the flow is assumed incomporessible.

The model of Lilley & Hodgson makes use of methods similar to those of Kreaichnan but assumes an incomporessible flow [89]:

$$\overline{p'^2} = (0.008q)^2 \tag{3.40}$$

The starting point of this model are the equations of continuity and motion under the assumption of incompressible flow. The terms that need to be known (e.g. the two-point velocity correlations, the mean velocity profile, and the turbulence intensity and scale) in order to arrive at the intensity of the pressure fluctuations are evaluated and adjusted using data from low turbulence wind tunnel experiments.

The model of Blake is developed from wall pressure measurement data beneath a TBL using small pinhole microphones allowing for improved resolution of the high frequency region [90]:

$$\overline{p'^2} = (0.00876q)^2 \quad \text{or} \quad \overline{p'^2} = (3.59\tau_w)^2 \tag{3.41}$$

Measurements were also collected for surfaces of various roughness and was determined that the mean square pressure for rough walls is dependent on the roughness height. The overall trend is that the magnitude of $\overline{p'^2}$ scales with an increase in the surface roughness. However, the usage of pinhole microphones might introduce disturbances in the turbulent boundary layer flow.

Schewe performed wind tunnel experiments using small flush mounted pressure transducers forming an integral part of the wall, thus not protruding into the boundary layer flow. The data resulting from the experiments yielded the following model [91]:

$$\overline{p'^2} = (0.0102q)^2 \tag{3.42}$$

Lueptow accounted for the impact that the size and shape of the pressure transducers will have upon the pressure fluctuations component by applying wave-number filters and comparing the results with the Corcos method [92]:

$$\overline{p'^2} = (0.012q)^2 \tag{3.43}$$

The $\overline{p'^2}$ models discussed so far have been developed with measurement data of zero pressure gradient turbulent boundary layer flow over flat surface. While these models might be relevant for applications to the turbulent boundary layer formed over an aerial vehicle's fuselage [74], the presence of an adverse pressure gradient in the turbulent boundary layer flows found over most wings will not be adequately represented. In such flows, the low frequency region of the spectrum scales approximately with the magnitude of the local maximum shear stress in the boundary layer, and the power in the high frequency region tends to increase as the streamwise pressure gradient increases [93]. As such, for boundary layer with an adverse pressure gradient, the model for $\overline{p'^2}$ will vary depending on the streamwise location along the surface. This is apparent from Figure 3.35 which depicts the distribution of pressure fluctuations within turbulent boundary layer over a flat surface experiencing an adverse pressure gradient. It can be seen that for $y/\delta^*_{in} = 0$, referring to the pressure fluctuation component at the wall, its magnitude changes at different x-locations for the same free stream flow. The adverse pressure gradient will also impact the wall pressure spectra. Figure 3.36 depicts wall pressure spectra of turbulent boundary layer with an adverse pressure gradient scaled using different methods. A distinct wall pressure spectrum is observed at different streamwise locations for all scaling variables.

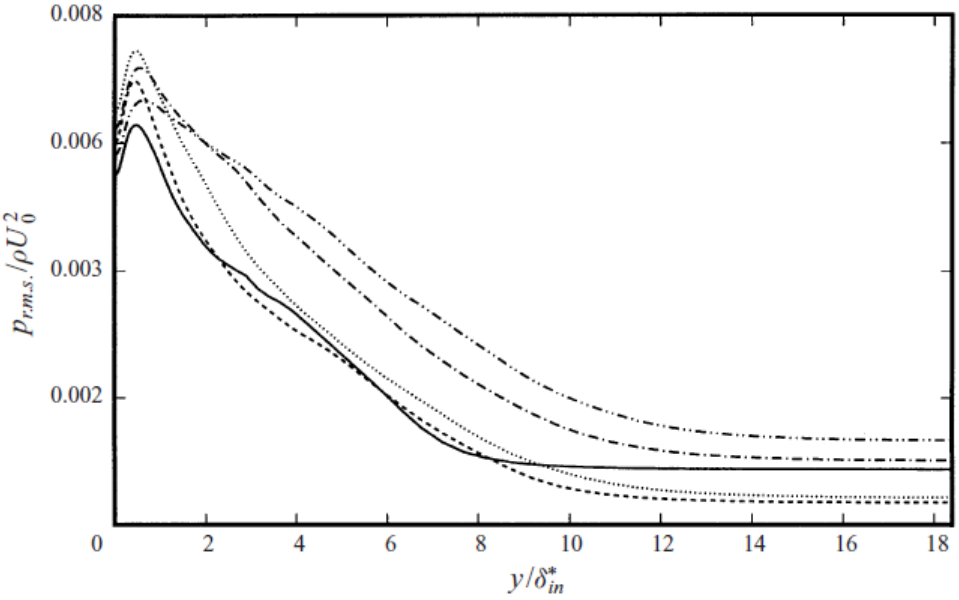

Figure 3.35: The distribution of pressure fluctuations across the turbulent boundary layer with an adverse pressure gradient. x = 0.5 (___); x = 0.6 (- - -); x = 0.7 (...); x = 0.8 (- . -); x = 0.85 (- . . -) [93].

The (semi-) empirical models discussed so far, both for the fluctuating wall pressure spectra and its mean square value, are not directly related to the airspeed, rather they are governed by parameters which in turn are related to the airspeed. The wall pressure spectra model of Chase-Howe and Goody contain a direct dependence on the free stream flow velocity via the U_∞ term. However, those models are also governed by other parameters affected by the free stream velocity, namely the boundary layer thickness δ, the boundary layer displacement thickness δ^*, and the R_T parameter defined as $R_T = \frac{U_\tau \delta}{U_\infty v}$. The models

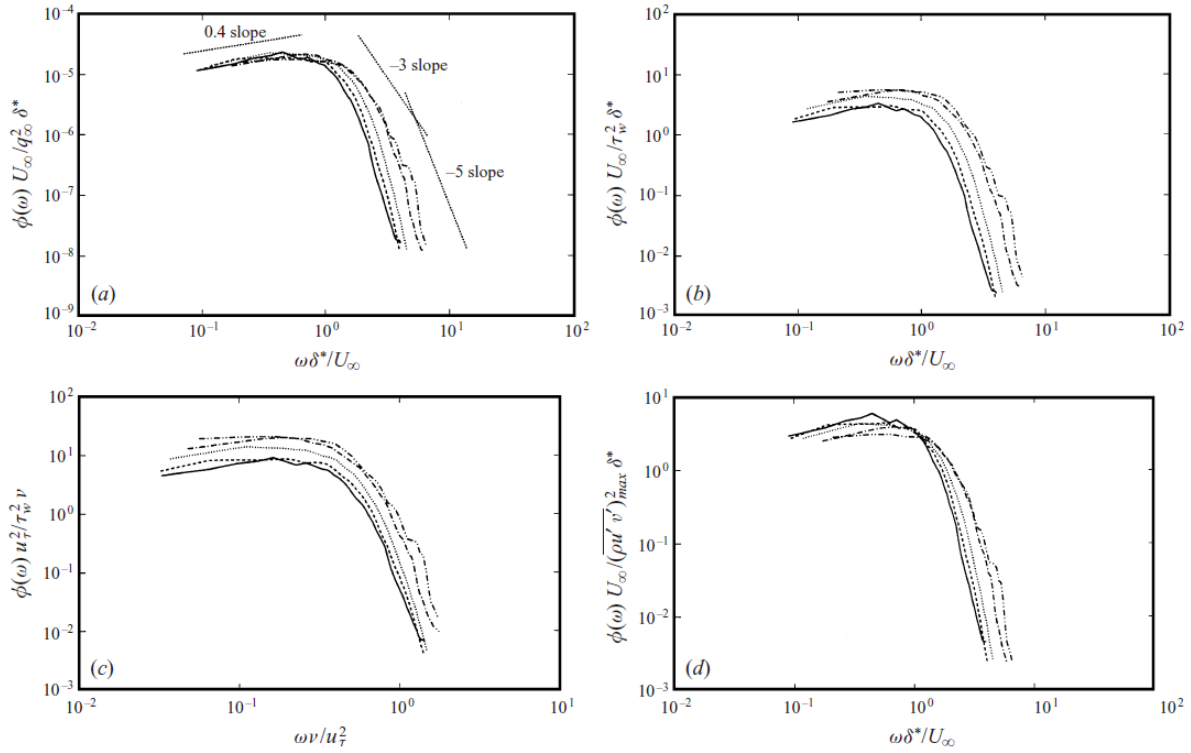

Figure 3.36: Frequency spectra of wall pressure fluctuations beneath a turbulent boundary layer with an adverse pressure gradient. (a) outer scaling with pressure scaled with q_∞^2; (b) outer scaling with pressure scaled with τ_w^2; (c) inner scaling; (d) outer scaling with pressure scaled with $(\rho\overline{u'v'})^2_{max}$. x = 0.5 (___); x = 0.6 (- - -); x = 0.7 (...); x = 0.8 (- . -); x = 0.85 (- . . -) [93].

of the mean square pressure are governed by the dynamic pressure, which is related to the square of the free stream velocity, and the other pressure spectra models are governed by various measures of the Reynolds number, which are all proportional to the airspeed. Therefore, the direct dependence of the wall pressure spectra and the mean square pressure on the free stream velocity can be obtain if all terms related to the velocity are expressed in terms of it and are subsequently substituted in the model equations. This will allow to rewrite the models such that they express the relation between the the properties of the fluctuating pressure component and the airspeed.

Both the mean square pressure and the wall pressure spectra can be obtained by methods other than established empirical models. The PSD can be obtained by performing a fast Fourier transform on the raw signal of the microphones, while the mean square pressure parameter can be calculated either by time averaging the square of the raw microphone signal, or by integration of the single-point wall pressure spectrum [73]:

$$\overline{p'^2} = \frac{1}{T}\int_0^T p'^2(t)dt \tag{3.44}$$

$$\overline{p'^2} = \int_0^\infty \Phi(\omega)d\omega \tag{3.45}$$

While time averaging the square of the microphone signal will provide a direct representation of the expected mean square pressure, using the integral of the PSD will result in an accumulation of error in the $\overline{p'^2}$ parameter in the frequency domain caused by the signal resolution [94]. Furthermore, in case the PSD has been obtained from an empirical model, there will be an additional source of error coming from any mismatch between the actual wall pressure signal PSD and the one predicted by the $\Phi(\omega)$ model. Thus, having the signal from a microphone placed beneath turbulent boundary layer, both the wall pressure spectra and the mean square pressure can be determined. As such, the errors due to model scaling and performance differences of the equipment used to obtain the dataset for the (semi-) empirical models can

be avoided if the models of the fluctuating pressure component are developed using data that has been collected over the same range of flow and environmental conditions and using the same microphones - or microphones with the same performance characteristics - as those that will be part of the airspeed instrument. However, this will introduce the need for carrying out practical experiments as part of the research project.

The data obtained from the experiments will be used to develop completely empirical models for the properties of the fluctuating pressure component for free stream flow velocities ranging up to 25 m/s, which is the typical extent of the UAV's operational airspeed. Having the free stream velocity as the independent variable in the experiments will allow for the created models to directly relate the wall pressure spectra and the magnitude of the wall pressure fluctuations to the airspeed. Furthermore, including the angle of attack as a second independent variable will also allow to determine how the pressure fluctuations beneath the attached TBL change with respect to this parameter and for what angles of attack the boundary layer starts to separate from the surface of the vehicle. Depending on the amount of gathered data, it might also be possible to create a model of the properties of the wall pressure fluctuations beneath separated flow for the current range of airspeed, which will broaden the range of operational conditions in which the instrument could be utilized.

The models that will be developed as part of the research project will be black-box models, modeling an input-output relation. As such, there is a wide variety in possible model structures that could be utilized, including polynomial models, splines, and supervised machine learning methods such as feedforward or radial basis function neural networks, random forest regressors, support vector machines, etc. [95]. Next to that, there are many available options for parameter estimation for the different model structures, as well as sampling algorithms that select the most appropriate input points such that the overall model accuracy is improved [96]. In recent years, machine learning methods have seen increased application in many fields of science and engineering due to their capabilities in tackling regression problems involving large, high-dimensional and non-linear datasets [97]. This makes them suitable for modeling complex phenomena such as those occurring in the turbulent boundary layer and giving rise to the pressure fluctuations, however their application in this field to date has been limited. Neural networks - trained using a gradient descent algorithm - and random forest regressors have been used to model the wall pressure spectra using data from a direct numerical simulation (DNS) for a compressed flow boundary layer over a flat plate at Mach 2 [98]. The target output for these models is the logarithmic PSD of the pressure fluctuations along points on the surface in the streamwise direction, and the inputs are the logarithmic pressure PSD at points above the surface, as depicted in Figure 3.37.

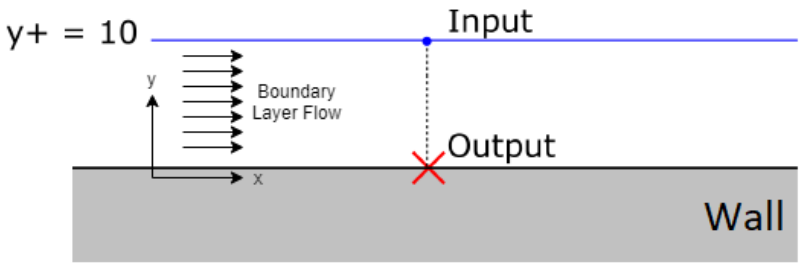

Figure 3.37: A visual depiction of the model inputs and outputs of machine leaning models, with y expressed as percentage of the boundary layer thickness [98].

While the flow conditions and some of the target inputs and outputs of the experiment discussed above differ than those of interest for the current research project, the results were promising in terms of accuracy, suggesting that these black-box models are able to provide improved models for the wall pressure fluctuation properties. Figure 3.38 shows the true PSD obtained by the DNS and used to train the machine learning models and the PSD predicted by the trained random forest regression model structure. It can be seen that the agreement between the observations and the model is high over a wide range of inputs. Overall, the random forest regression yielded better accuracy than the neural networks, however this can be attributed to the fact the dataset used was small (1001 input-output pairs), which makes it difficult to train neural networks since they are prone to over-fitting and converging to local minima [98].

Therefore, it is recommended to evaluate the performance of neural network model structures over larger datasets. In general, these finding give confidence in the ability of machine learning methods to develop highly accurate models for the properties of interest of the wall pressure fluctuations. Therefore, they will be utilized to create the models as part of the research project.

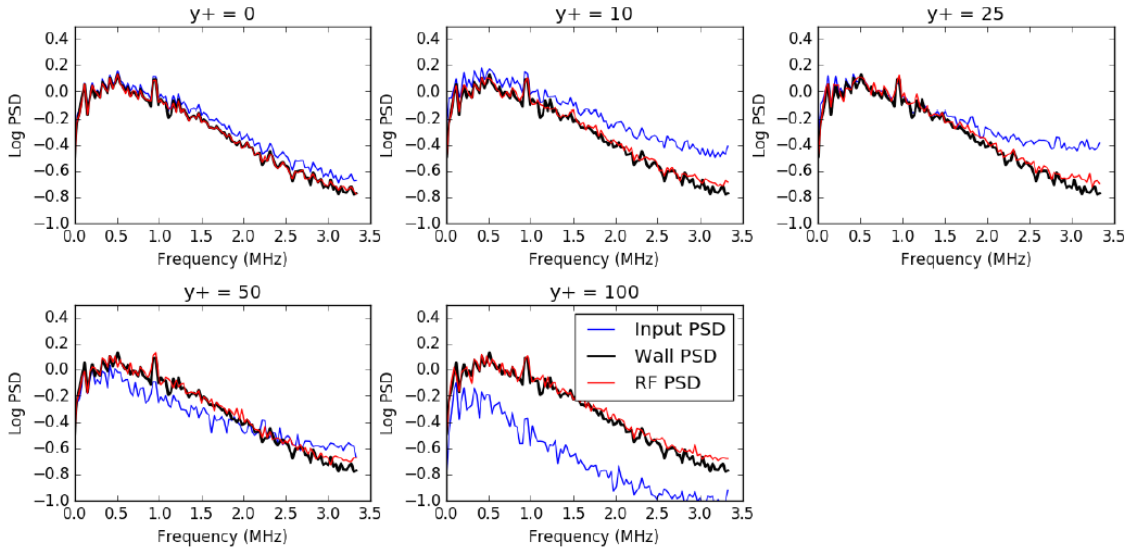

Figure 3.38: The trained random forest regression models for the wall pressure PSD at streamwise location of $x = 66.5\delta_0$ using as input data pressure fluctuations PSDs referring to different distances from the wall. Black lines refer to the PSD obtained from DNS, the red line is the random forest regression model, and the blue line depicts the input PSD [98].

The models relevant for the research project will have two target outputs. The first one will be PSD of the wall pressure fluctuations in the audible frequency range, and the second one will be the mean square pressure. The true PSD will be obtained by performing fast Fourier transform of the microphone signals, while the mean square pressure will be computed via Equation (3.44), where p' will be the pressure difference registered by the microphones. The model inputs will be two as well, the free stream flow velocity (equivalent to the vehicle's airspeed during flight) and the vehicle's angle of attack. The dataset that will be obtained from the experiments that will be conducted as part of the current research project will be much larger than those from previous experiments. This will allow for a better evaluation of the suitability and performance of the neural network model structures for the purposes of modeling the turbulent wall pressure fluctuations. Random forest regression will also be utilized in the current research project as it showed very good performance in previous studies [98]. Furthermore, the machine learning method of support vector machines will also be tested as in general it has similar approximation power as the neural network model structures [97]. In addition, black-box models structures such as radial basis functions, Kriging, Gaussian processes, and splines will be assessed as well due to their proven suitability for non-linear regression [99]. A comparison based on the model error will be used to determine the best resulting models, which in turn will be implemented in the airspeed instrument.

3.3. Conclusions

A literature review was carried out for a research project aimed at developing a novel airspeed instrument targeted at small tailsitter UAVs, whose working principle is to estimate the vehicle's airspeed by relating it to the properties of the sound caused by the hydrodynamic pressure fluctuations that arise from the turbulent flow structures present in the turbulent boundary layer and captured by microphones mounted on the body of the UAV. Due to the innovative nature of the project, the literature review was focused on the fundamental physical principles upon which the instrument will rely in order to estimate the vehicle's airspeed, as well as the methods of measuring, processing and modeling them such that they can be successfully implemented as the working basis of the airspeed instrument.

The literature review that has been carried out first focused on the nature of sounds and boundary layers. It was established that the boundary layer flow experiences hydrodynamic pressure fluctuations which can be perceived as pressure fluctuations caused by a sound wave. However, due to the fact that they propagate at the boundary layer convective velocity, and thus behave differently than the pressure fluctuation caused by an acoustic wave, they are referred to as pseudo-sound. Reviewing the flow structures and pressure fluctuations in the different types of boundary layers determined that the turbulent boundary layer experiences pressure fluctuations of higher magnitude than those found in laminar and even transition boundary layers. Furthermore, due to the higher energy of the turbulent flow, it will be harder for the TBL to separate from the surface compared to the LBL. Therefore, it was decided to mount the airspeed instrument's microphones in regions where the boundary layer will be turbulent. Based on the reviewed literature on experiments utilizing microphones in order to study the characteristics of the TBL pressure fluctuations, it was found that the microphones are best mounted flush such that they provide the most accurate depiction of the fluctuating pressure component and electret condenser microphones were utilized due to their small diameter and protruded shape, making them suitable for flush mounting. However, placing the microphones beneath the turbulent boundary layer introduces limitations in the usability of the instrument. In order to make sure that the boundary layer is turbulent, it is recommended that the instrument is implemented on UAVs that have turbulators installed upstream of the microphones. During the review of boundary layer theory, it was found that separated flows contain structures similar to those found in the attached turbulent boundary layer, however they are of larger scale. As such, the produced pressure fluctuations are of greater magnitude. This presents another limitation in the utilization of the airspeed instrument. Due to the different character of the pressure fluctuations in the separated flow, the instrument will not be able to correctly estimate the vehicle's airspeed based off on their properties. As the main governing factor behind flow separation is the angle of attack of the vehicle, this means that the airspeed instrument will be limited with respect to the angle of attack range over which it can be used. It is noted that a tailsitter UAV takes-off and lands vertically at 90 degrees pitch angle, however, due to the fact that the vehicle moves in the vertical direction during those phases of the flight, the relative motion between the vehicle and the air is also in the vertical axis, meaning that the angle of attack can be treated as if the vehicle was in horizontal flight. This will allow for the instrument to be utilized during these phases of the flight. Lastly, the already existing models that describe the pressure fluctuations at the surface beneath turbulent boundary layers were reviewed and was found that both the magnitude and the spectra of the wall pressure fluctuations are dependent on the free stream flow velocity, which for a UAV in-flight is the airspeed. This confirmed the hypothesis formed after analyzing the on-board footage of the UAV in-flight, namely that the sound signal captured by the microphone is affected by the airspeed of the vehicle, meaning that it is possible to use it as the working basis of an airspeed instrument. However, all of the models have been - at least to some extend - developed using data from practical experiments, thus making them (semi-) empirical. Therefore, different models will be better suited for different flow conditions. Furthermore, the pressure transducers used to take the experimental measurements will also impact the resulting data. As such, using any of the reviewed models will introduce sources of error related to the scaling of the model and to the performance of the pressure transducers used to obtain the dataset upon which the model is based. Therefore, it was decided to develop models of the relation between the wall pressure magnitude and spectra and the free stream velocity based on data gathered by the researcher from both wind tunnel and flight tests, making use of the same microphones and processing techniques as those that will be part of the airspeed instrument on the UAV. Various possible model structures were reviewed and it was decided that a number of them will be constructed in order to find the one yielding the most accurate models for the collected data. Implementing the resulting models in order to estimate the airspeed will impose a limitation on the operationability of the instrument with respect to the vehicle's airspeed, which will be limited by the range of free stream velocities contained in the dataset obtained from the wind tunnel and flight tests that will be carried out as part of the research project and will be used to construct the models.

The major contribution of the proposed research project will be to fill the existing gap for light and accurate airspeed sensors - that have negligible effects on the aerodynamic and performance properties of the vehicle and are able to operate during all flight phases - for small tailsitter UAVs flying in an incompressible flow at airspeed below 25 m/s. Next to that, the research will contribute to the body of knowledge of wall pressure fluctuations beneath turbulent boundary layers by modeling their dependence on free stream velocities in the range of up to 25 m/s, which can be of use for noise control purposes in aerial vehicles flying in an incompressible flow at very low airspeeds. Furthermore, the models will be

developed using machine learning methods, whose application in modeling TBL phenomena is quite limited. Thus, the research project will also be able to contribute to the evaluation of the suitability of machine learning methods for the purposes of modeling the properties and behavior of the pressure fluctuations - caused by the turbulent flow structures - beneath attached turbulent boundary layers of incompressible flows at very low free stream velocities. More specifically, it will be able to better evaluate the performance of neural network model structures in this field as the dataset that will be gathered from the experiments that will be performed as part of the research project will be much larger than the ones used in previous studies. Lastly, a comparison between the machine learning methods and other black-box modeling methods will be carried out, which would be a useful reference for future research taking an entirely empirical approach in modeling the turbulent wall pressure fluctuations.

4

Methodology

In his work, Lighthill [100] established a detailed theoretical basis characterizing the radiated sound field to the medium when turbulent airflow is considered as an acoustic source. However, no such detailed theoretical basis has been developed in literature regarding the sound field properties inside the turbulent airflow itself, and how they are being affected by the flow's velocity. This is mainly due to its highly complex and unpredictable nature, which makes theoretical derivations challenging. Therefore, it will be beneficial to work with data obtained from experiments, instead of making use of existing theoretical approaches.

In order to achieve the research objectives and answer the research questions stated in Subsection 1.1.2, a variety of different research method types will be required. At the early stages of the project, data about the TBL-induced noise's PSD at different flow velocities of interest will need to be collected in order to be able to study the impact of airspeed upon the resulting noise. Barnard [47] went about gathering this type of data - expressing the PSD's magnitude in terms of the SPL - for the purposes of studying the effect of various microphone accessories aimed at reducing the noise due to airflow pressure. This was done by performing wind tunnel experiments. A turbulence generator, in the form of wires, was used to make the airflow in the wind tunnel chamber turbulent. Then, microphones immersed in the airflow together with surface mounted ones on the sides of the wind tunnel's chamber were used to take measurements of the SPL. Airflow velocities of up to 25 m/s were tested, and the results showed that the overall SPL increases, over the complete frequency range, as the airflow velocity increases. Similarly, Yokoi [48] carried out sound measurements of non-disturbed airflow in a wind tunnel test section, using surface mounted microphones on the chamber's walls, which allowed the microphones to also capture noise due to the formed TBL. Airflow velocities of up to 28 m/s were tested and they also indicated that the overall SPL increases as the airflow speed increases. Thus, as first step in the research project, wind tunnel experiments will be performed, placing an UAV with surface mounted microphones at different locations on its body and recording the measurements at various airflow speeds, simulating the vehicle's airspeed during flight. Multiple experimental runs will be performed for different microphone mounting locations, as well as different angles of attack of the UAV.

However, this setup is not representable of an actual flight, as neither motors and propellers noise is present, nor random sounds from the environment, that all will contribute to the PSD of microphones' recordings. Therefore, to gather real world measurements, flight experiments will need to be conducted, which is a standard practice in the MAVLab when having to obtain data of interest. The flight experiments will consist of a piloted flight, at various airspeeds but same altitude. Wind and gusts affect the vehicle's airspeed, meaning there will be an impact on the TBL-induced noise captured by microphones. Therefore, it will be beneficial to have a wind vane and anemometer present at the location where the flights will be performed in order to gather wind data.

Once measurements have been collected, both from the wind tunnel and the flight experiments, the data needs to be analyzed and processed. First, the data needs to be analyzed statistically, making sure that it is of high quality, meaning there are no outliers and/or bias present. However, when it comes to the flight data, outliers could result from the vehicle encountering environmental sounds captured by the microphones. Therefore, the data needs to be processed, such that the TBL-induced noise is isolated from the any other sounds recorded by the microphones. Since the interest of the current research lies in the noise signal, traditional noise filtering techniques, such as summarized by Shraddha et al. [101],

would be of little practical use. When it comes to the wind tunnel data, the only contributing factors to the TBL-induced noise will be the noise due to the wind tunnel operation, its resonant behavior at specific frequencies [47] and any echoes reflected by the walls of the facility, but the latter could be completely avoided if anechoic wind tunnel is used for conducting the experiments. Typically, both the operational noise level and the resonant frequencies are known for a wind tunnel facility, and as such they can be directly accounted for in the obtained data measurements. The flight data, on the other hand, will contain sounds from the environment that cannot always be known or predicted. Furthermore, as the goal is to be able to implement the instrument on a wide range of vehicles, their motors and propellers - and subsequently their noise characteristics - will differ. As such, a signal filtering algorithm will be needed. It is also important to keep in mind that this algorithm will need to be of sufficiently low computational load, such that it can be used in real-time during flight. Gabrea et al. [102] has proposed a method for Adaptive Noise Cancellation (ANC) using adaptive Kalman filtering that does not require noise variance estimation. Its goal is to retrieve a speech signal that exists within noisy observations, captured by a microphone. This approach could prove viable for the current research, as it can be modified such that the noise due to the TBL is the desired signal to be retrieved, while every other sound is treated as part of the noisy observation. By completing the steps above, the first research sub-question posed in Subsection 1.1.2 will be answered.

The second research sub-question will be answered by looking at the PSD of the microphones' recordings gathered during the experimental phase of the research and analyzing how its magnitude changes with the angle of attack. This parameter could also be implemented in the models as a separate input in order to determine its impact on the airspeed prediction accuracy. Similarly, the next research sub-question will be answered by looking at the PSD of recordings of microphones mounted at different locations on the vehicle's body. Additionally, the expected regime of the boundary layer over different parts of the vehicle's surface could be predicted using the theory explained in Subsection 3.2.2, thus allowing to form an expectation for the PSD function of a recording of a microphone mounted on a particular location on the vehicle's body.

The next step in the research work will be the instrument integration. This refers to both hardware integration, meaning physically connecting the components that will constitute the instrument via a bus, and software integration, meaning making sure that the components can communicate to the other hardware connected to the bus, as well as that the instrument can feed data to the flight control computer. Software integration will also include the implementation of the signal acquisition program, and later on the filtering algorithm and constructed model, in the instrument. The exact methods to carry out the integration will depend on the selected components. Once they are finalized, desk research will be carried out to determine the most appropriate integration techniques and tools. As such, the last two research sub-questions posed in Subsection 1.1.2 will be answered. After the instrument is integrated, it needs to be tested. This will be done by conducting an actual flight test.

At the same time, models will be constructed that will serve as the instrument's basis for estimating the airspeed. As discussed in Chapter 3, black-box models will be utilized in order to model the relation between the airspeed and the TBL-induced noise's PSD. This includes training model structures such as artificial neural networks. At the same time, surrogate modeling techniques could also be explored, since the models are to be created with a data-driven approach. Surrogate models are defined as mimicking the behavior of a real system, or simulation model, as closely as possible, while having lower computational load [103]. As such, they can be of any model structure suitable for regression. Typically, the models are constructed based on the response of a simulation, or real system, to a number of selected data points. However, they can also be built using preexisting datasets that contain input-output data, much like those obtained from the experiments conducted at the starting phase of the research project. Gorissen et al. [99] have developed a dedicated surrogate modeling and adaptive sampling toolbox written for MATLAB© that is freely licensed for pure academic research purposes. It lets the user select any of the available model structures, optimization algorithms and initial/sequential designs, as well as to provide a dataset from which data will be sampled to construct the selected model, thus alleviating the need for coding all the different model structures, optimization algorithms, and data sampling designs of interest. As a result, many different (combinations of) modeling techniques can be tested within a short period of time. This is beneficial, since computer experiments will need to be carried out in order to determine the best modeling techniques. This will allow to answer the main research question posed in Subsection 1.1.2. Using a dedicated software tool will greatly reduce the time needed to evaluate different modeling methods, allowing to keep the research schedule within reasonable time frame.

Part III

Additional Results

5

Experimental Data: Wind Tunnel

This chapter depicts the PSDs of the microphones' recordings collected during the wind tunnel experiments. Section 5.1 shows the PSDs of both the left- and right-mounted microphones' signals, with Subsection 5.1.1 providing PSD plots of changing airspeed for fixed AoA value and motor configuration and Subsection 5.1.2 depicting PSD plots of changing AoA for fixed airspeed and motor configuration. Section 5.2 shows the PSDs of the subtracted microphones' signals. The subsections are organized in the same manner as for Section 5.1, with Subsection 5.2.1 organizing the PSDs for changing airspeed for fixed AoA value and motor configuration and Subsection 5.2.2 - for changing AoA for fixed airspeed and motor configuration. All PSDs are estimated using Welch's method. The wind tunnel data provides clear data from a controlled environment, making them more suitable to study the effects of the airspeed and the angle of attack upon the characteristics of the microphones' signals PSDs.

5.1. Signals from the Microphones

The PSDs provided in this section are for the complete duration of the microphone recordings, taken for both the left- and right-mounted microphones, having a length of 15 seconds. The signals are passed through a high-pass filter with a cut-off frequency of 250 Hz. The magnitude of the PSD plots is expressed in dB SPL, meaning that the raw microphones' voltage signals are converter to pressure measurements using the microphones' sensitivity.

5.1.1. Power Spectral Densities for Changing Airspeed

The PSD plots depicted in this subsection provide a better understanding of the effects of the airspeed upon the estimated PSDs. The figures are organized in the following manner, Figure 5.1 to Figure 5.10 show the PSD plots for changing airspeed over all angles of attack tested for motor configuration D, Figure 5.11 to Figure 5.20 depict this for motor configuration M, and finally Figure 5.21 to Figure 5.30 provide the PSD plots corresponding to motor configuration R. Looking at the plots, it is observed that the peak at 1.5 kHz present in the PSD plots for motor configuration R is absent from the PSD plots corresponding to motor configurations D and M. As such, it can be concluded that this peak is caused by the motors of the vehicle. At the same time, the peaks at around 3 kHz, 4 kHz, 5 kHz, 6 kHz, 7 kHz, 8 kHz and 9 kHz can be seen in the PSD plots across all motor configurations, meaning that they are most likely harmonics of the 50 Hz component dominating the wind tunnel microphone data. Overall, as the airspeed increases, so does the power of the signals, especially in the lower frequency ranges. Furthermore, the decay rate is greater for higher airspeeds. For angles of attack of 45^o-60^o and higher, the effects of changing airspeed are less pronounced, which could be attributed to the formation of an area of lower pressure over the top side of the vehicle's nose cone [104, 105].

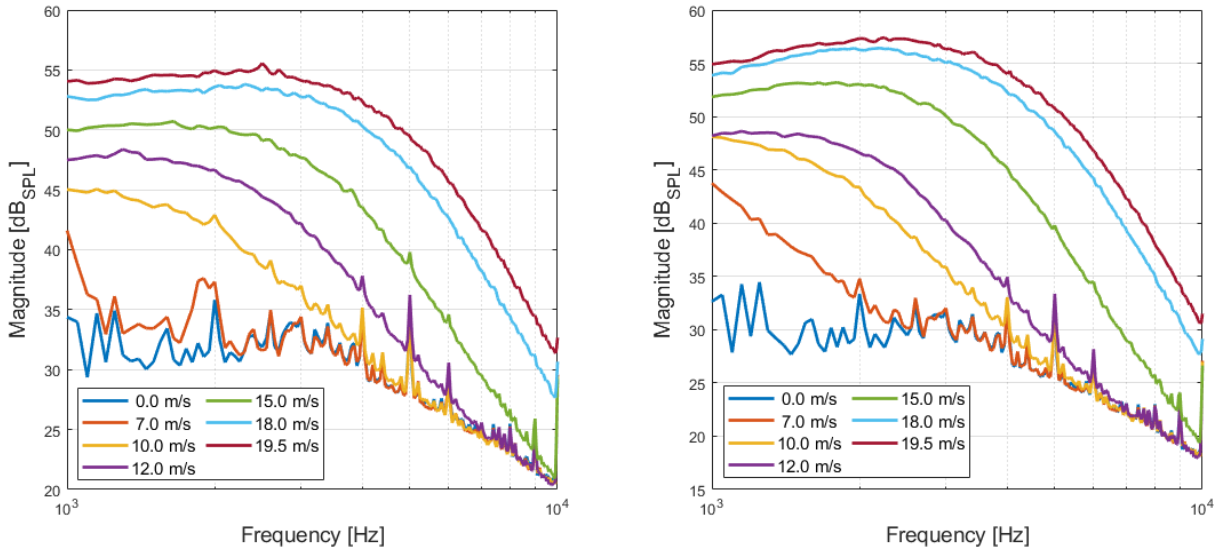

Figure 5.1: PSDs for left-mounted (left plot) and right-mounted (right plot) microphones for AoA = 0º and motor configuration - D.

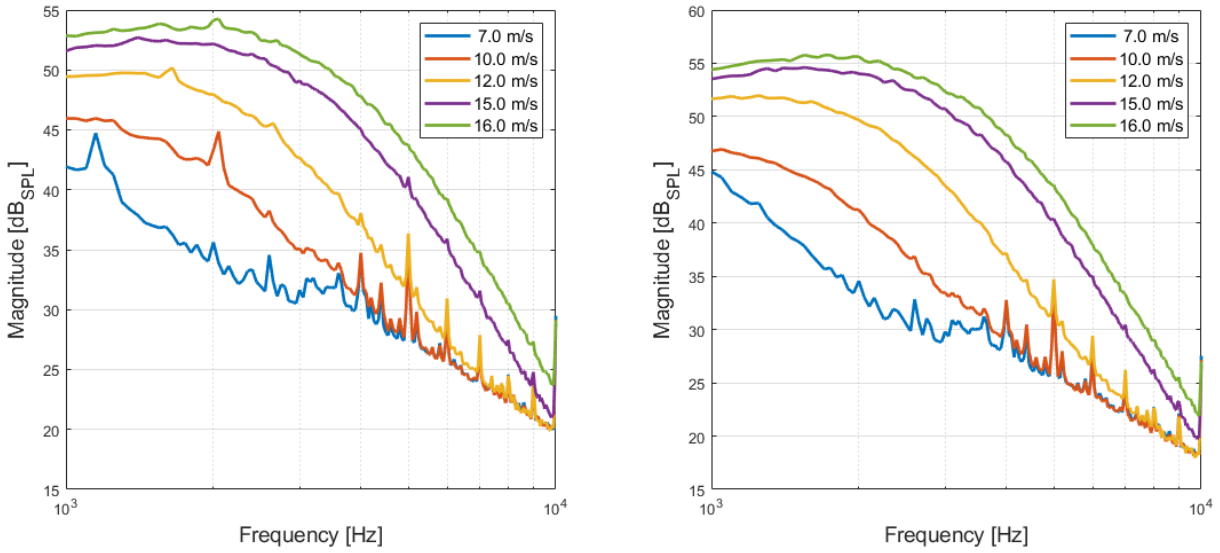

Figure 5.2: PSDs for left-mounted (left plot) and right-mounted (right plot) microphones for AoA = 5º and motor configuration - D.

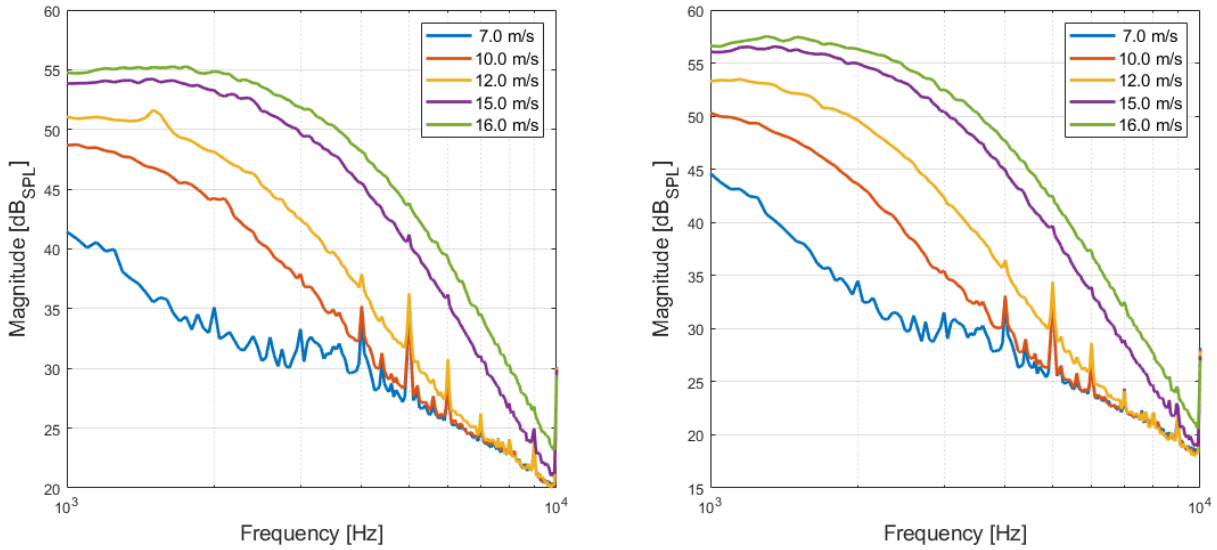

Figure 5.3: PSDs for left-mounted (left plot) and right-mounted (right plot) microphones for AoA = 10^o and motor configuration - D.

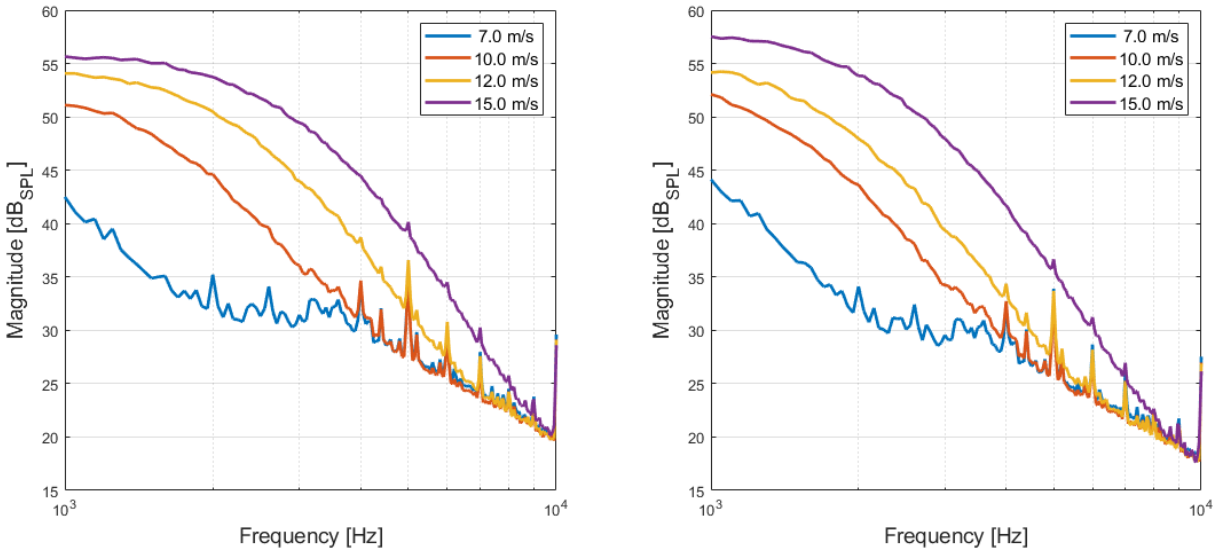

Figure 5.4: PSDs for left-mounted (left plot) and right-mounted (right plot) microphones for AoA = 15^o and motor configuration - D.

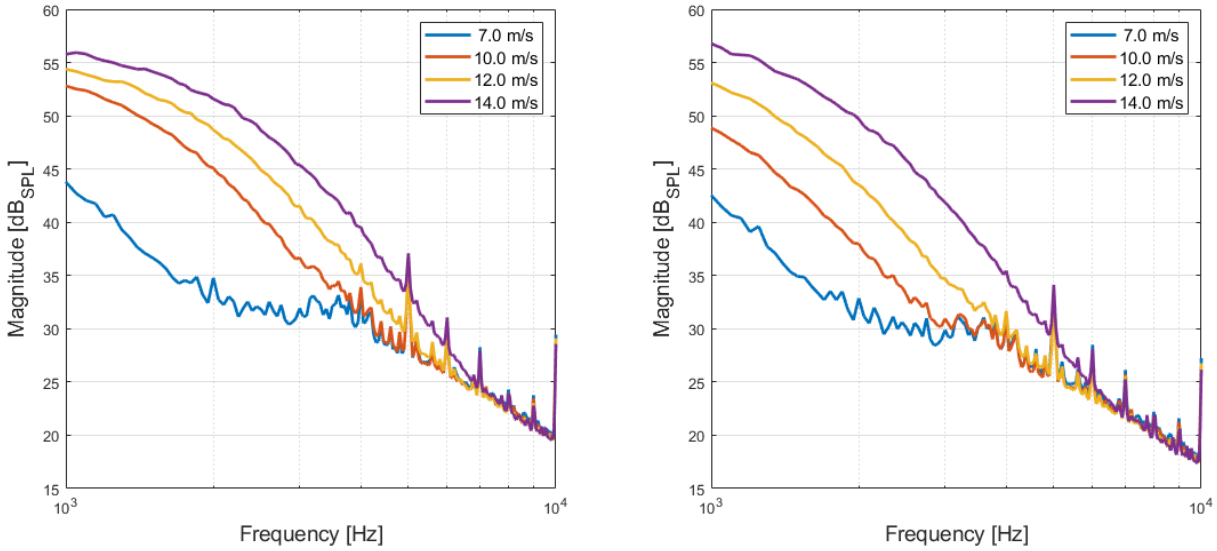

Figure 5.5: PSDs for left-mounted (left plot) and right-mounted (right plot) microphones for AoA = 20^o and motor configuration - D.

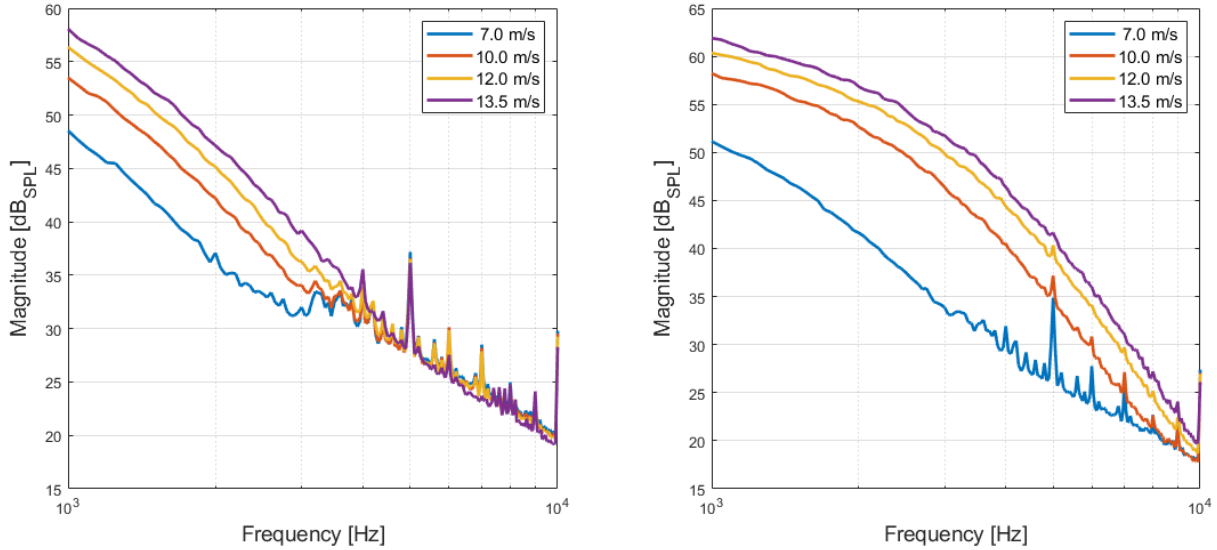

Figure 5.6: PSDs for left-mounted (left plot) and right-mounted (right plot) microphones for AoA = 30^o and motor configuration - D.

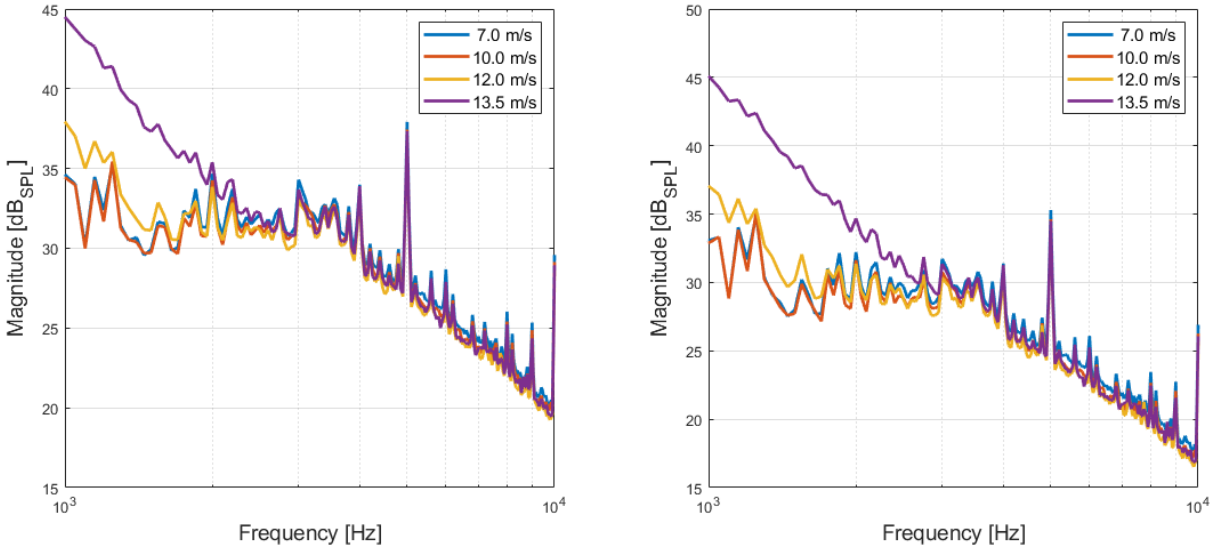

Figure 5.7: PSDs for left-mounted (left plot) and right-mounted (right plot) microphones for AoA = 45^o and motor configuration - D.

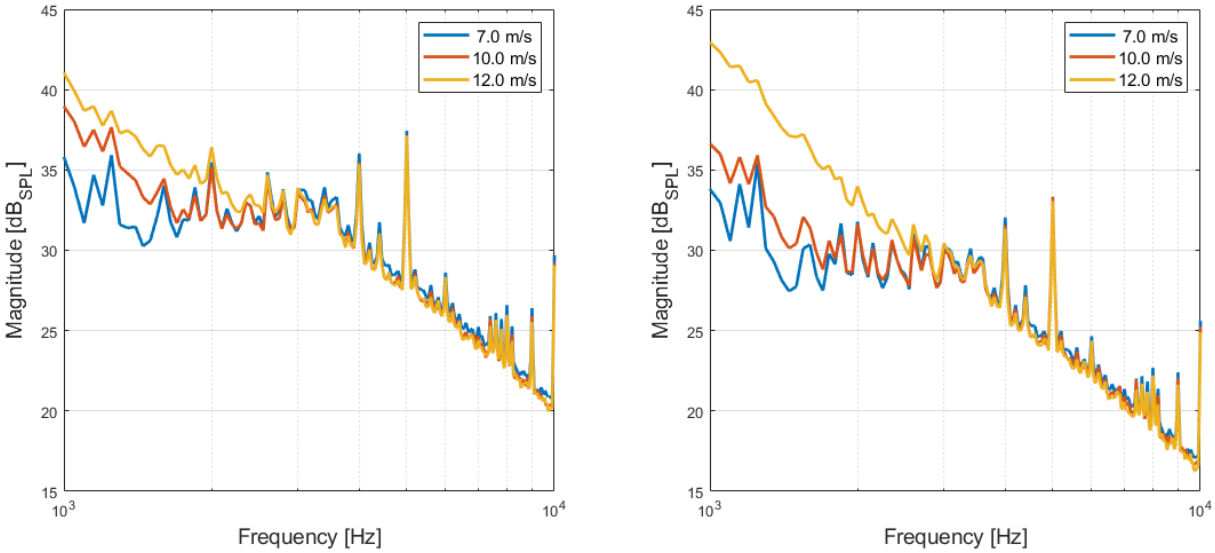

Figure 5.8: PSDs for left-mounted (left plot) and right-mounted (right plot) microphones for AoA = 60^o and motor configuration - D.

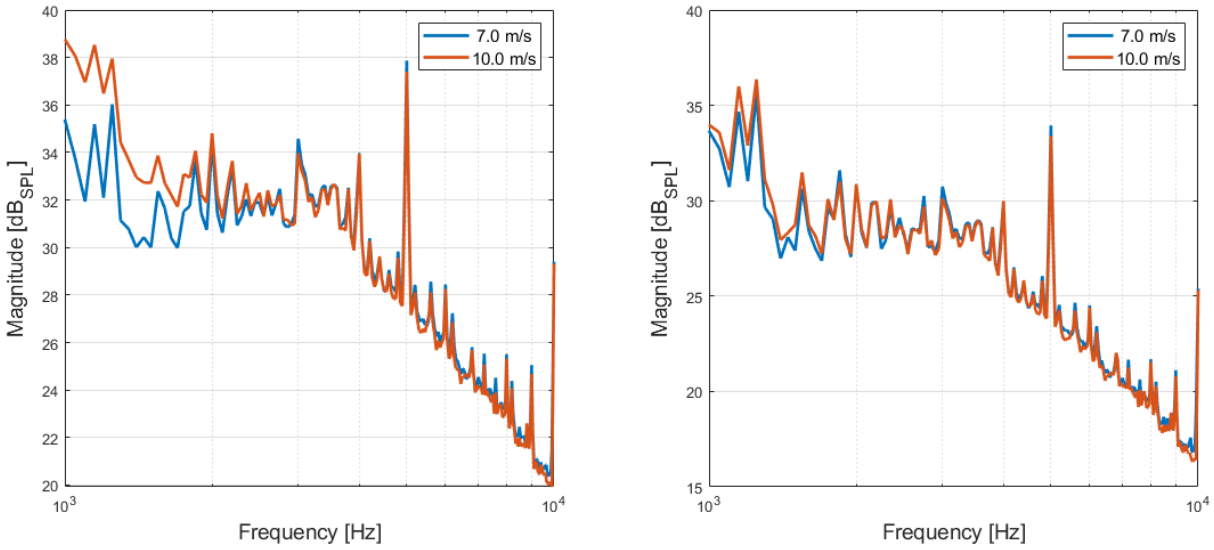

Figure 5.9: PSDs for left-mounted (left plot) and right-mounted (right plot) microphones for AoA = 75º and motor configuration - D.

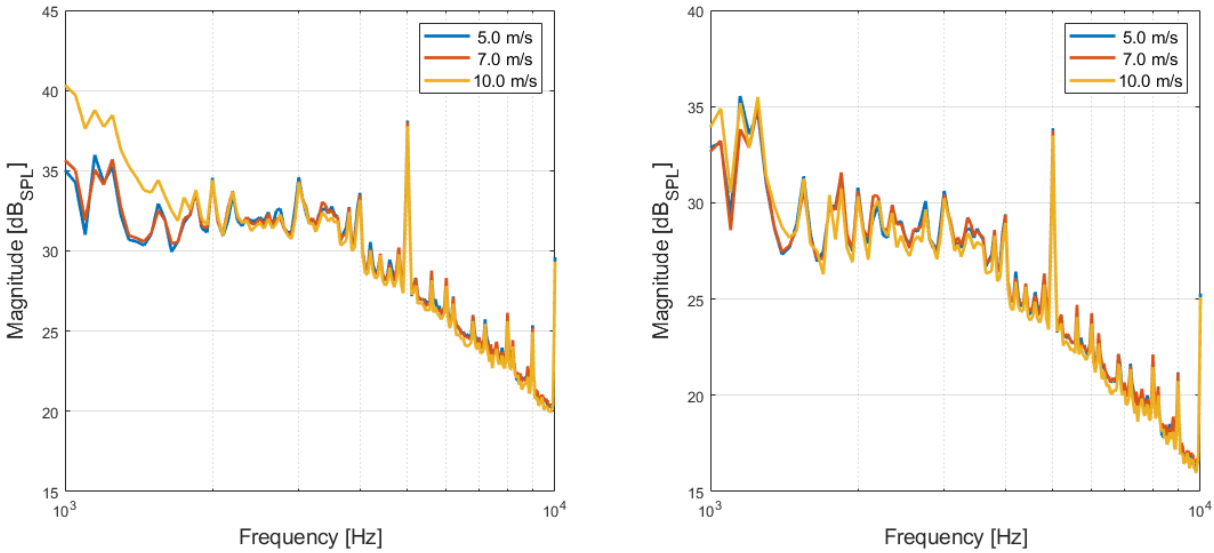

Figure 5.10: PSDs for left-mounted (left plot) and right-mounted (right plot) microphones for AoA = 90º and motor configuration - D.

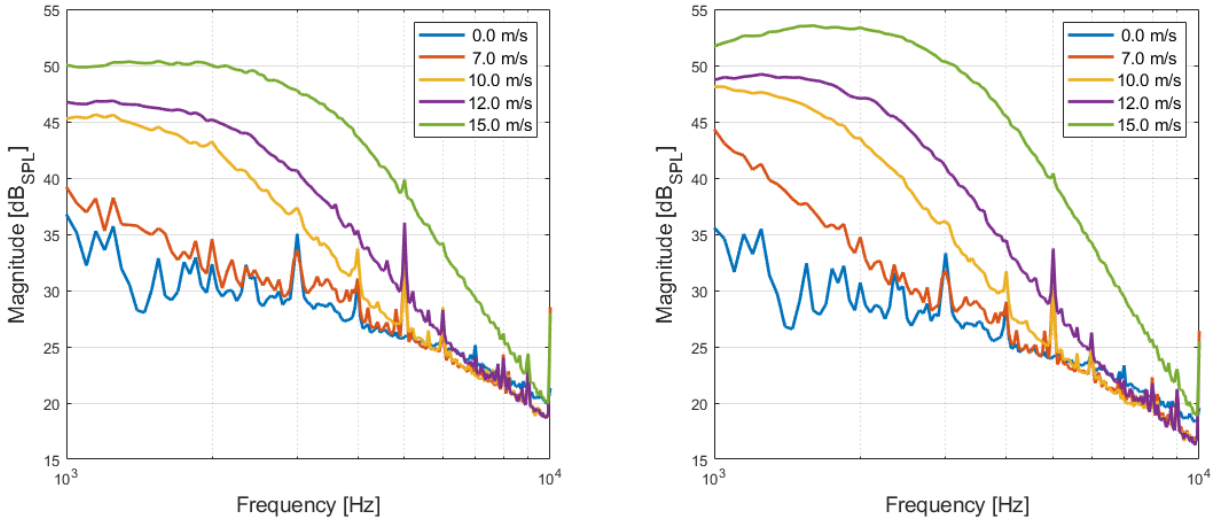

Figure 5.11: PSDs for left-mounted (left plot) and right-mounted (right plot) microphones for AoA = 0^o and motor configuration - M.

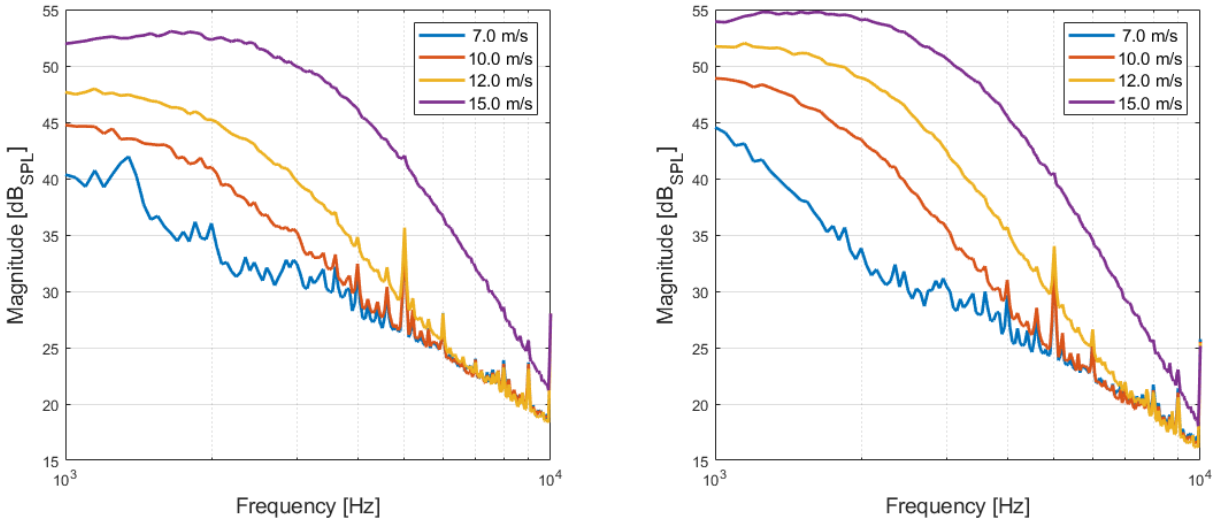

Figure 5.12: PSDs for left-mounted (left plot) and right-mounted (right plot) microphones for AoA = 5^o and motor configuration - M.

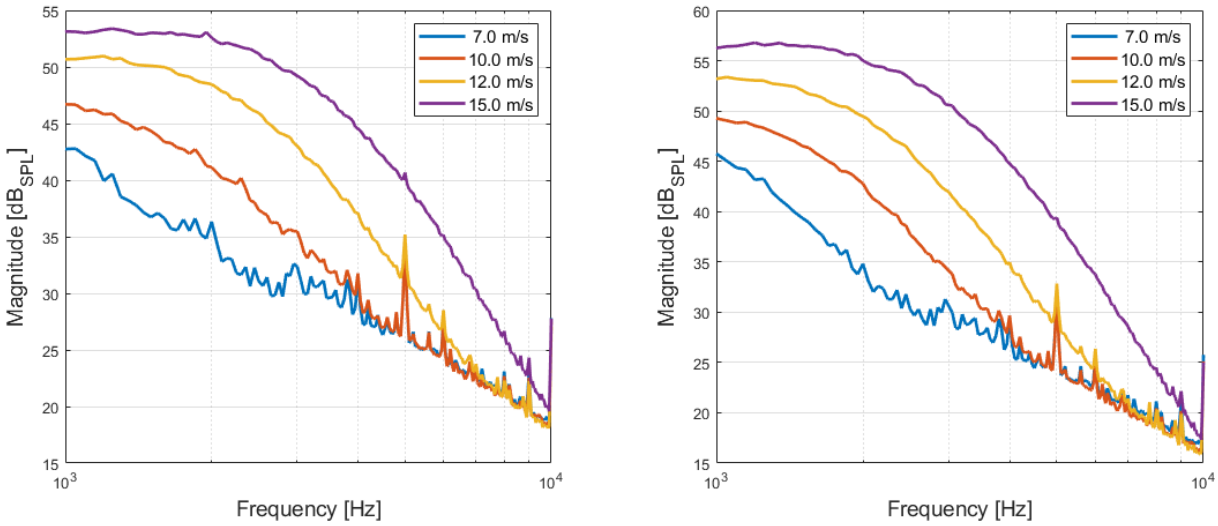

Figure 5.13: PSDs for left-mounted (left plot) and right-mounted (right plot) microphones for AoA = 10^o and motor configuration - M.

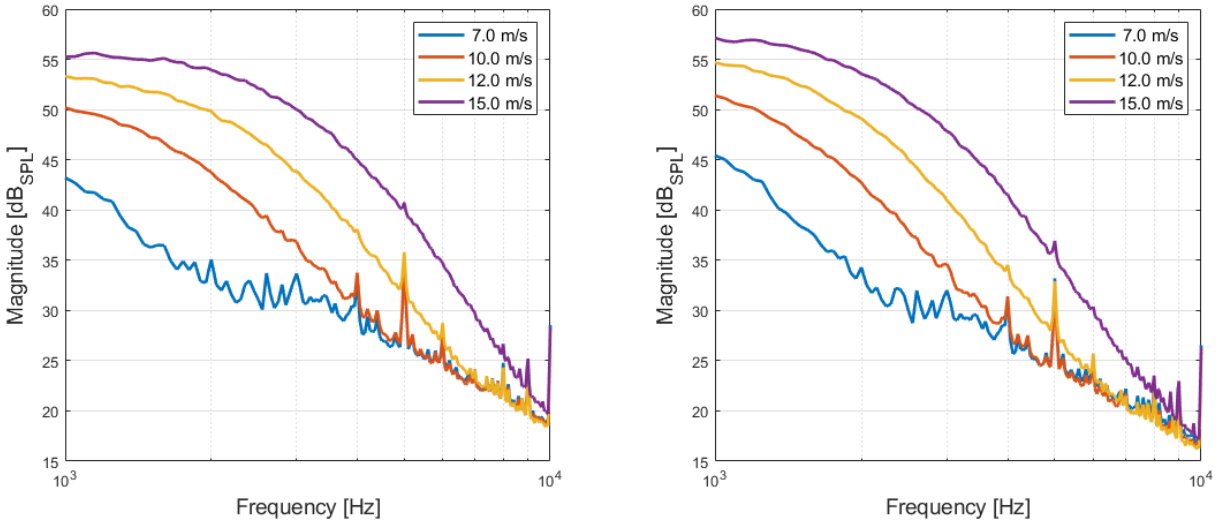

Figure 5.14: PSDs for left-mounted (left plot) and right-mounted (right plot) microphones for AoA = 15^o and motor configuration - M.

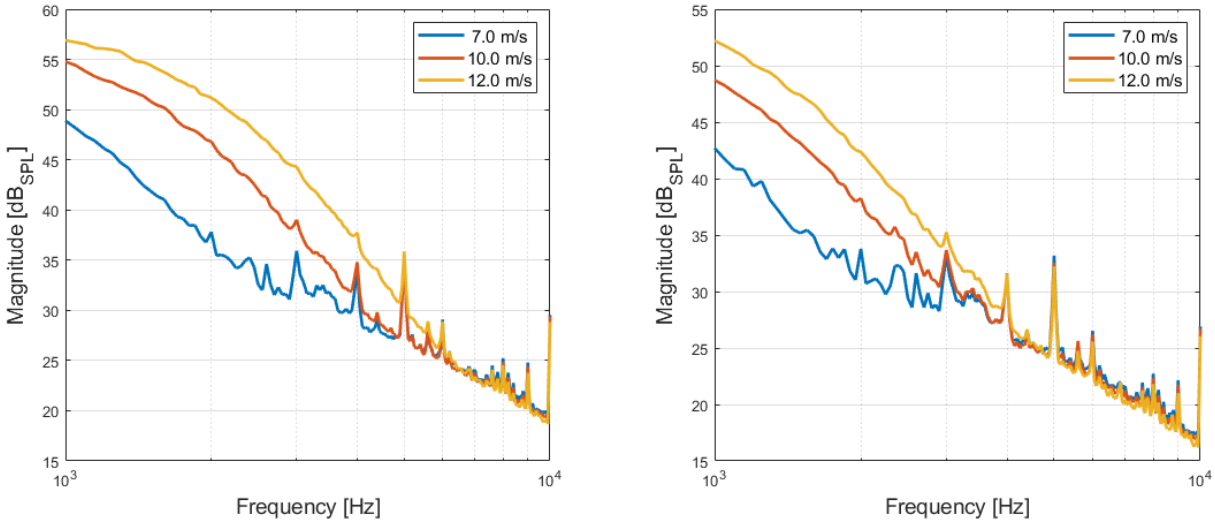

Figure 5.15: PSDs for left-mounted (left plot) and right-mounted (right plot) microphones for AoA = 20^{o} and motor configuration - M.

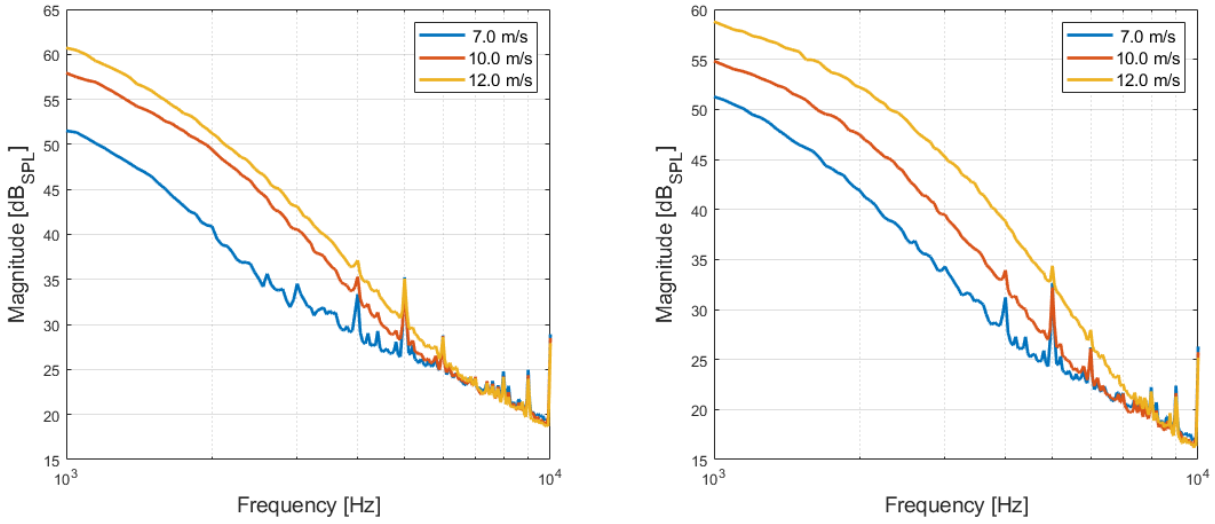

Figure 5.16: PSDs for left-mounted (left plot) and right-mounted (right plot) microphones for AoA = 30^{o} and motor configuration - M.

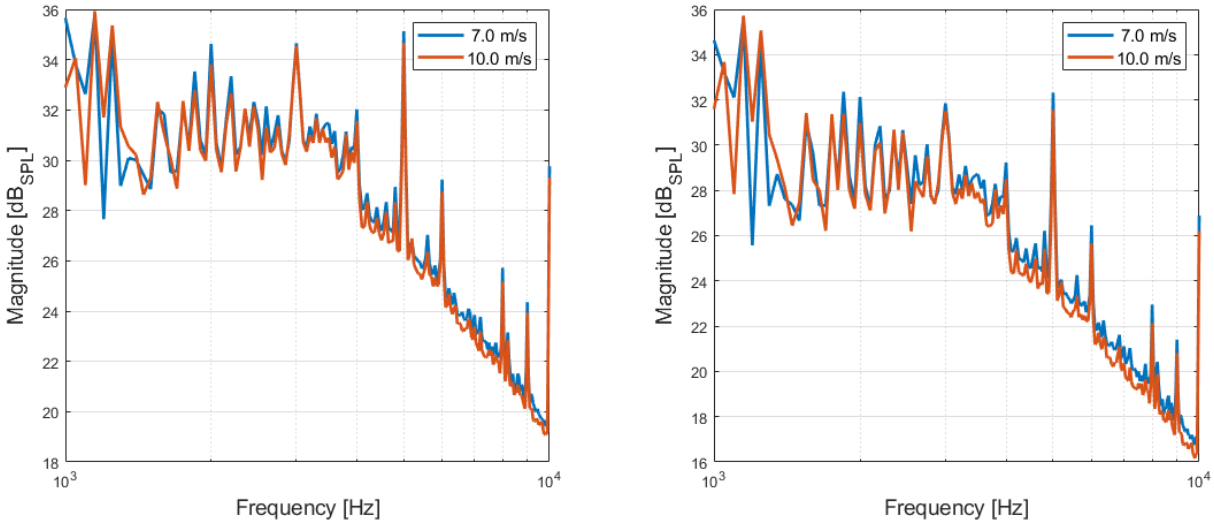

Figure 5.17: PSDs for left-mounted (left plot) and right-mounted (right plot) microphones for AoA = 45^{o} and motor configuration - M.

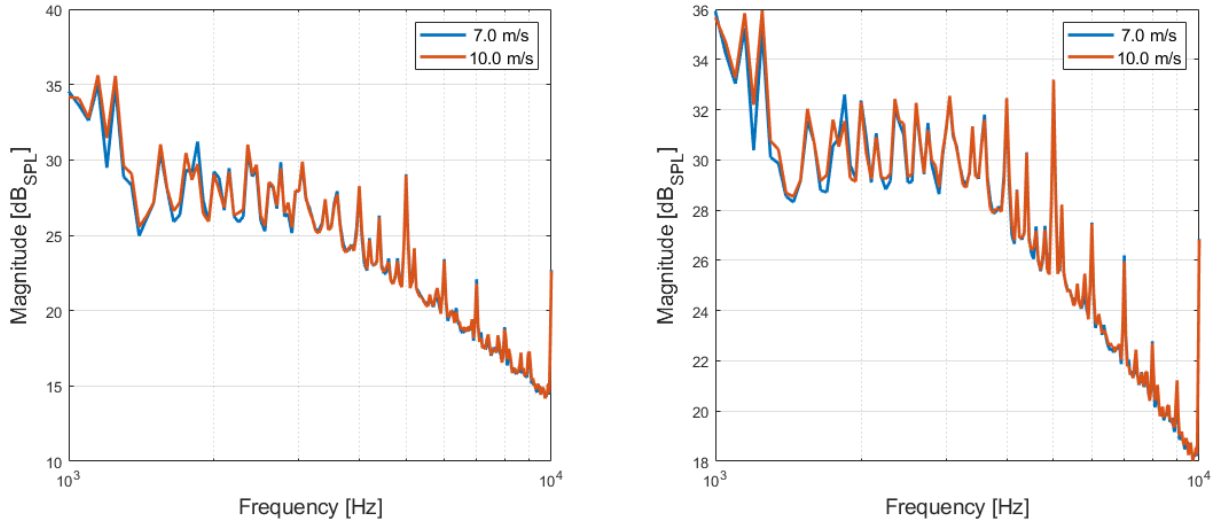

Figure 5.18: PSDs for left-mounted (left plot) and right-mounted (right plot) microphones for AoA = 60^{o} and motor configuration - M.

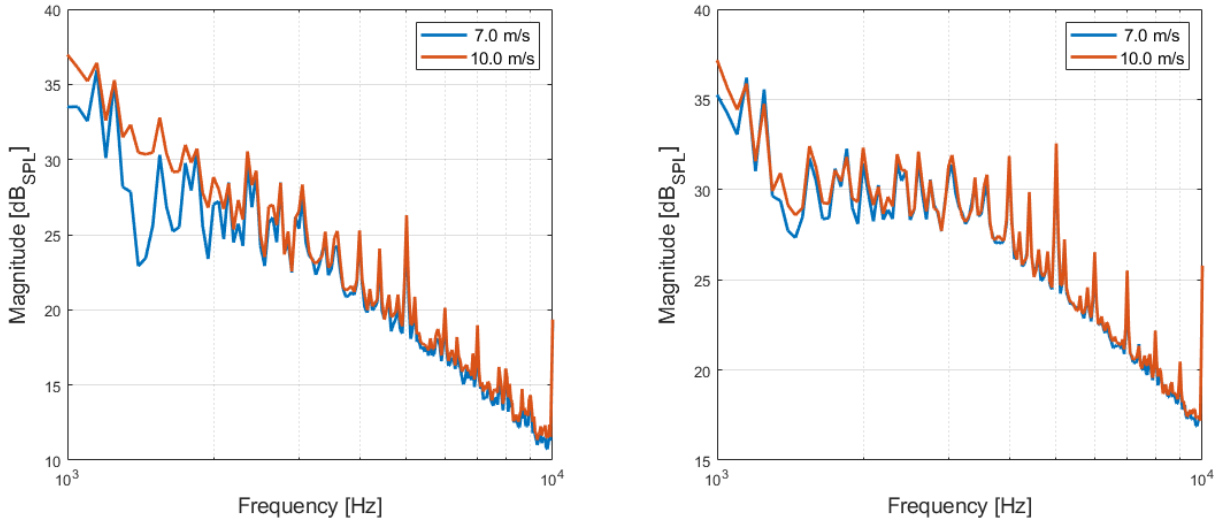

Figure 5.19: PSDs for left-mounted (left plot) and right-mounted (right plot) microphones for AoA = 75^{o} and motor configuration - M.

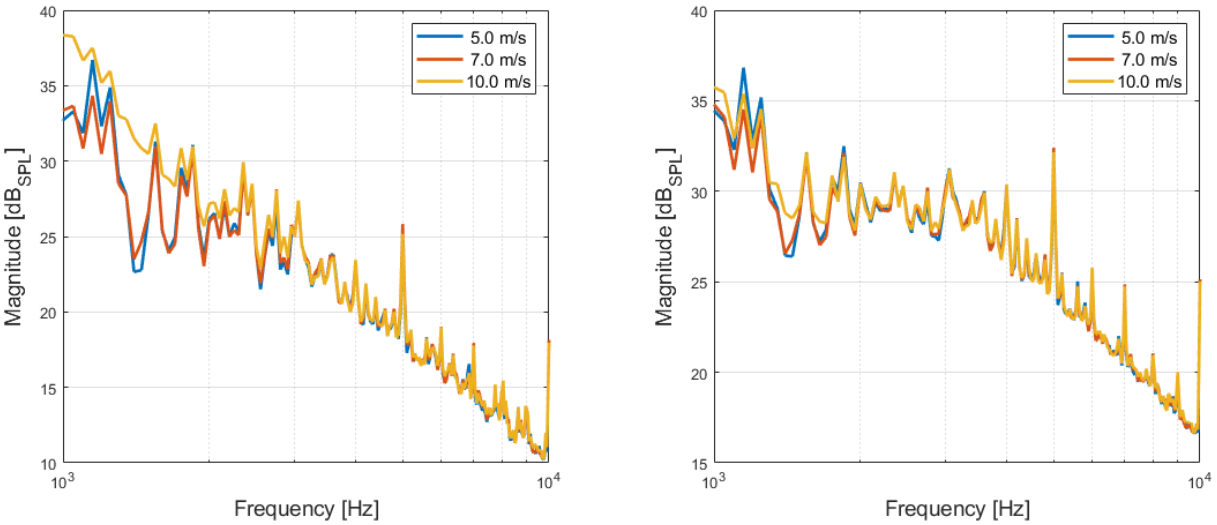

Figure 5.20: PSDs for left-mounted (left plot) and right-mounted (right plot) microphones for AoA = 90^{o} and motor configuration - M.

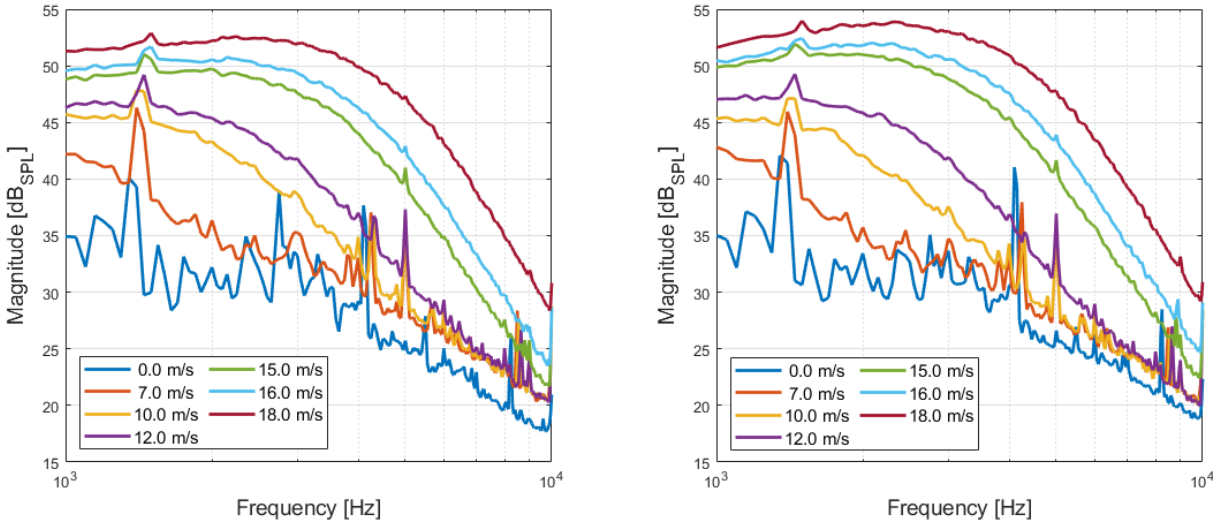

Figure 5.21: PSDs for left-mounted (left plot) and right-mounted (right plot) microphones for AoA = 0^o and motor configuration - R.

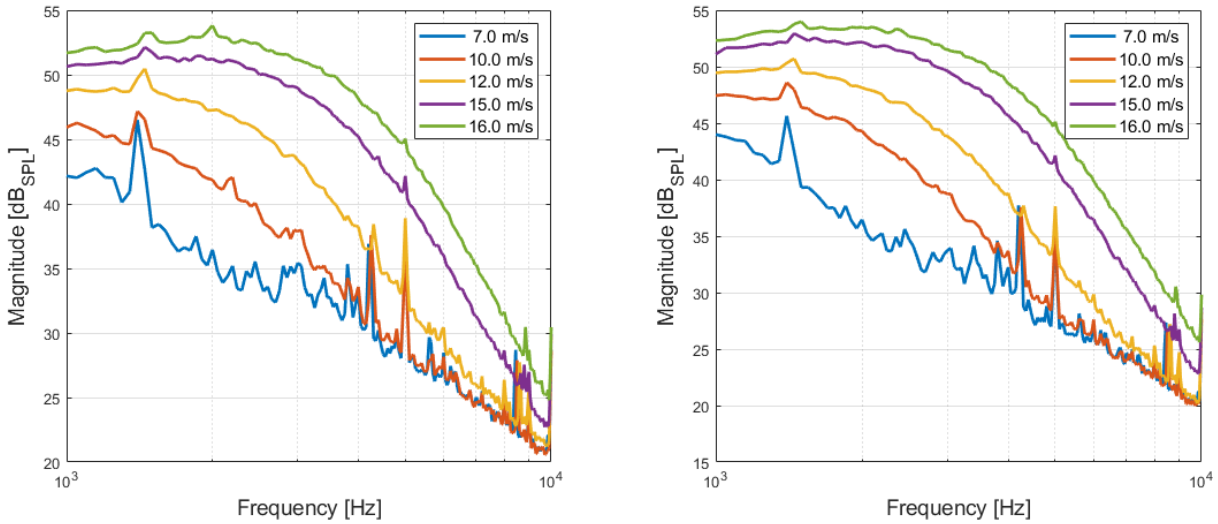

Figure 5.22: PSDs for left-mounted (left plot) and right-mounted (right plot) microphones for AoA = 5^o and motor configuration - R.

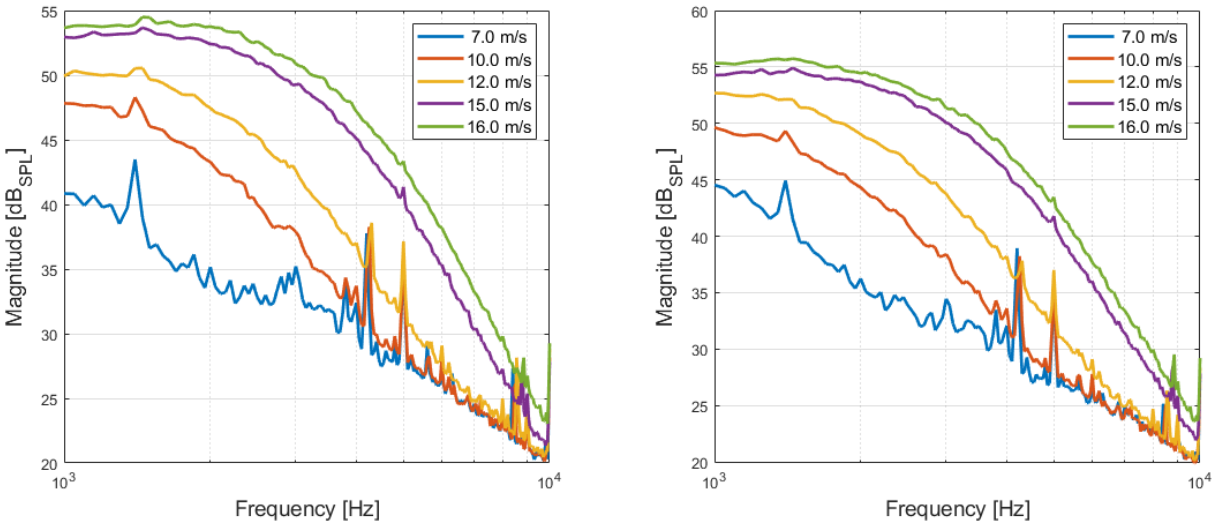

Figure 5.23: PSDs for left-mounted (left plot) and right-mounted (right plot) microphones for AoA = 10º and motor configuration - R.

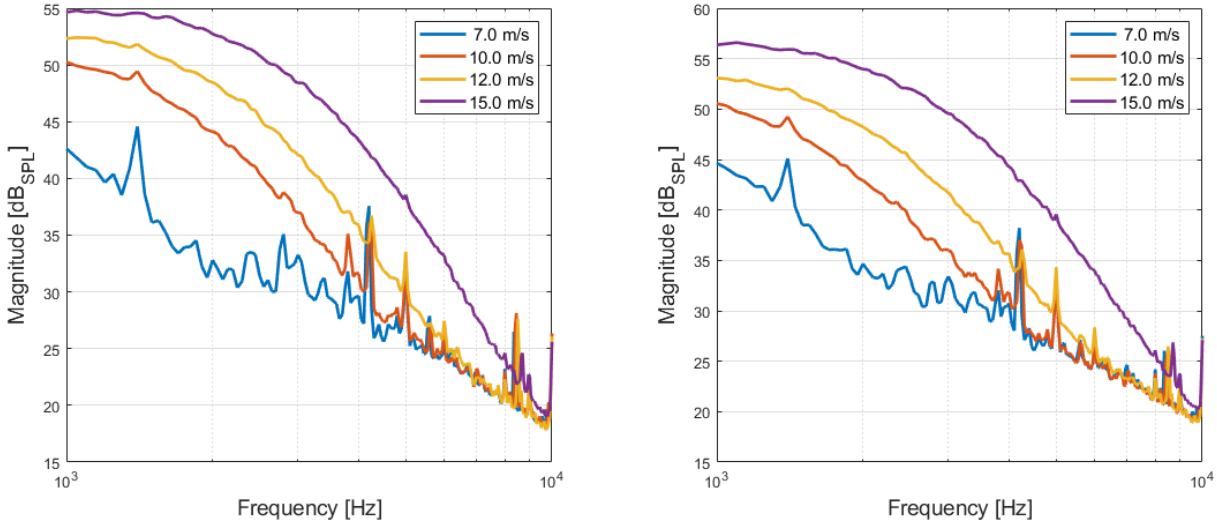

Figure 5.24: PSDs for left-mounted (left plot) and right-mounted (right plot) microphones for AoA = 15º and motor configuration - R.

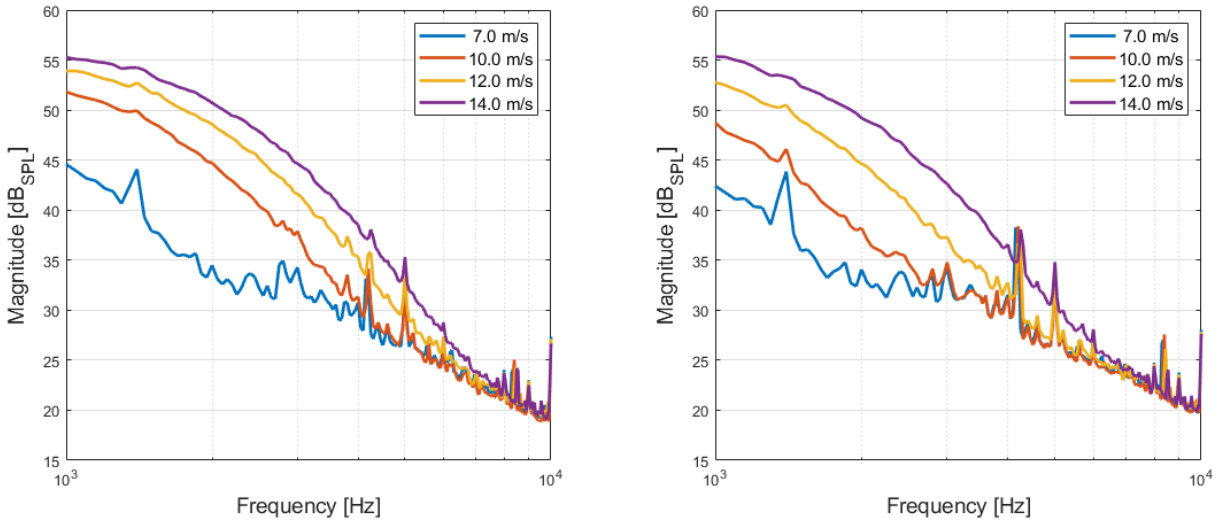

Figure 5.25: PSDs for left-mounted (left plot) and right-mounted (right plot) microphones for AoA = 20^o and motor configuration - R.

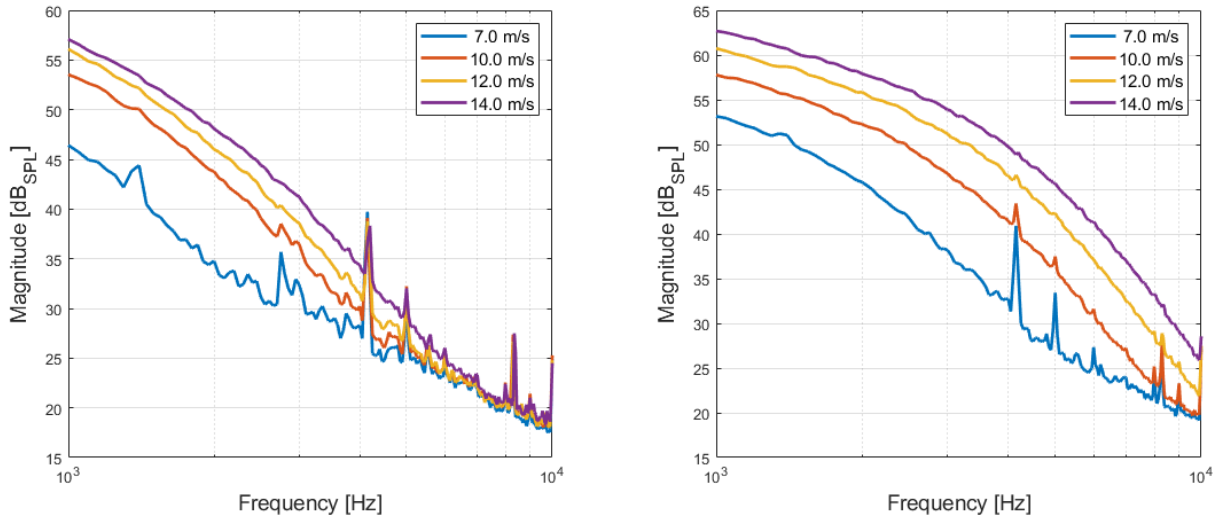

Figure 5.26: PSDs for left-mounted (left plot) and right-mounted (right plot) microphones for AoA = 30^o and motor configuration - R.

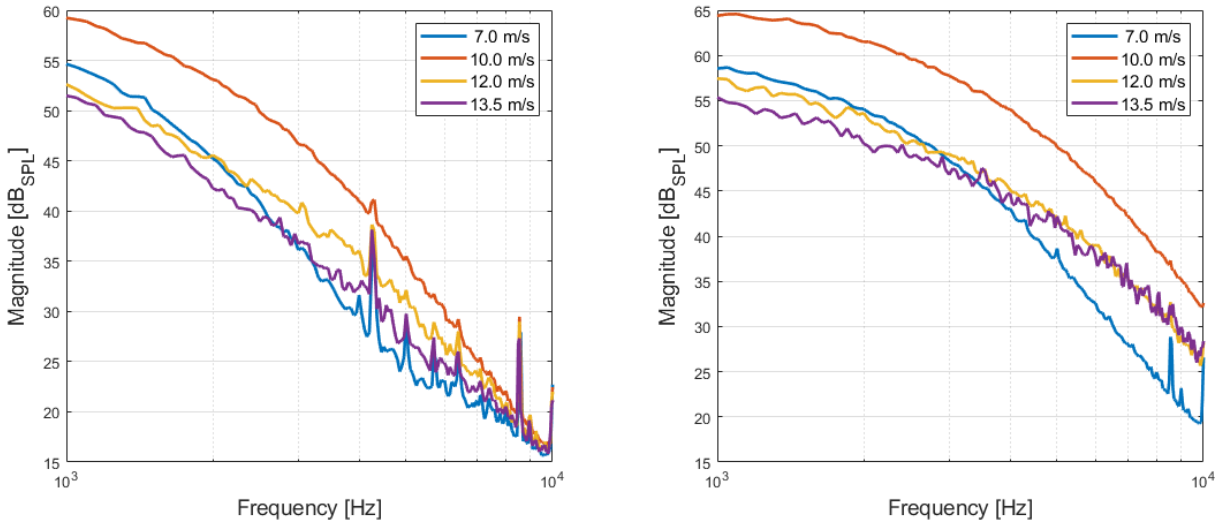

Figure 5.27: PSDs for left-mounted (left plot) and right-mounted (right plot) microphones for AoA = 45º and motor configuration - R.

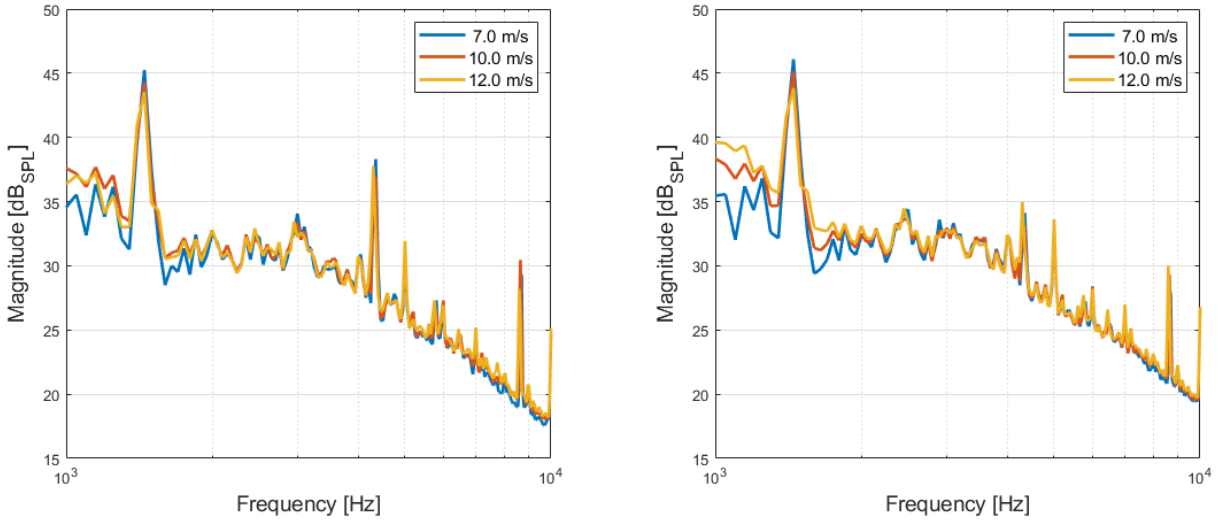

Figure 5.28: PSDs for left-mounted (left plot) and right-mounted (right plot) microphones for AoA = 60º and motor configuration - R.

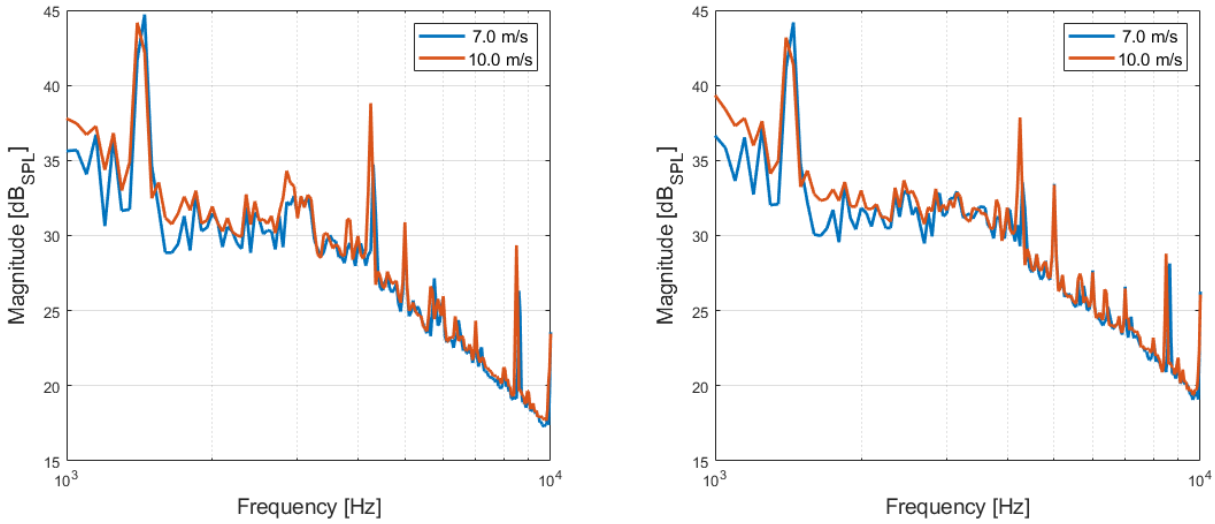

Figure 5.29: PSDs for left-mounted (left plot) and right-mounted (right plot) microphones for AoA = 75^{o} and motor configuration - R.

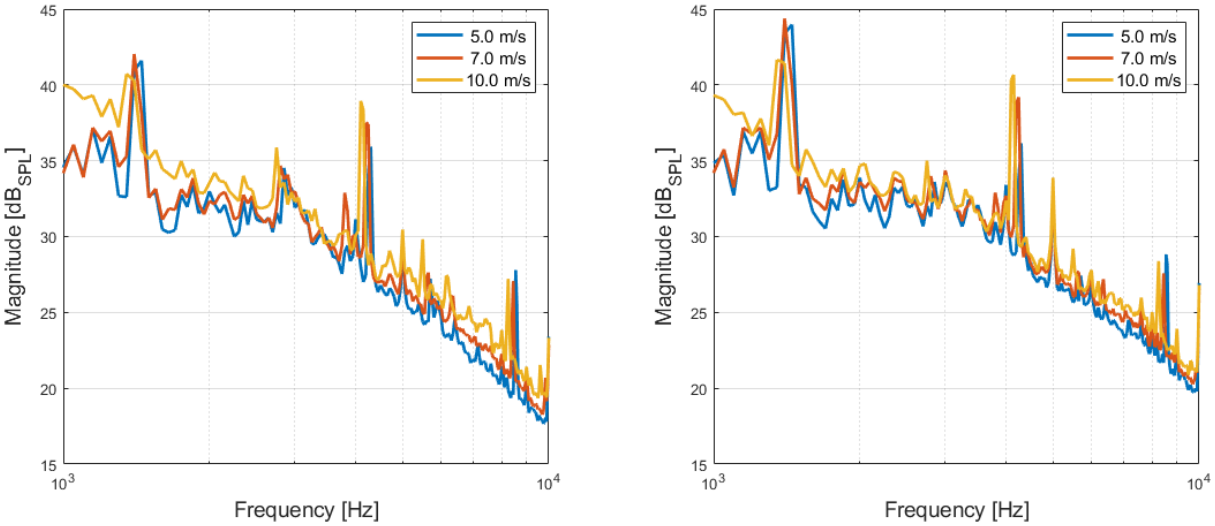

Figure 5.30: PSDs for left-mounted (left plot) and right-mounted (right plot) microphones for AoA = 90^{o} and motor configuration - R.

5.1.2. Power Spectral Densities for Changing Angle of Attack

The PSD plots depicted in this subsection provide a better understanding of the effects of the AoA upon the PSD characteristics of the TBL-induced hydrodynamic pressure fluctuations, which relates to one of the research questions posed in Subsection 1.1.2. Inspecting the figures in this subsection serves as a basis to reflect on said research question in Section 6.1. The figures are grouped together according to the motor configuration with Figure 5.31 to Figure 5.34 showing the PSD plots for all AoA at airspeed from 7 m/s to 15 m/s and motor configuration D, Figure 5.35 to Figure 5.38 depicting this for motor configuration M, and Figure 5.39 to Figure 5.42 - for motor configuration R.

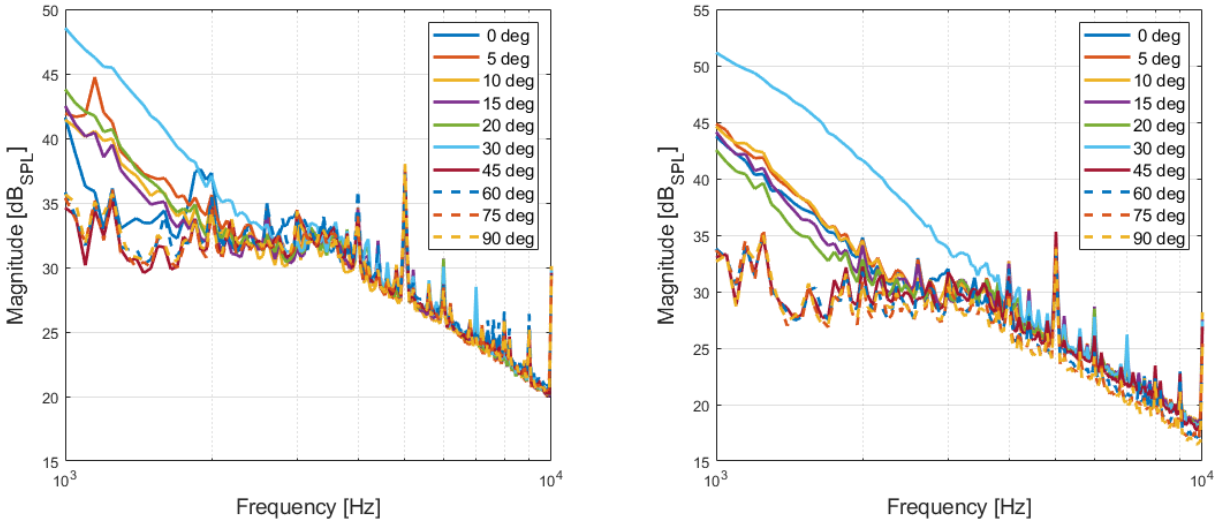

Figure 5.31: PSDs for left-mounted (left plot) and right-mounted (right plot) microphones for Airspeed = 7 m/s and motor configuration - D.

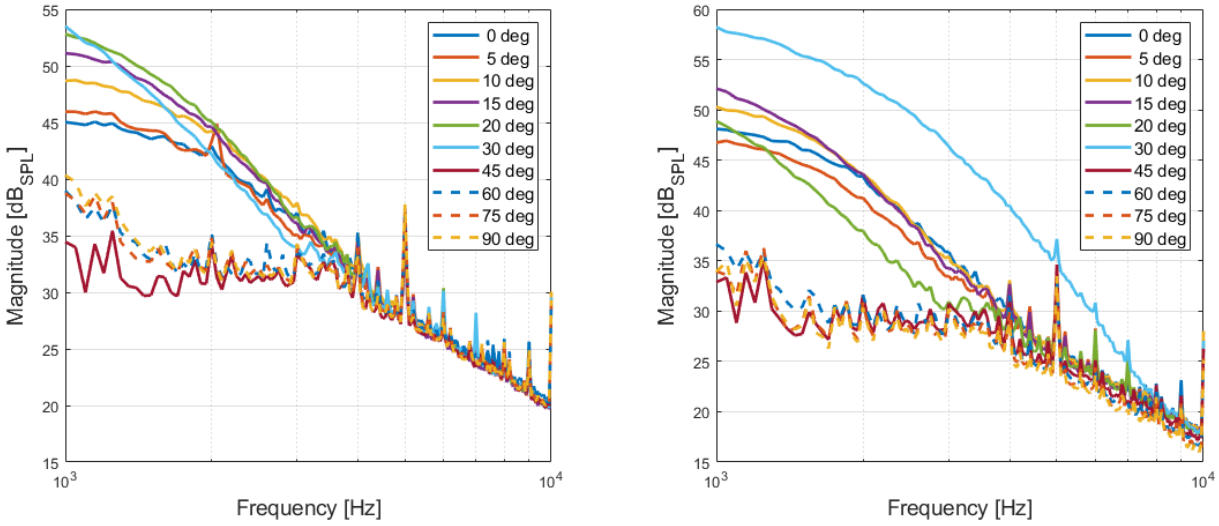

Figure 5.32: PSDs for left-mounted (left plot) and right-mounted (right plot) microphones for Airspeed = 10 m/s and motor configuration - D.

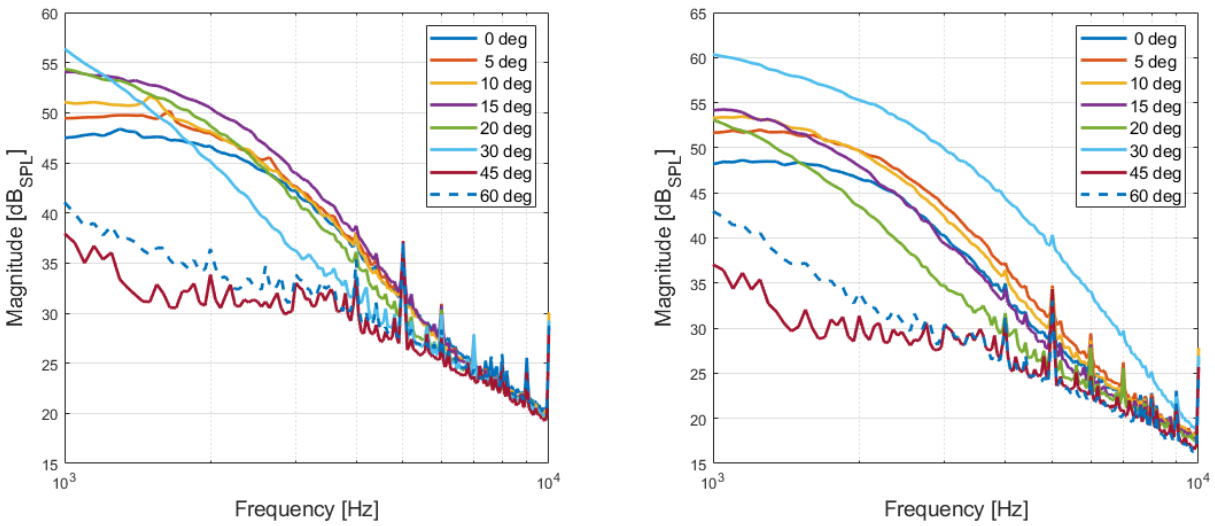

Figure 5.33: PSDs for left-mounted (left plot) and right-mounted (right plot) microphones for Airspeed = 12 m/s and motor configuration - D.

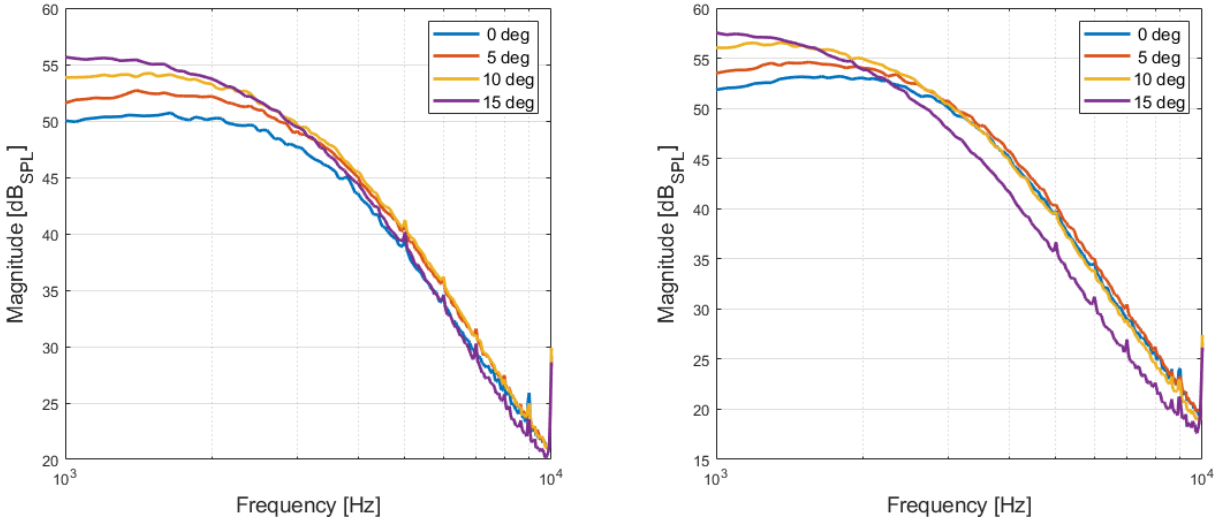

Figure 5.34: PSDs for left-mounted (left plot) and right-mounted (right plot) microphones for Airspeed = 15 m/s and motor configuration - D.

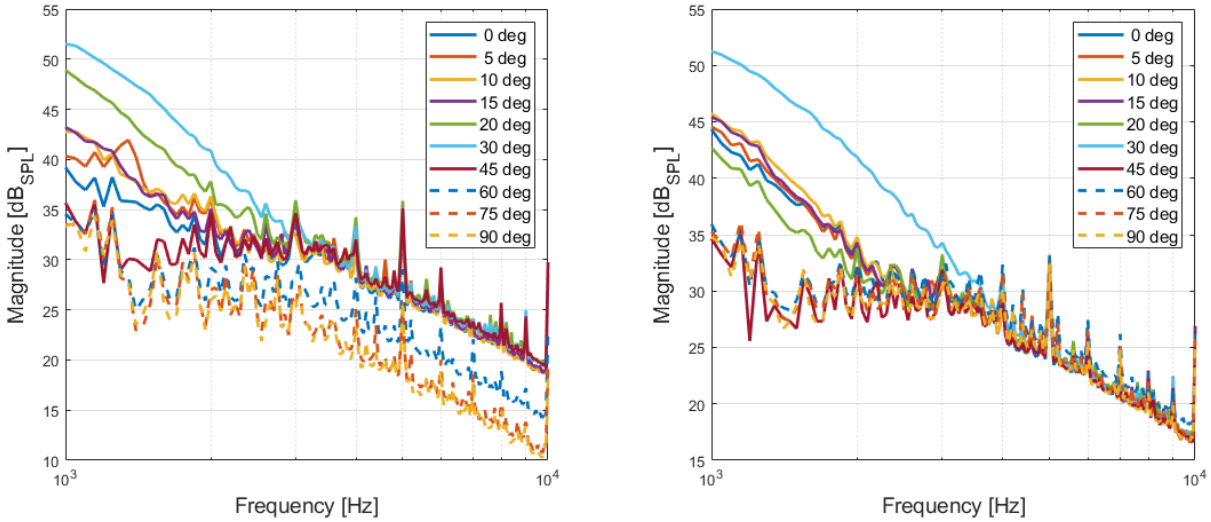

Figure 5.35: PSDs for left-mounted (left plot) and right-mounted (right plot) microphones for Airspeed = 7 m/s and motor configuration - M.

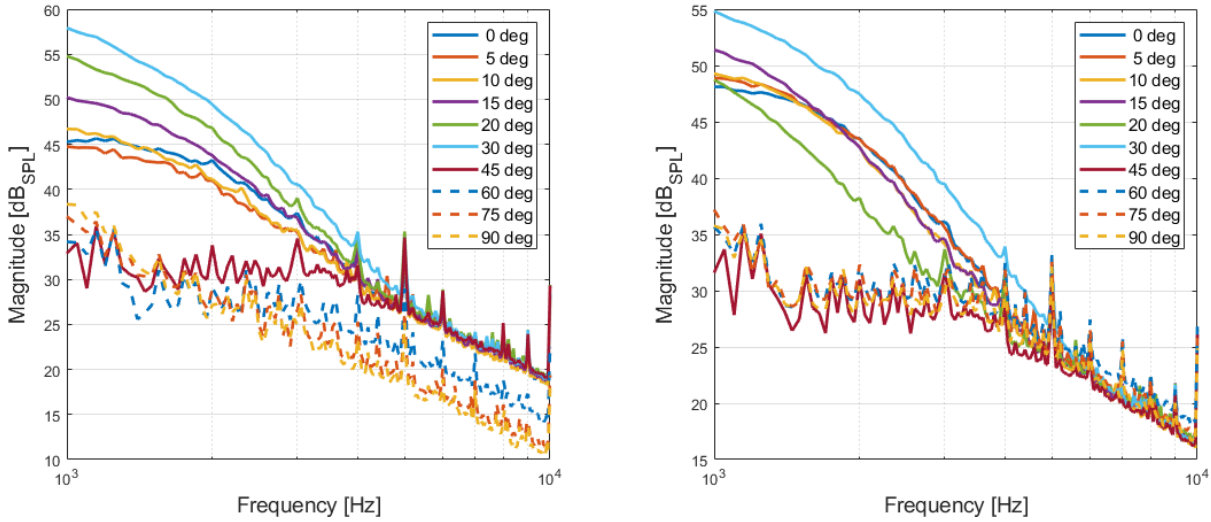

Figure 5.36: PSDs for left-mounted (left plot) and right-mounted (right plot) microphones for Airspeed = 10 m/s and motor configuration - M.

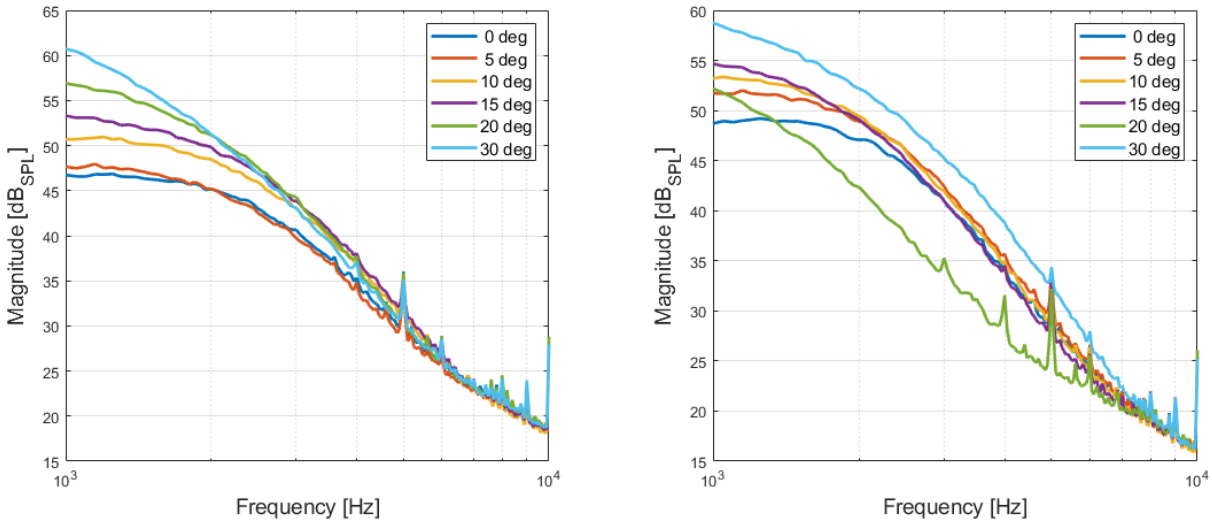

Figure 5.37: PSDs for left-mounted (left plot) and right-mounted (right plot) microphones for Airspeed = 12 m/s and motor configuration - M.

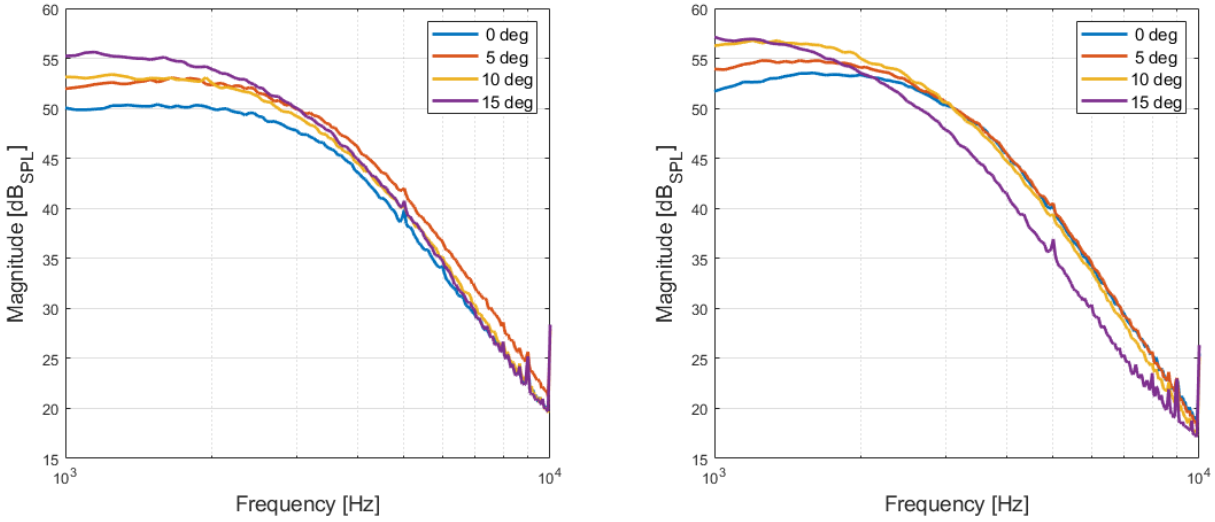

Figure 5.38: PSDs for left-mounted (left plot) and right-mounted (right plot) microphones for Airspeed = 15 m/s and motor configuration - M.

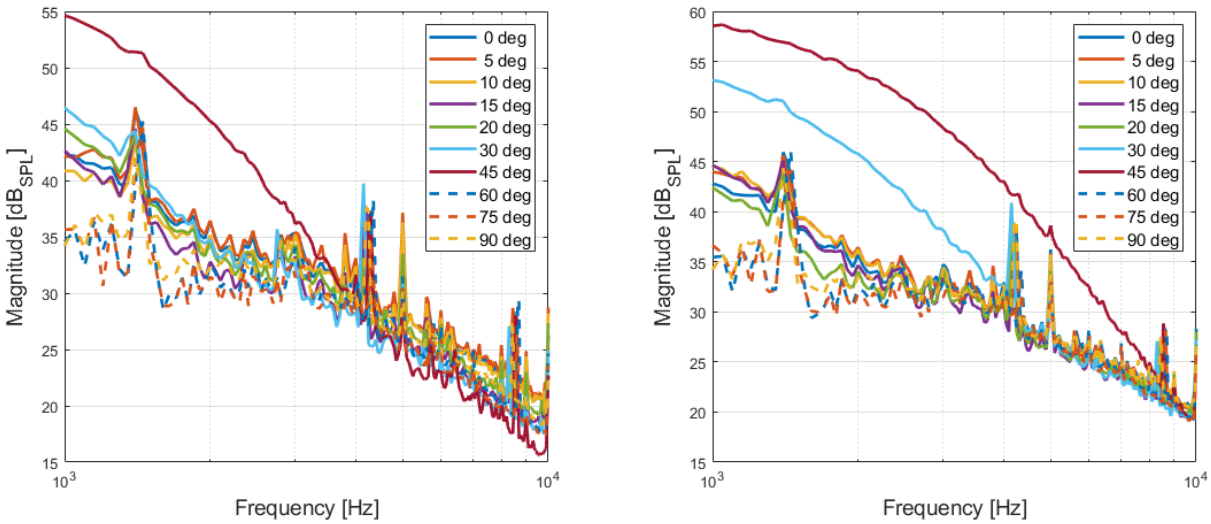

Figure 5.39: PSDs for left-mounted (left plot) and right-mounted (right plot) microphones for Airspeed = 7 m/s and motor configuration - R.

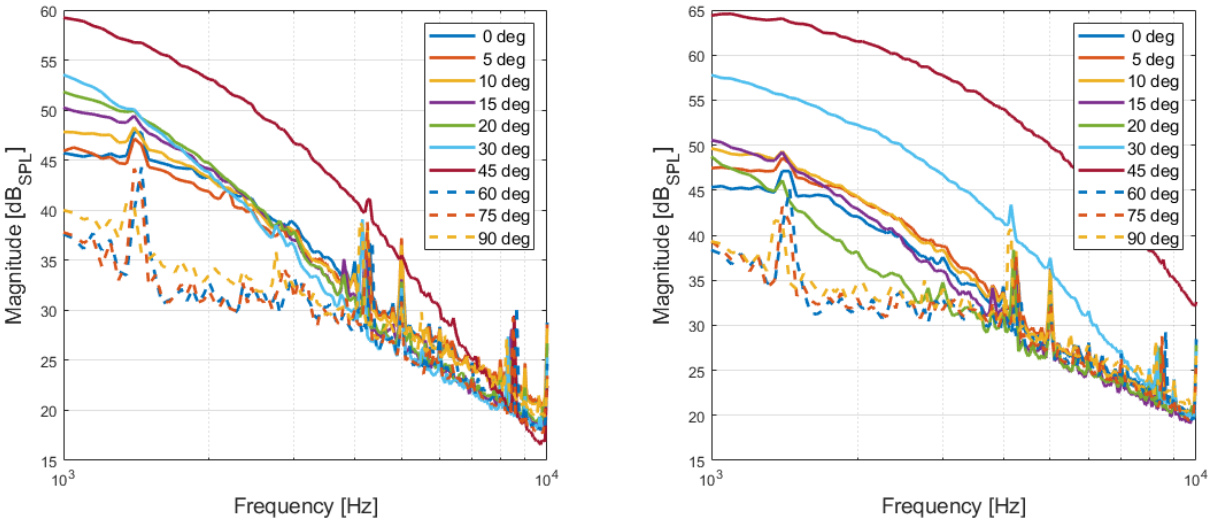

Figure 5.40: PSDs for left-mounted (left plot) and right-mounted (right plot) microphones for Airspeed = 10 m/s and motor configuration - R.

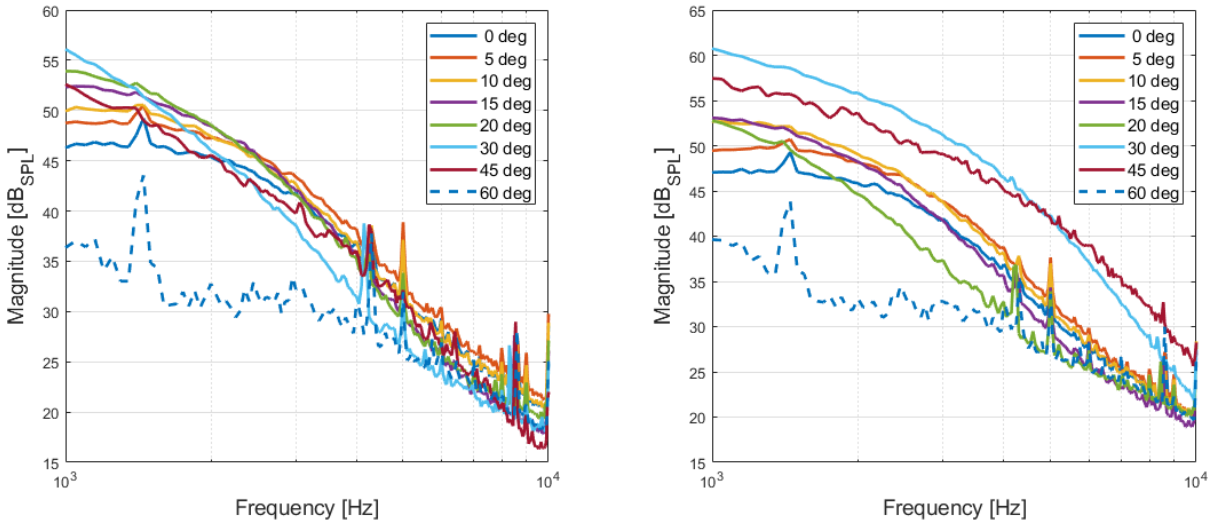

Figure 5.41: PSDs for left-mounted (left plot) and right-mounted (right plot) microphones for Airspeed = 12 m/s and motor configuration - R.

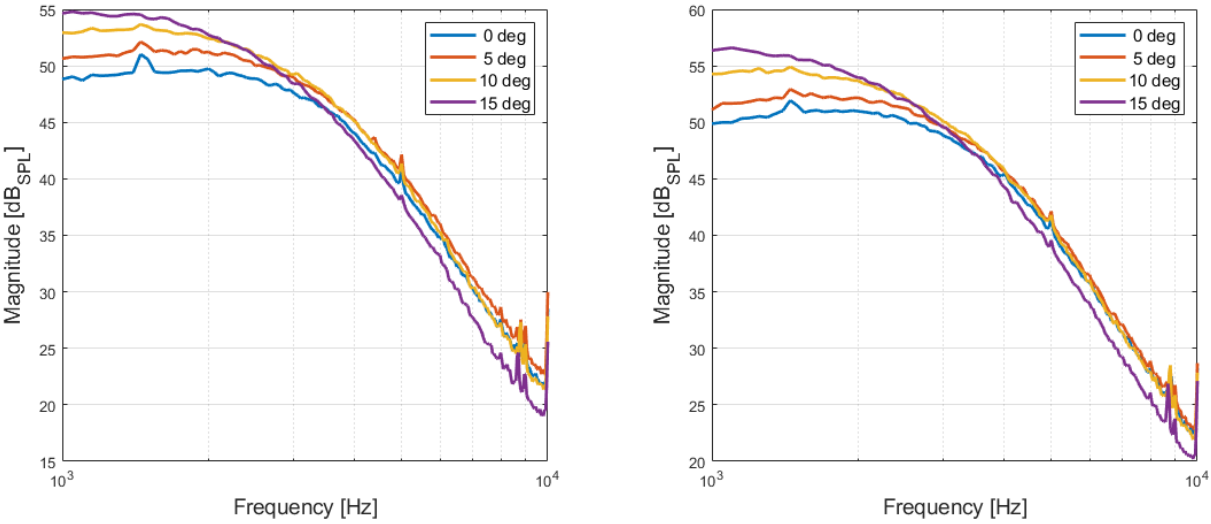

Figure 5.42: PSDs for left-mounted (left plot) and right-mounted (right plot) microphones for Airspeed = 15 m/s and motor configuration - R.

5.2. Subtracted Microphone Signals

The PSDs depicted in this section are of the signal resulting from the subtraction of the left- and right-mounted microphone data:

$$V_{sub} = V_{left} - V_{right}$$

Prior to the subtraction, the microphones' signals are passed though a high-pass filter with a cut-off frequency of 250 Hz. The magnitude of the estimated PSDs is expressed in dB SPL. The conversion from voltage signals to a pressure measure is applied on the signals resulting from the subtraction - V_{sub}.

5.2.1. Power Spectral Densities for Changing Airspeed

The figures are organized according to the motor configuration with Figure 5.43 to Figure 5.52 showing the PSD plots for changing airspeed over all AoA tested for motor configuration D, Figure 5.53 to Figure 5.62 depicting this for motor configuration M, and finally Figure 5.63 to Figure 5.72 providing the PSD plots corresponding to motor configuration R. From the latter, it can be seen that the subtraction method successfully filters the contribution from the vehicle's motors to the microphones' recordings. However, this is not the case at higher AoA when the boundary layer collapses, where the peaks corresponding to the sound of the motors are visible. This could be due to the selected mounting configuration of the microphones. Lastly, the subtraction method is not successful at filtering the harmonics of the 50 Hz component present in all recorded microphones' signals in the wind tunnel.

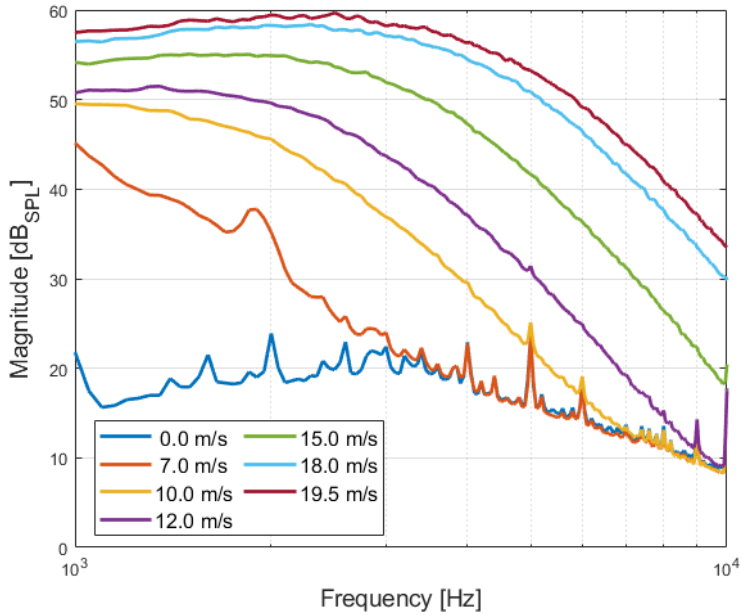

Figure 5.43: PSDs of signals resulting from the subtraction method for AoA = 0^o and motor configuration - D.

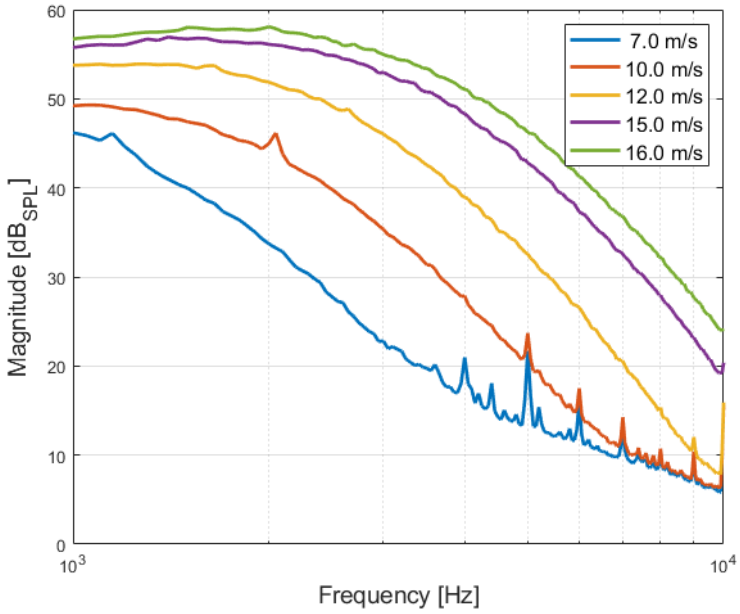

Figure 5.44: PSDs of signals resulting from the subtraction method for AoA = 5º and motor configuration - D.

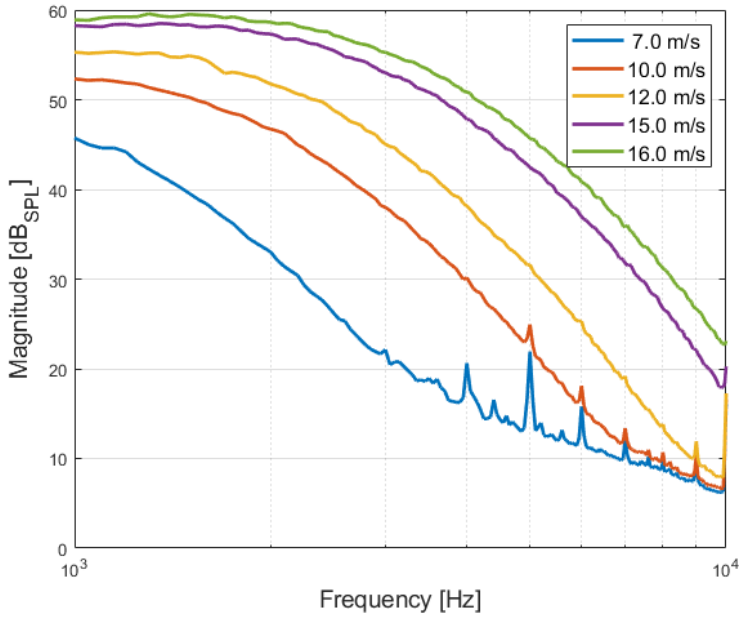

Figure 5.45: PSDs of signals resulting from the subtraction method for AoA = 10º and motor configuration - D.

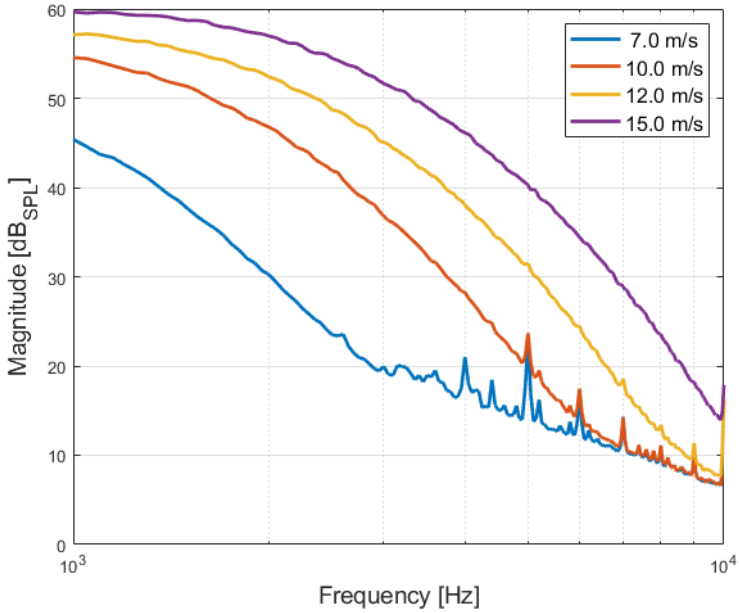

Figure 5.46: PSDs of signals resulting from the subtraction method for AoA = 15º and motor configuration - D.

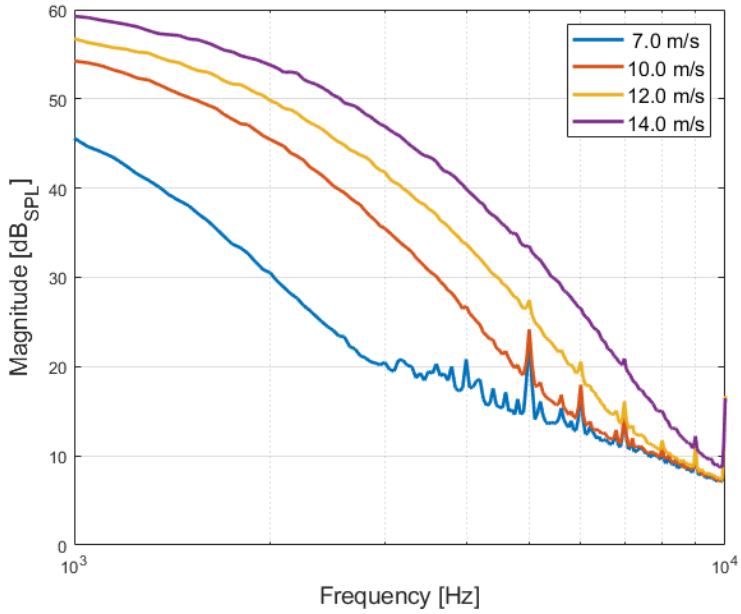

Figure 5.47: PSDs of signals resulting from the subtraction method for AoA = 20º and motor configuration - D.

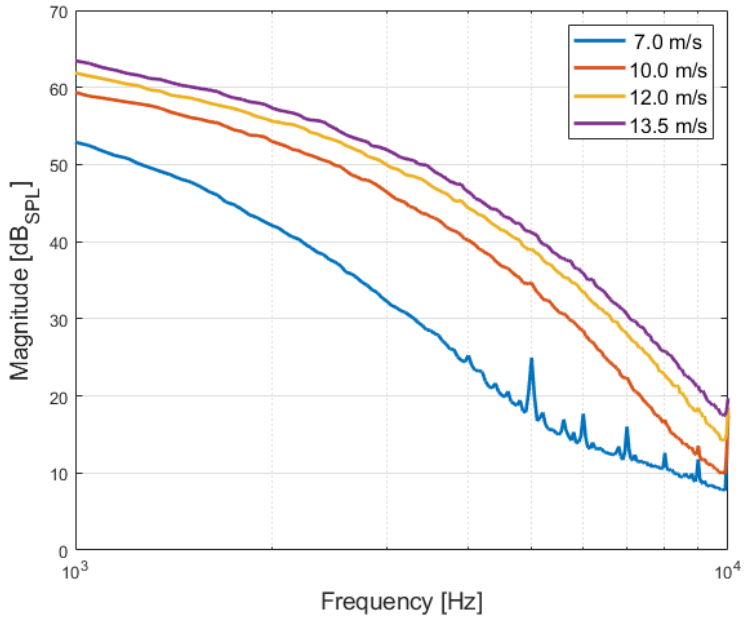

Figure 5.48: PSDs of signals resulting from the subtraction method for AoA = 30º and motor configuration - D.

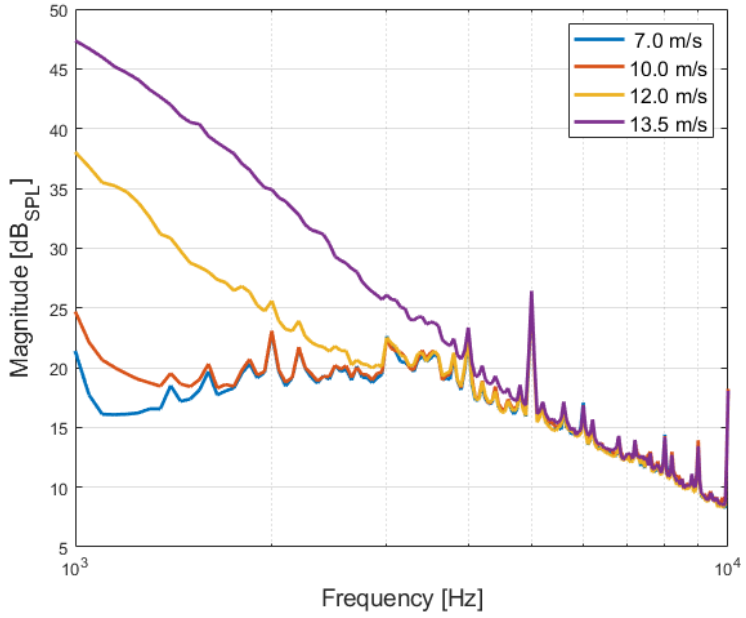

Figure 5.49: PSDs of signals resulting from the subtraction method for AoA = 45º and motor configuration - D.

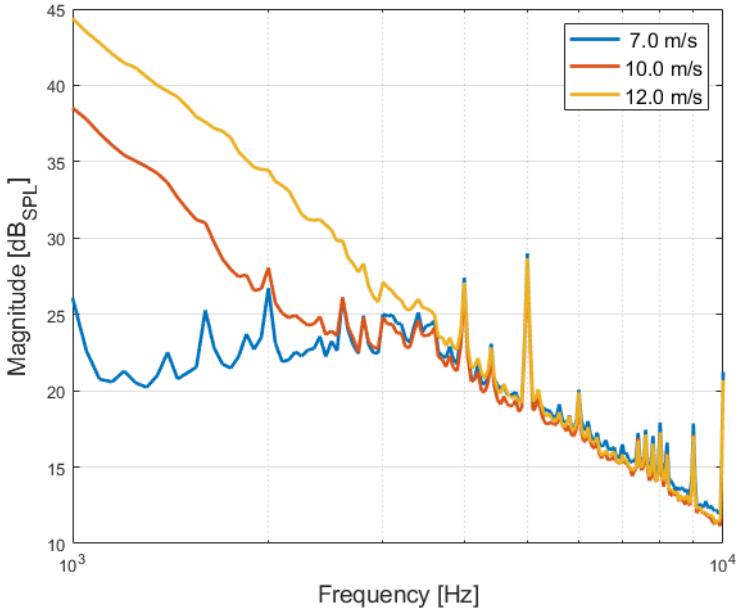

Figure 5.50: PSDs of signals resulting from the subtraction method for AoA = 60^o and motor configuration - D.

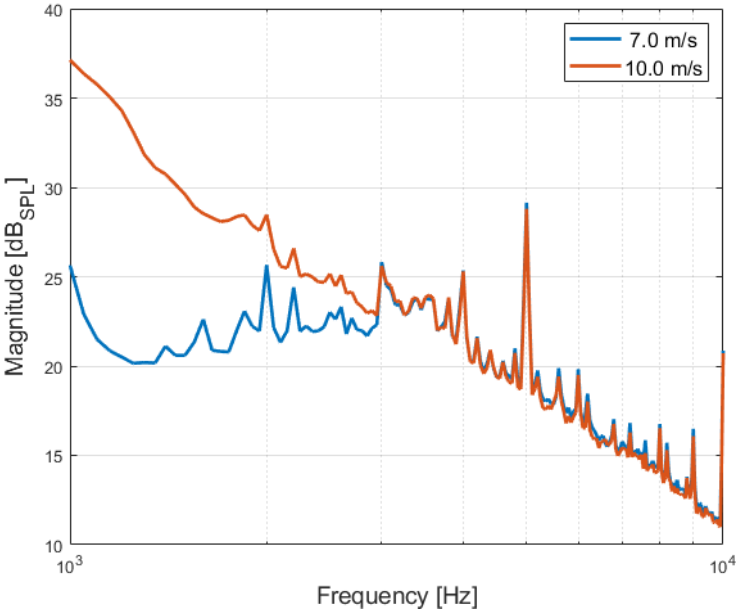

Figure 5.51: PSDs of signals resulting from the subtraction method for AoA = 75^o and motor configuration - D.

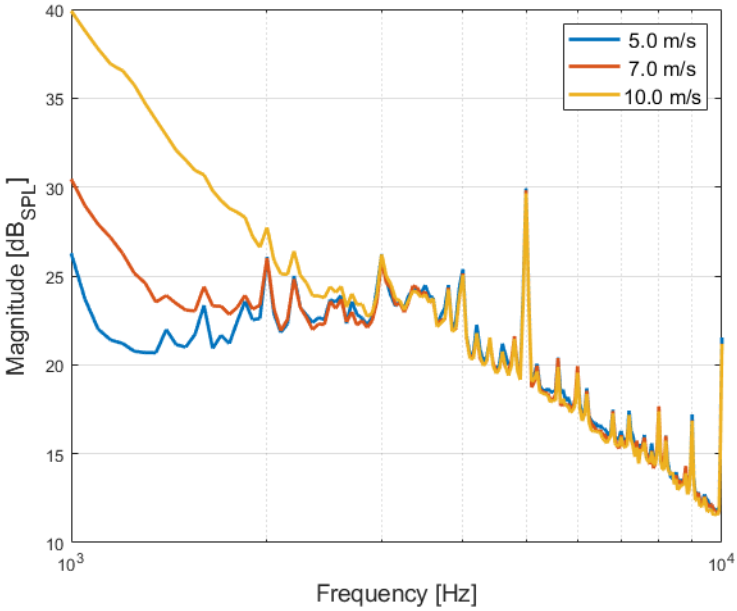

Figure 5.52: PSDs of signals resulting from the subtraction method for AoA = 90º and motor configuration - D.

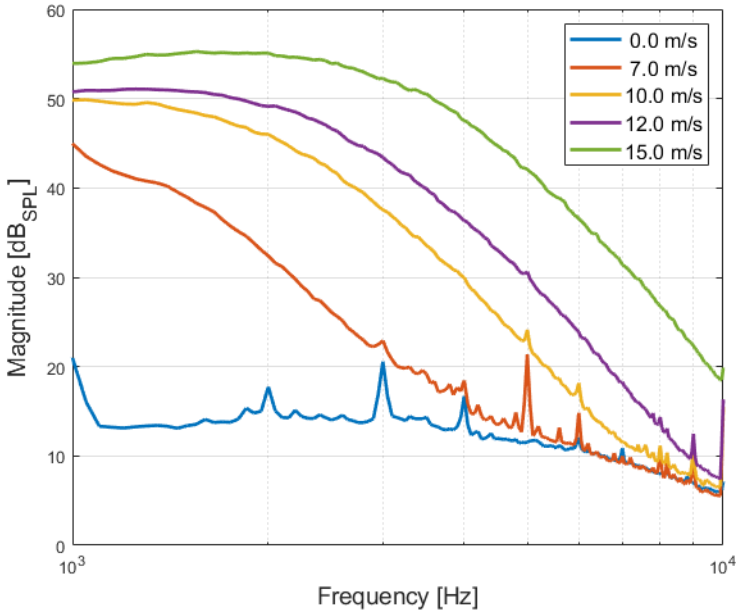

Figure 5.53: PSDs of signals resulting from the subtraction method for AoA = 0º and motor configuration - M.

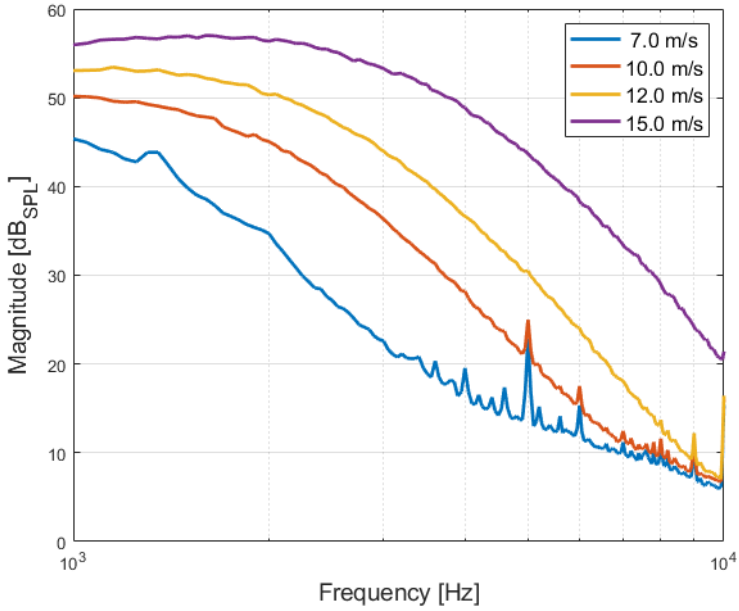

Figure 5.54: PSDs of signals resulting from the subtraction method for AoA = 5^o and motor configuration - M.

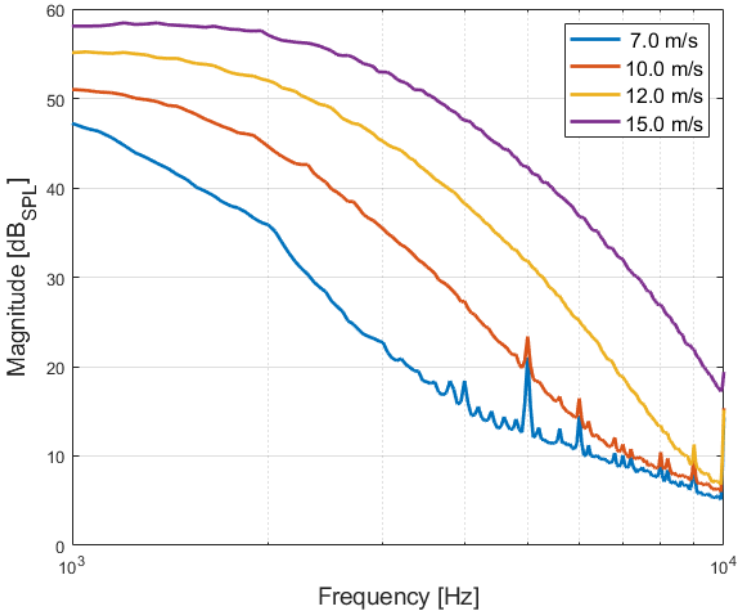

Figure 5.55: PSDs of signals resulting from the subtraction method for AoA = 10^o and motor configuration - M.

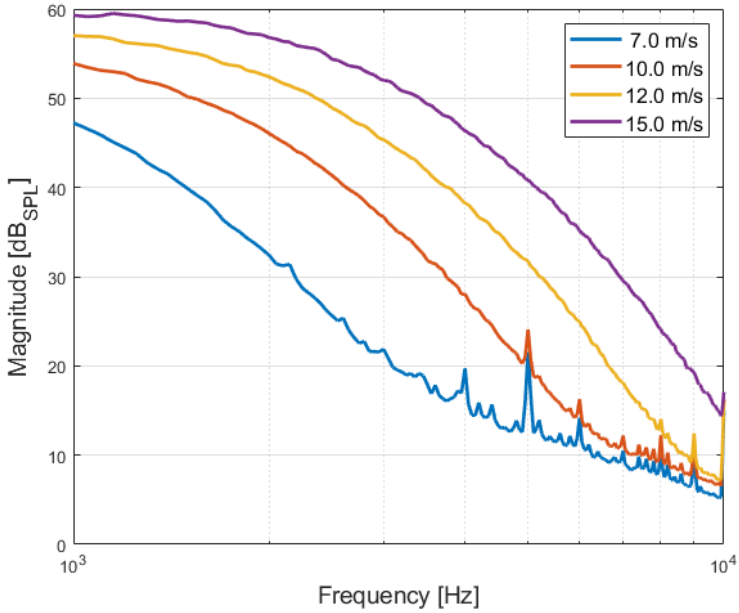

Figure 5.56: PSDs of signals resulting from the subtraction method for AoA = 15º and motor configuration - M.

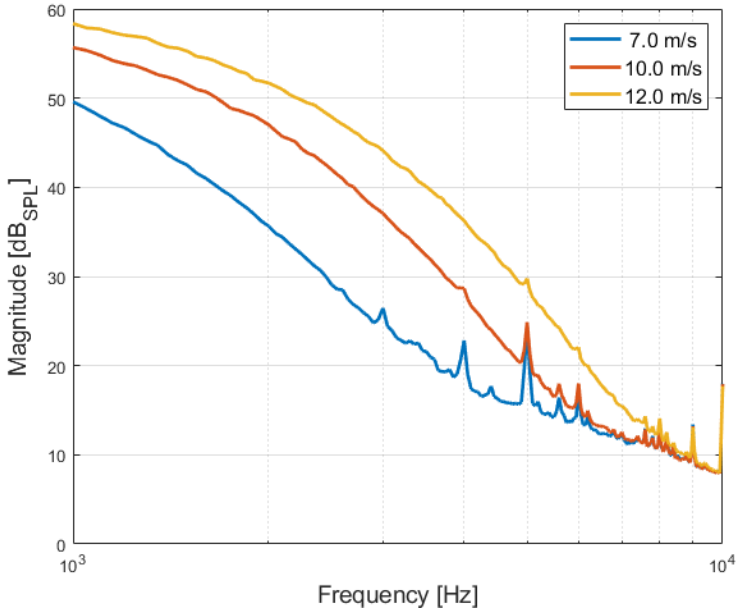

Figure 5.57: PSDs of signals resulting from the subtraction method for AoA = 20º and motor configuration - M.

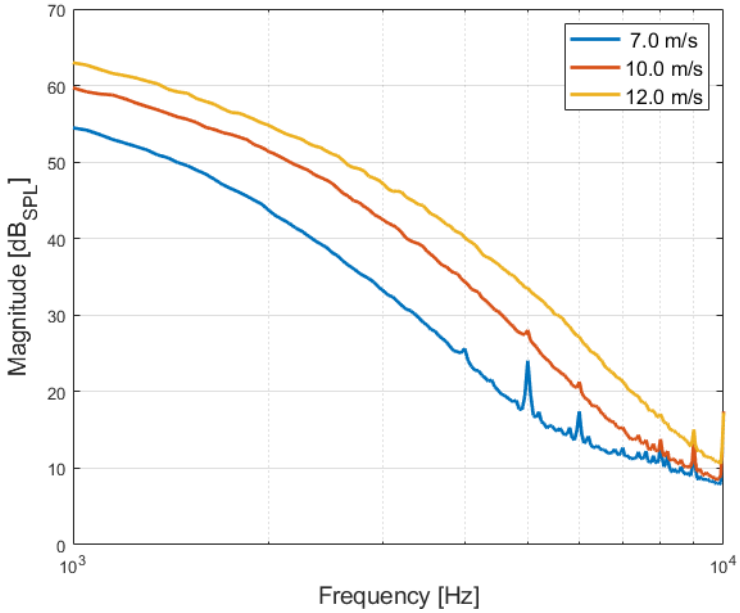

Figure 5.58: PSDs of signals resulting from the subtraction method for AoA = 30º and motor configuration - M.

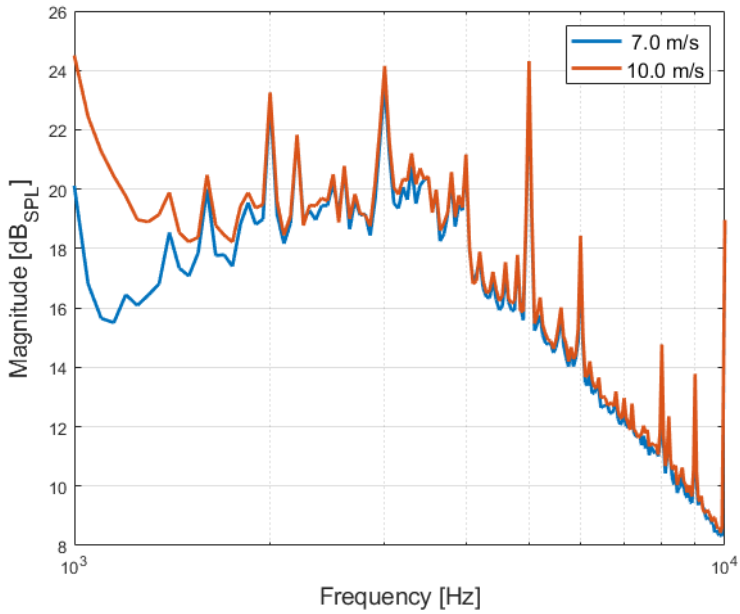

Figure 5.59: PSDs of signals resulting from the subtraction method for AoA = 45º and motor configuration - M.

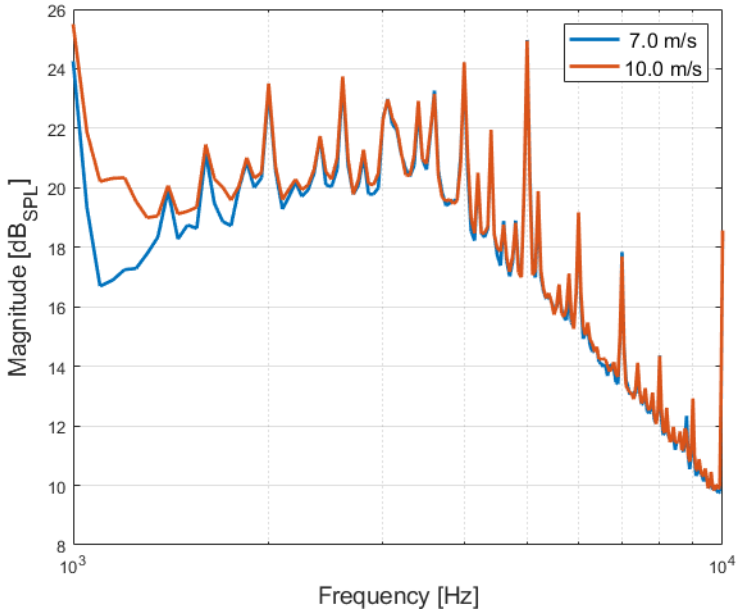

Figure 5.60: PSDs of signals resulting from the subtraction method for AoA = 60º and motor configuration - M.

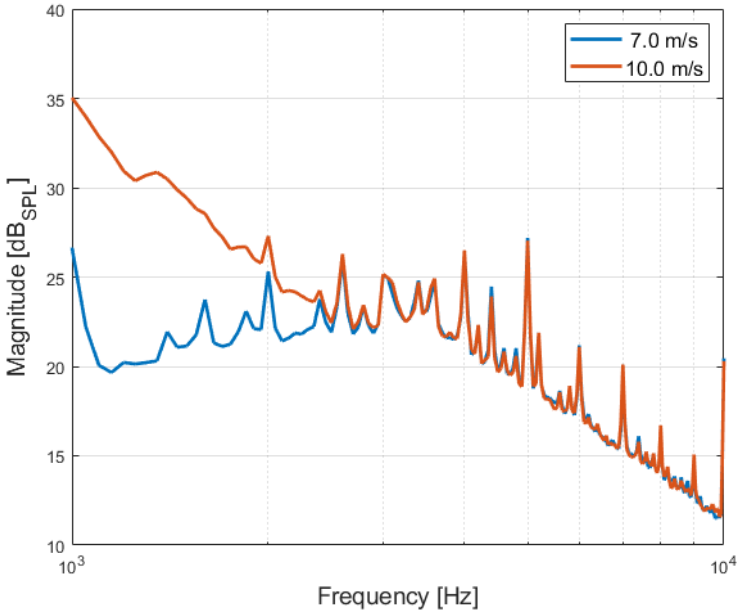

Figure 5.61: PSDs of signals resulting from the subtraction method for AoA = 75º and motor configuration - M.

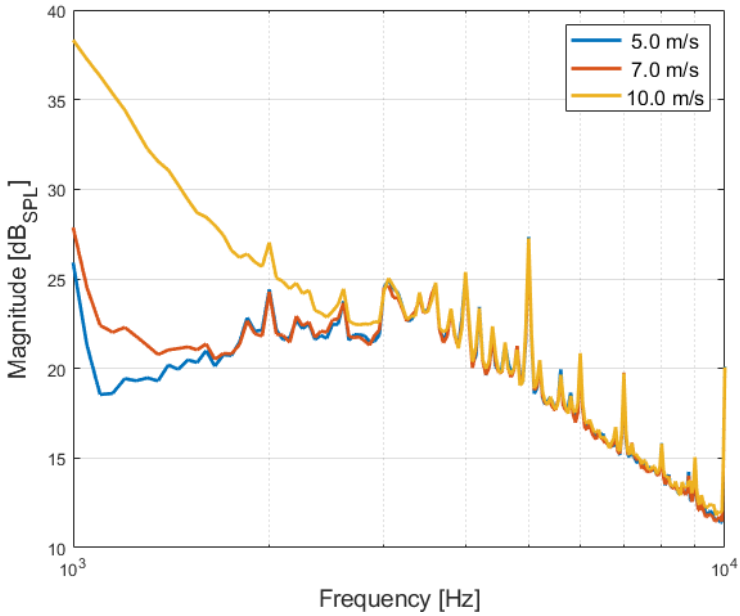

Figure 5.62: PSDs of signals resulting from the subtraction method for AoA = 90º and motor configuration - M.

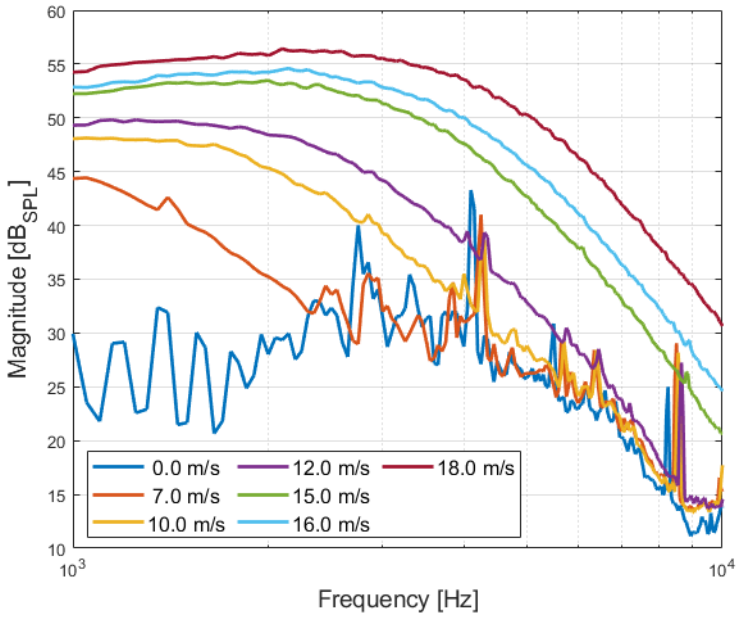

Figure 5.63: PSDs of signals resulting from the subtraction method for AoA = 0º and motor configuration - R.

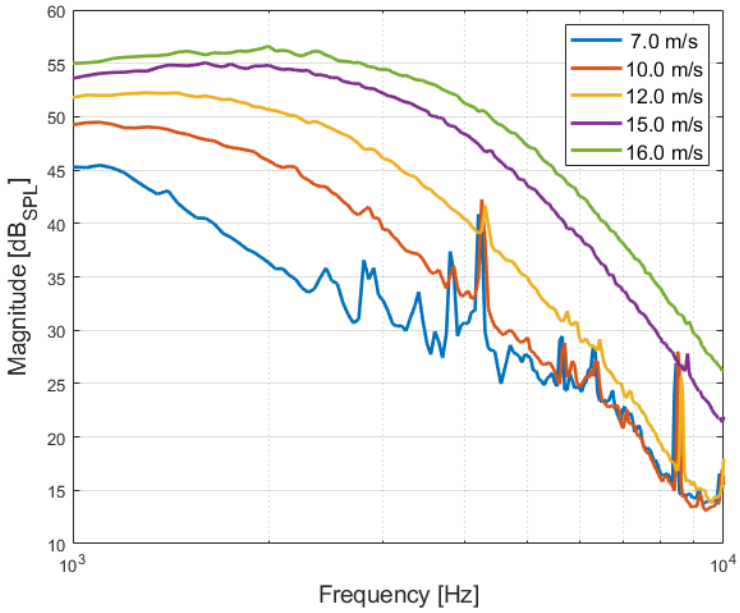

Figure 5.64: PSDs of signals resulting from the subtraction method for AoA = 5^o and motor configuration - R.

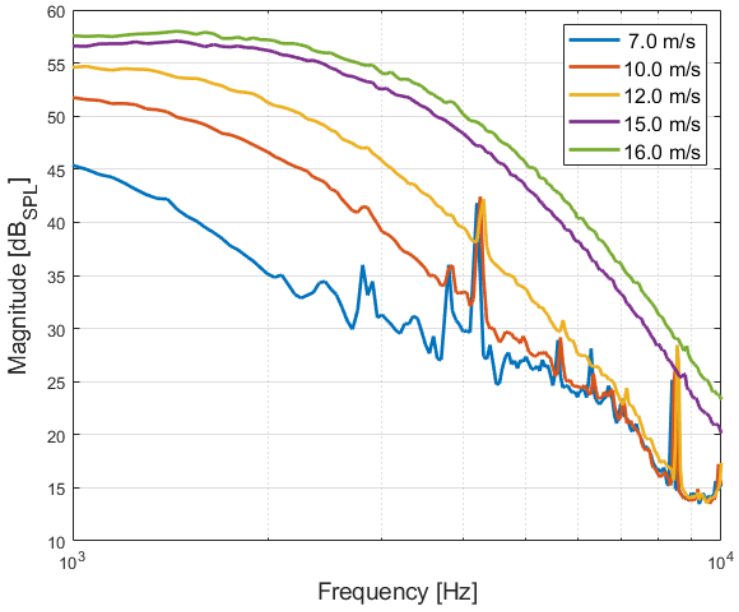

Figure 5.65: PSDs of signals resulting from the subtraction method for AoA = 10^o and motor configuration - R.

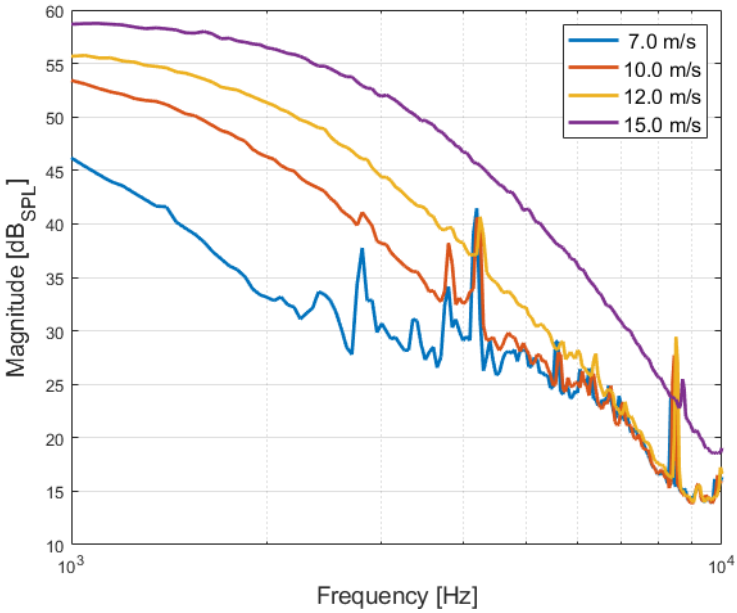

Figure 5.66: PSDs of signals resulting from the subtraction method for AoA = 15º and motor configuration - R.

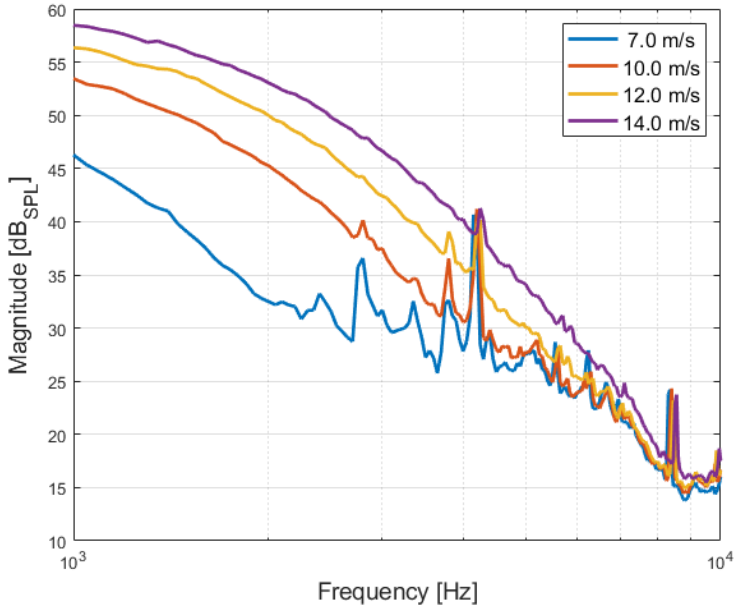

Figure 5.67: PSDs of signals resulting from the subtraction method for AoA = 20º and motor configuration - R.

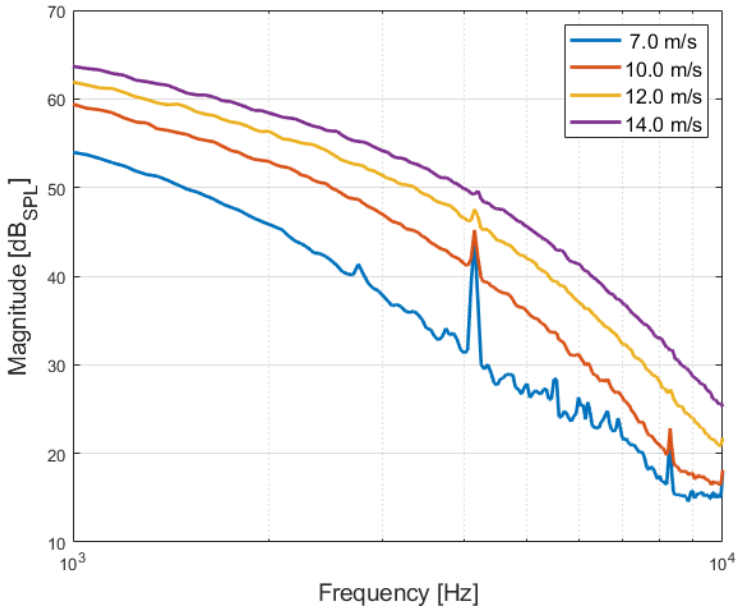

Figure 5.68: PSDs of signals resulting from the subtraction method for AoA = 30º and motor configuration - R.

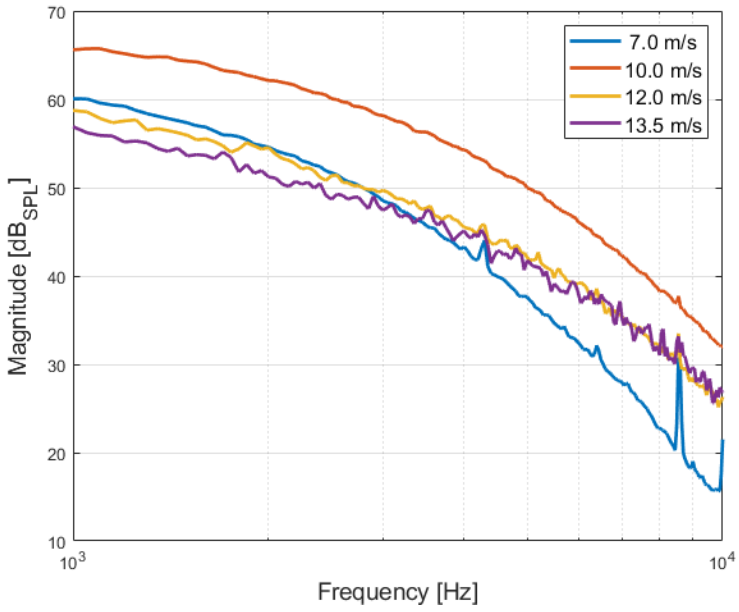

Figure 5.69: PSDs of signals resulting from the subtraction method for AoA = 45º and motor configuration - R.

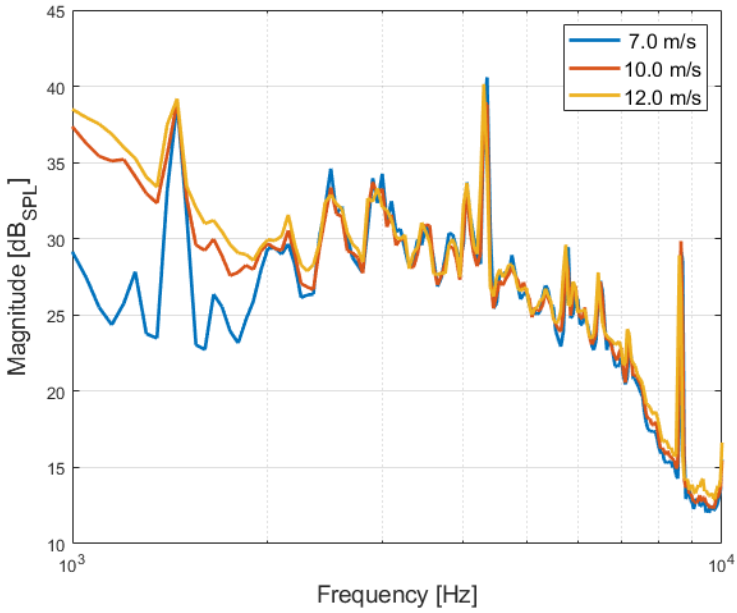

Figure 5.70: PSDs of signals resulting from the subtraction method for AoA = 60º and motor configuration - R.

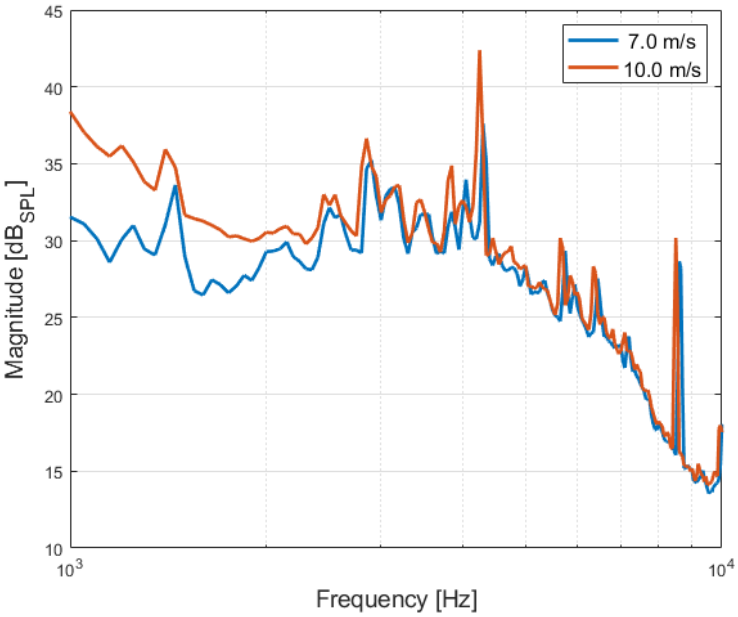

Figure 5.71: PSDs of signals resulting from the subtraction method for AoA = 75º and motor configuration - R.

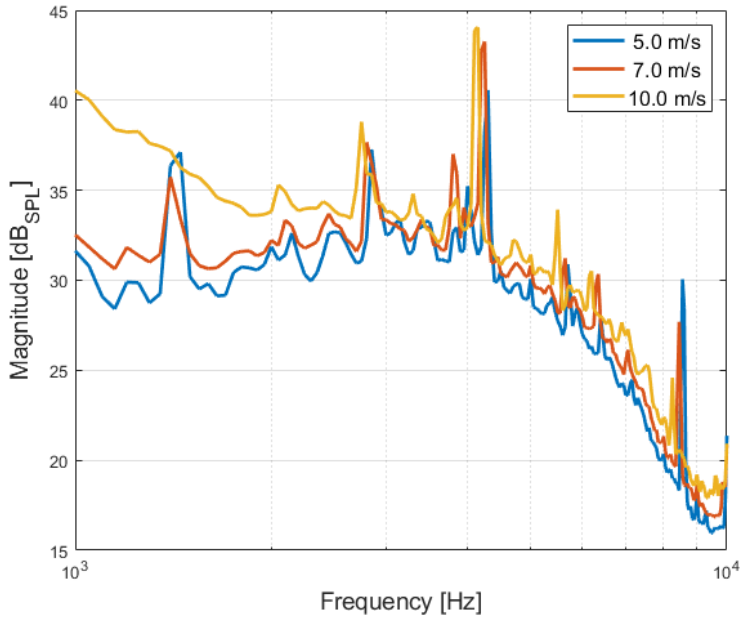

Figure 5.72: PSDs of signals resulting from the subtraction method for AoA = 90º and motor configuration - R.

5.2.2. Power Spectral Densities for Changing Angle of Attack

The figures are again organized according to the motor configuration in order of increasing airspeed value. Figure 5.73 to Figure 5.76 depict the PSDs of the subtracted signals for all AoA tested at airspeed from 7 m/s to 15 m/s and motor configuration D, while Figure 5.77 to Figure 5.80 correspond to motor configuration M, and Figure 5.81 to Figure 5.84 - to motor configuration R. Similarly to the PSD plots of the subtracted signals for changing airspeed found in Subsection 5.2.1, the signals subtraction method successfully limits the impact of the motors' sound in the resulting V_{sub} signals, but has limited effect on the electrical noise.

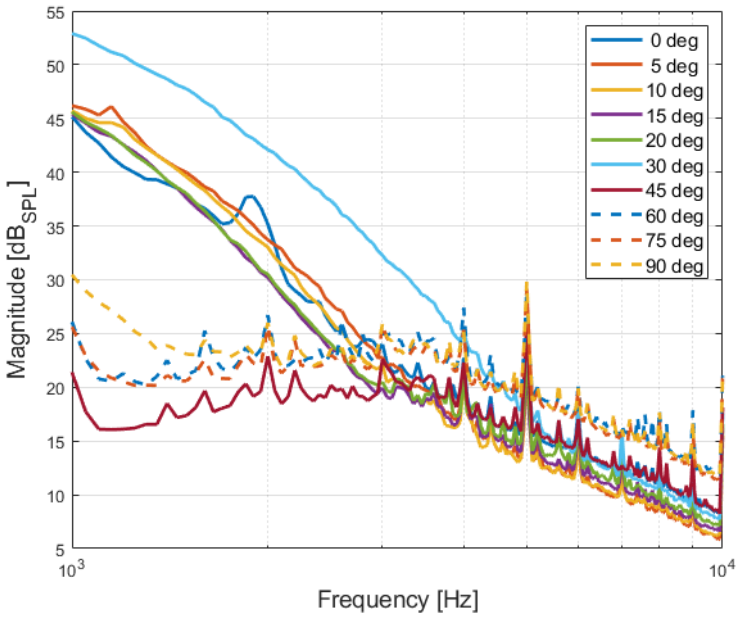

Figure 5.73: PSDs of signals resulting from the subtraction method for Airspeed = 7 m/s and motor configuration - D.

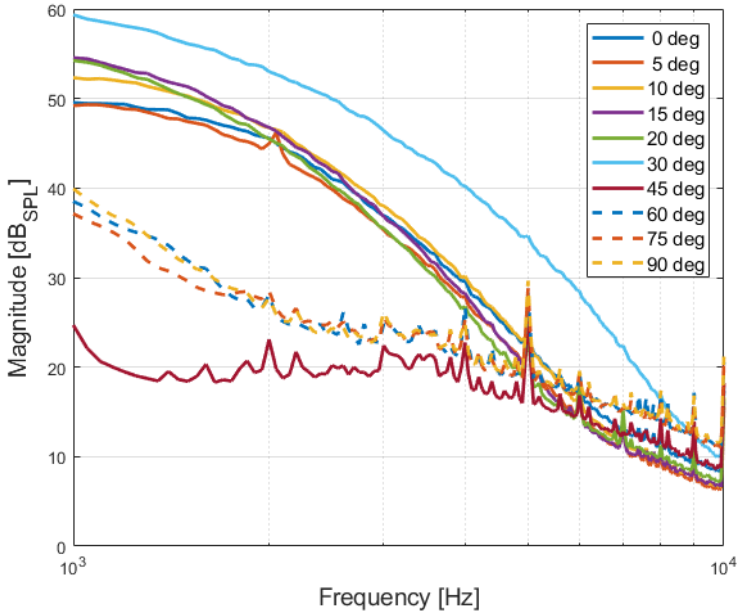

Figure 5.74: PSDs of signals resulting from the subtraction method for Airspeed = 10 m/s and motor configuration - D.

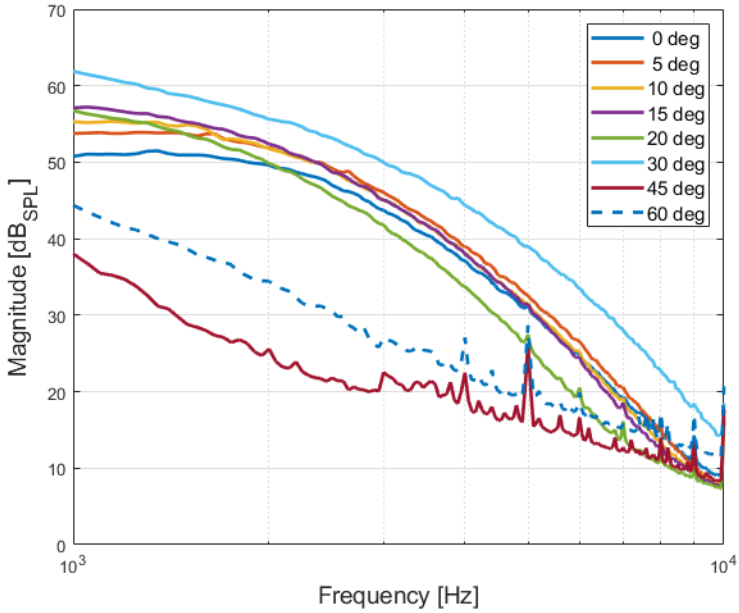

Figure 5.75: PSDs of signals resulting from the subtraction method for Airspeed = 12 m/s and motor configuration - D.

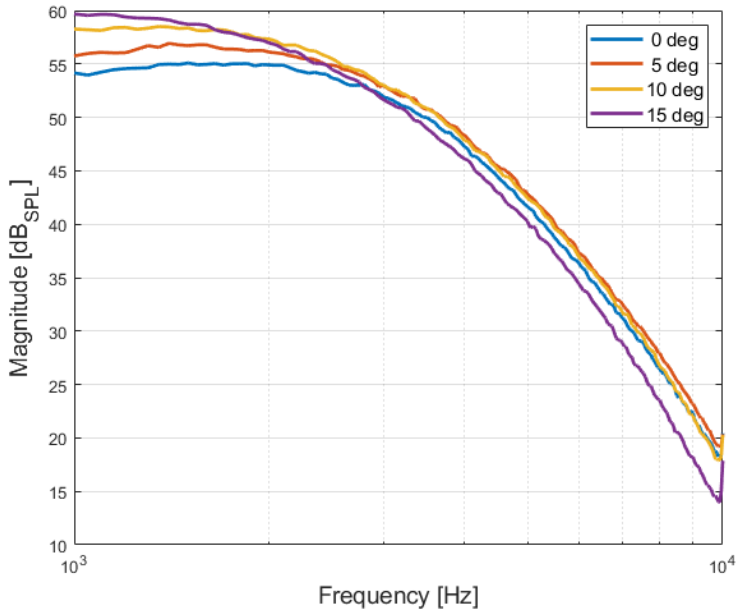

Figure 5.76: PSDs of signals resulting from the subtraction method for Airspeed = 15 m/s and motor configuration - D.

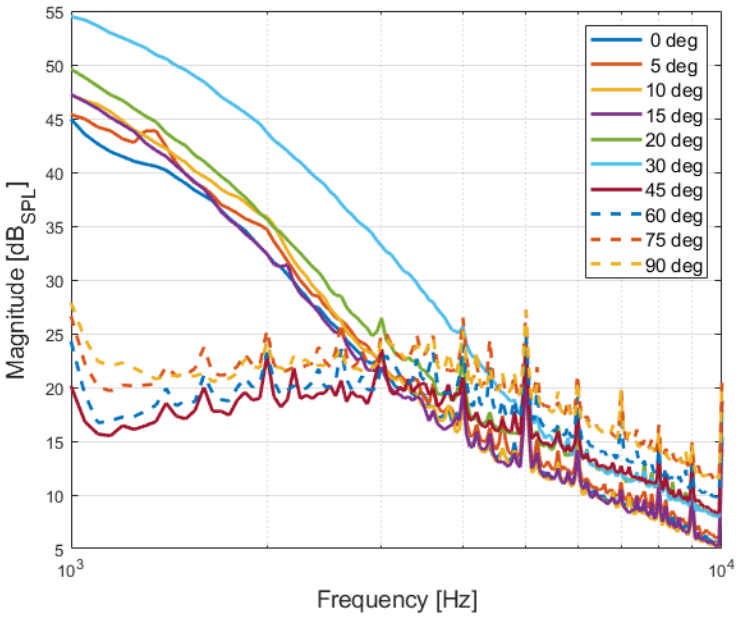

Figure 5.77: PSDs of signals resulting from the subtraction method for Airspeed = 7 m/s and motor configuration - M.

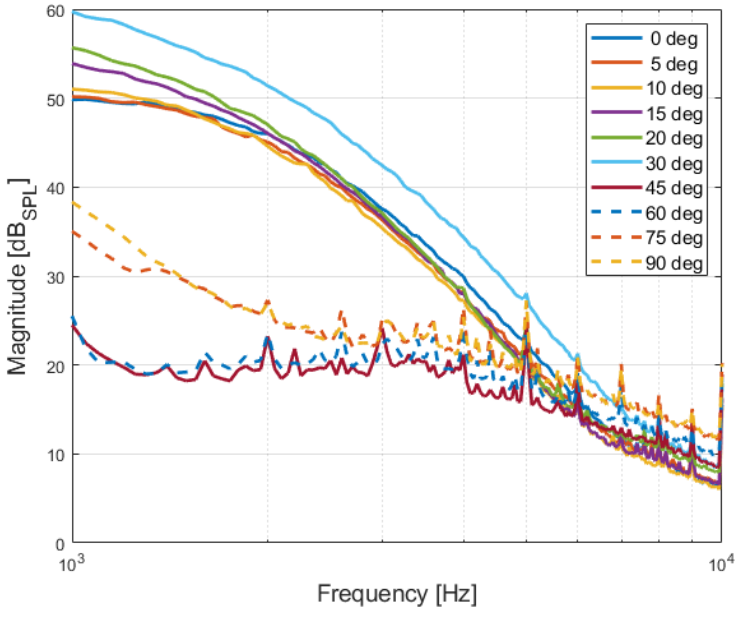

Figure 5.78: PSDs of signals resulting from the subtraction method for Airspeed = 10 m/s and motor configuration - M.

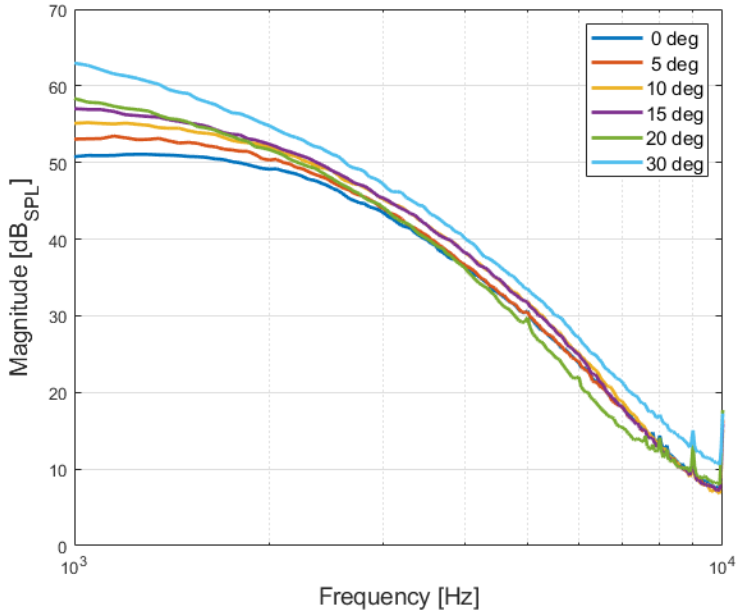

Figure 5.79: PSDs of signals resulting from the subtraction method for Airspeed = 12 m/s and motor configuration - M.

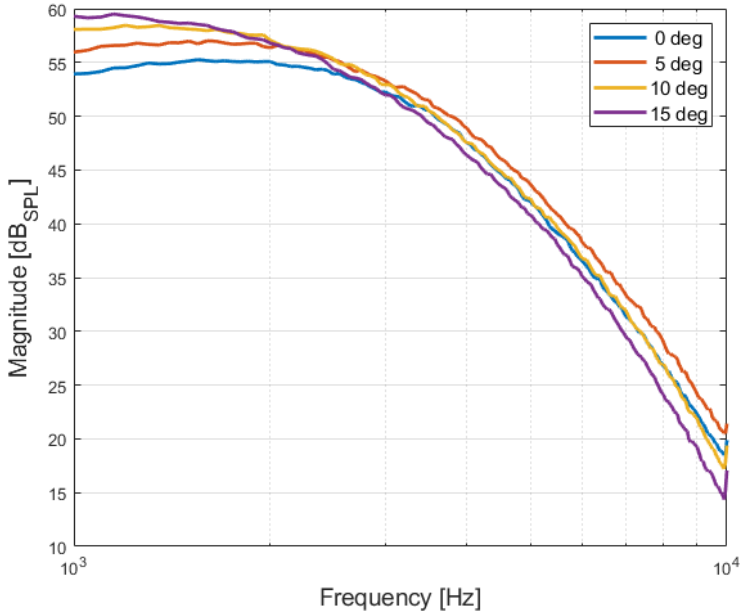

Figure 5.80: PSDs of signals resulting from the subtraction method for Airspeed = 15 m/s and motor configuration - M.

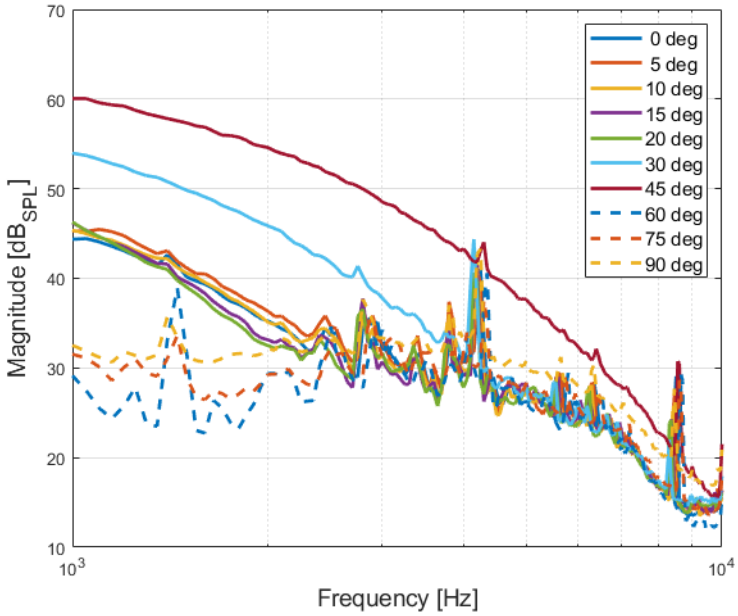

Figure 5.81: PSDs of signals resulting from the subtraction method for Airspeed = 7 m/s and motor configuration - R.

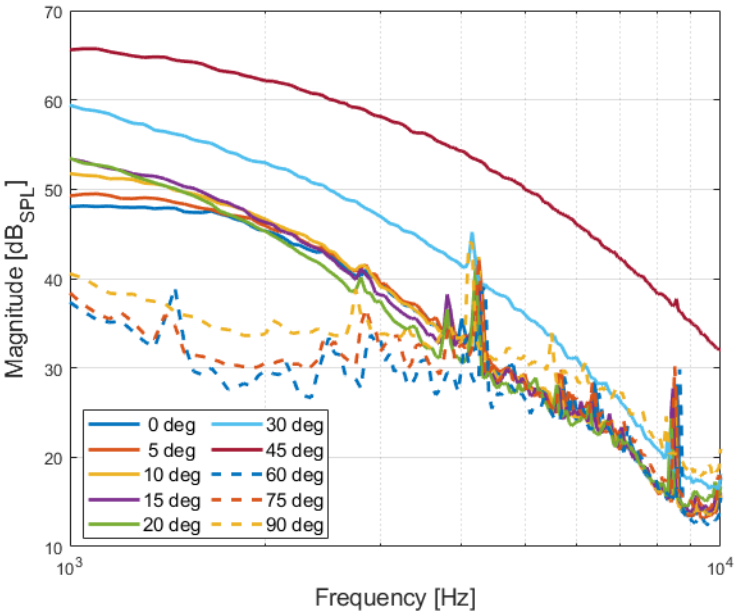

Figure 5.82: PSDs of signals resulting from the subtraction method for Airspeed = 10 m/s and motor configuration - R.

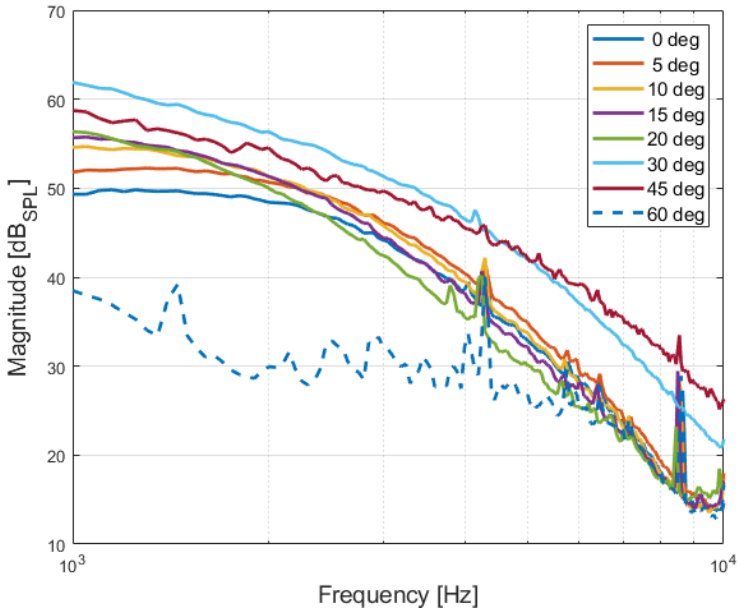

Figure 5.83: PSDs of signals resulting from the subtraction method for Airspeed = 12 m/s and motor configuration - R.

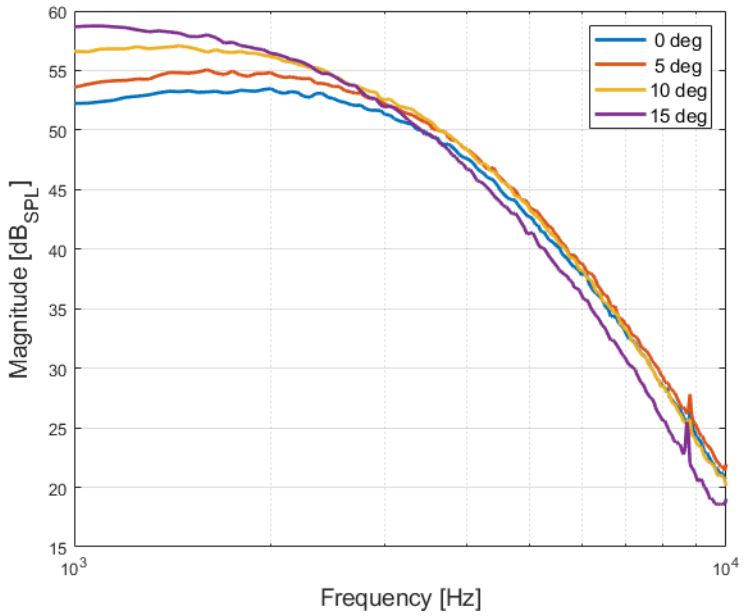

Figure 5.84: PSDs of signals resulting from the subtraction method for Airspeed = 15 m/s and motor configuration - R.

Part IV

Closure

6

Conclusion

This research project proposed an airspeed instrument concept that estimates the vehicle's airspeed using the PSD of the TBL-induced pressure fluctuations at the surface of the vehicle's body, captured by flush mounted microphones. A detailed review of the theory of flow structures in boundary layers confirmed the dependency of the their characteristics on the free-stream velocity, with the most important one being the hydrodynamic pressure fluctuations emitted by the turbulent flow structures, thus substantiating the feasibility of the proposed airspeed instrument's working principle.

The proposed airspeed instrument concept includes two flush mounted microphones on the vehicle's nose cone, an ADC (TI PCM1808), a micro-controller board (Teensy 4.1™) and a dedicated power source in the form of a battery, with the different components being integrated on a prototyping board. The configuration of the microphones was chosen with the aim of being able to subtract the microphone signals, which would suppress acoustic sounds captured by the microphones. This particular design of the instrument was tested for data acquisition during the flight experiments and showed that it could successfully read, process and save the recorded signals from both microphones in real-time, with an achieved signal sampling frequency of approximately 43 kHz. However, it was found that the pseudo-sound due to the flow structures in the TBL was dominant in the microphones' signals, leading to the subtraction method having minimal benefits.

Dedicated models relating the PSD of the hydrodynamic pressure fluctuations induced by the flow structures in the TBL and the vehicle's airspeed were created using data collected from both flight and wind tunnel experiments performed as part of the research. The most suitable model structure was found to be feed-forward artificial neural network, trained with a supervised learning approach, where the PSD of microphones' signals and corresponding airspeed measures obtained from the experiments constituted the input-output dataset. It was found that models trained on the PSDs of the left-mounted microphone's signals alone achieved the lowest approximation error over the validation dataset, lower than those trained on the PSDs of the subtracted signals, which is a further argument for the lack of need for the signal subtraction method. The best model achieved a RMSE of 1.037 m/s. Its mean approximation error is 0.043 m/s with a standard deviation of 1.039 m/s.

Theory suggested that the AoA also impacts the properties of the TBL flow-induced hydrodynamic pressure fluctuations for otherwise the same airspeed. This was confirmed by the data gathered during the wind tunnel experiments. As the AoA increases, so does the power, especially in the lower frequencies. This is true for AoA of less than 60^{o} as for higher AoA values, there is an abrupt decrease in the power of the recorded microphone signals. Therefore, models including the AoA as an additional input were trained. The corresponding input-output dataset contained the PSDs of the left-mounted microphone only from the wind tunnel experiments as there the AoA was measured and recorded. An uncertainty of up to 15% was added to the AoA inputs that were part of the validation dataset to simulate the performance of a non-perfect sensor. Taking the best model, its RMSE is 0.364 m/s. Its mean approximation error is 0.027 m/s with a standard deviation of 0.486 m/s. Furthermore, the sensitivity analysis showed that the model is more sensitive towards the PSD of the microphones' signals than towards the AoA.

Based on the research's findings, it can be concluded that the utilization of the proposed instrument concept for estimating the airspeed of a vehicle in-flight at a wide range of AoA is feasible, thus substantiating its further development.

6.1. Research Questions

This section elaborates on the research questions posed in Chapter 1. They are repeated below for convenience and a brief reflection is provided afterwards for each one of them.

Research Question 1

"How is the power spectral density of the pressure fluctuations stemming from the boundary layer related to the vehicle's airspeed?"

From both literature and experiments it was determined that as the airspeed increases, so does the energy of the hydrodynamic pressure fluctuations and subsequently, the power of the recorded microphones' signals. In literature, single-point frequency spectrum models have been described that predict the spectra of the flow-induced wall-pressure fluctuations beneath a TBL. However, in those models the airspeed is provided as an independent variable. The Navier-Stokes equations as well as the equations of continuity and motion also can be used to derive a relation between the fluctuating pressure component at the surface beneath a TBL and the airspeed. However, these equations will relate to the mean of the fluctuating pressure component, rather than the PSD and are not directly related to the airspeed, rather to parameters which in turn are directly related to the airspeed.

In the current research, the relation between the TBL-induced hydrodynamic pressure fluctuations and the airspeed was modeled using feed-forward ANN, which can be expressed as a mapping function:

$$y = f(x; \theta)$$

with x representing the inputs, in this case the PSD of the microphones' signals, and θ - the model's hyperparameters. The output of the network can be expressed as the sum of the values of all activation functions in the hidden layer times the output weights, plus the bias of the output neuron:

$$y = b_o + \sum_{j=1}^{n} w_{jk} \phi_j(v_j)$$

for $j = 1, 2, \ldots, n$ with n being the number of the hidden neurons in the network's hidden layer. The b_o is the bias of the output neuron, w_{jk} corresponds to the output weight of the j^{th} hidden neuron, ϕ_j is the activation function of the j^{th} hidden neuron and v_j is the argument of the j^{th} hidden neuron's activation function. The argument of an activation function in the hidden layer is the input data multiplied by the input weights of the network, plus the bias of the hidden neuron:

$$v_j = b_{h_j} + \sum_{i=1}^{m} w_{ij} PSD_i$$

for $i = 1, 2, \ldots, m$ with m being the number of input neurons in the network's input layer. b_{h_j} represent the bias of the j^{th} hidden neuron, w_{ij} - the weight of the i^{th} input neuron with respect to the j^{th} hidden neuron and PSD_i corresponds to the input provided to the ANN model, which is the magnitude of the PSD for the i^{th} frequency value in its range. Substituting the equation of the activation function - the hyperbolic tangent - and its argument in the expression for the output of the neural network gives the mapping function in terms of the input-output data. This can be seen as the equation relating the airspeed to the microphones' signals PSD:

$$V_{air} = b_o + \sum_{j=1}^{n} w_{jk} \tanh\left(b_{h_j} + \sum_{i=1}^{m} w_{ij} PSD_i \right)$$

$$V_{air} = b_o + \sum_{j=1}^{n} w_{jk} \frac{\exp\left(2(b_{h_j} + \sum_{i=1}^{m} w_{ij} PSD_i)\right) - 1}{\exp\left(2(b_{h_j} + \sum_{i=1}^{m} w_{ij} PSD_i)\right) + 1}$$

Research Question 1.1

"What part of the captured sound's power spectral density can be attributed to the pressure fluctuations induced by the phenomena inside the boundary layer and how it can be isolated from the overall microphone signals?"

The shape of the microphones' signals PSDs collected from both the wind tunnel and flight experiments indicate that the hydrodynamic pressure fluctuations induced by the turbulent flow structures in the TBL are dominating the microphones' recordings. Other major contributors to the PSD are the sound from the motors and propellers as well as the electrical noise, both of which take the form of peaks in the PSD plots. Subtracting the two signals, from the left- and right-mounted microphones, successfully filters the contribution from the motors. However, for higher AoA when the boundary layer collapses, the microphones' data is no longer dominated by hydrodynamic pressure fluctuations from a TBL and the peaks corresponding to the sound of the motors are visible in the PSD plots. Furthermore, the subtraction method is not successful in filtering the electrical noise, mostly evident from the presence of harmonics of the 50 Hz component in the PSDs of the microphones' signals collected during the wind tunnel experiments, visible from the figures in Section 5.2.

Research Question 1.2

"How does the angle of attack affect the characteristics of the pressure fluctuations captured by a microphone mounted on the vehicle's surface?"

Looking at the figures in Subsection 5.1.2 depicting the PSD plots for changing AoA at a given airspeed and motor configuration, as the AoA starts to increase, so does the power of the signal, with the biggest impact being seen in the lower frequencies, mostly below 4 kHz. At the same time, the decay rate of the PSD appears to increase with the AoA as well. As the AoA continues to increase, the overall power of the signal increases over the whole frequency range of interest. This seems to happens at AoA of 30^o to 45^o. Going to even higher AoA leads to an abrupt decrease in the power of frequencies up to 4 kHz.

The observed behavior is determined by a number of factors discussed in the scientific paper in Part I. These include the nose cone's geometry, which is more impactful at lower AoA, the separation of the boundary layer with a wake of recirculating flow forming over the vehicle's surface at slightly higher AoA, and finally the forming of an area of lower pressure over the top side of the nose cone where the microphones are mounted at very high AoA.

Research Question 1.3

"How does the microphone mounting location affect the measured characteristics of the pressure fluctuations stemming from the boundary layer?"

During the experiments only one mounting configuration for the microphones was trialed, namely two microphones placed a distance of 55 mm downstream from the top of the nose cone, separated 40 mm apart. From the figures provided in Subsection 5.1.1 and Subsection 5.1.2 it can be seen that for microphones mounted at the same distance downstream, differences appear in the PSD of their signals. This is due to the fact that for two points at the same distance downstream, but separated by more than a single boundary layer thickness apart, the hydrodynamic pressure fluctuations from the turbulent flow structures should are uncorrelated [11].

At the same time, from the theory reviewed in Section 3.2, conclusions can be drawn whether any impact is expected when mounting the microphones at different locations on the vehicle's body. Mounting the microphones further downstream on the fuselage skin should result in the PSDs of their signals having overall higher magnitude for the same airspeed and AoA as the boundary layer flow could already have separated, forming a wake with stronger vortical structures in it. This behavior would be valid until a high enough AoA is reached, where the boundary layer flow would collapse, leading to an abrupt decrease in the PSD magnitude. The further downstream the microphones will be mounted, the earlier the boundary

layer flow will collapse, or in other words, for lower AoA. Mounting the microphones on the wings would impact the shape and magnitude of their signals' PSD depending on the shape of the airfoil as it impacts the pressure gradient of the boundary layer flow over it. Finally, mounting the microphones further upstream on the vehicle's body could place them under boundary layer flow that has not yet transitioned to a fully turbulent state, meaning that the energy of the hydrodynamic pressure fluctuations would be lower.

Research Question 1.4

"What are the required hardware components that will constitute an airspeed instrument, whose working principle is to estimate the vehicle's airspeed by relating it to the characteristics of the pressure fluctuations originating from the phenomena inside the boundary layer?"

An instrument that could estimate the vehicle's airspeed by making use of the proposed working principle needs to be composed of microphones to capture the hydrodynamic pressure fluctuations caused by the flow structures in the TBL and a micro-controller to process the microphones' signals, compute the resulting PSD, and relate it to the airspeed using a dedicated model. These two components are enough to deliver the desired functionality of the airspeed instrument. However, supporting components might be needed depending on the characteristics on the microphones and micro-controller.

In the current design of the airspeed instrument, the microphones output analog signals and the micro-controller has limited analog-to-digital conversion capabilities. As such, an external ADC is required in order to achieve the desired sampling frequency and provide higher resolution for the analog microphones' signals. Furthermore, all of the components needs to be powered, so a dedicated battery is included as part of the airspeed instrument in order to provide clean voltage, free from fluctuations in the vehicle's power supply. A linear voltage regulator brings the battery voltage from 7.4 V to 5 V to power the micro-controller, which in turn converts the voltage to 3.3V to power the microphones and the analog line of the ADC.

Research Question 1.5

"How can the different airspeed instrument components be integrated to form a functioning system?"

In the current design, put forward as part of this research project, the different components are integrated on a prototyping board and communicate using the I2S protocol. The inclusion of a dedicated ADC makes it possible to feed the analog microphones' signals in digital form to the micro-controller. The micro-controller and the ADC sync their clocks by connecting their clock pins, with the micro-controller being the master and the ADC - the slave. The micro-controller is programmed to read the data from its digital pin to which the ADC feeds the converted microphones' signals and save it in binary format. All of the components that are part of the airspeed instrument are powered by a dedicated battery, part of the instrument itself.

7

Recommendations

In its current state, additional work is needed in order to improve the instrument's functionality and bring it to a technology demonstration level. As such, this chapter provides a brief overview of the major recommendations for the future continuation of this research project. The recommendation are aimed not only at the design of the airspeed instrument, but also at the methodology of the research.

Recommendation 1
From the research's findings it was concluded that the subtraction method for the microphones' signals yielded little to no benefits due to the TBL-induced hydrodynamic pressure fluctuations being dominant. This means that the configuration of two microphones mounted at the same location downstream, separated by a distance greater than the expected boundary layer thickness at the given location, can be scrapped.

One recommendation is to keep the number of microphones the same, but change the mounting configuration to have the microphones behind one another at different distances downstream. This configuration can be used to detect boundary layer flow separation by analyzing the magnitude and shape of the PSDs of the two microphones' signals and also detect separation bubbles.

Alternatively, the number of microphones can be reduced to just one. A major benefit of this recommendation is the reduced amount of data that needs to be read and processed by the micro-controller, which will consequently decrease the time needed to complete the airspeed estimation, essentially increasing the number of times the airspeed can be computed per unit of time. However, to achieve this, it is recommended to retrain the feed-forward ANN model on PSD data of microphones' signals with length of less than a second.

Recommendation 2
The second recommendation stems from the setup of the flight experiments carried out as part of this research project. It is to conduct new flight tests with a dedicated AoA sensor installed on the vehicle, allowing to collect accurate data about this parameter during flight. As such, the models that include the AoA as an input parameter can be trained and validated using representative real world flight data. This will allow to judge the impact of having the AoA as an input in the airspeed estimation upon the accuracy and precision of the models for a wide range of AoA. The expectation is that the performance of the models will be improved based on the findings for model structures including the AoA as an input parameter but trained over the wind tunnel data as outlined in the scientific paper in Part I.

Recommendation 3
This recommendation is again related to the setup of the flight experiments. It will be beneficial to install an additional airspeed sensor, more specifically a hot-wire anemometer that will be used to validate the airspeed measurements. Furthermore, as the hot-wire anemometer does not suffer from reduced accuracy at lower airspeed, it can also be used to calibrate the Pitot tube.

Recommendation 4
It will be beneficial to carry out wind tunnel testing utilizing the same vehicle configuration as that for the flight tests. This means reading and processing the microphones' signals using the instrument's own micro-controller and measuring the airspeed using a Pitot tube mounted on the vehicle. A further recommendation

is to also include AoA sensor on the vehicle, validating the accuracy of its AoA measurements, and a hot-wire anemometer to calibrate the Pitot tube's measurements at low airspeed. This will allow for better assessment of the differences between the wind tunnel and flight data stemming from the distinct equipment and experimental setup used, as well as the environmental conditions. Lastly, it can serve to confirm that the 50 Hz component present in the collected wind tunnel data is indeed caused by the equipment utilized during those experiments.

Recommendation 5
The current design of the airspeed instrument includes several different components integrated on a prototyping board and connected via soldered wires. The quality of the soldering and the components can impact the electrical noise that will be present in the acquired signals. Therefore, building a custom PCB for the instrument, with an integrated microprocessor, ADC, and voltage regulators, can improve the quality of the signal acquisition. Reducing the electrical noise can also lead to the PSDs of the subtracted microphones' signals being better suited for constructing the models as the large discrepancies in the peaks between the wind tunnel and flight data will be removed. Furthermore, it will substantially decrease the instrument's size and weight, thus limiting its impact on the vehicle's flight dynamics.

Recommendation 6
The range of operations of the airspeed instrument can be further extended by performing experiments to study the effects of air density, temperature and humidity on the resulting PSD of the microphones' signals, and consequently on the performance of the airspeed instrument. This will allow to refine the airspeed estimations for a wide range of conditions by using data from sensors on the vehicle measuring the relevant parameters. However, to achieve this, the modeling process will need to be adjusted accordingly by including the environmental parameters as inputs in the model structure. At this point, sensor fusion can also be considered.

Recommendation 7
It was shown that the AoA has a distinct effect upon the PSD of the microphones' signals for otherwise the same airspeed, motor settings and environmental conditions. Therefore, it is recommended to investigate whether the proposed instrument concept can also be used to predict the vehicle's AoA in conjunction with the airspeed. This can be achieved by modifying the feed-forward ANN's structure to have two outputs, namely the airspeed and the AoA, while keeping the inputs to be the PSD of the microphones' signals.

References

[1] J.D. Anderson. *Fundamentals of Aerodynamics*. New York, NY, United States: McGraw-Hill Education, 2016.

[2] Gabriel Hugh Elkaim et al. “Principles of Guidance, Navigation, and Control of UAVs”. In: *Handbook of Unmanned Aerial Vehicles*. Ed. by K. Valavanis et al. Netherlands: Springer, 2015, pp. 347–380.

[3] E. H. J. Pallet et al. *Aircraft Instruments & Integrated Systems*. first. London: Pearson, 1992.

[4] Icaro de Oliveira Buscarini et al. “Impact of Pitot tube calibration on the uncertainty of water flow rate measurement”. In: *Journal of Physics: Conference Series* 648 (2015), pp. 12005–12015. DOI: 10.1088/1742-6596/648/1/012005.

[5] Sebastian L. Verling et al. “Full Envelope System Identification of a VTOL Tailsitter UAV”. In: *Proceedings of American Institute of Aeronautics and Astronautics: Scitech Forum 2021*. 2021. DOI: 10.2514/6.2021-1054.

[6] Sunyi Wang et al. “Battle the Wind: Improving Flight Stability of a Flapping Wing Micro Air Vehicle Under Wind Disturbance With Onboard Thermistor-Based Airflow Sensing”. In: *IEEE Robotics and Automation Letters* 7.4 (2022), pp. 9605–9612. DOI: 10.1109/LRA.2022.3190609.

[7] G. P. Obi Reddy et al. *Geospatial Technologies in Land Resources Mapping, Monitoring and Management*. 1st. Berlin Heidelberg: Springer Berlin Heidelberg, 2018.

[8] Frank M. White. *Viscous Fluid Flow*. McGraw-Hill international edition. New York, NY, United States: McGraw-Hill, 2006.

[9] W W Willmarth. “Pressure Fluctuations Beneath Turbulent Boundary Layers”. In: *Annual Review of Fluid Mechanics* 7.1 (1975), pp. 13–36. DOI: 10.1146/annurev.fl.07.010175.000305.

[10] Timothy A. Brungart et al. “Outer-flow effects on turbulent boundary layer wall pressure fluctuations”. In: *The Journal of the Acoustical Society of America* 105.4 (1999), pp. 2097–2106. DOI: 10.1121/1.426815.

[11] Michael Roger. *Microphone Measurements in Aeroacoustic Installations*. Tech. rep. 36 Avenue Guy de Collongue, 69134 Ecully cedex, France: University of Lyon, Dec. 2017. DOI: 10.14339/STO-EN-AVT-287-03-PDF.

[12] Finn Jacobsen. “Sound intensity and its measurements”. In: pp. 2231–2246.

[13] J. Eargle. *The Microphone Book: From Mono to Stereo to Surround - a Guide to Microphone Design and Application*. Boca Raton, FL, United States: Taylor & Francis, 2012.

[14] K.Z. Huang et al. *Machine Learning: Modeling Data Locally and Globally*. Advanced Topics in Science and Technology in China. Berlin Heidelberg: Springer Berlin Heidelberg, 2008.

[15] S.M. Belotserkovsky et al. *Two-Dimensional Separated Flows*. Boca Raton, FL, United States: Taylor & Francis, 1992.

[16] J. Zhu et al. *Calculations of Turbulent Separated Flows*. NASA technical memorandum. National Aeronautics and Space Administration, 1993.

[17] M. Brandstein et al. *Microphone Arrays: Signal Processing Techniques and Applications*. Digital Signal Processing. Berlin Heidelberg: Springer Berlin Heidelberg, 2013.

[18] Robert F. Stengel. *Flight Dynamics*. 1st. Princeton, NJ, USA: Princeton University Press, Oct. 2004.

[19] Alan T. J. Hayward. *Flowmeters: A Basic Guide and Source-Book for Users*. 1st. London, United Kingdom: Palgrave Macmillan, 1979.

[20] *American National Standard on Acoustical Terminology*. Standard. New York, NY, United States: American National Standards Institute, Oct. 2013.

[21] Douglas C. Giancoli. *Physics for Scientists & Engineers with Modern Physics*. 4th. London, United Kingdom: Pearson, 2008.

[22] Lawrence E. Kinsler et al. *Fundamentals of Acoustics*. 4th. New York, NY, United States: John Wiley & Sons, Jan. 2000.

[23] M. E. Delany. “Sound Propagation in the Atmosphere: A Historical Review”. In: *Acta Acustica united with Acustica* 38.4 (Oct. 1977).

[24] S. Spors et al. “Spatial Sound With Loudspeakers and Its Perception: A Review of the Current State”. In: *Proceedings of the IEEE* 101.9 (2013), pp. 1920–1938. DOI: 10.1109/JPROC.2013.2264784.

[25] J.P. Lefebvre. “Chapter 1 - Physical Basis of Acoustics”. In: *Acoustics*. Ed. by Paul Filippi et al. London: Academic Press, 1999, pp. 1–39. DOI: 10.1016/B978-012256190-0/50002-6.

[26] Marshall Long. “2 - Fundamentals of Acoustics”. In: *Architectural Acoustics (Second Edition)*. Ed. by Marshall Long. Second Edition. Boston: Academic Press, 2014, pp. 39–79. DOI: 10.1016/B978-0-12-398258-2.00002-7.

[27] Ross J. Roeser et al. *Audiology: Diagnosis*. Thieme Publishers Series. Thieme, Aug. 2007.

[28] Julian W. Gardner et al. *Microsensors, MEMS, and Smart Devices*. 1st. New York, NY, United States: John Wiley & Sons, Dec. 2001.

[29] M.P. Norton et al. “VIBRATION GENERATED SOUND | Fundamentals”. In: *Encyclopedia of Vibration*. Ed. by S. Braun. Oxford: Elsevier, 2001, pp. 1443–1455. DOI: 10.1006/rwvb.2001.0207.

[30] David Morin. *Seminar 5: Longitudinal Waves*. Cambridge, MA, United States: Harvard University, Aug. 2014.

[31] Roger A. Kendall. “The Role of Acoustic Signal Partitions in Listener Categorization of Musical Phrases”. In: *Music Perception* 4.2 (Dec. 1986), pp. 185–213. DOI: 10.2307/40285360. eprint: https://online.ucpress.edu/mp/article-pdf/4/2/185/191580/40285360.pdf.

[32] David T. Blackstock. *Fundamentals of Physical Acoustics*. 1st. New York, NY, United States: John Wiley & Sons, Apr. 2000.

[33] OpenStax. *Speed of Sound*. [Online; accessed 2021-04-01]. Nov. 12, 2020. URL: https://chem.libretexts.org/@go/page/4077.

[34] Claus Borgnakke et al. *Fundamentals of Thermodynamics*. 10th. New York, NY, United States: John Wiley & Sons, Feb. 2019.

[35] John E. Oliver. “Standard atmosphere”. In: *Climatology*. Boston, MA: Springer US, 1987, pp. 801–803. DOI: 10.1007/0-387-30749-4_167.

[36] David Borthwick. *Introduction to Partial Differential Equations*. 1st. Boston, MA, United States: Springer US, 2016.

[37] J. Eargle. *The Microphone Handbook*. Elar Publishing, 1982.

[38] M. Clifford. *Microphones: How They Work & how to Use Them*. TAB Books. G/L Tab Books, 1977.

[39] I. Corbett. *Mic It!: Microphones, Microphone Techniques, and Their Impact on the Final Mix*. Boca Raton, FL, United States: Taylor & Francis, 2014.

[40] Nicolas Collins et al. “Electret Microphones”. In: *Handmade Electronic Music*. Boca Raton, FL, United States: Taylor & Francis, June 2020, pp. 74–81. DOI: 10.4324/9780429264818-14.

[41] D. Grigoriev et al. “Condenser MEMS Microphone”. In: *Russian Microelectronics* 49 (Jan. 2020), pp. 37–42. DOI: 10.1134/S1063739720010084.

[42] E. Brixen. *Audio Metering*. Boca Raton, FL, United States: Taylor & Francis, 2012.

[43] Michel Rieutord. *Fluid Dynamics - An Introduction*. 1st. 1868-4513. Boston, MA, United States: Springer International, 2015.

[44] Philip M. Gerhart et al. *Fundamentals of Fluid Mechanics*. 8th. New York, NY, United States: John Wiley & Sons, Mar. 2020.

[45] D. J. Auld et al. *Aerodynamics for students*. 1st. Aerospace, Mechanical & Mechatronic Engeneering at the University of Sydney, 1995.

[46] Spencer Everett Lillywhite. “Microphone-based pressure diagnostics for boundary layer transition”. MA thesis. San Luis Obispo, CA, United States: California Polytechnic State University, July 2013.

[47] Andrew R. Barnard. *Flow Induced Noise Reduction Techniques for Microphones in Low Speed Wind Tunnels*. Primary research report. 1400 Townsend Dr, Houghton, MI 49931, United States: Michigan Technological University, Oct. 2014.

[48] Yoshifumi Yokoi. “Experimental Study of Internal Flow Noise Measurement by Use of a Suction Type Low Noise Wind Tunnel”. In: *Wind Tunnel Designs and Their Diverse Engineering Applications*. Ed. by Noor Ahmed. Sydney, Australia: IntechOpen, 2013. Chap. 7, pp. 147–164.

[49] Ehab Banihani et al. “Boundary-Layer Theory of Fluid Flow past a Flat-Plate: Numerical Solution using MATLAB”. In: *International Journal of Computer Applications* 180.18 (Feb. 2018). DOI: 10.5120/ijca2018916374.

[50] G. Falkovich. *Fluid Mechanics*. 2nd. Cambridge University Press, 2018.

[51] G. Castiglioni et al. “Numerical simulations of separated flows at moderate Reynolds numbers appropriate for turbine blades and unmanned aero vehicles”. In: *International Journal of Heat and Fluid Flow* 49 (2014). 8th Symposium on Turbulence & Shear Flow Phenomena (TSFP8), pp. 91–99. DOI: 10.1016/j.ijheatfluidflow.2014.02.003.

[52] Javier Jiménez. “Coherent structures in wall-bounded turbulence”. In: *Journal of Fluid Mechanics* 842 (Mar. 2018). DOI: 10.1017/jfm.2018.144.

[53] Cunbiao Lee et al. “Flow structures in transitional and turbulent boundary layers”. In: *Physics of Fluids* 31 (Oct. 2019). DOI: 10.1063/1.5121810.

[54] M. R. Head et al. “New aspects of turbulent boundary-layer structure”. In: *Journal of Fluid Mechanics* 107 (1981), pp. 297–338. DOI: 10.1017/S0022112081001791.

[55] R. J. Adrian et al. “Vortex organization in the outer region of the turbulent boundary layer”. In: *Journal of Fluid Mechanics* 422 (2000), pp. 1–54. DOI: 10.1017/S0022112000001580.

[56] S. K. Robinson. “Coherent Motions in the Turbulent Boundary Layer”. In: *Annual Review of Fluid Mechanics* 23.1 (1991), pp. 601–639. DOI: 10.1146/annurev.fl.23.010191.003125.

[57] R. E. Falco. “A coherent structure model of the turbulent boundary layer and its ability to predict Reynolds number dependence”. In: *Philosophical Transactions of the Royal Society of London. Series A: Physical and Engineering Sciences* 336 (1641 1991). DOI: 10.1098/rsta.1991.0069.

[58] R. E. Falco et al. “Vortex ring/viscous wall layer interaction model of the turbulence production process near walls”. In: *Experiments in Fluids* 6 (5 1988), pp. 305–315. DOI: 10.1007/BF00538821.

[59] M. S. Acarlar et al. “A study of hairpin vortices in a laminar boundary layer. Hairpin vortices generated by a hemisphere protuberance”. In: *Journal of Fluid Mechanics* 175 (1987), pp. 1–83. DOI: 10.1017/S0022112087000272.

[60] Cunbiao Lee et al. “Transition in Wall-Bounded Flows”. In: *Applied Mechanics Reviews* 61 (May 2008). DOI: 10.1115/1.2909605.

[61] Ron F. Blackwelder et al. “Streamwise vortices associated with the bursting phenomenon”. In: *Journal of Fluid Mechanics* 94.3 (1979), pp. 577–594. DOI: 10.1017/S0022112079001191.

[62] Zambri Harun et al. “Generation, Evolution, and Characterization of Turbulence Coherent Structures”. In: *Turbulence and Related Phenomena*. Ed. by Régis Barillé. Rijeka, Croatia: IntechOpen, 2019. Chap. 4. DOI: 10.5772/intechopen.76854.

[63] Yutaka Miyake et al. “The Regeneration of Quasi-Streamwise Vortices in the Near-Wall Region”. In: *JSME International Journal Series B* 40.2 (1997), pp. 257–264. DOI: 10.1299/jsmeb.40.257.

[64] B. J. McKeon. “The engine behind (wall) turbulence: perspectives on scale interactions”. In: *Journal of Fluid Mechanics* 817 (2017), P1. DOI: 10.1017/jfm.2017.115.

[65] David J. C. Dennis et al. “Experimental measurement of large-scale three-dimensional structures in a turbulent boundary layer”. In: *Journal of Fluid Mechanics* 673 (2011), pp. 218–244. DOI: 10.1017/S0022112010006336.

[66] Romain Mathis et al. “Comparison of large-scale amplitude modulation in turbulent boundary layers, pipes, and channel flows”. In: *Physics of Fluids* 21 (11 2009). DOI: 10.1063/1.3267726.

[67] Colin Van Der Creek et al. *Evaluation of the effect of microphone cavity geometries on acoustic imaging in wind tunnels*. Tech. rep. Kluyverweg 1, 2629 HS Delft, The Netherlands: Delft University of Technology, Oct. 2020.

[68] P. A. Krogstad et al. “Convection velocities in a turbulent boundary layer”. In: *Physics of Fluids* 10 (4 1998). DOI: 10.1063/1.869617.

[69] Donald Coles. “The law of the wake in the turbulent boundary layer”. In: *Journal of Fluid Mechanics* 1.2 (1956), pp. 191–226. DOI: 10.1017/S0022112056000135.

[70] M. V. Lowson. *Pressure fluctuations in turbulent boundary layer*. Tech. rep. Washington D.C., USA: National Aeronautics and Space Administration, Dec. 1965.

[71] Yves Doisy. “Modelling wall pressure fluctuations under a turbulent boundary layer”. In: *Journal of Sound and Vibration* 400 (2017), pp. 178–200. DOI: 10.1016/j.jsv.2017.04.004.

[72] Andrew R. Barnard. *Flow Induced Noise Reduction Techniques for Microphones in Low Speed Wind Tunnels*. Tech. rep. 1400 Townsend Dr, Houghton, MI 49931, United States: Michigan Technological University, Oct. 2014.

[73] Creighton Lane. “Measurement of Turbulent Boundary Layer Induced Surface Pressure Fluctuations”. MA thesis. North York, ON M3H 5T6, Canada: University of Toronto, July 2018.

[74] Michael Goody et al. “Surface pressure fluctuations and pressure-velocity correlations produced by a separated flow around a prolate spheroid at incidence”. In: *35th Aerospace Sciences Meeting and Exhibit*. DOI: 10.2514/6.1997-485.

[75] R. Goldstein. *Fluid Mechanics Measurements*. CRC Press, 2017.

[76] G. M. Corcos. “Resolution of Pressure in Turbulence”. In: *The Journal of the Acoustical Society of America* 35 (2 1963), pp. 192–199. DOI: 10.1121/1.1918431.

[77] M. W. Wambsganss et al. *Measurement, interpretation, and characterization of near-field flow noise*. Tech. rep. Lemont, IL, USA: Argonne National Laboratory, 1970.

[78] Roger L. Simpson et al. “Surface pressure fluctuations in a separating turbulent boundary layer”. In: *Journal of Fluid Mechanics* 177 (1987), pp. 167–186. DOI: 10.1017/S0022112087000909.

[79] N. K. Agarwal et al. “A new technique for obtaining the turbulent pressure spectrum from the surface pressure spectrum”. In: *Journal of Sound Vibration* 135.2 (Dec. 1989), pp. 346–350. DOI: 10.1016/0022-460X(89)90731-1.

[80] Semih M. Olcmen et al. “Influence of Wing Shapes on Surface Pressure Fluctuations at Wing-Body Junctions”. In: *AIAA Journal* 32.1 (1994), pp. 6–15. DOI: 10.2514/3.48283.

[81] Nathaniel D. Varano. “Fluid dynamics and surface pressure fluctuations of turbulent boundary layers over sparse roughness”. PhD thesis. Virginia Tech, 2010.

[82] Martin Nilsson. *Kalman Filtering with Unknown Noise Covariances*. Tech. rep. POB 1263, 164 29 Kista: Swedish Institute of Computer Science, May 2006.

[83] Y. Wang et al. *Spectral Analysis of Signals: The Missing Data Case*. Synthesis Digital Library: Signal processing and communications collection I. Morgan & Claypool Publishers, 2005.

[84] Robert Rackl et al. *Modeling of Turbulent Boundary Layer Surface Pressure Fluctuation Auto and Cross Spectra – Verification and Adjustments Based on TU-144LL Data*. Tech. rep. Seattle, WA, USA: The Boeing Company, 2005.

[85] Michael Goody. “Empirical Spectral Model of Surface Pressure Fluctuations”. In: *AIAA Journal* 42.9 (2004), pp. 1788–1794. DOI: 10.2514/1.9433.

[86] A.V. Smol’yakov. “Calculation of the spectra of pseudosound wall-pressure fluctuations in turbulent boundary layers”. In: *Acoustical Physics* 46 (2000), pp. 342–347. DOI: 10.1134/1.29890.

[87] T. S. Miller. “Turbulent boundary layer models for acoustic analysis”. PhD thesis. Wichita State University, 2011.

[88] Robert H. Kraichnan. “Pressure Fluctuations in Turbulent Flow over a Flat Plate”. In: *The Journal of the Acoustical Society of America* 28 (1956), pp. 378–390. DOI: 10.1121/1.1908336.

[89] G. M. Lilley et al. *On surface pressure fluctuations in turbulent boundary layer*. Primary research report. College Rd, Cranfield, Wharley End, Bedford MK43 0AL, United Kingdom: The College of Aeronautics Cranfield, Apr. 1960.

[90] William K. Blake. “Turbulent boundary-layer wall-pressure fluctuations on smooth and rough walls”. In: *Journal of Fluid Mechanics* 44.4 (1970), pp. 637–660. DOI: 10.1017/S0022112070002069.

[91] Günter Schewe. “On the structure and resolution of wall-pressure fluctuations associated with turbulent boundary-layer flow”. In: *Journal of Fluid Mechanics* 134 (1983), pp. 311–328. DOI: 10.1017/S0022112083003389.

[92] Richard M. Lueptow. “Transducer resolution and the turbulent wall pressure spectrum”. In: 97 (1995), pp. 370–378. DOI: 10.1121/1.412322.

[93] Y. Na et al. “The structure of wall-pressure fluctuations in turbulent boundary layers with adverse pressure gradient and separation”. In: *Journal of Fluid Mechanics* 377 (1998), pp. 347–373. DOI: 10.1017/S0022112098003218.

[94] M. Bull. “Wall-pressure fluctuations beneath turbulent boundary layers: some reflections on forty years of research”. In: *Journal of Sound and Vibration* 190 (1996), pp. 299–315.

[95] Robert Haber et al. *Nonlinear System Identification — Input-Output Modeling Approach*. 1st. Vol. 7. Dordrecht, Netherlands: Springer Netherlands, 1999.

[96] Zhengming Wang et al. *Measurement Data Modeling and Parameter Estimation*. 1st. Boca Raton, FL, United States: CRC Press, 2017.

[97] J. Brownlee. *Better Deep Learning*. Machine Learning Mastery, 2018.

[98] Julia Ling et al. “Development of Machine Learning Models for Turbulent Wall Pressure Fluctuations”. In: Jan. 2017. DOI: 10.2514/6.2017-0755.

[99] Joachim van der Herten et al. “Adaptive classification under computational budget constraints using sequential data gathering”. In: *Advances in Engineering Software* 99 (2016), pp. 137–146. DOI: 10.1016/j.advengsoft.2016.05.016.

[100] Michael James Lighthill. “On sound generated aerodynamically II. Turbulence as a source of sound”. In: *The Royal Society Publishing* 222 (1954). DOI: 10.1098/rspa.1954.0049.

[101] C. Shraddha et al. “Noise Cancellation and Noise Reduction Techniques: A Review”. In: pp. 159–166.

[102] Marcel Gabrea et al. “A Single Microphone Kalman Filter-Based Noise Canceller”. In: *IEEE Signal Processing Letters* 6.3 (1999). DOI: 10.1109/97.744623.

[103] Michael Asher et al. “A review of surrogate models and their application to groundwater modeling”. In: *Water Resources Research* 51.8 (July 2015). DOI: 10.1002/2015WR016967.

[104] Ankit Mishra et al. “Analysis of flow variation over elliptical nose cone at different angle of attack”. In: 20 (Sept. 2020), pp. 01–06.

[105] Imran Afgan et al. “Flow Over a Flat Plate with Uniform and Coherent Gust Inlets”. In: *Journal of Fluid Mechanics* 720 (Apr. 2013), pp. 457–485. DOI: 10.1017/jfm.2013.25.